Dottorato di Ricerca in Ingegneria delle Strutture - XXXIV Ciclo

Dipartimento di Ingegneria
Università degli Studi di Palermo
Viale delle Scienze, 90128 Palermo (Italy)

Coordinatore: Prof. Antonina Pirrotta

Out of Plane response of Unreinforced Masonry infills: Comparative analysis of experimental tests for the definition of strategies of macro modelling and fragility prediction

Tesi di Dottorato di

Ing. Bharat Pradhan

Relatori:

Prof. Liborio Cavaleri (Università degli Studi di Palermo, Italy)

Prof. Vasilis Sarhosis (University of Leeds, UK)

PALERMO, 2021

Settore Disciplinare ICAR 09

ABSTRACT

During an earthquake, an interaction between the in-plane and out-of-plane seismic forces occurs and the infilled frames suffer damage in both in-plane and out-of-plane directions simultaneously. Particularly, the out-of-plane collapse of unreinforced masonry infill walls is critical even for new buildings complying with the modern seismic codes, resulting in high casualties and huge economic losses. However, the out-of-plane behaviour of infill walls is yet not fully understood. This study is therefore aimed towards characterizing the out-of-plane seismic capacity of unreinforced masonry infill walls.

First of all, available out-of-plane experimental tests performed on unreinforced masonry infill walls are reviewed with a detailed comparison of the experimental results. The influence of parameters like slenderness ratio, aspect ratio, boundary conditions, openings, vertical load, in-plane damage level, the strength of masonry and plaster, and frame stiffness are evaluated, and research gaps are identified.

Based on the collected experiments, all available analytical capacity models are checked for their accuracy in the prediction of the out-of-plane capacity of unreinforced masonry infill walls. In doing so, both types of capacity models are evaluated: Type (I) for the estimation of the out-of-plane strength in the in-plane undamaged state; Type-II for the estimation of out-of-plane strength reduction factor for the in-plane damaged state. Afterwards, the best pairs of models from two groups i.e. Type I and Type II, are coupled and checked with the experimented specimens where the reference infill specimen (specimen tested in out-of-plane without prior in-plane damage) is not

available. In addition, the influence of orthotropy of the infill masonry in the out-of-plane capacity predicted by the capacity models is analysed. The possibility of using the capacity models in the cases of infill-beam gap and infill with openings is also checked.

Different available macro-modelling techniques are investigated and a simple macro-element model which can simulate the behaviour of unreinforced masonry infill walls under in-plane and out-of-plane loads is developed. The model is validated with different sets of experiments. The model takes into account the decrease in out-of-plane capacity due to prior in-plane damage and is capable to capture in-plane/out-of-plane interaction effects of the seismic forces. From the correlation between the experimental and macro-model results, empirical equations are developed that can be used to calculate the stress-strain parameters required for defining the compressive behaviour of the struts. With the provided strategy, the geometrical and mechanical parameters required for the struts can be easily identified for numerical modelling of the infill wall. Using the model, in-plane and out-of-plane responses of the infill wall in lateral loads can be checked.

To enrich the information obtained from the experiments regarding the out-of-plane behaviour of infill walls, numerical experimentation is performed by using the developed macro-model covering the range of infill's geometrical and mechanical properties. From the detailed parametric analysis, the out-of-plane strength of the infill wall is found to be largely influenced by compressive strength, slenderness ratio, aspect ratio, and more importantly by the level of in-plane damage. The decay of strength and stiffness due to prior in-plane damage is also largely governed by the strength and the slenderness ratio of the unreinforced masonry infill. Based on the numerical results, empirical equations are proposed for the evaluation of the infilled frame's out-of-plane capacity under in-plane damaged or undamaged conditions. The

reliability of the proposed equations is proved by comparisons with experimental results.

Finally, a procedure for developing the out-of-plane fragility functions is proposed by using the developed macro-model. The fragility is calculated assuming the uncertainty in the geometric and mechanical properties of infill walls instead of the uncertainty in the seismic input. The fragility is defined with respect to the position of the infill wall in a low-rise RC building. Experimental data available in the literature are used for the validation of the output. Overall, the results indicated lower vulnerability in the out-of-plane direction for infill walls without prior in-plane damage and high vulnerability when the infill wall is prior damaged in the in-plane. The proposed procedure can be extended to other types of infill walls depending on the construction technique of the site of interest, obtaining different and specific fragility curves for perming a large-scale risk analysis.

ACKNOWLEDGEMENTS

The research work reported in this thesis was conducted in the Department of Engineering, University of Palermo, Palermo, Italy, under the supervision of Professor Liborio Cavaleri, to whom I express my deepest gratitude for his invaluable guidance, motivation and continuous support.

I would like to greatly acknowledge the University of Palermo for the generous scholarship provided throughout this PhD research. I am grateful for the support of the coordinator Professor Antonina Pirrrotta.

Many thanks to my co-supervisor Professor Vasilis Sarhosis from the School of Civil Engineering, University of Leeds, Leeds, UK, for his advice and support in this research work.

Special thanks to Professor Davorin Penava from the Faculty of Civil Engineering and Architecture Osijek, Josip Juraj Strossmayer University of Osijek, Osijek, Croatia for his motivation and encouragement in this research journey.

I would also like to thank my colleagues and friends at the Department of Engineering, especially Dr. Marco F. Ferrotto and Maria Zizzo for their collaborations in the research works. I am also very thankful to my friends Vincenzo Sucato, Dr. Salvatore Pagnotta, Dr. Francesco Cannella, Prof. Giovanni Minafò for all the small help.

Thanks also go to my friends in Italy, Germany, Nepal and abroad who make my living lively and joyous.

Finally, I would like to thank my family for their love, support and encouragement.

TABLE OF CONTENTS

LIST OF FIGURES

FIGURES # PAGE #

LIST OF TABLES

TABLE # PAGE #

LIST OF NOTATIONS

A = total area of the infill

A_o = area of the opening

d = length of the diagonal strut

dof = degree of freedom of each node

E = Young's modulus of the frame member materials

E_m = Young's modulus of masonry

d_{meas} = displacement measured during the experiment

d_{pred} = displacement predicted by using analytical equation

E_{mh} = elastic modulus of masonry in the horizontal direction

E_{mv} = elastic modulus of masonry in the vertical direction

ε_{mo} = peak strain corresponding to peak stress

ε_{mu} = ultimate strain corresponding to the ultimate stress

f_{mo} = peak stress

f_{mu} = ultimate stress

f_{mh} = compressive strength of masonry in the horizontal direction

f_{mv} = compressive strength of masonry in the vertical direction

f_c = compressive strength of concrete

f_m = compressive strength of masonry

G = shear modulus of the frame member materials

g = acceleration due to gravity

h = height of the infil wall

h/t = slenderness ratio

IDR = inter-storey drift ratio

$\overline{IM}$ = median value

I_w = moment of inertia of the infill wall cross-section

I_b = moment of inertia of the surrounding beams

I_c = moment of inertia of the surrounding columns

IP = in-plane

iso = isometric

J_b = torsional constants of beams

J_c = torsional constants of columns

$K_{r,ini}$ = residual initial stiffness of infill wall in OoP direction

l = length of infill wall

L = length of infill wall

$\frac{l_s}{t}$ = slenderness ratio of the strut

l/h = aspect ratio

L/h = aspect ratio

m_w = mass of the infill per unit

M_{yh} = horizontal strips' resisting moments corresponding to horizontal arching

M_{yv} = vertical strips' resisting moments corresponding to vertical arching

M^* = participating mass corresponding to the first OoP mode of vibration

OoP = out-of-plane

ortho = orthotropic

PGA = Peak Ground Acceleration

q_{ult} = OoP capacity

q_{meas} = OoP capacity measured during the experiment

q_{pred} = OoP capacity predicted by using analytical equation

q_{cr} = OoP capacity of infill wall due to crushing of masonry

$q_{\max}$ = OoP capacity of infill wall due to transverse instability

R_o = OoP strength reduction factor due to the openings

R_{ar} = OoP capacity reduction factor due to aspect ratio

R_1 = OoP capacity reduction factor due to IP damage

R_2 = OoP capacity reduction factor due to stiffness of the frames

S_a = pseudo acceleration

t = thickness of infill wall

T_a = fundamental period of the panel in OoP direction

T_1 = fundamental period of the structure (building)

w = width of the strut

w_d = width of the horizontal strut

w_h = width of the horizontal strut

w_v = width of the vertical strut

$\overline{w}$ = surrogate width of the strut

$\overline{w_d}$ = surrogate widths of the diagonal strut

$\overline{w_h}$ = surrogate width of the horizontal strut

$\overline{w_v}$ = surrogate width of the vertical strut

x_{yh} = maximum OoP displacements at the centre of the central horizontal strip

x_{yv} = maximum OoP displacements at the centre of the central vertical strip

Δ_{crack} = in-plane displacement at which the first crack is expected to occur

β = log-standard deviation that accounts for the uncertainties

Δ = OoP mid-height deflection

α = parameter that considers the effect of columns in the horizontal arching

α_{gap} = parameter α when there is a gap between the infill and the top beam

β = parameter that considers the effect of beams in the vertical arching

γ = coefficient depending on the thickness and the slenderness ratio *h/t*

θ = the angle defining the slope of the diagonal struts

ϕ is the standard normal cumulative distribution function

$\dot{\varepsilon}_0$ = axial strain rate at the centroidal axis of the beam

$\dot{e}^s(x)$ = rate of increment of the section deformation

$\dot{s}^s(x)$ = rate of internal force increment

$k_T^S(x)$ = tangent stiffness matrix

$\dot{M}(x)$ = rate of change of the bending moment

$\dot{N}(x)$ = rate of change of axial force

$\dot{k}$ = rate of change of section curvature

1 INTRODUCTION

1.1 Background

Reinforced concrete (RC) framed structures, infilled with unreinforced masonry (URM) walls, are one of the most common techniques of building construction all over the world. In some countries, masonry infilled steel frame buildings are also used. For a long, infill walls were thought of only as partition elements and were never considered in the design of such buildings by the engineers. However, after seismic events across the globe, it was observed that the role of infill walls is non-negligible. The interaction between masonry infills and frames plays a significant role in the overall seismic response of such framed structures (Papia et al. 2003, Di Trapani et al. 2015).

During an earthquake, infill walls are subjected to continuous in-plane (IP) and out-of-plane (OoP) forces because of which they undergo failure either in IP or OoP, although the damage mechanism is a combination of both. Widespread damages have been observed in past and recent earthquakes (Braga et al. 2011, Ricci et al. 2011, Del Gaudio et al. 2017, Varum et al. 2017, Gautam et al. 2021). Damages in infill walls result in huge economic losses due to a significant cost of downtime and repair (Del Vecchio et al. 2018, De Risi et al. 2019a, Del Gaudio et al. 2019). In fact, from the post-earthquake reconstruction after the 2009 L'Aquila earthquake, it was found that the most damaged components in RC buildings were the infill partitions and the total

repair costs of the RC buildings were affected mostly by the repair cost of infill walls (De Martino et al. 2017). In addition, OoP failure of infill walls is a big threat to the safety of the people living around the building.

The topic of masonry infills and their interaction with the RC frames is not new. It has been studied for more than 50 years and is still today not definitively known. Past research was focused on the IP interaction of infill and frames mainly studying the effects of infill walls on the strength and stiffness of the infilled frame structures (Mehrabi et al. 1996, Cavaleri et al. 2005). Typical IP failures of infill walls have been understood and worldwide seismic codes have been modified to take them into account. However, there are still very few provisions to prevent OoP failure of infill walls in design codes (e.g. Eurocode 8 and ASCE/SEI 41-17). The post-earthquake damage surveys show that the OoP collapse of infill walls is critical even for new buildings complying with the modern seismic codes i.e. the OoP seismic vulnerability of infill walls remains also in the modern structures designed to resist earthquake forces (Abrahamczyk et al. 2021). Therefore, accurate characterization of the OoP behaviour of the infill wall is very important to enhance safety and minimize the economic losses in the frequently occurring moderate earthquakes.

Past studies have shown that the OoP capacity of infill walls is influenced by arching action caused by confinement provided by the surrounding frame (McDowell et al. 1956, Dawe and Seah 1989; Angel 1994; Flanagan and Bennett 1999a). The extent of arching depends on the slenderness ratio (height over thickness ratio) of the infill walls. The lower the slenderness ratio, the higher the OoP strength of the infills (Dawe and Seah 1989; Angel 1994; Flanagan and Bennett 1999b; Ricci et al. 2018b). Arching is also influenced by the aspect ratio (length-to-height ratio) of infill walls. Higher aspect ratio decreases the OoP capacity (Lunn and Rizkala 2011;

Moreno-Herera et al. 2016). However, the extent of damage to the infill wall in the IP direction is equally significant for their residual OoP capacity. Experimentally, it has been found that IP damage to infill walls can significantly reduce their OoP capacity (Angel 1994; Calvi and Bolognini 2001; Furtado et al. 2016; Ricci et al. 2018a, Ricci et al. 2018b). During earthquake events, the OoP collapse of masonry infills is often observed at lower to intermediate storeys rather than at the top, where higher OoP acceleration is expected. This is due to IP/OoP interaction effects: higher IP damage occurs in the masonry infills on the lower floors and, as a consequence, they are easily thrown out by OoP seismic (inertial) forces. And the capacity of the infill wall is highly dependent upon its geometrical (slenderness ratio) and mechanical features. Because of the varying nature of these properties (according to places and practices), prediction of the OoP behaviour of infill walls has remained challenging for design engineers due to a lack of an appropriate capacity prediction model or simple numerical modelling technique.

1.2 Aims and Objectives

The aim of this research work is to understand and expand the knowledge on the out-of-plane behaviour of unreinforced masonry infill walls regarding their seismic performance. Within the scope, the following main objectives are summarised:

1. To review the experimental behaviour of URM infill walls in the out-of-plane load. This includes studies of the available experimental tests where masonry infill is tested in OoP load or combined OoP and IP loads and investigating the main parameters affecting the OoP response of infill walls.

2. To study the available analytical capacity models for predicting the OoP capacity of URM infill walls. This includes studying both types of models i.e. i) models for predicting the OoP capacity in IP-undamaged state, ii) models for predicting the OoP capacity reduction in IP-damaged state, and understanding their reliability in the prediction of capacity.
3. To investigate the available strategies for modelling the OoP response of masonry infill walls using macro-element models that are also able to capture the IP capacity of infilled frames.
4. To propose a new macro-element modelling approach for predicting the out-of-plane capacity of URM Infill walls with varying geometrical and mechanical properties. The model should be able to take into account the reduction of the OoP capacity due to prior IP damage in the infill wall.
5. To propose simple analytical equations for predicting the OoP capacity based on parametric analyses performed using the developed macro-model.
6. To compute the OoP fragility functions by using a developed macro-model to understand the seismic vulnerability of URM infill walls.

1.3 Organization

This report is organized into six main chapters. Chapter 1 is an introduction to the topic highlighting the importance, aims and objectives of the research. Chapter 2 deals with the available literature with separate sections about the past experimental studies, analytical capacity models and macro-element modelling of masonry infill walls. Chapter 3 introduces a new macro-element model and discusses its validation with the experimental results. Chapter 4 is a parametric study by varying geometrical and mechanical

properties of masonry infill along with proposals of empirical equations to evaluate the OoP capacity of URM infill walls. In Chapter 5, a standard procedure to derive the OoP fragility functions of URM infill walls in seismic loads is proposed. Finally, Chapter 6 concludes this study with recommendations.

2 LITERATURE REVIEW

In this chapter, literature related to the study of the OoP behaviour of infill walls is reviewed. The investigation covers the past experimental studies, analytical models and macro-element models and each of them is discussed separately in the following sections.

2.1 Experimental studies

Experimental investigations are very important for understanding the OoP behaviour of infill walls. However, the number of available experiments is still very low. Starting from Moghaddam et al. (1988), there are now more than 50 different experimental campaigns conducted so far by various researchers.

In the literature, it can be found that the experiments were conducted by using both quasi-static and dynamic methods with the use of a shake table. Usually, dynamic testing involves large and expensive equipment. Therefore, the decision to use a quasi-static or dynamic loading approach is largely affected by the cost of experimentation. At the same time, the objective of the test is a governing factor. For example, to understand the maximum OoP force that the infill wall can sustain, loading under static conditions is more appropriate. However, to know the level of the actual ground acceleration that an infill wall can sustain, dynamic excitation by the shaking table is better.

In the available experiments, tests on infill walls were conducted either under pure OoP loads, IP and OoP loads applied sequentially, or combined IP and OoP loads applied together. While in a real earthquake, IP and OoP loads

are acting simultaneously, it is difficult to achieve these conditions in quasi-static test settings.

Available experiments were conducted on small to full-scale specimens on single storey single-bay infilled frame to multi-storey frame structures which is mainly determined by the financial aspects and limitations in the lab facilities.

For this study, OoP tests on masonry panels without frames have not been used. Experiments on URM infilled frames tested either in OoP load or in a combination of IP and OoP loads have been considered. Additionally, to augment the understanding, OoP experiments on confined masonry (CM) walls surrounded by frames and tested under similar loading conditions have been used (e.g. Varela-Rivera et al. 2011, Komaraneni et al. 2011, Moreno-Herera et al. 2016). The OoP behaviour of CM walls is similar to that of infill walls. In fact, the OoP capacity of CM walls can be higher for the same size frames due to more effective contact between the masonry and RC elements (Pasca et al. 2017). The difference between the two is that in the infilled frame construction, the infill wall is constructed after the frame has been built (and hardened), while in the other, the RC elements are completed after the masonry walls.

In the experimental tests considered, there are also tests on infill wall specimens with some sort of strengthening elements like bed joint reinforcements, surface reinforcements, textile reinforced mortar, etc. (Dawe and Seah 1989; Pereira et al. 2011; Da Porto et al. 2013, Panto et al. 2019). Definitely, with such measures, specimens showed higher OoP strength compared to the un-strengthened cases. However, the results of such specimens from any experiments have not been used for comparisons in this study.

Similarly, there are OoP experiments on new infill systems designed to reduce the vulnerability seen in the existing infill system. The construction techniques in these new infill types are different from infill walls normally used in practice. For example, Petrus et al. (2015) and Moșoarcă et al. (2016) tested masonry made with a consolidation technique. Preti et al. (2015) and Milanesi et al. (2020) have tested infill systems made with sliding joints, and others (Silva et al. 2016; Verlato et al. 2016; Vailati et al. 2018; Palieraki et al. 2018) proposed infill walls with masonry enclosure systems with a possibility of including horizontal or vertical steel reinforcements. Such new infill systems were found to be very efficient in both IP and OoP loads. These experiments have been included in this study to complete the frame of investigation of OoP experimental tests in infilled frames.

Table 2.1 lists some of the important details from the experimental studies considered in this study. It contains information about the types of frames, type of construction (infill or confined masonry), type of masonry units, the direction of the hole in hollow units, loading types, aspect ratios, slenderness ratios, boundary conditions (gaps with beam and columns), openings, etc. involved in different experimental campaigns. Moreover, the experimental campaigns involving the study of the effect of plaster and the new infill types have been indicated. Due to the high number, the description of each of the experimental campaigns is lengthy and is avoided here, although it could be very insightful. In brief, the properties of masonry infill walls, frames and the loading types involved in different experimental campaigns have been summarised in the following subsections.

Table 2.1 Overview of OoP experimental studies on infill walls

S.N.	Experimental Study	Scale	Frame	Type	No. of tests	Masonry unit	Hole direction	SR h/t	AR l/h	Loading	IP load	OOP load	Vertical load	Gaps with		Opening
														Beam	column	
1	Moghaddam et al. (1988)	<1	Steel	IF	4	SCB	NA (S)	12, 13.9	1.3, 1.4	IP, OoP		D	+	-	-	-
2	Dawe and Seah (1989)	1:1	Steel	IF	9	HCB	V	14.7, 20, 31.1	1.3	OoP		M (AB)	-	- , +	-	- , +
3	Frederiksen (1992)	1:1.36	Steel	IF	16	SCB	NA (S)	26.2	1.2	OoP		M (AB)	-	-	-	-
4	Henderson et al. (1993)	1:1	Steel	IF	2	HCT	H	22.6	1.2	IP, OoP+IP		C (ISD)	-	-	-	-
5	Fowler (1994)	1:1	Steel	IF	20	HCBR	H	11.2	1.5	IP, OoP+IP	D	D	-	-	-	-
6	Angel (1994)	1:1	RC	IF	22	SCB, HCB	NA (S), V	8.7, 11.4, 16.5, 17.7, 34.1	1.5	IP, OoP, IP+OoP	C	M (AB)	- , +	-	-	-
7	Klingner et al. (1996)	1:2	RC	IF	58	SCB	NA (S)	18.4	1.5	IP+OoP, OoP, IP	D	D	+	-	-	-
8	Fardis et al. (1999)	1:1	RC	IF	2	HCBR	NK	21.7, 31.2	1.2	IP / OoP	D	D	+	-	-	-
9	Flanagan and Bennett (1999b)	1:1	Steel	IF	9	HCBL	H	6.8, 11.2, 22.4	1.0	IP, IP+OoP, OoP, OoP+IP, IP / OoP	C	LUR (AB) C (ISD	-	-	-	-
10	Calvi and Bolognini (2001)	1:1	RC	IF	11	HCBL	H	20.4	1.5	OoP, IP+OoP	C	M (PL)	+	-	-	-
11	Žarni´c et al. (2001)	1:4	RC	IF	2	SCB	NA (S)	18.6	1.2, 2.3	IP / OoP	D	D	+	-	-	-
12	Tu et al. (2007)	1:1	RC	CM	2	SCB	NA (S)	NK	NK	OoP		M (ISD)	+	-	-	-
13	Corte et al. (2008)	1:1	RC	IF	2	HCT, HCB	NK	NK	NK	OoP		C (ISD)	+	-	-	-
14	Tu et al. (2010)		RC	IF		SCB		14.4, 29.5	1.0	OoP		D				

S.N.	Experimental Study	Scale	Frame	Type	No. of tests	Masonry unit	Hole direction	SR h/t	AR l/h	Loading	IP load	OOP load	Vertical load	Gaps with		Opening
														Beam	column	
		1:1		CM	28		NA (S)						+	-	-	-
15	Komaraneni et al. (2011)	1:2	RC	IF, CM	3	SCB	NA (S)	10.8, 21.7	1.8	OoP+IP	C	D	+	-	-	-
16	Liu et al. (2011)	1:3	CES	IF	2	SCB	NA (S)	15.80	2.0	OoP		D	-	- , +	-	-
17	Lunn and Rizkala (2011)	1:1	RC	IF	18	SCBR	NA (S)	NK	1., 1.2, 1.6	OoP		M (AB)	-	-	-	-
18	Pereira et al. (2011) ##	2:3	RC	IF	7	HCBR	H	10, 11.3	2.0	IP+OoP	C	C (AB)	+	-	-	-
19	Rabinovitch and Madah (2011)	1:1	RC	IF	2	HCB	V	10.5, 21.1	0.6	OoP		D	+	-	+	-
20	Varela-Rivera et al. (2011)	1:1	RC	CM	6	HCBR	V	11.7	2.0	OoP		M (AB)	-	-	-	-
21	Varela-Rivera et al. (2012a)	1:1	RC	CM	6	HCB	V	18.1, 19.2, 22.7, 24	1, 1.1, 1.3, 1.35	OoP		M (AB)	-	-	-	-
22	Varela-Rivera et al. (2012b)	1:1	RC	CM	3	HCB	V	18.1, 19.2, 24	1.3, 1.3	OoP		M (AB)	- , +	-	-	-
23	Da Porto et al. (2013)) ##	1:1	RC	IF	7	HCBR	V	8.8, 22	1.6	IP+OoP	C	M (PL)	+	-	-	-
24	Hak et al. (2014)	1:1	RC	IF	5	HCBR	V	8.43	0.5, 1.4	IP+OoP, OoP	C	M (PL)	+	-	- , +	-
25	Ingham et al. (2014)	1:1	RC, CES	IF	21	HCBR	V	21, 22, 25, 27, 35, 40	.3, .4,.5,.8, .9,1.1,1.2,1.3	OoP		LUR(AB)	+	-	- , +	-
26	Da Porto et al. (2015)) ##	1:1	RC	IF	8	HCBR	H	17.7	1.6	IP+OoP	C	M (PL)	+	-	-	-
27	Petrus et al. (2015) **	1:1	Steel	IF	5	HCBL	V	14.0	0.8	OoP		C (PL)	-	-	+	-

S.N.	Experimental Study	Scale	Frame	Type	No. of tests	Masonry unit	Hole direction	SR h/t	AR l/h	Loading	IP load	OOP load	Vertical load	Gaps with		Opening
														Beam	column	
28	Preti et al. (2015) **	1:1	Steel	IF	2	HCBR	V	12.9	1.2	IP+OoP	C	LUR (PL)	+	+	-	- , +
29	Akhoundi et al. (2016)	1:2	RC	IF	3	HCBR	H	20.4	1.5	OoP		LUR (AB)	+	- , +	-	- , +
30	Furtado et al. (2016)	1:1	RC	IF	3	HCBR	H	15.3	1.8	IP+OoP, OoP	C	M (AB), LUR (AB)	+ - , +	-	-	-
31	Misir et al. (2016)	1:1	RC	IF	5	HPB, HCBR, SCBL	V, H, NA (S)	7.4, 8.7, 9.1, 13.33	1.6	IP / OoP	C	M (PL)	+	-	-	-
32	Moșoarcă et al. (2016) **	1:1	Steel	IF	2	HCBL	V	14	0.8	OoP		C (PL)	-	-	+	-
33	Moreno-Herera et al. (2016)	1:1	RC	CM	8	HCB, HCBR, SCB	V, NA (S)	23, 24.2, 24.4	1.1, 1.4	OoP		M (AB)	+	-	-	-
34	Silva et al. (2016) **	2:3	RC	IF	4	HCBR	V	16.3	1.5	IP, OoP	C	LUR (AB)	+	-	-	-
35	Singhal and Rai (2016)	1:2	RC	IF, CM	8	SCB	NA (S)	22.8	0.8	OoP+IP	C	D	+	-	-	- , +
36	Tondelli et al. (2016)	1:2	RC	IF	1	HCBR	NK	14.7	1.1	IP, OoP	D	D	+	-	-	-
37	Verlato et al. (2016)	1:1	RC	IF	5	HCBR	V	9.1	0.5, 1.5	OOP, IP+OOP	C	LUR (PL)	+	-	-	-
38	Spesdar (2017)	1:2	RC	IF	4	HCB	V	10.90	1.4	OoP, IP+OoP, OoP+IP+OoP	M	M (AB)	-	-	-	- , +
39	Wang (2017)	1:2	RC, Steel	IF	5	HCB	V	10.9	1.4	IP+OoP, OoP	M	M (AB)	-	- , +	- , +	- , +
40	Di Domenico et al. (2018)	2:3	RC	IF	3	HCBR	H	22.8	1.3	OoP		M (PL)	-	- , +	- , +	-
41	Onat et al. (2018)	1:1	RC	IF	2	HCBR	H	10.2	2.5	IP / OoP	D	D	+	-	-	-

S.N.	Experimental Study	Scale	Frame	Type	No. of tests	Masonry unit	Hole direction	SR h/t	AR l/h	Loading	IP load	OOP load	Vertical load	Gaps with		Opening
														Beam	column	
42	Palieraki et al. (2018)	1:1	RC	IF	2	HCBR	H	25.9	1.3	IP, OoP+IP	C	LUR (PL)	-	-	-	-
43	Ricci et al. (2018a)	2:3	RC	IF	4	HCBR	H	22.8	1.3	IP+OoP, OoP	C	M (PL)	-	-	-	-
44	Ricci et al.(2018b)	2:3	RC	IF	4	HCBR	H	15.2,22.8	1.3	IP+OoP, OoP	C	M (PL)	-	-	-	-
45	Vailati et al. (2018) **	1:1	RC	IF	3	HCBL	V	8	1.7	OoP		LUR (AB)	-	-	-	-
46	Butenweg et al. (2019)	1:1	RC	IF	4	HCBR	V	6.9	1.1	OoP, [P+OoP+IP, IP/OoP	C	CP (AB), LUR (AB)	+	-	- , +	-
47	De Risi et al. (2019b)	2:3	RC	IF	4	HCBR	H	22.8	1.0	IP+OoP, OoP	C	M (PL)	-	-	-	-
48	Di Domenico et al. (2019a)	2:3	RC	IF	4	HCBR	H	15.2, 22.8	1.3	OoP		M (PL)	-	- , +	- , +	-
49	Koutas and Bournas (2019)	1:2	RC	IF	6	SCB	NA (S)	8.9, 19.2	1.4	OoP		M (PL)	-	-	-	-
50	Pantò et al. (2019)	2:3	RC	IF	2	HCBR	V	11.6, 16.3	1.5	OoP		LUR(AB)	+	-	-	-
51	Sagar et al. (2019)	1:2	RC	IF	6	SCB	NA (S)	17.10	1.8	OoP+IP	C	D	+	-	-	-
52	Akhoundi et al. (2018)	1:2	RC	IF	3	HCBR	H	20.4	1.5	IP+OoP	C	LUR (AB)	+	- , +	-	- , +
53	Da Porto et al. (2020)	1:1	RC	IF	5	HCBR	V	8.8	1.6	OoP, IP+OoP	C	M (PL)	+	-	-	- , +
54	Furtado et al. (2020)	1:1	RC	IF	2	HCBR	H	15.30	1.8	OoP		LUR (AB)	+	-	-	-
55	Milanesi et al. (2020) **	1:1	RC	IF	2	HCBR	V	8.43	0.5, 1.4	IP+OoP	C	D	+	-	-	- , +

S.N.	Experimental Study	Scale	Frame	Type	No. of tests	Masonry unit	Hole direction	SR h/t	AR l/h	Loading	IP load	OOP load	Vertical load	Gaps with		Opening
														Beam	column	
56	Wu et al. (2020)	1:1	RC	IF	4	HCBR	H	7.1	1.1	OoP		D	-	-	-	-
57	Anić et al. (2021)	1:2.5	RC	IF	6	HCBR	V	22.8	1.4	OoP		LUR (ISD)	-	-	-	- , +
58	Di Domenico et al. (2021)	1:1	RC	IF	3	HCBR	H	15.3	1.0	OoP, IP+OoP	C	M (PL)	-	-	-	-

Note: ** indicates the experiment on new infill types as mentioned in the text, ## indicates experiment where the effect of plaster is investigated
RC = Reinforced concrete, CES = concrete encased steel; IF = Infill Wall, CM = Confined Masonry Wall, SR = Slenderness ratio, AR = Aspect ratio
HCB = Hollow concrete block, HCBR = Hollow clay brick, HCT = Hollow clay tile, SCB = Solid clay brick, SCBL = Solid concrete block, HPB = Hollow pumice block
H = Horizontal, V= Vertical, NA = Not Applicable, S = Solid, NK =Not Known, + = exist, - = does not exist
IP = IP load only, OoP = OoP load only, IP+OoP = IP load followed by OoP load, OoP + IP = OoP load followed by IP load, IP+OoP+IP = IP load followed by OoP load and IP load again, OoP+IP+OoP = OoP load followed by IP load and OoP load again, IP / OoP = simultaneously acting IP and OoP load, LUR = Load-unload-reload (unidirectional cyclic loading), D = Dynamic (shake table), M= monotonic, C= Cyclic, ISD = Inter-storey drift, CP = constant pressure, PL = Point load, AB = Airbag

2.1.1 Variation of frame and infill wall properties

From a detailed study of the experimental campaigns mentioned above, it was found that most of the tests were conducted on single-storey single-bay (in one direction) specimens. Some tests used multi-storey frame structures and very few experimental campaigns were conducted on real buildings (Tu et al. 2007; Corte et al. 2008), while Ingham et al. (2014) only tested infill walls at building sites. In some studies, single-storey infilled structures with 4 columns (connected by beams) with RC slabs were used to perform OoP tests (Fowler 1994; Klingner et al. 1996; Tu et al. 2010). The majority of the experimental campaigns (i.e. 47) used infill wall specimens in reinforced concrete frames, while some of them (i.e. 11) tested infills in steel frames (Fig 2.1a). Most of the experimental campaigns (i.e. 34) adopted full-scale infilled frames, while 10 of them used half-scaled infilled frames, and some others used 2/3 scaled infilled frames (Fig 2.1b). The distribution of the types of frames and the scale of infilled frames used in different experimental campaigns is described by the bar charts in Fig 2.1a-b.

Clay masonry units were commonly utilized as a building material for infill walls or confined masonry wall specimens. Out of 58 experimental campaigns, 51 were conducted on masonry made with clay bricks or blocks, and only in 10 experimental campaigns, masonry was made with concrete units (Fig 2.2a) (in some experimental campaigns clay units and concrete units were used alternatively). In the majority of the experimental campaigns (i.e. 46), infills made with hollow masonry units were used and solid masonry units were adopted in 15 of them (Fig 2.2b). For infills with hollow masonry units, the masonry units were laid with holes either in a horizontal or a vertical direction, representing the construction practices (Fig 2.2c). Few experimental campaigns involved infill walls made of both solid and hollow masonry units (Angel 1994; Misir et al. 2016; Moreno-Herera et al. 2016). Furtado et al.

(2018a) found that the OoP strength of infill walls reduces when the percentage of the void in hollow masonry units is increased.

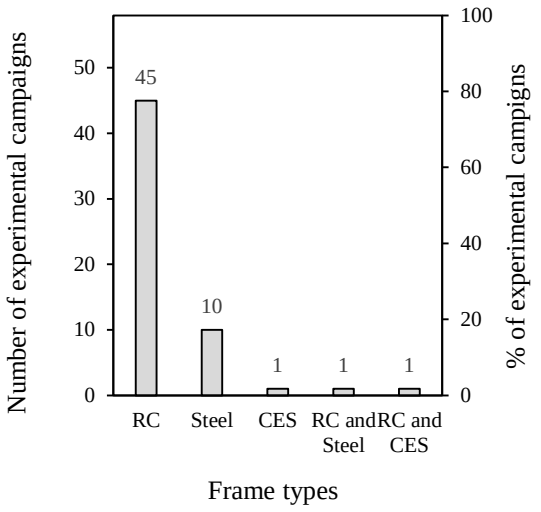

a)

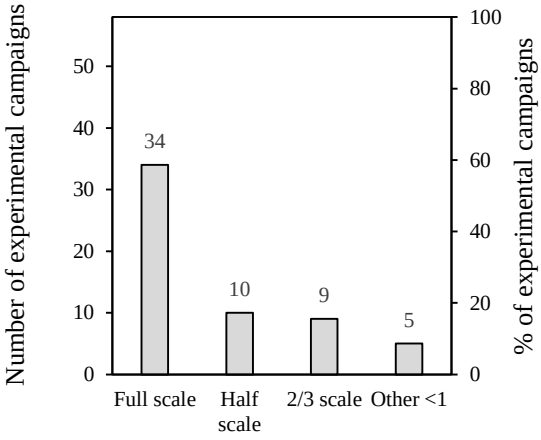

b)

Note: CES = Concrete Encased Steel

Figure 2.1 Properties of infilled frame specimens in different experimental campaigns: a) Types of frames, and b) scale of specimens

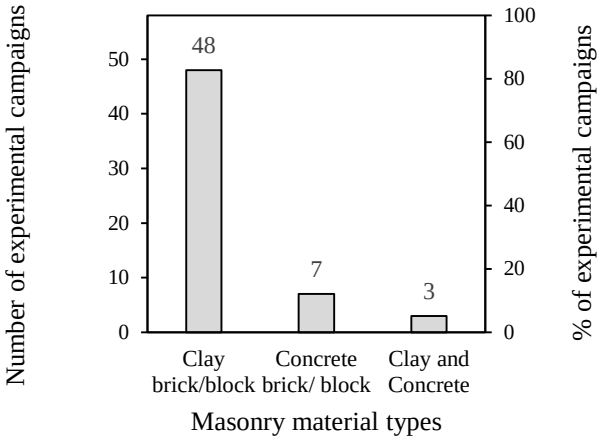
Number of experimental campaigns
% of experimental campaigns
48
7
3
0
10
20
30
40
50
0
20
40
60
80
100
Clay brick/block
Concrete brick/ block
Clay and Concrete
Masonry material types

a)

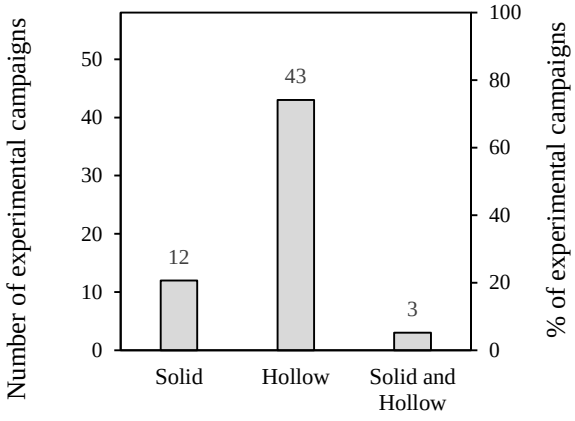
Number of experimental campaigns
% of experimental campaigns
12
43
3
0
10
20
30
40
50
0
20
40
60
80
100
Solid
Hollow
Solid and Hollow
Masonry unit types

b)

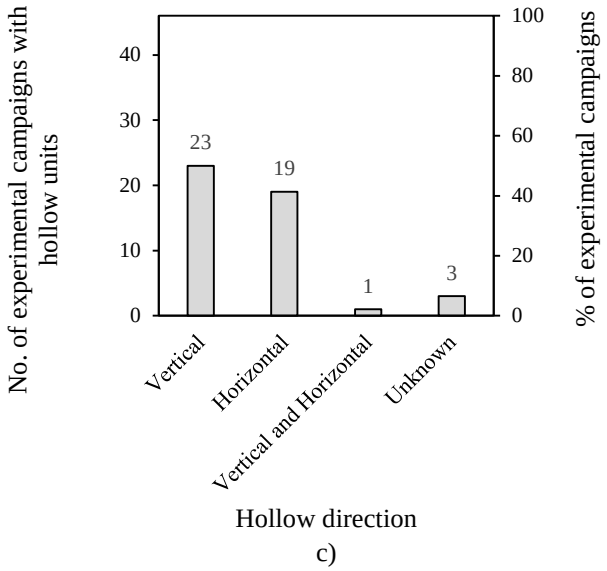

Figure 2.2 Characteristics of infills in different experimental campaigns: a) material types, b) masonry unit types, and c) direction of holes in units

The geometrical properties of the URM infill walls used in different experimental campaigns also have high variations. The tested infills had a slenderness ratio in the range of 6.8 to 34.2, while the infills' aspect ratio ranged from 0.5 to 2.5 as shown in Table 2.1. The distribution of the aspect ratio of the experimented infills or confined masonry specimens is shown in Fig 2.3. The length of the infill specimens tested is generally greater than the height. Most of the experimental campaigns involve specimens with an aspect ratio in the range of 1.0 - 1.6. The distribution of the slenderness ratio of the specimens used in different experimental campaigns is shown in Fig 2.4. In detail, the range of thickness of infill wall specimens varied from 30 mm to 365 mm (Fig 2.5).

It has to be noted that in Fig 2.3, the total number of experimental campaigns is more than 58. It is because, in a few experimental campaigns, infill wall specimens with more than one aspect ratio were tested (the same applies to

the distribution of slenderness ratio in Fig 2.4 and the distribution of thickness in Fig 2.5 - details in Table 2.1). Therefore, those experimental campaigns were counted more than one time.

From Fig 2.5, it can be observed that in 4 cases, infill specimens with thicknesses even below 50 mm were used. However, only one of them (Angel 1994) refers to full-scale tests while 3 others (Frederiksen 1992; Klingner et al. 1996; Žarnić et al. 2001) used small-scaled specimens. The same figure also shows that there are not many experimental campaigns conducted on thick infill walls (200 mm or higher). Among the listed in Table 2.1, 5 of them belong to the category of innovative infill types, characterized by different construction techniques as discussed at the beginning of section 2 (these innovative infills, provided with sliding joints or enclosure systems for reinforcement, partitioned, etc., cannot be directly compared to URM infill walls normally used in construction practices). This highlighted a serious lack of tests for understanding the OoP capacity of thick infill walls.

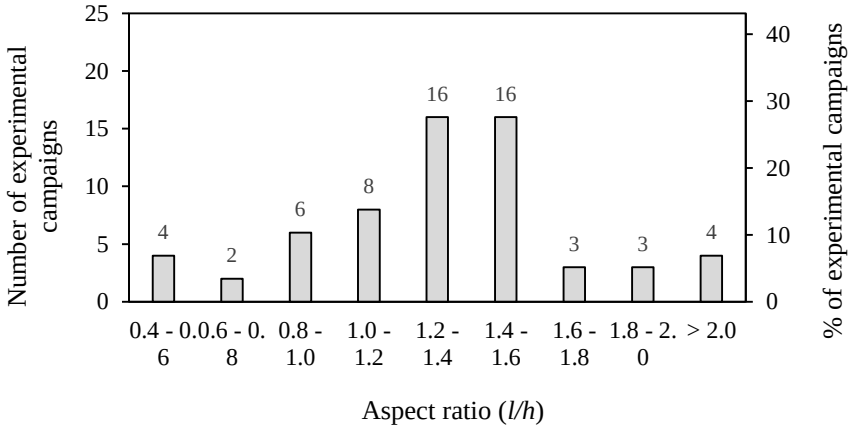

Figure 2.3 Distribution of the experimented infill specimens as per their aspect ratio

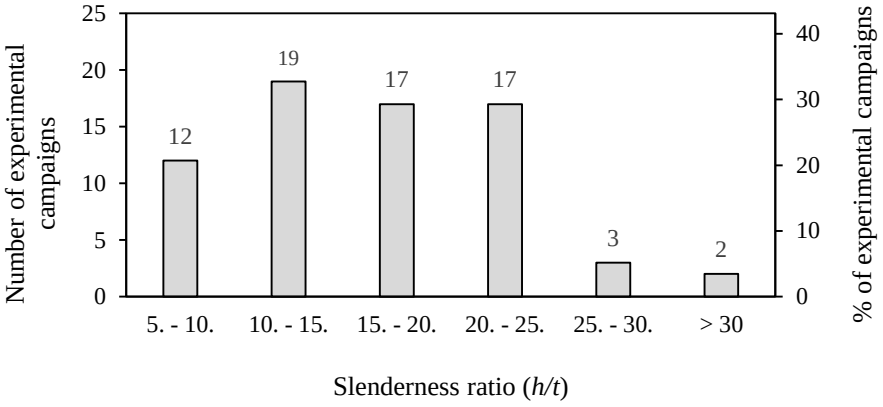

Figure 2.4 Distribution of the experimented infill specimens as per their slenderness ratio

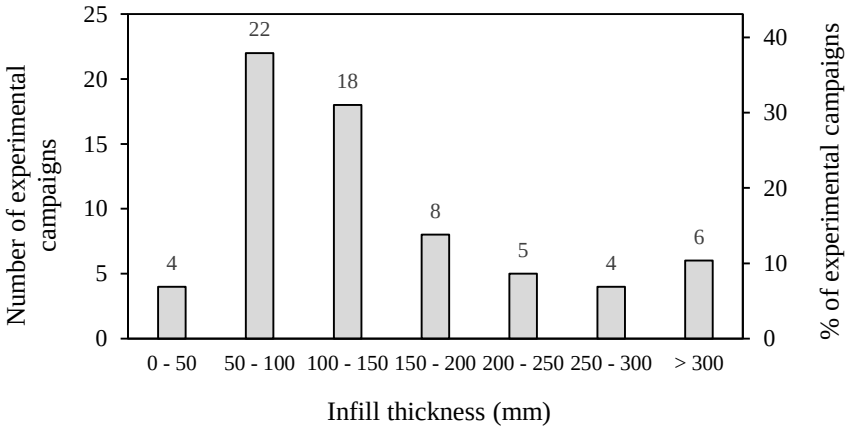

Figure 2.5 Distribution of thickness of infills used in the experimented specimens

The compressive strength of the masonry used as infill wall specimens tested in different experimental campaigns varied from 0.5 to 35 MPa. In some of the experimental campaigns, such mechanical property of masonry was not known, and in most cases, properties of the masonry units and mortar were not published by the authors. Further, in the case of infill walls with hollow

masonry units, typically, the compressive strength of the masonry is different in the directions parallel and perpendicular to the holes in the unit due to the different strengths of the units in these two directions. However, different experimental campaigns report the strength of masonry only in one direction which is usually the direction of the gravity loads.

Fig 2.6 summarizes the range of compressive strength of the infill wall specimens made with solid units used in different experimental campaigns. The figure shows that the number of experimental campaigns is very low in each range of compressive strengths. In some range of strengths, no infill specimens with solid masonry units were tested. Similarly, Fig 7 shows the variation of the compressive strength of infill specimens made with hollow units in the directions parallel and perpendicular to the unit holes (in Fig. 7a & 7b the strengths in the horizontal and vertical directions refer to the same experimental campaigns; in some cases, the strength perpendicular to holes, when the holes are in the gravity direction, is not provided by the authors). The majority of experimental campaigns used infill specimens with low compressive strength (0 to 4 MPa). Figs 2.6 & 2.7 highlight that experimental investigations on different ranges of infill masonry's strength are lacking.

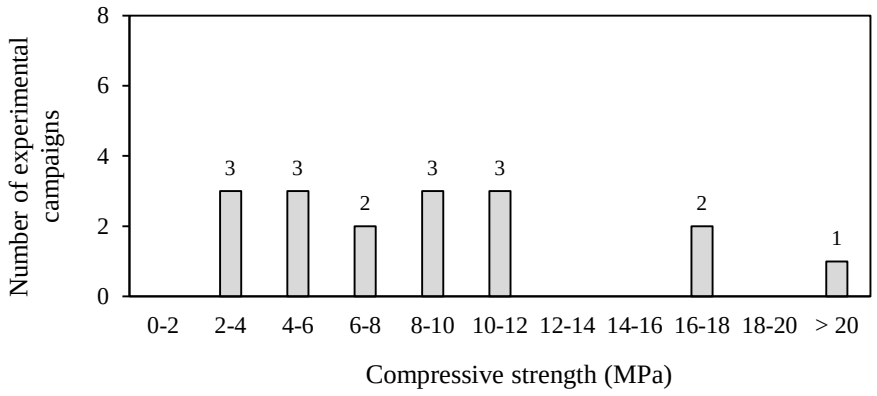

Figure 2.6 Compressive strength of masonry with solid units in different experimental campaigns

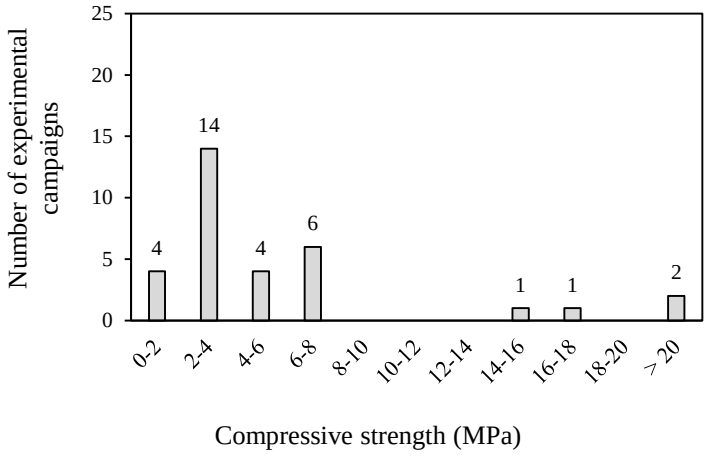

a)

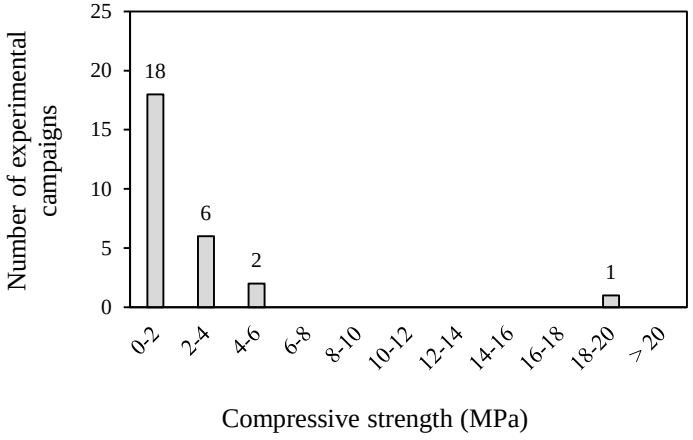

b)

Figure 2.7 Compressive strength of masonry in the experimental campaigns involving masonry infills with hollow units: a) parallel to hole; b) perpendicular to hole

2.1.2 Variation of loads and loading methods

Out of 58 experimental campaigns, in 27 of them, infill specimens were tested only with OoP loads, whereas in 15, the infill specimens were tested

with combined IP and OoP loads applied sequentially or simultaneously. In the remaining 16 experimental campaigns, infilled specimens were tested both with OoP loads and combined IP and OoP loads (Fig 2.8a). The majority of the experimental campaigns (i.e. 43 which is almost 75%) were conducted using quasi-static loading methods while the other 15 were performed under dynamic settings with the use of a shake table (Fig 2.8b). The decision to use a quasi-static or dynamic approach is largely affected by the cost of experimentation and the objective of the test.

Most of the quasi-static tests (i.e 39) were performed by applying an OoP load on the infill wall directly. This method is also known as the inertial method of loading (Anić et al. 2020). In such loadings, either uniform pressure was maintained all over the infill area by using an airbag, or the infills were pushed at some local points by using concentrated loads (22 experimental campaigns - airbags, 17 experimental campaigns - point loads) as shown in Fig 2.8c. Very few experimental campaigns used inter-storey drift load, either monotonic or cyclic, applied to the frames (e.g. Henderson et al. 1993; Flanagan and Bennett 1999b; Tu et al. 2007, Corte et al. 2008; Anić et al. 2021). In the inertial method of loading, damage primarily occurs to infill walls, but in the case of an inter-storey drift load, the damage is concentrated more in the frames since the loads are directly applied to them.

The difference in the load shape used for loading an infill (point loads or uniform pressure) can influence the OoP capacity of the infill (Di Domenico et al. 2018; Di Domenico et al. 2019b). In the inertial method of loading, normally three different approaches were found to be adopted: i) application of monotonically increasing force or pressure; ii) application of unidirectional cyclic (load-unload- reload cycles) of force or pressure; and iii) application of cyclic force or pressure. Furtado et al. (2016) experimented using both (i) and (ii) types of loading. Repeatedly applied unidirectional loading is a simplified

representation of cyclic loading (distribution of types (i), (ii) and (iii) is shown in Fig 2.8d).

In dynamic test conditions, very few experimental campaigns used simultaneously applied IP and OoP shaking (e.g. Fardis et al. 1999; Žarni´c et al. 2001; Onat et al. 2018), and in other cases loading was a unidirectional shaking. For IP testing, monotonic or cyclic drift loads were applied at the frame top in quasi-static settings, or else a shake table was used. In the majority of the cases, cyclic IP loads were adopted (24 experimental campaigns) and monotonic IP loads were rarely used (only in 2 experimental campaigns). The use of different loading methods for IP testing of infilled frames can be seen in Fig 2.8e.

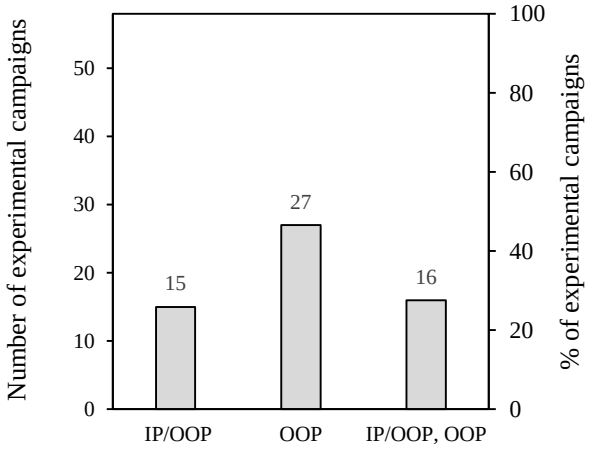

(a)

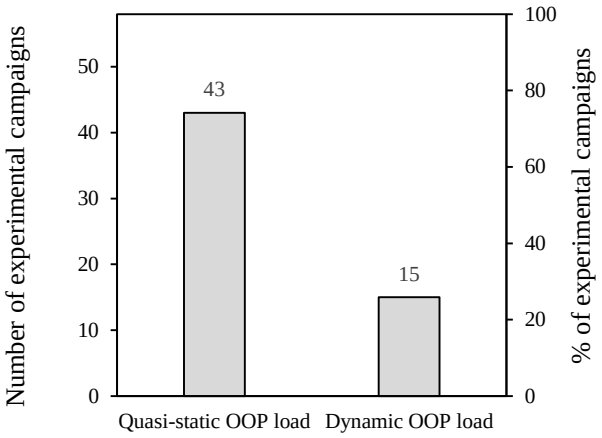
Number of experimental campaigns
% of experimental campaigns
0
10
20
30
40
50
0
20
40
60
80
100
43
15
Quasi-static OOP load
Dynamic OOP load

(b)

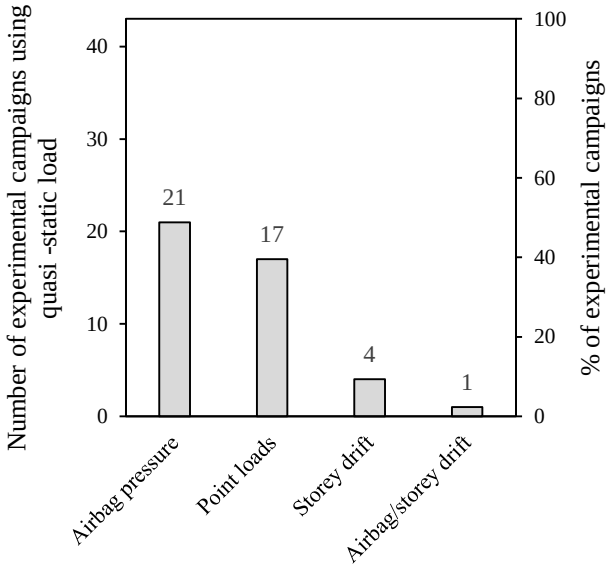
Number of experimental campaigns using quasi -static load
% of experimental campaigns
0
10
20
30
40
0
20
40
60
80
100
21
17
4
1
Airbag pressure
Point loads
Storey drift
Airbag/storey drift

(c)

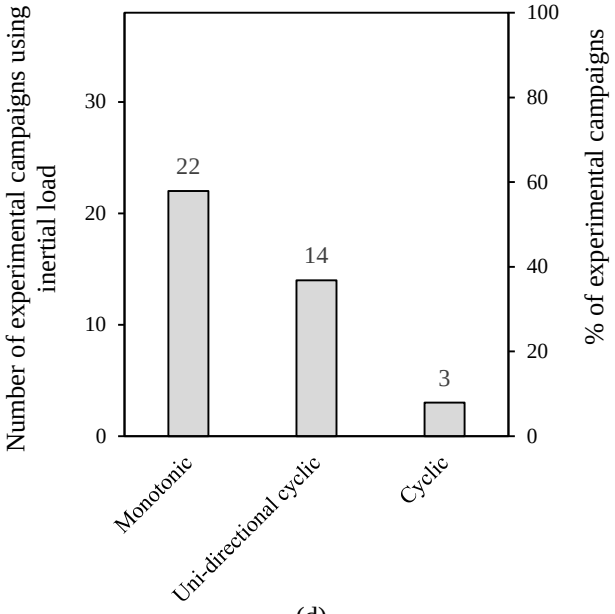
Number of experimental campaigns using inertial load
% of experimental campaigns
0
10
20
30
0
20
40
60
80
100
22
14
3
Monotonic
Uni-directional cyclic
Cyclic

(d)

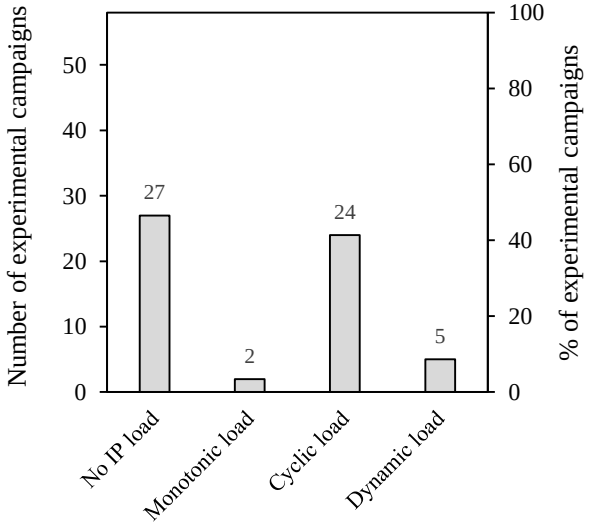
Number of experimental campaigns
% of experimental campaigns
0
10
20
30
40
50
0
20
40
60
80
100
27
2
24
5
No IP load
Monotonic load
Cyclic load
Dynamic load

(e)

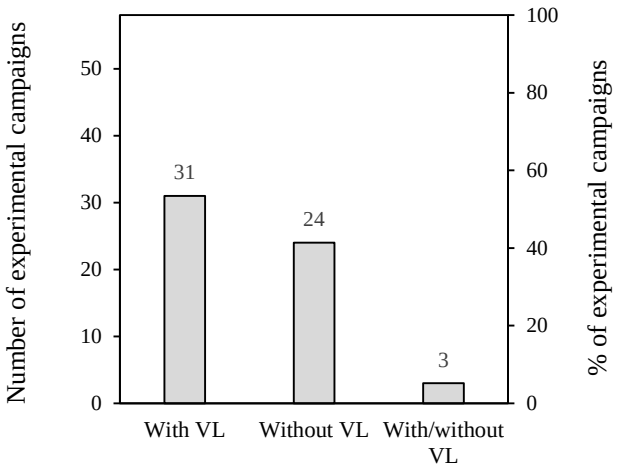

(f)

Figure 2.8 Summary of types of loading applied to specimens: a) load used, b) OoP loads types, c) quasi-static OoP loads, d) types of inertial loads, e) IP loads, and f) use of vertical load (VL)

Tests were carried out either in the presence or absence of vertical load. Vertical loads are used to simulate the gravity load coming from the upper floors. Vertical loads were used in 34 experimental campaigns and among them, 3 also involved specimens without gravity load (as shown in Fig 2.8f). In such experimental campaigns, 19 of them (approximately 55%) applied gravity loads directly over the columns and others applied gravity loads on the beam or RC slab.

Variations like mechanical properties of masonry, dimensions of infill walls (slenderness ratio, aspect ratio), tests on IP damaged or undamaged specimens, etc. resulted in different OoP capacities. For a quick look, the plot of the OoP capacities of infilled or confined masonry specimens against the slenderness ratio is shown in Fig 2.9. 120 specimens have been included in the plot. The effect of the slenderness ratio is evident, the higher the

slenderness ratio the lower the capacity. However, it has not to be forgotten that there are influences of several other factors that are dealt with in detail in the next sections.

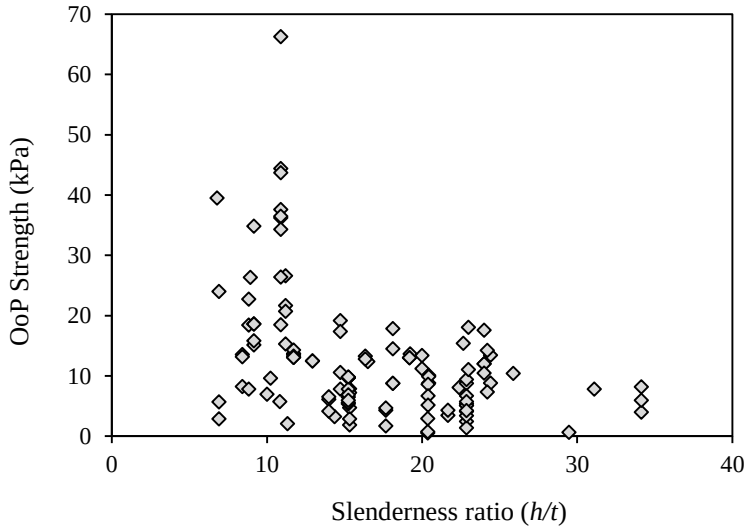

Figure 2.9 Experimental OoP capacities of the infilled/ confined masonry specimens versus slenderness ratio

2.1.3 Parameters affecting the OoP capacity of infill walls

In this section, different parameters that affect the OoP capacity of URM infill walls are explained and results from different experimental tests are compared to illustrate the idea clearly. To compare the OoP capacities of masonry infills with different characteristics used in different experiments, OoP capacity has been expressed in terms of kiloPascal (kPa). For all OoP load-displacement plots, the displacement at the centre of the infill has been used. OoP displacement is also expressed in terms of OoP drift (%) with respect to half the height of the infill wall.

2.1.4.1 Slenderness ratio

OoP capacity is connected with the arching action and experiments have demonstrated that the arching mechanism is very effective in thick infill walls. Therefore, the amount of arching differs depending upon the slenderness ratio (height/thickness) in the vertical and horizontal directions. According to Angel (1994), arching occurs when the slenderness is less than a limit known as the critical slenderness ratio. When the slenderness ratio of the infill wall is higher than the critical slenderness ratio, snapping failure occurs. Dawe and Seah (1989) investigated the influence of the slenderness ratio (h/t) on the OoP response of masonry infill walls with the same mechanical characteristics. From their results, it was found that the masonry infill wall specimens called WE2, WE4 and WE5 having thicknesses 190 mm (h/t =14.7), 140 mm (h/t =20) and 90 mm (h/t =31) respectively obtained a peak OoP capacity of 19.2 kPa, 11.2 kPa, and 7.8 kPa.

Similarly, Angel's (1994) specimens 3, 6 and 8 with thicknesses of 47.6 mm (h/t =34), 98.4 mm (h/t =14.7) and 187.3 mm (h/t =8.7) respectively made of the same material (brick and lime mortar) but with different mechanical properties (elastic modulus and compressive strength) exhibited an OoP strength of 6 kPa, 12.4 kPa, and 32.1* kPa (* indicates that tests were stopped due to the limited capacity of the testing equipment). The high strength in the case of thick infills was attributed to higher arching action. Flanagan and Bennett (1999b) also obtained similar results. Specimens 25, 18 and 22 having thicknesses 100 mm (*h/t* =22.4), 200 mm (*h/t* =11.2), and 330 mm (*h/t* =6.8) respectively, and similar mechanical properties showed OoP strengths of 8.1 kPa, 26.6 kPa and 39.5 kPa respectively. However, experimental tests carried out by Varela-Rivera et al. (2012a) did not show significant changes in OoP strength with a small difference in slenderness ratio, confined masonry wall E2 (with a thickness of 150 mm i.e. *h/t* =19.2) and E3 (with a thickness of 120

mm i.e. *h/t* =24) with a similar compressive strength bounded with confining elements having almost equal IP stiffness demonstrated the strength of 13 kPa and 12 kPa respectively.

Koutas and Bournas (2019) also found that the OoP capacity of the thick infill specimen D_CON (thickness of 140 mm or *h/t* =8.9) was almost two times that of the thin infill specimen S_CON (thickness of 65 mm or *h/t* =19.2). Likewise, experimental investigations by Ricci et al. (2018a, 2018b) on infills' thicknesses of 80 mm (*h/t* =22.8) and 120 mm (*h/t*=15.2) demonstrated that the OoP capacity for a thick infill was double that of a thin infill wall (results in Fig 2.10). It is worth pointing out that the two infills had similar mechanical properties. Shake table tests by Tu et al. (2010) also showed that the OoP resistance was increased significantly when the thickness of the confined masonry panel was doubled (case of *h/t* =29.5 and 14.4).

Fig 2.10 highlights the effect of the slenderness ratio in the OoP behaviour of URM infills observed in some experimental studies. It has to be noted that the infill specimens compared in the figure have different masonry strengths (compressive strength was less than 2 MPa in the case of Ricci et al. 2018a and 2018b, while it was about 10 MPa in the case of Koutas and Bournas 2019). These experimental results indicate the strong influence of the slenderness ratio on the OoP capacity of infill walls.

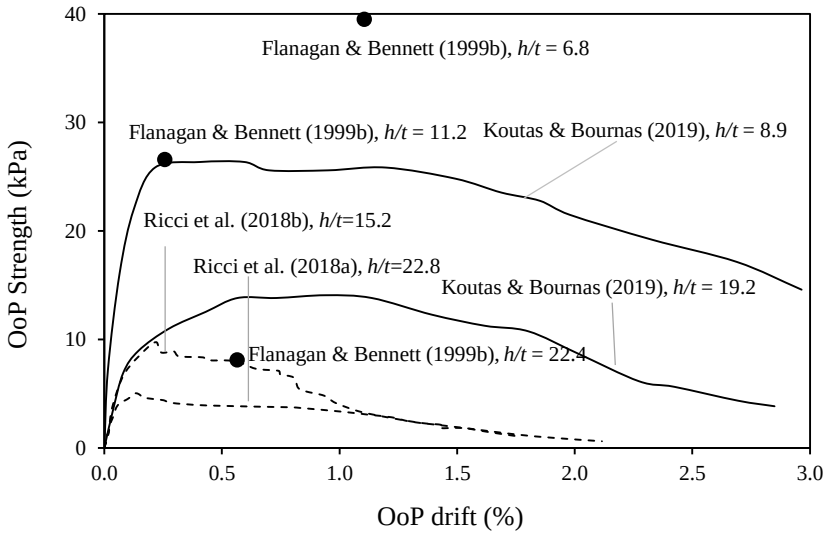

Figure 2.10 Influence of slenderness ratio (h/t) on the OoP capacity of masonry infill wall panels

Although it has been confirmed that OoP strength increases with an increase in the thickness of the infill wall, there are still very few experimental campaigns conducted on thick infill walls as discussed in section 2.1.

2.1.4.2 Aspect ratio

De Risi et al. (2019b) compared the OoP performance of infill walls having an aspect ratio (*l/h*) 1.0 with specimens tested by Ricci et al. (2018a) having an aspect ratio 1.28. The thickness of the infill specimens in both tests was 80 mm and the mechanical characteristics (masonry compressive strength and elastic modulus) of the infill walls were similar (slightly higher in the former). OoP capacity of the infilled specimen was lower when the *l/h* value increased (Fig 2.11). Experimental comparisons by Di Domenico et al. (2019a) and Di Domenico et al. (2021) also showed a higher OoP strength in the case of square infill compared to infill with *l/h* equal to 1.28 for a 120 mm

thick wall although the compressive strength of masonry was slightly higher in the former case.

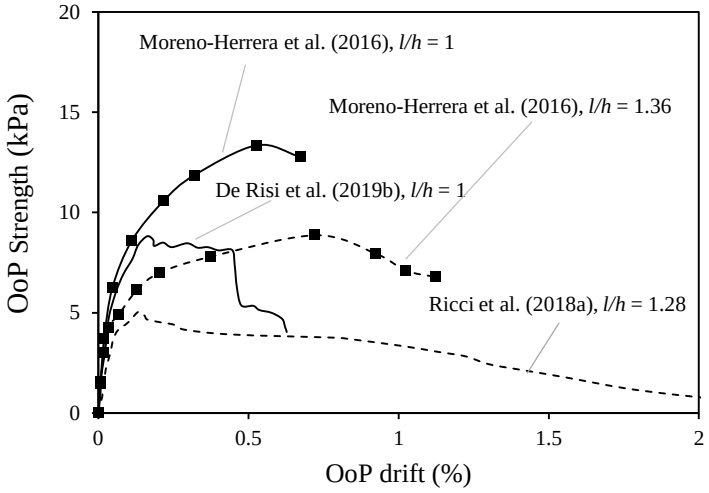

Figure 2.11 Influence of infill's aspect ratio in the OoP capacity

Moreno-Herera et al. (2016) also observed a reduction in OoP strength and stiffness due to an increase in the aspect ratio (from 1 to 1.36) of the confined masonry walls made of both concrete blocks and clay bricks. Two cases of hollow concrete blocks (particularly specimens W2 and W5) are shown in Fig 2.11.

An experiment by Varela-Rivera et al. (2012a) also showed a decrease in the OoP capacity of a confined masonry wall with an increase in aspect ratio. In detail, specimen E1 with *l/h* value of 1.35 showed OoP strength of almost half compared to specimen E5 with *l/h* value of 1.08; nonetheless, the confining elements for the latter had slightly higher IP stiffness. Similarly, the experiment of Lunn and Rizkala (2011) also showed the reduction of the OoP strength when the aspect ratio of confined walls with fibre reinforced polymer

(FRP) overlaying increased. Thus, the OoP capacity can be expected to be maximum for an infill when its aspect ratio is close to 1.

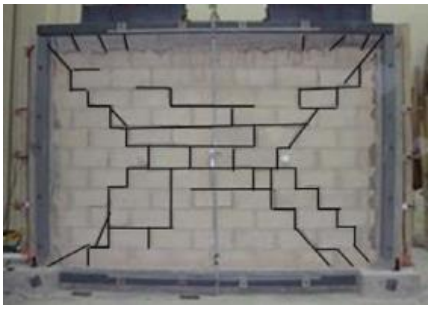

Concret block masonry (*l/h = 1.36)*

Hollow Clay brick masonry (*l/h* = 1.36)

Concrete block masonry (*l/h = 1.0)*

Hollow Clay brick masonry (*l/h = 1.0)*

Figure 2.12 Influence of aspect ratio in failure mode of infills due to OoP load (after Moreno-Herrera et al. 2016)

Fig 2.12 shows the differences in the cracking pattern of infill walls as observed in the experiment of Moreno-Herera et al. (2016) due to changes in the aspect ratio. It can be observed that the horizontal cracking length at mid-height is longer when there is an increase in the span length.

2.1.4.3 In-plane (IP) damage in infill walls

Several experimental studies have dealt with the OoP behaviour of pre-damaged masonry infill walls (Angel 1994; Flanagan and Bennett 1999b; Calvi and Bolognini 2001; Furtado et al. 2016; Spesdar 2017; Wang 2017; Ricci et al. 2018a, Ricci et al. 2018b; De Risi et al. 2019b; Akhoundi et al. 2018, Di Domenico et al. 2021). In the experimental campaigns, IP drift load (expressed as inter-storey drift ratio or IDR) applied before the application of OoP load, is commonly taken as a measure of IP damage. The ratio of OoP strength of the IP damaged and undamaged specimens (i.e. the strength reduction factor R_1) from different experimental campaigns can be viewed in Fig 2.13. Simply, an increase in the IP damage caused a decrease in OoP strength in every test. But, some specimens with higher IP drift also showed lower strength reduction. This highlights that the rate of decrease is not only dependent on the amount of prior IP drift.

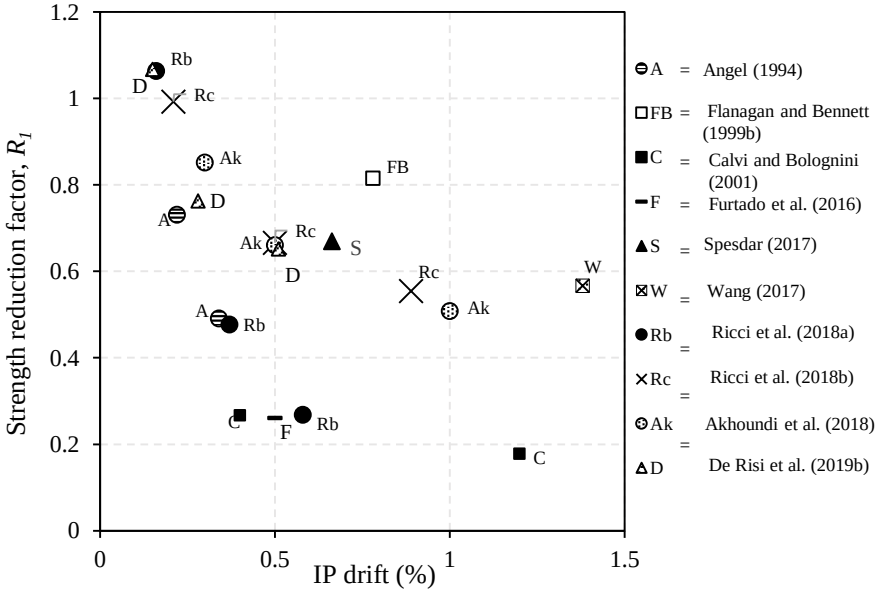

Figure 2.13 OoP strength reduction observed from experimental studies

In the experimental campaign of Angel (1994), the author experienced a higher reduction of OoP capacity due to increasing IP drift. In particular, specimen 1 without any IP damage (IDR=0%) showed OoP capacity of 8.3 kPa while specimen 3 suffering IP damage (IDR=0.22%) showed a capacity of 5.85 kPa (approximately 70% of specimen 1), and specimen 2 (IDR=0.34%) showed about 4.1 kPa (approximately 50% of specimen 1). Specimens 1, 2 and 3 had the same thickness (48 mm), but specimen 3 was cast with weak lime mortar while specimen 2 was made of strong N-type (cement, lime, sand) mortar. Specimen 2 had almost double the elastic modulus of specimen 3, although both specimens had similar compressive strength. The higher reduction of strength was due to a very small thickness of infill specimens (h/t = 34). It was strange that specimen 2 which experienced an IP drift only 0.12% higher than that of specimen 3, showed OoP strength reduction by more than 20%, although the former was made with strong mortar (Fig 2.14).

By contrast, an experiment by Flanagan and Bennett (1999b) showed a reduction of only 20% of OoP strength due to 0.78% IP drift. Similarly, the experimental results by Hak et al. (2014) also did not show a major difference between OoP strengths of two infill specimens which were loaded beforehand to an IP drift of 1% and 1.5% (Fig 2.14). However, degradation of the OoP stiffness was significant (about 40%). In the case of 1.5% drift, IP cracking was spread in the frames while in the case of 1.0% drift, no cracking in the frames was observed. Cracking in the infills, especially in the upper bricks near the top beam, was similar in both cases (slightly more extensive in the case of 1.5% drift). But, the OoP damage was higher in the case of 1% IP drift: extensive damage occurred in the region where the upper right stepwise crack joined the central horizontal crack.

Dynamic tests by Klingner et al. (1996) also revealed a decrease in stiffness by two-thirds of the previously cracked infill due to IP load in comparison to the undamaged specimen. But, Spesdar's (2017) tests indicated a reduction of capacity by only 33% after damage in IP by 0.64% drift. Further tests by Wang (2017) on an infill similar to the one examined by Spesdar (2017) showed a reduction of capacity by 43% after a 1.37% IP drift (Fig 2.14). In these tests, since the IP loads were applied monotonically, the reduction of OoP strength could have been smaller. It could be also because Spesdar's (2017) and Wang's (2017) tests were carried out in small-scale specimens, and the slenderness ratio was low (<11). At the same time, their specimens failed in relatively small OoP drift.

Findings by Ricci et al. (2018a, 2018b) also support that the decay of OoP strength can be lower for infills with a low slenderness ratio. In particular, tests on 80 mm thick infill (h/t = 22.9) indicated a 73% decay while tests on 120 mm (h/t= 15.2) thick infill specimen showed a reduction by 45% although the latter was damaged in IP by 0.89% and the former was damaged by 0.58% IP drift, despite both types of infills had similar mechanical characteristics of masonry (Fig 2.14). Experimental results in Di Domenico et al. (2021) further support this claim.

The results by Calvi and Bolognini (2001) showed a sharp decrease in OoP strength (reduction by approximately 73%) due to a prior IP drift of only 0.45%. A similar result was observed by Furtado et al. (2016): when an infill was OoP loaded only after 0.5% IP drift, the strength reduction was about 75%. Ricci et al. (2018a) also reported an OoP strength reduction of 73% due to IP drift of 0.58% for the case of 80 mm thick slender infills. Interestingly, while testing in IP, Furtado et al. (2016) tested double-leaf infills (150 mm+110 mm) and loaded in OoP only the 150 mm (h/t=15.3) thick leaf, and Ricci et al. (2018a) tested the slender 80 mm thick (h/t=22.9) infill and used

the highest IP drift among the three, but the strength reduction was larger for the former. Although the thickness of infill was the biggest for Furtado et al. (2016) among the three, masonry was very weak (the lowest compressive strength). For Ricci et al (2018a), infill thickness was lower but the masonry was comparatively stronger. This highlights that the decay of OoP strength is significantly influenced by masonry strength. This is supported by the result of Calvi and Bolognini (2001) as well: although the infill thickness of 135 mm (h/t=20.3) was used, masonry strength was too low, and only with 0.45% prior IP drift, there was a large reduction in OoP capacity.

The results from Calvi and Bolognini (2001), Ricci et al. (2018b) and De Risi et al. (2019b) were similar in the sense that the specimens loaded purely in OoP reached the peak strength within a small OoP displacement (drift) and the capacity dropped quickly afterwards. In other experimental campaigns, the OoP strength dropped more gradually for the undamaged specimens. These results also indicate that if the masonry is very weak (too low compressive strength), the OoP strength of the IP-undamaged infill wall can degrade quickly after attaining peak strength (Fig 2.14).

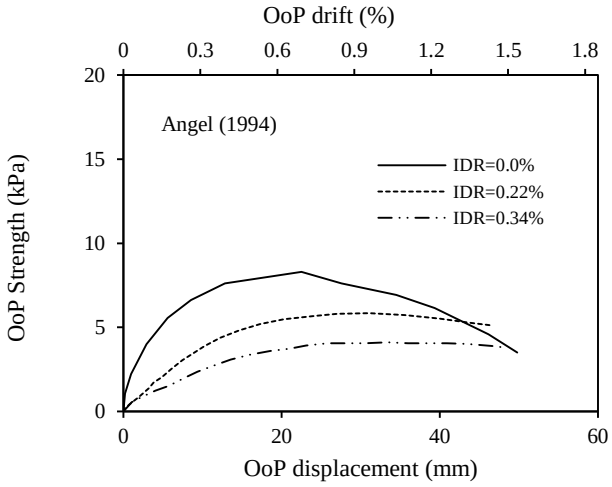

a)

Fig 2.14 Continue…

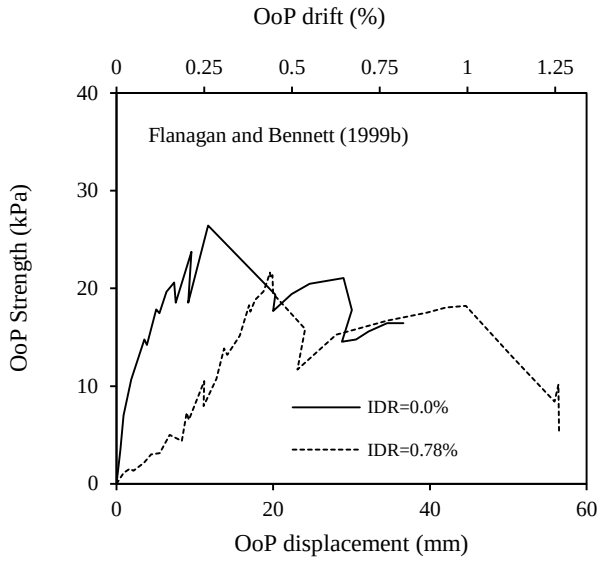

b)

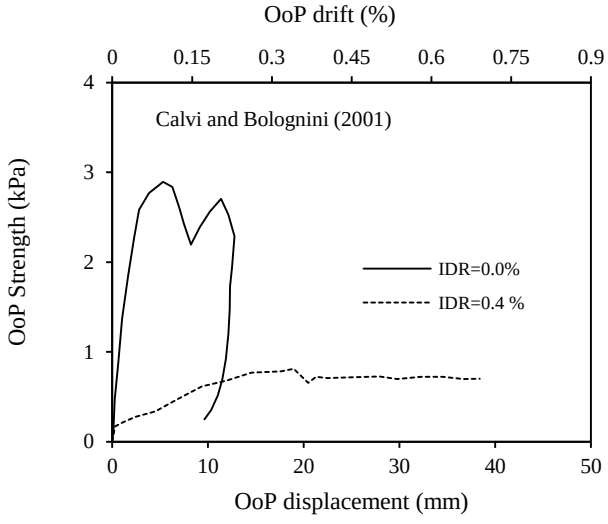

c)

Fig 2.14 Continue…

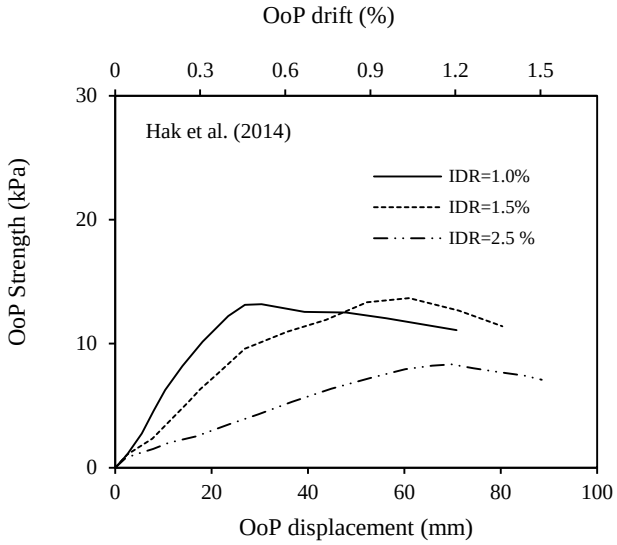

d)

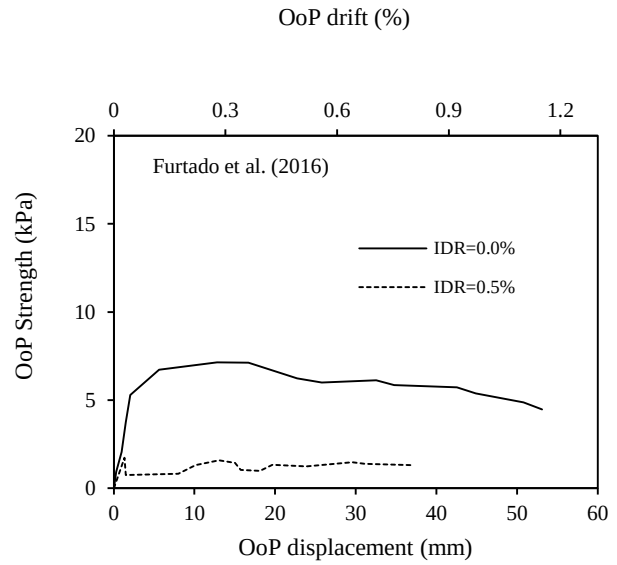

e)

Fig 2.14 Continue…

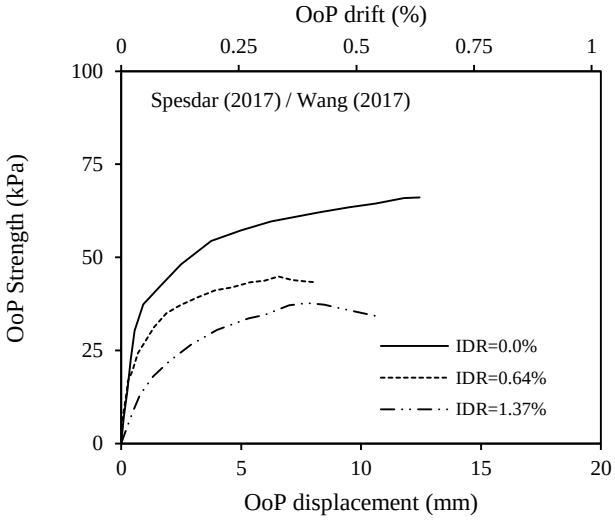

f)

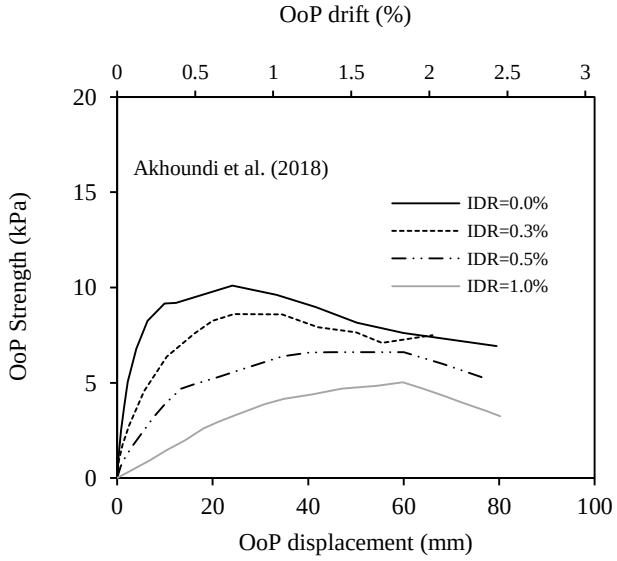

g)

Fig 2.14 Continue…

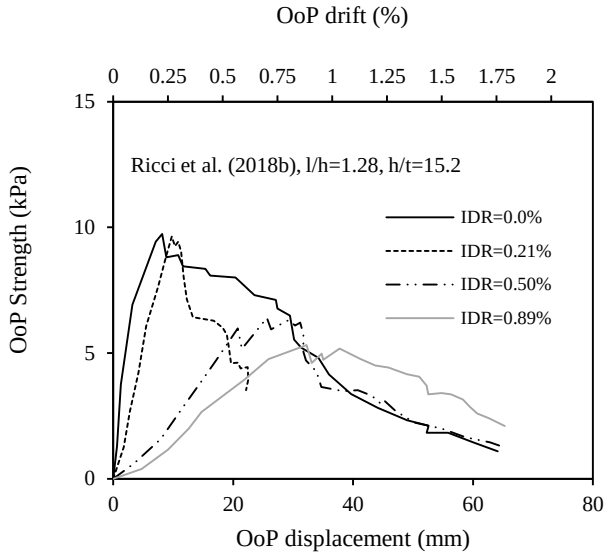

h)

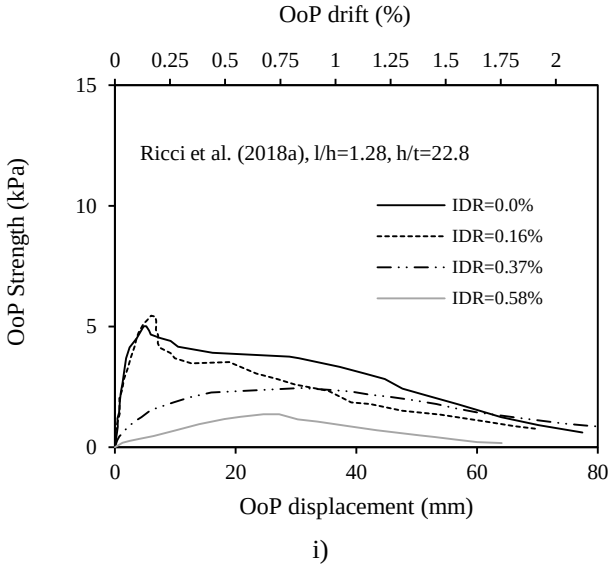

i)

Fig 2.14 Continue…

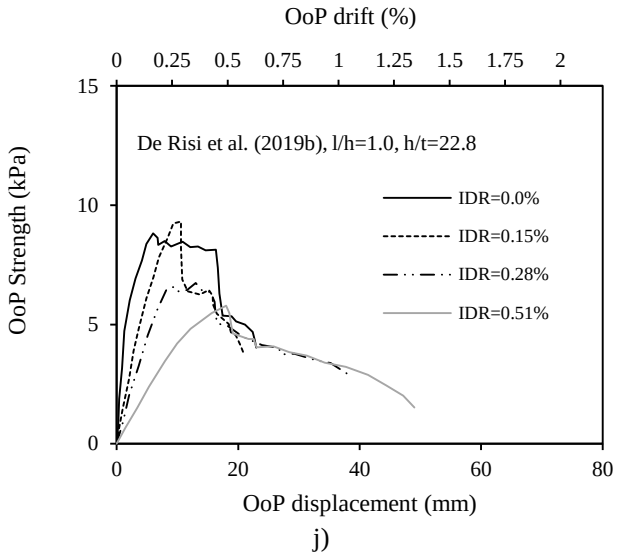

Figure 2.14 OoP strength – displacement curves according to IP damage level defined by inter-storey drift ratio (IDR): a) Angel (1994); b) Flanagan and Bennett (1999b); c) Calvi and Bolognini (2001); d) Hak et al. (2014); e) Furtado et al. (2016); f) Spesdar(2017) / Wang (2017); g) Akhoundi et al. (2018); h) Ricci et al. (2018b); i) Ricci et al. (2018a); j) De Risi et al. (2019b)

Unlike OoP strength, the OoP deformation capability seems to be affected differently due to IP damage. In the experimental studies by Calvi and Bolognini (2001), Ricci et al. (2018b) and De Risi et al. (2019b), peak strength was achieved at higher drift and the infill specimens failed at large OoP deflection for IP-damaged specimens. This is because the arching effect is delayed due to IP damage. Also, in the experimental studies by Angel (1994), Hak et al. (2014), Spesdar (2017), Wang (2017) and Akhoundi et al. (2018), OoP capacity was reduced by almost half (although at different levels of IP drift), but the specimens failed by reaching almost the same OoP deformation for different levels of IP damage considered (Fig 2.14). This

indicates that even if the infills are severely damaged in IP, they can maintain stability in the OoP direction due to the arching.

The above experimental results indicated that the OoP strength reduction depends upon factors that interact with the level of IP damage (IP drift) sustained by the infill wall. The huge variability in the reduction of OoP strength is affected by the nature of IP loads (cyclic or monotonic), masonry strength, infill thickness, etc., interacting with each other. Such dependencies have been highlighted through numerical studies as well (Agnohotri et al. 2013; Wang et al. 2020).

2.1.4.4 Boundary conditions

It is often difficult to make tight contact between the infill wall and the bounding frames due to practical difficulties. Especially between the upper beam and the infill wall, it is difficult to fill mortar properly. Therefore, the formation of gaps is largely influenced by the nature of the workmanship (Akhoundi et al. 2016). Gaps between frames and infill may arise also due to practical necessity. These gaps change the boundary condition between infill and frame and influence the OoP capacity of infill walls.

Dawe and Seah (1989) found a reduction of OoP strength by 45% due to a 5 mm gap between infill and top beam (specimen WE2 vs. WE6). Also, Akhoundi et al. (2016) observed a reduction of the OoP capacity in infill walls by 10% because of a gap with the top beam due to poor workmanship (Fig 2.15). Furthermore, experimental studies carried out by Spesdar (2017) and Wang (2017) demonstrated that a 10-mm gap between infill and top beam resulted in a higher reduction (72%) of the OoP strength than in the case of 5-mm gaps with the columns that caused only a 45% reduction.

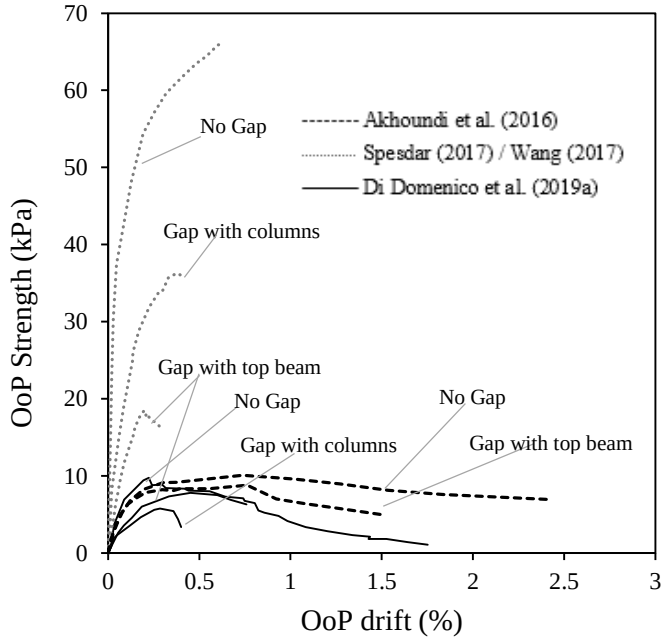

Figure 2.15 Effect of boundary conditions in the OoP capacity of infill walls

Di Domenico et al. (2018) found contrasting results. According to their findings, the OoP strength of an 80-mm thick infill with no gap was about 5.1 kPa and that with a small gap (i.e. 2 mm) at the top was about 4.1 kPa while the third infill specimen having gaps with columns showed a strength of 3.4 kPa. A small gap at the top of the infill wall only delayed vertical arching but did not eliminate it. Di Domenico et al.'s (2019a) experimental tests on the same thickness infill confirmed that with a larger gap at the top (i.e. 40 mm), vertical arching was not present and capacity was reduced to 4.3 kPa. Further tests by Di Domenico et al. (2019a) on 120 mm thick infill specimens followed a similar strength pattern. The capacity was the highest for the infill with no gap (9.7 kPa), while, for the infill with a 40 mm gap at the top, it was about 7.8 kPa. The capacity was the lowest for the infill with a 30 mm gap with both columns (5.6 kPa) as shown in Fig 2.15.

The effect of the boundary conditions can also be confirmed from tests on confined masonry walls where the confining elements were built after the masonry wall. The chances of formation of gaps between the wall and frame are less in such constructions. During OoP shake table tests by Tu et al. (2010), normal infill specimens exhibited arching at low motion intensity but separated from the boundary frames at a higher intensity. However, confined walls remained intact even at higher intensity motion.

The reduction of OoP strength due to gaps is influenced by the incapacity of the infill to form arching or due to delayed activation of arching. On one hand, the gap with the beam affects vertical arching and on the other hand, the gaps on the sides affect horizontal arching. Although the reduction of strength due to gaps is clear, there is still no consensus about the cases in which gaps with the beam are detrimental compared to gaps with the columns. This can be related to the infill's aspect ratio or compressive strength of masonry in the directions parallel and perpendicular to the holes, especially in the case of hollow masonry units, as indicated in Di Domenico et al. (2019a). Wang (2017) laid masonry with holes in the vertical direction while in Di Domenico et al. (2018) and Di Domenico et al. (2019a), masonry was laid with holes in the horizontal direction. Fig 2.16 shows the influence of gaps on the cracking patterns in masonry infill walls due to the OoP load.

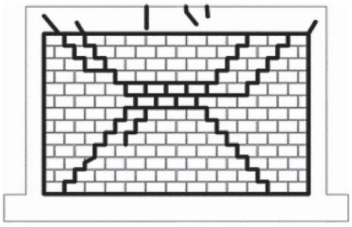

No gap

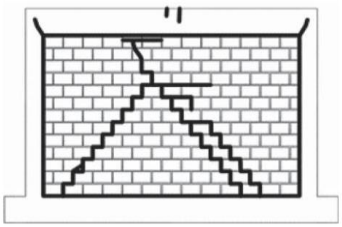

Top gap

Study by Akhoundi et al. (2016)

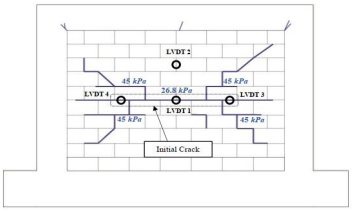

No gap

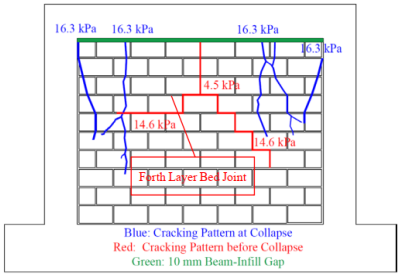

Top gap

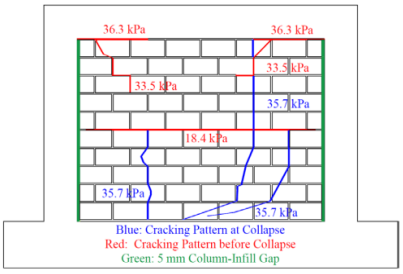

Side gaps

Study by Wang (2017)

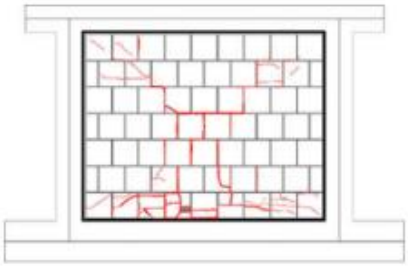

No gap

Top gap

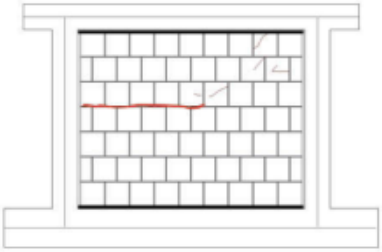

Side gaps

Study by Di Domenico et al. (2018)

No gap (120 mm infill)

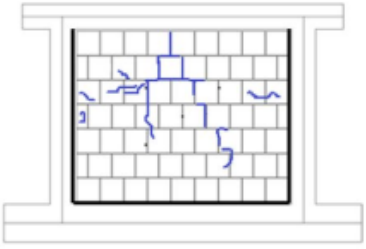

Top gap (80 mm infill)

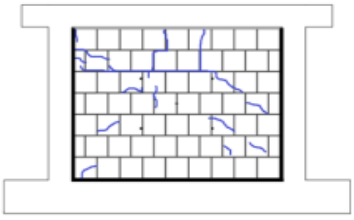

Top gap (120 mm infill)

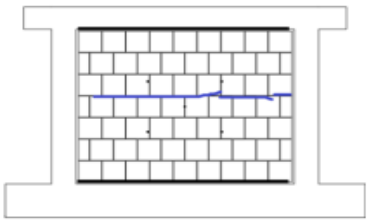

Side gaps (120 mm infill)

Study by Di Domenico et al. (2019a)

Figure 2.16 Influence of gaps in cracking pattern of infill walls developed due to an OoP load

2.1.4.5 Openings

Openings like doors and windows are practically necessary for any building and they are built in the infill walls. The location and size of openings vary according to their function. The presence of an opening modifies the mass, strength and stiffness of the infill walls and also affects their OoP capacity. A few experiments have shown that the OoP strength of the infill wall is not highly influenced by the presence of a small opening. But if the opening is big, it can significantly reduce the OoP capacity (Eurocode 8).

Experimental results showed that OoP strength is not highly influenced by the presence of small openings like doors and windows. For example, Dawe and Seah (1989) experienced a reduction of only 10% of the OoP capacity due to the presence of a central window (specimen WE9) measuring 1.6 m×1.2 m (19% area of infill) in comparison to the OoP capacity of a solid infill (specimen WE2). Akhoundi et al. (2016) also found that a central window of 80 cm×63.5 cm (12 .8 % area of infill) did not reduce the OoP capacity at all, but the deformation capacity of the infill was reduced significantly, infill collapsed within a small OoP drift (Fig 2.17). Despite the presence of an opening, the crack pattern indicates that the two-way arching was effective (Fig 2.18).

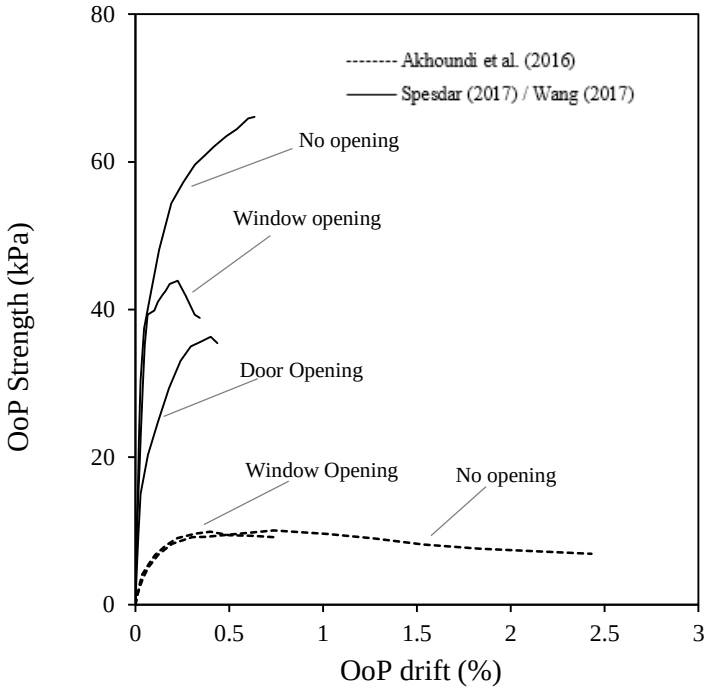

Figure 2.17 Influence of openings on the OoP capacity of the infill wall

However, experimental studies by Spesdar (2017) and Wang (2017) showed different results. An infill with a centric window (17% area of infill) showed a 35% decrease in capacity while the same infill with a centric door opening measuring 59.2 cm×39.2 cm (17.5% area of infill) in Wang (2017) showed a 45% reduction of the OoP capacity. This is a big reduction in the capacity and it can significantly increase the OoP vulnerability of infill walls in earthquakes. The higher reduction of strength in the case of a door opening can be associated with a different cracking pattern compared to the case of a window opening. Typical diagonal cracking was not observed, which indicates that the two-way arching mechanism was ineffective in the infill wall in the case of door opening (Fig 2.18).

In the cases of Dawe and Seah (1989), Spesdar (2017) and Wang (2017), the OoP pressure was monotonically increased while in the case of Akhoundi et al. (2016), unidirectional cyclic increasing pressures were applied using an airbag. Since there are not enough tests, it is difficult to connect loading types and the observed OoP behaviour of masonry infill walls.

For infill walls with eccentric openings, the crack patterns due to OoP load (airbag or point loads) on infill walls can be different. However, such tests on infill walls with eccentric openings are not available. Comparison of the cracking patterns in masonry walls having eccentric openings and observed during OoP tests on URM walls (without frames) can be found in Anić et al. (2020).

Moreover, Anić et al. (2021) performed OoP tests on URM infilled frames by applying unidirectional cyclic loads to the top of the infilled frame. Infill specimens with or without opening (centrically and eccentrically positioned window and door) were tested. Since the infilled frames were subjected to bending, infill walls showed cracks parallel to the bed joints. But the cracks were severe in the case of infill with openings, and in the case of eccentric openings, cracks were uneven (Fig 2.18). These results further indicate that the position of the opening affects the OoP behaviour of infill walls.

Considering that openings are important and a non-avoidable part of infill wall constructions, investigation in this area has not received sufficient priority. More tests are deemed necessary to better understand how openings influence the OoP capacity of infill walls although in general, they cause failure earlier than in the case of solid infill walls.

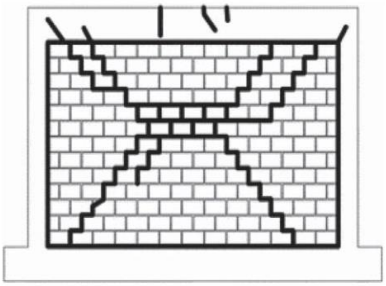

No opening - Akhoundi et al. (2016)

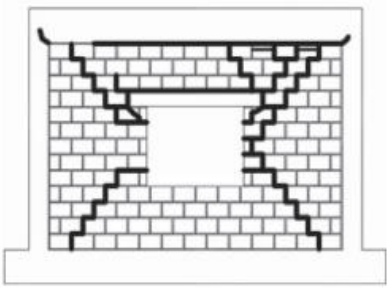

Window opening - Akhoundi et al. (2016)

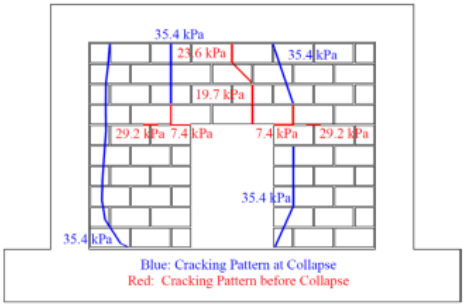

Door opening - Wang (2017)

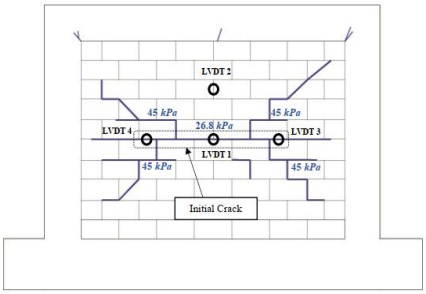

No opening – Spesdar (2017)

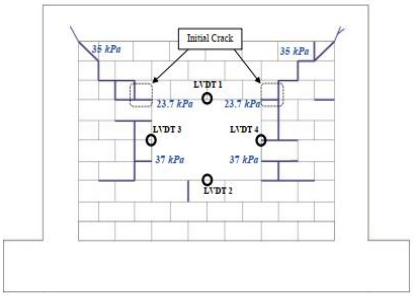

Window opening - Spesdar (2017)

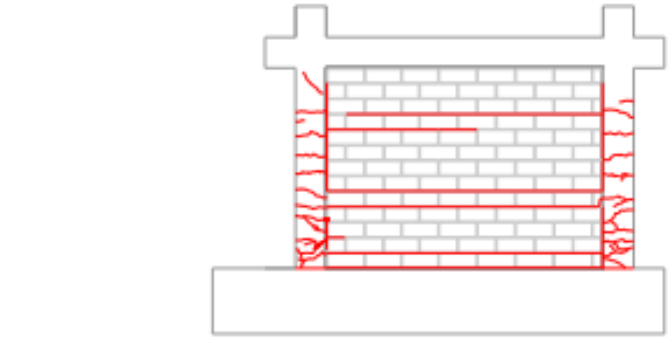

No opening - Anić et al. (2021)

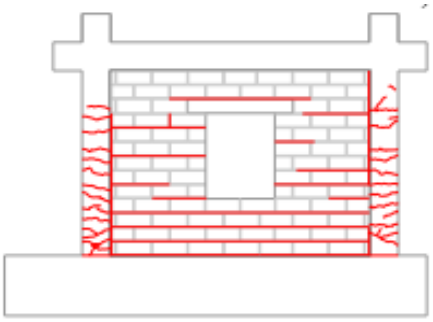

Centric window opening –

Anić et al. (2021)

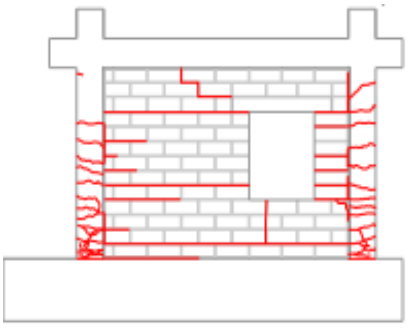

Eccentric window opening –

Anić et al. (2021)

Figure 2.18 Influence of openings in the cracking pattern of infill walls developing due to OoP load

2.1.4.6 Vertical load

Very few experimental campaigns have investigated the effect of gravity loads applied over columns on the OoP response of the URM infill, e.g. Angel (1994). In this experimental campaign, an infill specimen without a vertical load (specimen 6t) and a specimen with a vertical load (specimen 6c) of 12.8 kN on each column (producing stress of 0.14 MPa), were tested in the OoP direction using an airbag pressure. The load-displacement curves of

those two specimens were similar to each other; the OoP strength of the masonry infill wall was not much affected. Vertical stress only increased the initial stiffness of specimen 6c. Angel (1994) also investigated the effect of vertical stress produced in infill due to vertical loads in columns. It was found that with a vertical load of 222.4 kN in each column, the infill carried only 7% of the vertical force on the columns. This was not sufficient to increase the OoP capacity of the infill.

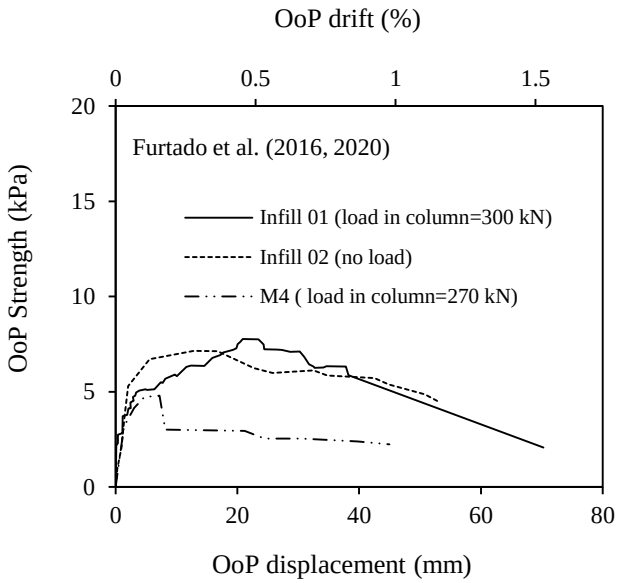

a)

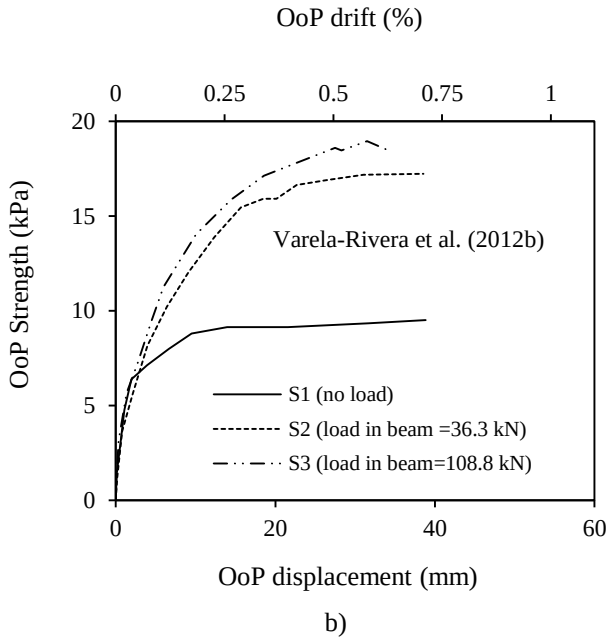

Figure 2.19 Influence of vertical pre-compression on the OoP capacity of masonry infill walls: a) Furtado et al. (2016); b) Varela-Rivera et al. (2012b)

Furtado et al. (2016) also tested infill specimens subjected to OoP pressure using an airbag, with and without a vertical load of 300 kN applied over the columns. The specimen with a gravity load i.e. Inf_01 showed slightly higher strength than the one without a gravity load i.e. Inf_02 (Fig 2.19). Inf_01 was subjected to continuously increasing OoP pressure while Inf_02 was subjected to load-unload cycles of pressure. Infill specimen M4 by Furtado et al. (2020) which was also subjected to unidirectional cyclic loads and a gravity load of 270 kN in the columns showed about 35% lower strength compared to Inf_02. Therefore, the results of the experimental campaigns are contrasting with each other. In one case, Inf_01 with gravity load showed a slightly higher capacity while gravity loaded specimen (M4) exhibited less strength. However, one should not neglect the fact that although

infill specimens were built with the same type of materials in Furtado et al. (2016) and Furtado et al. (2020), the mechanical properties were slightly different between the panels. The cracking pattern of M4 showed that interfacial gaps were created between infill and beams at the top and bottom, and vertical cracking was observed almost at mid-span. This indicated that vertical arching was not effective in the infill wall and this could be the primary reason for the decreased strength.

Experimental studies by Varela-Rivera et al. (2012b) showed that a vertical load applied over the top beam influences the OoP capacity of confined masonry walls. The capacity was enhanced when the vertical load was increased (Fig 2.19). Rabinovitch and Madah (2011) also investigated the OoP behaviour of infill walls under different compression levels applied to the top beam but under dynamic shake table tests. The test results demonstrated that under higher compression the magnitude of the OoP displacement and acceleration were smaller than at lower levels of compression, consequently increasing the OoP infill capacity. From what above reported, it is clear univocally the advantageous contribution of vertical stress on infills.

2.1.4.7 Surface finish in infill walls

The use of surface finish like plaster is common in infill walls. The thickness of the plasters can be different depending upon the function and finish of the wall. Usually, the thickness ranges from 10 mm to 15 mm. Experimental test results show that the type of plasters can affect the OoP performance of infill walls.

Experimental studies carried out by Pereira et al. (2011) compared the performance of infill walls made of 150 mm thick masonry units with and without the surface finish. Pereira et al. (2011) found that 10 mm plaster

without reinforcement on both sides (specimen Wall_REF_02) resulted in about 40 kN (7kPa) OoP lateral strength, while the URM specimen without plaster (Wall_REF_01) showed a peak resistance of only 12 kN (2 kPa). The masonry of infill specimens had similar compressive strength but the one with plaster had higher elastic modulus and shear strength. For the specimen without plaster, the upper frame-infill interface was completely damaged and the upper zone of the wall had a partial or total collapse of the masonry units. Significant OoP tilting of the infill wall at the top level was observed with a horizontal crack at the bottom, indicating cantilever type structural failure. On the other hand, the specimen with the plaster showed a different failure pattern. In particular, there was some damage at the interface between the infill and top beam with the formation of horizontal and vertical cracks in the central area of the panel. Diagonal cracking was also observed on the lower half of the panel, indicating the possibility of a two-way arching mechanism. This could be the reason for such a difference in the OoP strength of specimens with and without the application of plaster.

Da Porto et al. (2015) also tested URM infill walls with different types of plaster (ordinary plaster, natural hydraulic lime, lime gypsum plaster) under sequential IP and OoP loads. Additionally, infill specimens with steel meshes in such plasters were tested. In all cases, 120 mm thick masonry units were used and 15 mm thick plaster was applied on both sides of the wall. Types of plasters affected the OoP capacity of the infill walls. In particular, in the case of unreinforced plaster, specimen 1-GP-UR, built with high strength mortar and plastered with low compressive strength ordinary plaster, showed less OoP strength (18.6 kN = 1.7 kPa) compared to specimen 7-BC-UR which was built with low strength mortar and plastered with relatively high strength natural hydraulic lime plaster. The latter showed OoP capacity of 47.4 kN (4.3 kPa). Similarly, specimen 5-BG-UR, which was built with mortar as in

specimen 7-BC-UR and plastered with low strength lime gypsum plaster, failed under IP drift (1.2%) and could not be tested in OoP load.

Although the influence of surface finishes is evident, there are not enough tests to understand to what degree these finishes affect the OoP behavior of an infill wall. Since plasters are used in almost every wall, it needs further experimental investigations.

2.1.4.8 Infill wall mechanical properties

The OoP strength of infill walls is derived from an arching action, which depends upon the compressive strength of the masonry. The compressive strength of masonry is largely dependent on the strength of the masonry units and mortar. However, only a few researchers have investigated the impact on OoP strength due to a change in masonry units, mortar type, or masonry strength in general.

In Angel (1994), specimens 6 and 7 made with clay bricks but with different types of mortar (6 with lime mortar and 7 with type N i.e. cement, lime and sand mixed mortar) showed differences in OoP capacity. Two infill walls had identical geometrical properties (thickness= 98.4 mm). But the strength of the lime mortar was comparatively lower compared to Type N mortar (6.2 MPa in the former and 8.2 MPa in the latter) and the compressive strength of the masonry for specimen 6 was less than half that of specimen 7 and both specimens were subjected to the same amount of prior IP drift (0.25%). Consequently, the OoP strength of specimen 6 was observed to be less than half that of specimen 7.

Moreno-Herera et al. (2016) experimented on infill walls (W1 to W8) built with hollow concrete blocks, hollow clay bricks and solid clay bricks having different compressive strengths but made in equal strength mortar. Experimental results showed OoP strength highly dependent on the

compressive strength of masonries. For example, walls W2 and W3 with a different types of unit (compressive strength of 16.3 MPa in the former and 18.9 MPa in the latter) but similar compressive strength of masonry (6.48 MPa in the former and 6.17 MPa in the latter) showed similar OoP strength (10.49 kPa in the former and 11.06 kPa in the latter). However, specimen W1 with masonry units' strength of 6.58 MPa and an average masonry compressive strength of 3.72 MPa had an OoP capacity of only 8.8 kPa.

From the above, it can be understood that with an increase in compressive strength of the mortar, masonry unit and masonry, the OoP capacity of the masonry infill wall increase. But, the available experimental campaigns have focused much less on this aspect. As also highlighted in section 2.1, only in a few experimental campaigns, infill specimens with masonry strength higher than 3 MPa in general for both solid and hollow masonry units, were tested. Therefore, more systematic experimental campaigns in the range of infill masonry properties are necessary to fill the voids in understanding the OoP behaviour of infill walls.

2.1.4.9 Stiffness of the surrounding frames

The arching action in infill walls depends on the stiffness of the surrounding frames. This has been understood and thus the effect of frame flexibility has been incorporated into analytical capacity models to define the OoP strength (Dawe and Seah 1989; Angel 1994; Flanagan and Bennett 1999a; Moghadam and Goudarzi 2010). Angel (1994) also defined the criteria of flexural stiffness required for frames to be sufficiently stiff. However, there are not many tests where the effect of frame stiffness is directly investigated. In Spesdar (2017) and Wang (2017), the OoP behaviour of URM infills in RC and steel frames was tested. The OoP capacity in the case of steel frames was significantly lower than in the case of RC frames (Fig 2.20). According to the

authors, the low capacity in the case of steel frames was due to the small bending stiffness of the flange of the steel sections, although the flexural stiffness of the whole steel cross-sections was higher than that of RC cross-sections. The authors also attributed the lower strength to the lower torsional stiffness of the steel frames. The OoP strength of infill walls in steel frames can be influenced by the bonding between the infill and the steel sections, not so effective as in the RC frame. However, this aspect has not been studied experimentally. Further tests with variations in the stiffness of bounding frames can be helpful to understand the stiffness criteria required for the optimum OoP performance of infill walls.

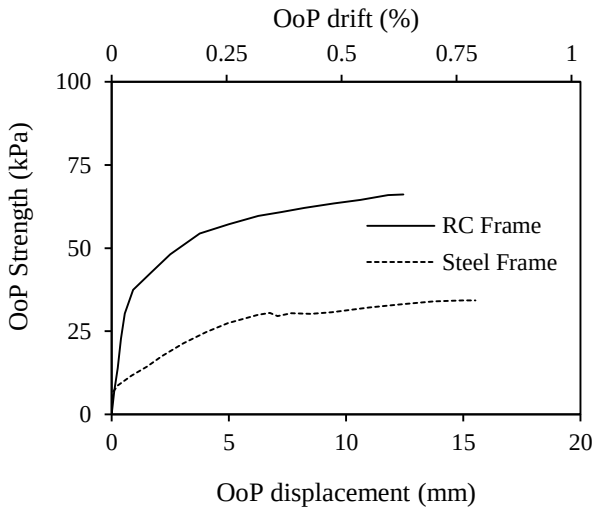

Figure 2.20 OoP capacity of infills in RC and steel frames by Spesdar (2017) and Wang (2017)

2.1.4 OoP damage and its effect on IP capacity

Some experimental campaigns can be found in the literature exploring the infill's IP behaviour after OoP loading. This section is devoted to this subject completing the frame of the OoP tests available in the literature and suggesting a higher influence of IP damage on OoP behaviour with respect to the influence of OoP damage on IP behaviour.

In the research of Flanagan and Bennett (1999b), the level of the influence of OoP damage on IP behaviour is immediately clear. During the experiment, specimen 20 was subjected to increasing OoP pressure (load-unload cycles) using an airbag up to 20.7 kPa and a mid-panel deflection of 10.9 mm. Likewise, specimens 11 and 13 were subjected to OoP lateral drift loads applied to the frame top or to the columns at mid-height. To specimen 11, a cantilever curvature was applied (restrained base and free top) at a drift of 1.7 % and specimen 13 was first subjected to a beam curvature (restrained base and top) followed by a cantilever curvature at a drift of 1.2%. After application of the OoP load, specimens 11, 13 and 20 were tested under IP cyclic loads until failure. These specimens reached the peak IP strength at lower displacements than the control specimen 2 (Fig 2.21). Moreover, specimen 13 showed slightly higher initial stiffness than the other specimens and specimen 11 showed less IP capacity comparatively. It is to be noted that specimens 2, 11, 13 and 20 had the same thickness (200 mm). The loss in IP capacity was higher in the case of specimen 11 due to a higher OoP drift applied to the frame. Therefore, OoP drift loads when non-negligible, can modify the IP behaviour of infilled frames.

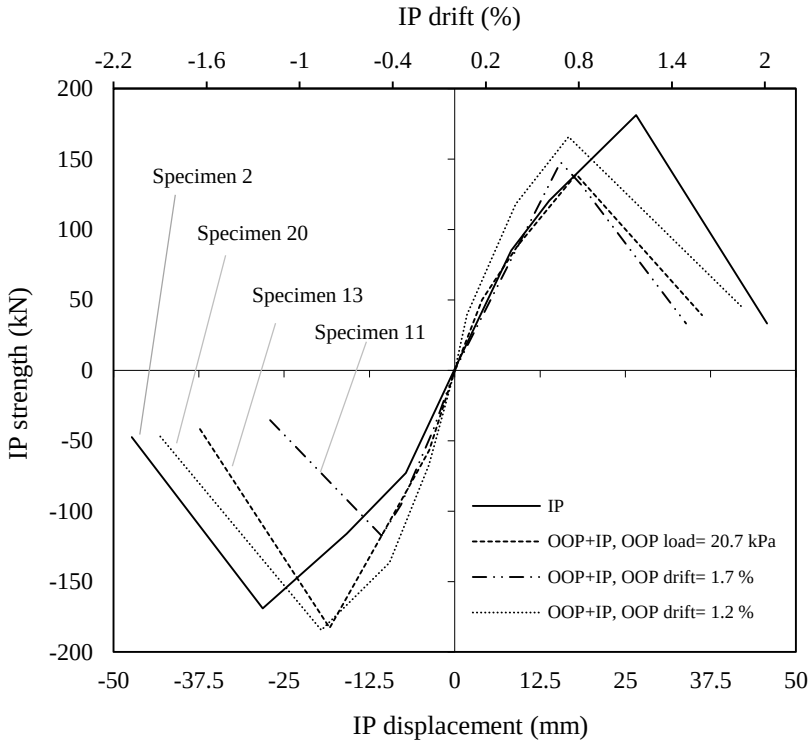

Figure 2.21 Influence of OoP damage in IP behaviour by Flanagan and Bennett (1999b)

Tests by Henderson et al. (1993) and Spesdar (2017) also showed that the IP capacities were little affected by prior OoP damage. In Henderson et al. (1993), infilled frame was subjected to an OoP cyclic drift load applied to the frame, while in Spesdar (2017), monotonic OoP pressure was applied to the infill, using an airbag. A cyclic IP load was applied in the former case and a monotonic IP load was applied in the latter. The prior OoP damage induced a slight loss of the initial IP stiffness of the specimens in both cases (Fig 2.22). The reason for the small loss in IP capacity in the case of Henderson et al. (1993) was the small OoP drift (<1%) which caused slight damage to the

columns and the infill. Similarly, in the case of Spesdar (2017), OoP load was applied only until the cracking of infill which did not affect the IP performance.

However, Palieraki et al. (2018) showed a decrease of about 20% in IP peak strength due to prior OoP damage. A uniform OoP load was applied in load-unload cycles up to an infill drift of 2.57%, causing a residual OoP displacement. This was the primary reason for the loss of capacity in the IP direction. Further, in the experimental research by Butenweg et al. (2019), a cyclic IP load was applied simultaneously at constant OoP pressure. Although the peak IP strength was slightly higher, the deformation capacity decreased by a factor of around 2 as compared to another specimen affected by IP+OoP+IP loads sequentially applied.

These results indicate that the damage due to loading in the OoP direction of infills can alter the IP capacity of infill walls and the infilled frames. Especially when OoP inter-storey drift loads are applied, the damage in the frames could be higher determining a lower IP capacity (Anić et al. 2021).

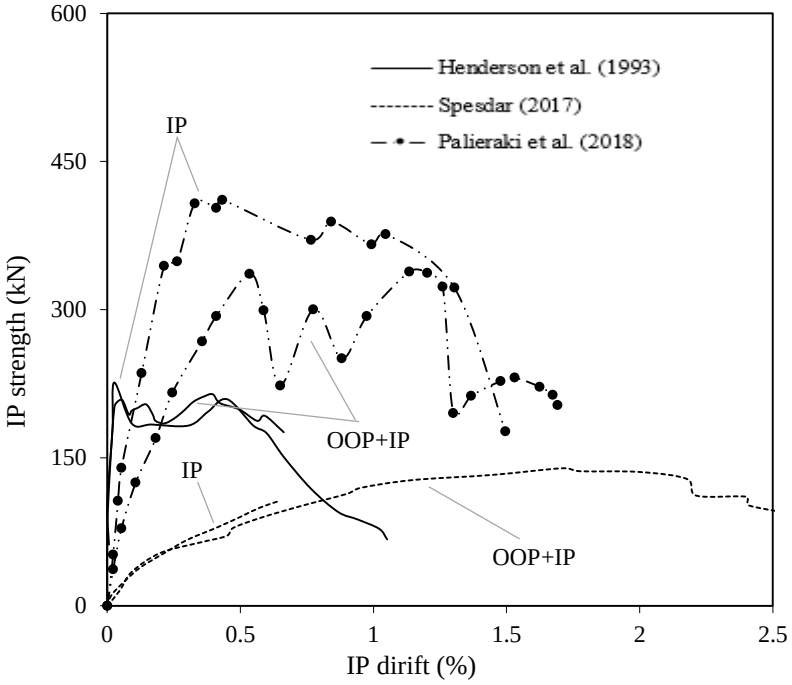

Figure 2.22 Influence of OoP damage in the IP behaviour of infill walls

2.2 Analytical capacity models

Analytical models are simple tools to predict the OoP capacity of infill walls. They can be very handy in the absence of simple and efficient numerical models to assess the OoP seismic vulnerability of infill walls. Several analytical models have developed over the years. These models are described below in detail.

2.2.1 Capacity models for strength calculation

The out-of-plane capacity of infills is generally measured by the maximum uniform lateral pressure causing the collapse. Two types of models

have been proposed to define the maximum load that can be resisted by the infill walls; i) flexural action-based models ;) arching action-based models.

2.2.1.1 Flexural action-based model

The flexure-based models were conceptualized on the basis that the tensile or flexure strength is the governing factor in determining the lateral OoP capacity of URM infill walls. The first flexure-based model was derived from the Timoshenko beam theory (Timoshenko and Woinowsh-Krieger 1959). In 1976, Haseltine (1976) gave another flexural model deriving the maximum load using the concept of the modified yield-line analysis for two-way action. In such models, the influence of the vertical compression level acting on the panel was first proposed by Hendry (1973).

However, as discussed in the previous section, experimental studies have revealed that the predominant resisting mechanism arises due to arching action, after the cracking of the panel in flexure. Therefore, the capacity derived from the flexure-based models is too conservative.

In this study, the models based on flexure are not discussed in detail and focus is given to the arching action-based models. Important information about such models can be found in Asteris et al. (2017).

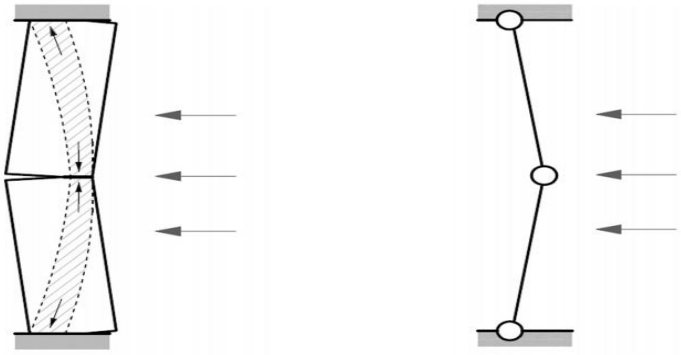

Figure 2.23 The arching concept: (a) Physical mechanism, (b) idealized 3-hinge arch mechanism

2.2.1.2 Arching action-based model

In OoP loads, the infill wall first cracks due to tension. After the cracking, two masonry elements rotate as rigid bodies and they form a three hinge arch which induces sufficient compressive thrust along the fibres of masonry to resist the lateral OoP load until collapse. Models in which the maximum capacity is derived based on arching are known as the arching action-based model. A schematic picture of the concept of arching is shown in Fig 2.23a, and an equivalent scheme for computation is represented by a three hinge arch shown in Fig 2.23b.

The arching mechanism developed by masonry infills was first investigated by McDowell et al. (1956). Based on the one-way arching behaviour of a masonry strip rigidly supported at the ends, the authors proposed an equation for the determination of the maximum OoP capacity q_{ult} as follows

$$q_{ult} = \gamma \frac{f_m}{2(h/t)} \tag{2.1}$$

where γ is a coefficient depending on the thickness and the slenderness ratio (*h/t*) and f_m is the compressive strength of the masonry. For *h/t* in the order of 10, γ takes a value of about 1. The unit of the f_m determines the unit of the OoP capacity q_{ult}.

Although the model is based on the arching theory the model took into account only the one-way arching behaviour of load-bearing masonry. However, a true OoP capacity of URM infills bounded from all sides by frames is influenced by the two-way arching action.

Dawe and Seah (1989) were the first to develop equations specifically for infilled frames based on the concept of two-way arching action. The

authors performed a comprehensive experimental campaign on steel frames infilled with hollow concrete blocks. Based on the experimental results, analytical formulations were derived. Two different empirical relations were proposed: the first one for infills supported on four sides, i.e. interested by two-way arching (Eq. 2.2), and the second one for infill walls supported on three sides and free at the top (gapped two-way arching - Eq. 2.3).

$$q_{ult} = 800(f_m)^{0.75} t^2 \left(\frac{\alpha}{l^{2.5}} + \frac{\beta}{h^{2.5}} \right) \tag{2.2}$$

$$q_{ult} = 800(f_m)^{0.75} t^2 \left(\frac{\alpha_{gap}}{l^{2.5}} \right) \tag{2.3}$$

In the equations proposed by Dawe and Seah (1989), the effect of the frame's stiffness was introduced by the factors α, β, α_{gap} (whose expressions are given in Eqs 2.4 – 2.6). The parameter α considers the influence of columns in the case of horizontal arching, while β corresponds to vertical arching due to beams. Dawe and Seah (1989) also included the effects of the torsional behaviour of the frames in their equation.

$$\alpha = \frac{1}{h}(EI_c h^2 + GJ_c th)^{0.25} \leq 50 \tag{2.4}$$

$$\beta = \frac{1}{l}(EI_b l^2 + GJ_b tl)^{0.25} \leq 50 \tag{2.5}$$

$$\alpha g_{ap} = \frac{1}{h}(EI_c h^2 + GJ_c th)^{0.25} \leq 75 \tag{2.6}$$

In the above equations, *l*, *h* and *t* are the length, height and thickness of infill walls respectively, while f_m is the compressive strength of masonry. Masonry is generally considered as made of a homogeneous material. Further, I_b and I_c are the moments of inertia of the surrounding beams and columns while J_b and J_c are the torsional constants of beams and columns correspondingly. *E* and *G* are Young's modulus and shear modulus of the frame member materials respectively.

The unit of each parameter plays an important role in the above equations. If *t*, *l* and *h* are in mm, f_m, *E* and *G* are in MPa and I_c, I_b, J_c and J_b are expressed in mm^4, the maximum OoP capacity q_{ult} is obtained in kPa. The maximum thickness of the infill wall is limited to one-eighth of the infill height while calculating the capacity using this equation.

Later, Angel (1994) and Abrams et al. (1996) developed a methodology based on the arching theory for a strip of infill wall between two rigid supports. Two failure modes were identified; one based on crushing of the masonry in the case of infill wall with low slenderness ratio and the other one characterized by the snapping of the panel for infill wall with high slenderness ratio. A critical slenderness ratio distinguishing the two possible failure modes was determined. The authors proposed an equation (Eq. 2.7) based on the experimental results conducted on infilled reinforced concrete frames. Moreover, the authors also proposed the equation for strength reduction factor R_1 (Eq. 2.8) to take into account the decrease in the OoP capacity due to the damage caused by IP loads. However, the equation involves the parameter Δ_{crack} (in-plane displacement at which the first crack is expected to occur) in the calculation of R_1 which is not easy to estimate. Further, the reduction factor R_2 was proposed (Eqs. 2.9 and 2.10) accounting

for the bounding frame's stiffness for the case of infill walls that are not continuous (infill walls at the top or at an exterior bay).

$$q_{ult} = R_1 R_2 \frac{2 f_m \lambda}{h/t} \tag{2.7}$$

$$R_1 = \left[1.08 + (h/t)(-0.015 + (h/t)(-0.00049 + 0.000013(h/t)))\right]^{\frac{\Delta}{2\Delta crack}} \tag{2.8}$$

$$R_2 = 0.357 + 2.49 \times 10^{-14}\, EI \tag{2.9}$$

for $5.74 \times 10^{12}\ Nmm^2 < EI < 25.83\ 10^{12}\ Nmm^2$

$$R_2 = 1 \qquad \textit{for } EI > 25.83\ 10^{12}\ Nmm^2 \tag{2.10}$$

In Eqs. 2.9 and 2.10, the factor R_2 depends upon *EI* (flexural rigidity) of the smallest frame member at the side where a neighbouring panel is missing. The unit of f_m (compressive strength of masonry) determines the unit of the output capacity q_{ult}.

The factor λ in Eq. (2.7) was inserted to address the effect of the slenderness ratio of the infill wall. The values given by the author are inserted in Table 2.2. An expression that fits the values of λ given by Angel (1994) was provided later by Flanagan and Bennett (1999a) with an Eq. (2.11):

$$\lambda = 0.154 e^{-0.0985(h/t)} \tag{2.11}$$

Table 2.2 Value of coefficient λ for *h/t* as per Angel (1994)

h/t	5	10	15	25	30	35
λ	0.129	0.060	0.034	0.013	0.008	0.005

Bashandy et al. (1995) and Klingner et al. (1996) developed an analytical equation wall (Eq. 2.12) to calculate the OoP resistance of URM infill wall. The model combined the resistance from both vertical and horizontal arching action by dividing the infill panel into vertical and horizontal strip segments. No effect of frames was taken into account in the equation. The OoP capacity q_{ult} was given as

$$q_{ult} = \frac{8}{h^2 l} M_{yv} \left[(l - h) + h \ln(2) \right] + \frac{8}{h^2 l} M_{yh} \left(\frac{x_{yv}}{x_{yh}} \right) \ln\left(\frac{l}{l - h/2} \right) l \tag{2.12}$$

where x_{yv} and x_{yh} (Eq. 2.13 and Eq. 2.14) are the maximum OoP displacements respectively at the centre of the central vertical and horizontal strips of the infill wall separately considered. M_{yv} and M_{yh} (Eq. 2.15 and Eq. 2.16) are the strips' resisting moments corresponding to the attainment of vertical and horizontal arching.

$$x_{yv} = \frac{t f_m}{1000 E_m \left[1 - \frac{h}{2\sqrt{(h/2)^2 + t^2}} \right]} \tag{2.13}$$

$$x_{yh} = \frac{t f_m}{1000 E_m \left[1 - \frac{l}{2\sqrt{(l/2)^2 + t^2}} \right]} \tag{2.14}$$

$$M_{yv} = 0.85 \frac{f_m}{4} \left(t - x_{yv} \right)^2 \tag{2.15}$$

$$M_{yh} = 0.85 \frac{f_m}{4} \left(t - x_{yh} \right)^2 \tag{2.16}$$

In the above equations, *l*, *h* and *t* are the length, height and thickness of infill walls respectively and f_m is the compressive strength of masonry. If *t*, *l*, and *h* are in mm and f_m is in kPa, q_{ult} is obtained in kPa. Although not explicitly mentioned, this model can be also used to estimate the OoP capacity for infill-beam gap conditions or infill-column gap conditions, taking into account only one-way arching.

FEMA 273 (1997) and FEMA 356 (2000) used a simplified version of Angel's (1994) equation by removing the factors R_1 and R_2. The ultimate OoP capacity q_{ult} was provided as

$$q_{ult} = \frac{0.7 f_m \lambda}{h/t} \tag{2.17}$$

ASCE/SEI 41-17 (2017) however has replaced FEMA methods with a slight change in the reduction factor R_1 for IP damaged cases (R_1 = 0.6). ASCE 41 also includes the reduction factor R_o to take into account the OoP strength reduction due to the openings, that is

$$R_o = \left(1 - \frac{A_o}{A}\right) \tag{2.18}$$

where A_o is the area of the opening and A is the total area of the infill wall.

Flanagan and Bennett (1999a) modified the equations of Dawe and Seah (1989) by removing torsional constants from the parameters and gave equation (Eq. 2.19) to calculate the OoP capacity as

$$q_{ult} = 729.1(f_m)^{0.75} t^2 \left(\frac{\alpha}{l^{2.5}} + \frac{\beta}{h^{2.5}} \right) \quad (2.19)$$

$$\alpha = \frac{1}{h}(EI_c h^2)^{0.25} \leq 50 \quad (2.20)$$

$$\beta = \frac{1}{l}(EI_b l^2)^{0.25} \leq 50 \quad (2.21)$$

where *l*, *h* and *t* are the length, height and thickness of infill walls respectively, while f_m is the compressive strength of masonry. Further, I_b and I_c are the moments of inertia of the surrounding beams and columns and *E* and *G* are Young's modulus and shear modulus of the frame materials respectively.

In the equations, the parameters α (Eq. 2.20) and β (Eq. 2.21) considered the effects of columns' and beams' stiffness respectively. This shows that in this model, total capacity is derived by summing the capacity of horizontal and vertical arching. Therefore, although not explicitly mentioned, like the model of Dawe and Seah, it can be also used to estimate the OoP capacity for infill-beam gap conditions or infill-column gap conditions. In the equation, if f_m is in MPa, *t, l* and *h* are in mm, *E* and *G* are in MPa, I_c and I_b are in mm^4, the OoP load capacity q_{ult} is obtained in kPa. In using the equation, for an infill wall with *h/t* less than 8, a value of *1/8* of the height should be used as the thickness of the infill wall.

Moghaddam and Goudarzi (2010) proposed two modes of failure based on the infill's slenderness and accordingly gave two expressions for determining the OoP load capacity. According to the authors, a thick infill wall derives the capacity q_{cr} until the crushing of masonry while a thin infill

wall derives the capacity $q_{\max}$ until failure takes place due to transverse instability while loaded in the OoP direction. The expressions for the q_{cr} and $q_{\max}$ are given by Eq. 2.22.

$$q_{ult}=\min\begin{cases} q_{cr}=\dfrac{0.85\,f_m}{(h/t)^2}-\left(0.12+\dfrac{0.045}{\alpha}\right)\dfrac{{f_m}^2}{E_m} \\ q_{\max}=\dfrac{0.18E_m}{\left(0.12+\dfrac{0.045}{\alpha}\right)\left(\dfrac{h}{t}\right)^4} \end{cases} \tag{2.22}$$

$$\alpha=\frac{k}{E_m tl/h} \tag{2.23}$$

$$k=\frac{385EI_b}{l^3} \tag{2.24}$$

where *l*, *h* and *t* are the length, height and thickness of infill walls respectively, and f_m and E_m are the compressive strength and modulus of elasticity of masonry respectively.

The ultimate OoP load capacity q_{ult} is the minimum between q_{cr} and $q_{\max}$. In the above equation, α is the ratio of vertical support stiffness to the vertical in-plane stiffness of the panel defined by Eq. 2.23 and *k* is the stiffness of the top beam (Eq. 2.24). If *t, l* and *h* are in mm, f_m, E_m and *E* are in MPa and I_b is in mm^4, the OoP capacity q_{ult} obtained from the equation is in MPa.

In 2013, Morandi et al. (Morandi et al. 2013) proposed an equation to calculate the OoP capacity of reinforced or URM infill walls based on the recommendation provided by Eurocode 6 (2005) which is a proposal for the

load-bearing masonry. Like in Angel (1994), the reduction of the OoP capacity due to IP damage was taken by the authors with a strength reduction factor R_1 in the equation as follows.

$$q_{ult} = \left(0.72\left(\frac{t}{h}\right)^2 f_m + 7.2\frac{t}{lh^2} A_s f_y \right) \times R_1 \tag{2.25}$$

Morandi et al.'s equation is the only equation that can take into account the contribution of vertical reinforcement to the OoP capacity of the infill wall. In the above equation, the first term represents the OoP strength due to arching and the second term represents the OoP resistance due to vertical reinforcement. A_s represents the cross-sectional area and f_y is the yield strength of the reinforcement. The term representing the resistance due to reinforcement can be dropped when evaluating the OoP capacity of the URM infill wall.

In the above equation, the factor R_1 depends upon the IP damage level defined by inter-storey drift (*IDR*) experienced by the infill wall before being loaded in the OoP direction. With increasing IP damage, there is a step-wise reduction of capacity. The expression for R_1 was given as

$$R_1 = \begin{cases} 1.0, \; for IDR \leq 0.3\% \\ 0.2, \; for 0.3\% \leq IDR \leq 1.0\% \\ 0, \; for IDR > 1\% \end{cases} \tag{2.26}$$

For more conservative results, R_1 was defined with a linear formulation for drifts lower than 0.3% as follows.

$$R_1 = 1 - 2.67\,IDR, \quad for \quad IDR \leq 0.3\% \tag{2.27}$$

In Eq. 2.25, *l*, *h* and t denote the length, height and thickness of the infill wall and f_m is the compressive strength of masonry. If *t*, *h* and *l* are expressed in mm, f_m and f_y in MPa, A_s in mm^2, OoP load capacity q_{ult} is obtained in MPa.

Ricci et al. (2018c) developed an empirical equation to calculate the maximum OoP strengths by observing the capacities of the tested specimens from different experiments (Angel 1994, Flanagan and Bennett 1999b, Calvi and Bolognini 2001, Hak et al. 2014 and Furtado et al. 2016). According to the authors, maximum OoP capacity q_{ult} can be calculated by the following relation.

$$q_{ult} = 1.95\, f_m^{0.35}\, \frac{t^{1.59}}{h^{2.96}} \tag{2.28}$$

In the above equation, if the thickness (*t)* and height (*h)* are expressed in meter (m) and the compressive strength of masonry in the direction of gravity f_m in MPa, the maximum OoP capacity q_{ult} is obtained in MPa.

Recently, Liberatore et al. (2020) proposed a capacity model to estimate the OoP strength of an infill wall bounded on 4 edges by a sufficiently stiff frame based on the results of numerical analysis (micro-modeling) with the following equation.

$$q_{ult} = 0.26\, f_m^{0.9}\, \frac{h}{l}\left(\frac{h}{t}\right)^{-1.23} \tag{2.29}$$

According to Liberatore et al., Eq. 2.29 is valid for infill walls with a height lesser or equal to their length, and for masonry with compressive strength f_m not larger than 15 MPa.

Liberatore et al. (2020) has also given an expression to compute the reduction factor R_o for openings as

$$R_o = \min\left(1; 0.64 - 0.124 \times \ln\left(\frac{A_o \times l \times t}{A \times h \times h} f_m\right)\right) \tag{2.30}$$

In Eq. (2.30), A_o is the area of the opening and A is the total area of the infill wall.

Besides Angel (1994) and Morandi et al. (2013), there are other equations proposed by the researchers specifically to calculate the strength reduction factor R_1, when the infill wall is damaged in IP previously.

Verlato et al. (2014) provided an empirical equation to calculate the reduction factor R_1 depending only on the experienced inter-storey drift ratio (*IDR*) expressed in percentage as follows

$$R_1 = \begin{cases} 1 - 0.86\,IDR, & for\ IDR \le 0.7\% \\ 0.4, & for\ 0.7\% \le IDR \le 1.20\% \\ 0, & for\ IDR > 1.2\% \end{cases} \tag{2.31}$$

New Zealand code (NZSEE 2017) recommends the reduction of strength due to IP damage based only on the slenderness ratio (*h/t*) of the infill wall as shown by Eq. (2.32). The equation is implicitly valid for values of IP drifts higher than two times the drift corresponding to the formation of the first visible cracks.

$$R_1 = \min\left[1.1\left(1-\frac{h/t}{55}\right);1\right] \tag{2.32}$$

According to Eq. (2.32), the OoP capacity reduction factor does not depend on the IP drift level which is in contrast to the provisions generally available in the other models. Assigning a constant strength reduction factor does not agree with the experimental observations (Fig 2.13).

Furtado et al. (2018a) also proposed an empirical equation to estimate the OoP strength reduction factor R_1 because of the previous IP damage. The empirical relation was derived based on the experimental results of Angel (1994), Calvi and Bolognini (2001), Furtado et al. (2016) and Ricci et al. (2018a) which is as follows

$$R_1 = 0.1638 \times IDR^{-0.946} \tag{2.33}$$

Similarly, by analysing the results from the same experiments taken by Furtado et al. (2018a) i.e. Angel (1994), Calvi and Bolognini (2001), Furtado et al. (2016) and Ricci et al. (2018a), Ricci et al. (2018a) also proposed empirical equation to calculate the OoP strength reduction factor in an alternative way. The expression for the reduction of OoP capacity given by Ricci et al (2018a) has the form

$$R_1 = \min\left(1; 0.14 IDR^{-1.12}\right) \tag{2.34}$$

Later, Ricci et al. (2018b) proposed a factor R_1 based on their experiments. The results from two types of infill walls (infill specimens of 80 mm and 120 mm) were used to derive the relation. According to the authors, the reduction factor depends upon the level of IP damage (*IDR* expressed in percentage*)* and the slenderness ratio *h*/*t* (Eq. 2.35).

$$R_1 = \min\left(16.7\,IDR^{-0.69}\left(\frac{h}{t}\right)^{-1.36};1\right) \tag{2.35}$$

Additionally, Ricci et al. (2018b) proposed another equation to calculate R_1 as shown in Eq. 2.36. The relation was given after some statistical analyses of the results obtained from the set of experiments i.e. Angel 1994, Calvi and Bolognini 2001, and Ricci et al. 2018b. This equation also depends upon both *IDR and h*/*t*.

$$R_1 = \min\left(\left[0.98 - 0.04\min\left(20.4;\frac{h}{t}\right)\right]IDR^{-0.97};1\right) \tag{2.36}$$

Recently, these equations proposed in Ricci et al. (2018b) have been updated in Di Domenico et al. (2021) where the equations are proposed separately for the case of thin infill walls (*h/t* higher than 15) and also extended to the case of the thick infill walls (*h/t* higher than 8). The infill wall can have any thickness. Therefore, the equation given for *h/t* >8 is discussed here. This equation (Eq. 2.37) considers the influence of aspect ratio (*l/h*) in the OoP strength reduction because of prior IP damage in addition to the *IDR* and *h*/*t*.

$$R_1 = \min\left\{1;\left(1.51 - 0.19\frac{l}{h} - 0.05\times\min\left(\frac{h}{t};20.4\right)\right)\times IDR^{-0.73}\right\} \tag{2.37}$$

The above equation by Di Domenico et al. (2021) is valid for aspect ratio (*length / h*eight) between 1 and 1.6, and *IDR* demand lower than 1.20%.

Akhoundi et al. (2018) proposed a very simple equation for the calculation of the strength reduction factor R_1 based on the result of their experiments in the following way:

$$R_1 = \frac{2 - IDR}{2} \tag{2.38}$$

Cavaleri et al. (2019) proposed the OoP strength and stiffness reduction equations based on numerical results. According to the authors, the OoP strength reduction factor R_1 was given as

$$R_1 = \min\left(1; 0.26 IDR^{-0.37}\right) \tag{2.39}$$

On the conservative side, a lower bound equation of R_1 was also given by Cavaleri et al. (2019) as follows

$$R_1 = \min\left(1; 0.15 IDR^{-0.49}\right) \tag{2.40}$$

2.2.2 Capacity models for displacement calculation

Excessive OoP deflection of the infill wall is a cause of its collapse during a seismic event. Normally, it is assumed that the maximum OoP deflection capacity is equal to the thickness of the infill wall. Therefore, to accurately characterize the OoP behaviour of the infill wall, it is important to understand its displacement capacity.

There are very few recommendations regarding the calculations of the OoP deflection at mid-height of the infill wall. For Example, FEMA 273 (1997) and FEMA 356 (2000) provided the expression for the calculation of the mid-height deflection (Δ) in the OoP direction of infill walls at the point of maximum OoP load it can resist. The equation is given below.

$$\frac{\Delta}{h} = \frac{0.002(h/t)}{1 + \sqrt{1 - 0.002(h/t)^2}} \tag{2.41}$$

The above equation is valid for slenderness ratio values up to 22. Later, Flanagan and Bennett (1999a) provided an equation to calculate the OoP mid-height deflection (Δ) modifying the equation from FEMA 273 (1997). This equation is valid slenderness ratio up to 31and is provided as:

$$\frac{\Delta}{h}=\frac{0.002(h/t)}{1+\sqrt{1-0.001(h/t)^2}} \tag{2.42}$$

Besides, the model for predicting the maximum OoP displacement capacity is not yet achieved. Normally, maximum displacement capacity is limited to the thickness of the infill wall.

2.2.3 Accuracy of the capacity models

Research on correlating OoP experimental results has also progressed in recent years (e.g. Pasca et al. 2017; Furtado et al. 2018a; Anić et al. 2020; Liberatore et al. 2020) whereby the reliability of the analytical models in describing the OoP capacity has been compared. For example, Pasca et al. (2017) found the model by Flanagan and Bennett (1999a) better for the infill specimens tested by Dawe and Seah (1989) while it was found conservative for the confined masonry specimens tested by Varella-Rivera et al. (2012a). Similarly, Anić et al. (2020) found that the models by Ricci et al. (2018b) and Moghadam and Goudarzi (2010) were relatively better for the case of infilled frames and Liberatore et al. (2020) found the equation in Eurocode 6 (2005), in average, better for the estimation of OoP capacity of masonry walls without frames, confined masonry walls or infill walls. However, the reliability of the available models is an open question. Especially for the case of predicting the OoP strength reduction factor (when infills are damaged previously by IP loads), only partially, the reliability of the available models has been checked.

In this section, available capacity models were checked for different cases: IP- undamaged, IP-damaged, gaps and openings, displacement calculation etc. In addition, the possibility of combining two types of models proposed separately for the case of P-undamaged and IP-damaged infill walls was checked. The necessary details of the infill walls and frames in the calculations are provided in Table 2.3 and Table 2.4.

Table 2.3 Details of the experiments, frame properties and loadings

Authors	Frame	Specimen	Column mm×mm	Beam mm×mm	Loading	*IDR* %	Gap with Top beam	Opening	E N/mm^2
Dawe & Seah (1989)	steel	WE2	W250×58	W200×46	OoP		No	No	199948
		WE4	W250×58	W200×46	OoP		No	No	199948
		WE5	W250×58	W200×46	OoP		No	No	199948
		WE8	W250×58	W200×46	OoP		No	No	199948
		WE6	W250×58	W200×46	OoP		Yes	No	199948
		WE9	W250×58	W200×46	OoP		No	Yes	199948
Angel (1994)	RC	1	304×304	254×304	OoP		No	No	24821
		2	304×304	254×304	IP+OoP	0.34	No	No	24821
		3	304×304	254×304	IP+OoP	0.22	No	No	24821
		6	304×304	254×304	IP+OoP	0.25	No	No	24821
Flanagan & Bennett (1999b)	steel	19	W250×45	W310×53	IP+OoP	0.78	No	No	199948
		18	W250×45	W310×54	OoP		No	No	199948
		25	W250×45	W310×59	OoP		No	No	199948
		22	W410×60	W460×113	OoP		No	No	199948
Calvi & Bolognini (2001)	RC	2	300×300	250×700	IP+OoP	0.4	No	No	25000[a]
		6	300×300	250×700	IP+OoP	1.2	No	No	25000[a]
		10	300×300	250×700	OoP		No	No	25000[a]
Pereira et al. (2011)	RC	Wall_REF_01	150×150	150×300	IP+OoP	0.8	No	No	27386[a]
		Wall_REF_02	150×150	150×300	IP+OoP	0.8	No	No	27386[a]
Da Porto et al. (2013)	RC	I	300×300	500×250	IP+OoP	1.2	No	No	26458[a]
Hak et al. (2014)	RC	TA1	350×350	350×350	IP+OoP	1.5	No	No	29155[a]
		TA2	350×350	350×350	IP+OoP	2.5	No	No	29155[a]
		TA3	350×350	350×350	IP+OoP	1	No	No	29155[a]
Furtado et al. (2016)	RC	Inf_01	300×300	300×500	OoP		No	No	24700
		Inf_02	300×300	300×500	OoP		No	No	24700
		Inf_03	300×300	300×500	IP+OoP	0.5	No	No	24700

Akhoundi et al. (2016)	RC	SIF-A	160×160	160×270	OoP		Yes	No	32000[a]
		SIF-B	160×160	160×270	OoP		No	No	32000[a]
		PIF-B	160×160	160×270	OoP		No	Yes	32000[a]
Spesdar (2017)	RC	IF-ND	1800×180	1800×180	OoP		No	No	16911
		IF-D1	1800×180	1800×180	IP+OoP	0.66	No	No	16911
		IF-W-ND	1800×180	1800×180	OoP		No	Yes	16911
Wang (2017)	RC	IF-RC-ID	1800×180	1800×180	IP+OoP	1.37	No	No	16911
	RC	IF-RC-D0	1800×180	1800×180	OoP		No	Yes	16911
	RC	IF-RC-TG	1800×180	1800×180	OoP		Yes	No	20357
	steel	IF-S	W150×30	W150×30	OoP		No	No	201172
Furtado et al. (2020)	RC	M4	300×300	300×500	OoP		No	No	24300
Ricci et al. (2018a)	RC	80_OOP_4E	200×270	200×270	OoP		No	No	30000[a]
		80_IP+OOP_L	200×270	200×270	IP+OoP	0.16	No	No	30000[a]
		80_IP+OOP_M	200×270	200×270	IP+OoP	0.37	No	No	30000[a]
		80_IP+OOP_H	200×270	200×270	IP+OoP	0.58	No	No	30000[a]
Ricci et al. (2018b)		120_OOP_4E	200×270	200×270	OoP		No	No	33985[a]
		120_IP+OOP_L	200×270	200×270	IP+OoP	0.21	No	No	33985[a]
		120_IP+OOP_M	200×270	200×270	IP+OoP	0.5	No	No	33985[a]
		120_IP+OOP_H	200×270	200×270	IP+OoP	0.89	No	No	33985[a]
Di Domenico et al. (2018)	RC	OOP_4E	200×270	200×270	OoP		No	No	30000[a]
		OOP_3E	200×270	200×270	OoP		Yes	No	30000[a]
Akhoundi et al. (2018)	RC	SIF-IO(0.3%)-B	160×160	160×270	IP+OoP	0.3	No	No	32000[a]
		SIF-IO(0.5%)-B	160×160	160×270	IP+OoP	0.5	No	No	32000[a]
		SIF-IO(1%)-B	160×160	160×270	IP+OoP	1.0	No	No	32000[a]
De Risi et al. (2019b)	RC	OOP	200×270	200×270	OoP		No	No	32749[a]
		IP_L-OOP	200×270	200×270	IP+OoP	0.15	No	No	32749[a]
		IP_M-OOP	200×270	200×270	IP+OoP	0.28	No	No	32749[a]
		IP_H-OOP	200×270	200×270	IP+OoP	0.51	No	No	32749[a]
Panto et al. (2019)	RC	Infill Sytem_1	160×160	160×270	OoP		No	No	16500

Koutas & Bournas (2019)	RC	S_CON	140×200	140×250	OoP	No	No	23505[a]
		D_CON	140×200	140×250	OoP	No	No	24495[a]

Note: OoP = OoP load only; IP+OoP = OoP load acting after IP load; OoP+IP = IP load acting after OoP load; RC =reinforced concrete

[a]Elastic modulus of frame material is estimated

Table 2.4 Details of the infill wall specimens from different experiments

Authors	Specimen	Masonry Cavity	l	h	t	f_{mv}	f_{mh}	E_{mv}	E_{mh}
			mm	mm	mm	N/mm^2	N/mm^2	N/mm^2	N/mm^2
Dawe & Seah (1989)	WE2	Vertical	3600	2800	190	24.3	18.4	17575	17400
	WE4	Vertical	3600	2800	140	24.3	18.4	17575	17400
	WE5	Vertical	3600	2800	90	24.3	18.4	17575	17400
	WE8	Vertical	3600	2800	140	24.3	18.4	17575	17400
	WE6	Vertical	3600	2800	190	24.3	18.4	17575	17400
	WE9	Vertical	3600	2800	190	24.3	18.4	17575	17400
Angel (1994)	1	NA	2438.4	1625.6	47.6	11.51	11.51	8046.2	8046.2
	2	NA	2438.4	1625.6	47.6	10.85	10.85	8046.2	8046.2
	3	NA	2438.4	1625.6	47.6	10.13	10.13	5212.4	5212.4
	6	NA	2438.4	1625.6	98.4	4.58	4.58	2137.4	2137.4
Flanagan & Bennett (1999b)	19	Horizontal	2240	2240	200	5.6	3	5300	2300
	18	Horizontal	2240	2240	200	5.6	3	5300	2300
	25	Horizontal	2240	2240	100	5.6	3	5300	2300
	22	Horizontal	2240	2240	330	2.29	2.6	5040	2800
Calvi & Bolognini (2001)	2	Horizontal	4200	2750	135	1.1	1.11	1873	991
	6	Horizontal	4200	2750	135	1.1	1.11	1873	991
	10	Horizontal	4200	2750	135	1.1	1.11	1873	991
Pereira et al. (2011)	Wall_REF_01	Horizontal	3500	1700	150	1.26	-	1577	-
	Wall_REF_02	Horizontal	3500	1700	170	1.34	-	1577	-
Da Porto et al. (2013)	I	Vertical	4150	2650	300	6	1.19	4312	1676
Hak et al. (2014)	TA1	Vertical	4220	2950	350	4.64	1.08	5299	494
	TA2	Vertical	4220	2950	350	4.64	1.08	5299	494
	TA3	Vertical	4220	2950	350	4.64	1.08	5299	494
Furtado et al. (2016)	Inf_01	Horizontal	4200	2300	150	0.531	-	1417.6	-
	Inf_02	Horizontal	4200	2300	150	0.531	-	1417.6	-
	Inf_03	Horizontal	4200	2300	150[c]	0.531	-	1417.6	-
Akhoundi et al. (2016)	SIF-A	Horizontal	2415	1635	80	1	-	1000[b]	-

Authors	Specimen	Masonry Cavity	l	h	t	f_{mv}	f_{mh}	E_{mv}	E_{mh}
			mm	mm	mm	N/mm^2	N/mm^2	N/mm^2	N/mm^2
	SIF-B	Horizontal	2415	1635	80	1	-	1000[b]	-
	PIF-B	Horizontal	2415	1635	80	1	-	1000[b]	-
Spesdar (2017)	IF-ND	Vertical	1350	980	90	9.4	-	7990	-
	IF-D1	Vertical	1350	980	90	9.7	-	8245	-
	IF-W-ND	Vertical	1350	980	90	9.4	-	7990	-
Wang (2017)	IF-RC-ID	Vertical	1350	980	90	7.9	-	6715	-
	IF-RC-D0	Vertical	1350	980	90	7.9	-	6715	-
	IF-RC-TG	Vertical	1350	980	90	9	-	7650	-
	IF-S	Vertical	1350	980	90	9	-	7650	-
Furtado et al. (2020)	M4	Horizontal	4200	2300	150	1.1	-	941.9	-
Ricci et al. (2018a)	80_OOP_4E	Horizontal	2350	1830	80	1.81	2.45	1090	1255
	80_IP+OOP_L	Horizontal	2350	1830	80	1.81	2.45	1090	1255
	80_IP+OOP_M	Horizontal	2350	1830	80	1.81	2.45	1090	1255
	80_IP+OOP_H	Horizontal	2350	1830	80	1.81	2.45	1090	1255
Ricci et al. (2018b)	120_OOP_4E	Horizontal	2350	1830	120	1.65	2.12	1455	1262
	120_IP+OOP_L	Horizontal	2350	1830	120	1.65	2.12	1455	1262
	120_IP+OOP_M	Horizontal	2350	1830	120	1.65	2.12	1455	1262
	120_IP+OOP_H	Horizontal	2350	1830	120	1.65	2.12	1455	1262
Di Domenico et al. (2018)	OOP_4E	Horizontal	2350	1830	80	1.8	2.21	1517	1188
	OOP_3E	Horizontal	2350	1830	80	1.8	2.21	1517	1188
Akhoundi et al. (2018)	SIF-IO(0.3%)-B	Horizontal	2145	1635	80[c]	1.17	-	1154.8	-
	SIF-IO(0.5%)-B	Horizontal	2145	1635	80[c]	1.17	-	1154.8	-
	SIF-IO(1%)-B	Horizontal	2145	1635	80[c]	1.17	-	1154.8	-
De Risi et al. (2019b)	OOP	Horizontal	1830	1830	80	2.67	4.63	1891	3452
	IP_L-OOP	Horizontal	1830	1830	80	2.67	4.63	1891	3452
	IP_M-OOP	Horizontal	1830	1830	80	2.67	4.63	1891	3452
	IP_H-OOP	Horizontal	1830	1830	80	2.67	4.63	1891	3452
Panto et al. (2019)	Infill Sytem_1	Vertical	2415	1635	100	3	1	1200	250
Koutas & Bournas (2019)	S_CON	NA	1700	1250	65	9.7	9.7	2500	2500

Authors	Specimen		l	h	t	f_{mv}	f_{mh}	E_{mv}	E_{mh}
		Masonry Cavity							
			mm	mm	mm	N/mm^2	N/mm^2	N/mm^2	N/mm^2
	D_CON	NA	1700	1250	140	9.7	9.7	2500	2500

Note: NA = Not Applicable; f_{mh} and E_{mh} indicates infill's properties in horizontal direction; f_{mv} and E_{mv} indicates infill's properties in vertical direction

– indicates not available and assumed equal to other direction

[b]Infill elastic modulus is estimated

[c]Infill thickness effective in OoP load

2.2.3.1 Capacity models for OoP strength calculation in IP-undamaged state

The above-discussed models which can be used to calculate the OoP capacity of URM infill walls in IP-undamaged state were tested with the results from experiments where infill wall was tested only in OoP loads. In detail, 9 different capacity models were checked with 22 different infill specimens from 15 experiments. The OoP capacities calculated from all 9 models for the case of IP-undamaged infill walls are presented in Table 2.5. The ratio of the strength predicted by the analytical capacity models to the experimental strength is given in Table 2.6. The results are discussed below.

The accuracy of Dawe and Seah's (1989) model is higher. The mean of the ratios between predicted and experimental strength is equal to 1.09 with a standard deviation and coefficient of variation (COV) of the strength ratios 0.66 and 0.61 respectively, which are comparatively among the lowest. According to Dawe and Seah, the application of their capacity equations to infills in moment-resisting frames can result in conservative estimates of the OoP load capacity. From the calculations, conservative estimation was found in different cases of reinforced concrete frames while overestimation of strength was found in the cases of steel frames. While checking the model against the experimental results, a difference between moment-resisting frames and frames designed to resist vertical loads was not considered. For 12 out of 22 specimens the model under-predicted the strength. Although the model underestimated the OoP strength in most cases of reinforced concrete frames there is no clear trend that allows understanding in which cases the model is conservative. The overall accuracy of this model can be considered good.

The model by Angel (1994) is comparatively conservative than the model by Dawe and Seah (1989). The mean of the ratios of the predicted to

the experimental strengths for this model was about 0.89. The model under-predicted for 16 specimens, and for the other 6, the capacities were over-predicted. In general, with a standard deviation of ratios between predicted and experimental strengths of about 0.88 and COV of about 0.99, the accuracy of the model is low. Just like the model of Dawe and Seah (1989), the model of Angel (1994) also under-predicted the OoP strength for most cases of the infilled reinforced concrete frames. The model under-predicted the OoP strength in a few cases of steel frames.

Bashandy et al.'s (1995) model also under-predicted the strength for 11 specimens while it over-predicted for the other 11 specimens. The predicted strength was as high as 7 times the experimental strength for the test specimen of Dawe and Seah (1989). The average of the ratios between predicted and experimental strength was 1.85 and the standard deviation was 1.88. This model is the least reliable among all capacity models.

Flanagan and Bennett's (1999a) model under-predicted 13 specimens out of the 22 specimens. Although the quality of prediction of OoP strength by Flanagan and Bennett (1999a) is similar to the model of Dawe and Seah (1989) (i.e. where one model under-predicts the strength the other also under-predicts and where one over-predicts the other over-predicts too), the former appears better than the latter, especially for the cases where Dawe and Seah's model over-predicted. The overall prediction by Flanagan and Bennett (1999a) is very good. The mean of the ratios between predicted and experimental strengths is 1.0 with a lower standard deviation of the strength ratios (0.62).

FEMA 356 (2000) was found to be the most conservative model in predicting the OoP strength in IP-undamaged conditions (the mean of the ratios of predicted and experimental strengths is only 0.53). The model under-

predicted for almost all the investigated specimens except for 3 infill specimens by Dawe and Seah (1989).

Moghaddam and Goudarzi's (2010) model gives the OoP strength of infills based on two criteria: failure due to crushing q_{cr} and failure due to transverse instability $q_{\max}$, and the minimum of the two is the OoP capacity. The capacity model can unexpectedly give crushing strength q_{cr} less than zero (Table 2.5) or close to zero. This occurs in the case of steel frames whose member moment of inertia is very low with respect to the case of reinforced concrete frames. This makes the application of the model questionable. For the studied infill specimens, the OoP strength was generally determined by crushing criteria, resulting in a lower OoP load than that corresponding to the transverse instability. The prediction by this model is relatively good for infills surrounded by reinforced concrete frames with an average of the ratios of the predicted to the experimental strengths equal to 0.9 and a standard deviation of ratios equal to 0.73.

Morandi et al.'s (2013) analytical model under-predicted the OoP strength for 14 specimens and over-predicted for 8 specimens. In some cases, the predicted strength is very high. The model is not so suitable to estimate the OoP capacity of IP-undamaged infill walls.

The empirical model of Ricci et al.'s (2018c) is one of the best when the ratio of the predicted to the experimental strength for each infill specimen is considered individually. For more than half of the infill specimens, the predicted strengths from this model were the closest to the experimental strengths in comparison to all other models. The model yielded an average ratio of predicted and experimental strength of 1.38 with a standard deviation of the ratios 0.70. Although the model has a good accuracy the model tends to

over-estimate the OoP strength (for 15 specimens, it over-predicted), which is not good from the aspect of structural safety of infill walls.

The model by Liberatore et al. (2020) also tends to over-predict the OoP strength. The model under-predicted for only 3 infill specimens. With the mean of the ratios of the predicted to the experimental strength equal to 1.66 and a standard deviation of the ratios equal to 0.95, the model has one of the lowest accuracies in predicting the OoP capacity of IP-undamaged URM infill walls.

From the detailed comparison of the available models, it emerges that the models of Flanagan and Bennett (1999a) and Dawe and Seah (1989) are better to predict the OoP strength of the IP-undamaged infill walls while the models of Ricci et al. (2018c), Moghaddam and Goudarzi (2010) and Angel (1994) are good but less preferable than the former two.

2.2.3.2 Capacity models for OoP strength calculation in IP-damaged state

In this section, OoP capacity reduction models are evaluated and R_1 factors are computed. For this, infill specimens from different experimental campaigns which were previously damaged due to IP load and subsequently loaded in the OoP direction were used. Only those infill specimens were taken for which the reference specimen was available. The infill specimen tested only in OoP load with no previous IP load is regarded as the reference specimen.

Among the 13 capacity models discussed earlier to predict R_1, 12 models were checked. 20 infill specimens from 10 different experiments were taken. Angel's (1994) expression to calculate R_1 was not used. In Angel's model, information about the cracking displacement is necessary which is not available in most of the experimented specimens.

After the evaluation of the capacity reduction factor R_1, reduced OoP capacity was predicted for the investigated specimens. The predicted strength was obtained by multiplying the factor R_1 with the experimental strength of the reference specimen for every model. The OoP strengths of IP-damaged infill specimens predicted by all 12 analytical models are given in Table 2.7. The ratios of the predicted to the experimental OoP strength of IP-damaged infill specimens are given in Table 2.8. The ratios of the strengths also correspond to the ratio of the analytical to the experimental strength reduction factors. The results from the calculation are discussed below.

Morandi et al.'s (2013) models are very conservative for the case of higher IP drifts. For IP drifts greater than 1%, the model gives zero OoP capacity which is not realistic when compared to experimental results. Stepwise formulation (Eq. 2.26) under-predicted the reduced OoP capacity for 16 specimens out of 20 specimens while linear formulation (Eq. 2.27) under-predicted for all infill specimens.

Verlato et al.'s (2014) expression is not as conservative as Morandi et al. (2013). The strength reduction predicted is also relatively better with the mean of the ratios between the predicted and experimental strengths equal to 1.11 and a standard deviation of the ratios equal to 0.62.

The New Zealand code (NZSEE 2017) assumes a constant value of reduction factor R_1 for every *IDR* value greater than drift corresponding to the first visible cracking. Therefore, it is not conservative for infill walls damaged by higher IP drifts. The model by NZSEE (2017) over-predicted the strength for 12 specimens with the mean of the ratios between predicted and experimental strength equal to 1.42 and a standard deviation of the ratios equal to 0.87.

The model by Furtado et al. (2018a) is also comparatively conservative. For 17 out of 20 IP-damaged specimens, the model under-predicted the reduced OoP strength.

The model by Ricci et al. (2018a) is very conservative in some cases of specimens subjected to higher IP drifts. However, their updated models in Ricci et al. (2018b) are not as conservative for thick infill walls or high IP drifts. The error in the prediction of strength reduction by Ricci et al.'s (2018b) first model (Eq. 2.35) is comparatively very low. The mean of the ratios of the predicted strength to the experimental strength is 1.0 and the standard deviation of the ratios is also lower (0.48). The second model (Eq. 2.36) proposed by Ricci et al. (2018b) gives results similar to their first model (Eq. 2.35), however, the former expression has slightly higher accuracy.

The model by Di Domenico et al. (2021) predicted the OoP strength reduction factor much better. In this case, the mean of the ratios of the predicted strength to the experimental strength was 1.05 with a standard deviation of the ratios equal to 0.43 and COV as low as 0.41. This shows that the model is very suitable to be used for the prediction of the OoP capacity reduction factor when the infill wall is damaged in IP previously.

Akhoundi et al.'s (2018) expression to calculate the reduction factor is simple but predicted the higher reduced OoP strength in 13 cases.

Cavaleri et al.'s (2019) equation (Eq. 2.39) produced good results, the result is conservative in general. The lower bound strength equation (Eq. 2.40) by Cavaleri et al. (2019) is very conservative. It under-predicted the reduced OoP strength of all the investigated infill specimens.

Overall, the equation by Di Domenico et al. (2021) was found to be comparatively better in predicting the OoP strength reduction factor among all the models.

In real earthquakes, infill walls are exerted by both IP and OoP forces simultaneously. Therefore, on the conservative side, the residual OoP capacity of the infill wall is to be estimated after defining a suitable IP damage level of the infill walls during the assessment of the seismic vulnerability of such infill walls. For this, it is necessary to know if these two types of models i.e. i) the models for predicting OoP load capacity in IP-undamaged state, and ii) the models for predicting the OoP strength reduction factor can be used in combination to estimate the OoP strength of any type of IP-damaged infill wall.

To verify this approach, IP-damaged specimens from different experiments for which there were no reference specimens (i.e. specimen tested in OoP load with no previous IP damage) were selected. In total, 7 URM infill specimens from 4 different experiments were used. The four better models from the first category (i.e. those proposed by Dawe and Seah 1989, Flanagan and Bennett 1999a, Moghaddam and Goudarzi 2010, Ricci et al. 2018c) were first used and OoP strength considering IP-undamaged conditions were estimated. Then, Di Domenico et al.'s (2021) equation was employed to find the OoP strength reduction factor R_1. Afterwards, OoP strengths predicted by the selected models from the first category were multiplied with the reduction factors estimated by using the model of Di Domenico et al. (2021), to calculate the reduced OoP strength.

The predicted OoP strength and the ratio of the predicted to the experimental strength from the combination of the two types of models are summarised in Table 2.9. In general, the model of Flanagan and Bennett (1999a) in combination with Di Domenico et al.'s (2021) model produced a better result. The average strength ratio of 1.30 and a low standard deviation of the ratios equal to 0.48 were observed. The model by Di Domenico et al. (2021) when used in combination with the model of Dawe and Seah (1989)

also gave satisfactory results. Therefore, for the prediction of the OoP capacity of IP-damaged URM infill walls, it appears better to pair Di Domenico et al.'s (2021) model with the model of Flanagan and Bennett (1999a) or Dawe and Seah (1989).

Table 2.5 OoP strength of IP-undamaged infill specimens: comparison between the experimental and predicted strength

Experimental studies	Specimens	h/t	q_{meas} (KPa)	q_{pred} (kPa)									
				D & S	Angel	B. et al.	F & B	FEMA	M & G		M. et al.	R. et al. (c)	Lib. et al.
									q_{cr}	q_{max}			
Dawe & Seah (1989)	WE2	14.7	19.2	37.6	67.7	136.1	34.3	40.9	-3.4	*22.9*	80.6	20.2	-
	WE4	20.0	11.2	20.4	29.6	49.9	18.6	17.9	-17.3	*9.6*	43.7	12.4	-
	WE5	31.1	7.8	8.4	6.6	3.7	7.7	4.0	-24.4	*2.5*	18.1	6.1	-
	WE8	20.0	13.4	20.4	29.6	49.9	18.6	17.9	-17.3	*9.6*	43.7	12.4	-
Angel (1994)	1	34.2	8.2	6.2	2.3	2.6	5.3	1.3	*4.9*	5.0	7.1	8.6	20.3
Flanagan & Bennett (1999b)	18	11.2	26.6	42.9	38.3	91.4	39.1	18.9	*36.9*	337.7	32.1	25.3	62.8
	25	22.4	8.1	10.7	6.0	14.1	9.8	3.0	*8.6*	25.3	8.0	8.4	26.8
	22	6.8	39.5	49.2	70.2	114.5	62.2	24.6	*42.1*	3052.4	35.8	41.1	52.0
Calvi & Bolognini (2001)	10	20.4	2.9	2.0	1.7	3.2	1.7	0.8	*2.1*	7.3	1.9	4.2	4.6
Furtado et al. (2016)	Infill_01	15.3	7.9	2.5	1.9	3.2	2.3	0.8	*1.9*	28.9	1.6	6.5	2.8
	Infill_02	15.3	7.2	2.5	1.9	3.2	2.3	0.8	*1.9*	28.9	1.6	6.5	2.8
Akhoundi et al. (2016)	SIF-B	20.4	10.1	2.2	0.8	2.2	2.0	0.7	*1.9*	7.2	1.7	8.2	4.3
Spesdar (2017)	IF-ND	10.9	66.3	53.8	37.7	114.6	48.3	33.5	*63.9*	326.8	57.1	98.6	75.2
Wang (2017)	IF-S	10.9	34.3	63.2	40.4	109.7	57.6	32.1	*62.4*	488.1	54.7	97.1	72.3
Furtado et al. (2020)	M4	15.3	4.8	4.3	3.8	5.1	3.9	1.7	*3.8*	20.9	3.4	8.4	5.4
Ricci et al. (2018a)	80_OOP_4E	22.9	5.1	3.3	1.6	1.6	3.0	0.9	*2.5*	5.2	2.5	7.2	7.3
Ricci et al. (2018b)	120_OOP_4E	15.3	9.7	7.1	4.6	9.1	6.5	2.5	*5.7*	32.2	5.1	13.3	11.1
Di Domenico et al. (2018)	OOP_4E	22.9	5.1	3.3	1.0	2.5	2.5	0.9	*2.6*	6.6	2.5	7.2	7.3
De Risi et al. (2019b)	120_OOP_4E	22.9	8.8	6.4	2.4	4.7	5.8	1.3	*3.8*	9.6	3.7	8.3	13.4
Panto et al. (2019)	Infill Sytem_1	16.4	13.3	6.5	2.3	6.9	5.9	2.1	*8.2*	17.4	8.1	17.2	15.2

Experimental studies	Specimens	h/t	q_{meas} (KPa)	q_{pred} (kPa)									
				D & S	Angel	B. et al.	F & B	FEMA	M & G		M. et al.	R. et al. (c)	Lib. et al.
									q_{cr}	q_{max}			
Koutas & Bournas (2019)	S_CON	19.2	13.4	17.3	6.8	3.9	15.7	5.8	*17.2*	24.2	18.9	28.9	38.9
	D_CON	8.9	26.4	80.4	14.7	139.0	72.7	12.5	*97.6*	457.4	87.6	97.9	100.0

Note: q_{meas} = capacity measured during experiment; q_{pred} = capacity predicted

For Moghaddam and Goudarzi (2010), the governing OOP strength is italicized and underlined.

D & S = Dawe and Seah (1989); Angel = Angel (1994); B. et al. = Bashandy et al. (1995); F & B = Flanagan and Bennett (1999a); FEMA = FEMA 356 (2000); M & G = Moghaddam and Goudarzi (2010); M. et al. = Morandi et al. (2013); R. et al. (c) = Ricci et al. (2018c), Lib et al. = Liberatore et al. (2020)

Table 2.6 Ratio of OoP strength predicted by the capacity models to the experimental strength for IP-undamaged infill specimens

Experimental studies	Specimens	h/t	$q_{pred.}/q_{meas}$								
			D & S	Angel	B. et al.	F & B	FEMA	M & G	M. et al.	R. et al. (c)	Lib. et al.
Dawe & Seah (1989)	WE2	14.7	**1.96**	**3.53**	**7.09**	**1.78**	**2.13**	**1.19**	**4.20**	**1.05**	**-**
	WE4	20.0	**1.82**	**2.64**	**4.46**	**1.66**	**1.59**	*0.86*	**3.91**	**1.11**	**-**
	WE5	31.1	**1.08**	*0.85*	*0.47*	*0.99*	*0.51*	*0.32*	**2.32**	*0.79*	-
	WE8	20.0	**1.52**	**2.21**	**3.73**	**1.39**	**1.33**	*0.72*	**3.26**	*0.93*	-
Angel (1994)	1	34.2	*0.75*	*0.28*	*0.32*	*0.64*	*0.16*	*0.59*	*0.87*	**1.05**	**2.48**
Flanagan & Bennett (1999b)	18	11.2	**1.61**	**1.44**	**3.44**	**1.47**	*0.71*	**1.39**	**1.21**	*0.95*	**2.36**
	25	22.4	**1.32**	*0.75*	**1.75**	**1.21**	*0.37*	**1.06**	*0.99*	**1.04**	**3.30**
	22	6.8	**1.24**	**1.78**	**2.90**	**1.58**	*0.62*	**1.07**	*0.91*	**1.04**	**1.32**
Calvi & Bolognini (2001)	10	20.4	*0.68*	*0.59*	**1.08**	*0.58*	*0.26*	*0.71*	*0.65*	**1.43**	**1.56**
Furtado et al. (2016)	Infill_01	15.3	*0.32*	*0.24*	*0.41*	*0.29*	*0.10*	*0.24*	*0.21*	*0.83*	*0.36*
	Infill_02	15.3	*0.35*	*0.26*	*0.44*	*0.31*	*0.11*	*0.26*	*0.23*	*0.90*	*0.39*
Akhoundi et al. (2016)	SIF-B	20.4	*0.21*	*0.08*	*0.22*	*0.19*	*0.07*	*0.19*	*0.17*	*0.81*	*0.43*
Spesdar (2017)	IF-ND	10.9	*0.81*	*0.57*	**1.73**	*0.73*	*0.50*	*0.96*	*0.86*	**1.49**	**1.13**
Wang (2017)	IF-S	10.9	**1.84**	**1.18**	**3.20**	**1.68**	*0.93*	**1.82**	**1.59**	**2.83**	**2.11**
Furtado et al. (2020)	M4	15.3	*0.91*	*0.81*	**1.08**	*0.82*	*0.35*	*0.80*	*0.71*	**1.76**	**1.13**
Ricci et al. (2018a)	80_OOP_4E	22.9	*0.64*	*0.31*	*0.30*	*0.58*	*0.18*	*0.49*	*0.49*	**1.41**	**1.44**
Ricci et al. (2018b)	120_OOP_4E	15.25	*0.73*	*0.47*	*0.93*	*0.66*	*0.26*	*0.59*	*0.52*	**1.37**	**1.14**
Di Domenico et al. (2018)	OOP_4E	22.9	*0.64*	*0.20*	*0.49*	*0.48*	*0.18*	*0.51*	*0.48*	**1.41**	**1.43**
De Risi et al. (2019b)	120_OOP_4E	22.9	*0.72*	*0.27*	*0.54*	*0.65*	*0.15*	*0.44*	*0.42*	*0.94*	**1.52**
Panto et al. (2019)	Infill Sytem_1	16.4	*0.49*	*0.17*	*0.52*	*0.44*	*0.16*	*0.62*	*0.61*	**1.29**	**1.14**

Experimental studies	Specimens	h/t	$q_{pred.}/q_{meas}$								
			D & S	Angel	B. et al.	F & B	FEMA	M & G	M. et al.	R. et al. (c)	Lib. et al.
Koutas & Bournas (2019)	S_CON	19.2	**1.29**	*0.51*	*0.29*	**1.17**	*0.43*	**1.29**	**1.41**	**2.16**	**2.91**
	D_CON	8.9	**3.05**	*0.56*	**5.27**	**2.75**	*0.47*	**3.70**	**3.32**	**3.71**	**3.79**
Mean			1.09	0.89	1.85	1.00	0.53	0.90	1.33	1.38	1.66
Standard deviation			0.66	0.88	1.88	0.62	0.52	0.73	1.21	0.70	0.95
COV [%]			60.5	98.8	101.9	61.5	99.1	81.2	91.1	50.4	57.3

Note: q_{meas} = capacity measured during experiment; q_{pred} = capacity predicted

In the cases where the predicted strength is lower than actual strength, the ratio is underlined and italicized and where higher they are bolded.

D & S = Dawe and Seah (1989); Angel = Angel (1994), B. et al. = Bashandy et al. (1995); F & B = Flanagan and Bennett (1999a); FEMA = FEMA 356 (2000); M & G = Moghaddam and Goudarzi (2010); M. et al. = Morandi et al. (2013); R. et al. (c) = Ricci et al. (2018c), Lib et al. = Liberatore et al. (2020)

Table 2.7 OoP strength of IP-damaged infill specimens: comparison between experimental and predicted strength (the predicted strength is obtained by multiplying the experimental strength of the undamaged reference specimen by the reduction factor from different authors)

Experimental Study	Specimen	IP drift %	q_{meas} (KPa)	q_{pred} (kPa)											
				Mo.-S Eq. 26	Mo.-L Eq. 27	Ver.	NZ.	Fur.	Ri. (a)	Ri. (b) Eq. 35	Ri. (b) Eq. 36	Di Dom.	Ak.	Cav. Eq. 39	Cav. Eq. 40
Angel (1994)	2	0.34	4.0	1.64	1.64	5.79	3.41	3.72	3.83	2.37	3.82	3.69	6.79	3.17	2.08
	3	0.22	6.0	8.18	3.37	6.63	3.41	5.61	6.24	3.19	5.83	5.06	7.28	3.72	2.58
Flanagan & Bennett (1999b)	19	0.78	21.7	5.32	5.32	10.64	23.30	5.51	4.92	19.75	18.01	24.24	16.23	7.58	4.51
Calvi & Bolognini (2001)	6	0.40	0.8	0.58	0.58	1.91	2.02	1.14	1.14	1.52	1.17	1.15	2.33	1.06	0.69
	2	1.20	0.5	0.00	0.00	1.17	2.02	0.40	0.33	0.71	0.40	0.51	1.17	0.71	0.40
Furtado et al. (2016)	Inf_03	0.50	1.9	1.43	1.43	4.07	5.67	2.25	2.17	4.70	5.13	4.70	5.36	2.40	1.50
Spesdar (2017)	IF-D1	0.66	44.4	13.26	13.26	28.44	58.49	16.01	14.70	57.21	53.76	62.97	44.31	20.07	12.16
Wang (2017)	IF_RC_ID	1.38	37.6	0.00	0.00	0.00	58.49	8.01	6.47	34.51	26.41	36.89	20.55	15.30	8.49
Ricci et al. (2018a)	OOP_L_80	0.16	5.4	5.12	2.93	4.41	3.29	4.74	5.12	4.29	4.96	4.80	4.71	2.62	1.88
	OOP_M_80	0.37	2.4	1.02	1.02	3.49	3.29	2.15	2.18	2.41	2.20	2.60	4.17	1.92	1.25
	OOP_H_80	0.58	1.4	1.02	1.02	2.56	3.29	1.40	1.32	1.76	1.42	1.87	3.63	1.63	1.00
Ricci et al. (2018b)	OOP_L_120	0.21	9.7	9.74	4.28	7.98	7.75	6.99	7.83	9.74	9.74	9.74	8.72	4.51	3.14
	OOP_M_120	0.50	6.5	1.95	1.95	5.55	7.75	3.07	2.96	6.46	7.06	8.14	7.31	3.27	2.05
	OOP_H_120	0.89	5.4	1.95	1.95	3.90	7.75	1.78	1.55	4.34	4.04	5.34	5.41	2.64	1.55
Akhoundi et al. (2018)	SIF-IO(0.3%)-B	0.3	8.6	10.11	2.01	7.50	6.99	5.17	5.45	6.41	5.33	5.10	8.59	4.10	2.74

Experimental Study	Specimen	IP drift %	q_{meas} (KPa)	q_{pred} (kPa)											
				Mo.-S Eq. 26	Mo.-L Eq. 27	Ver.	NZ.	Fur.	Ri. (a)	Ri. (b) Eq. 35	Ri. (b) Eq. 36	Di Dom.	Ak.	Cav. Eq. 39	Cav. Eq. 40
	SIF-IO(0.5%)-B	0.5	6.7	2.02	2.02	5.76	6.99	3.19	3.08	4.50	3.25	3.51	7.58	3.40	2.13
	SIF-IO(1%)-B	1.0	5.1	2.02	2.02	4.04	6.99	1.66	1.42	2.79	1.66	2.12	5.06	2.63	1.52
De Risi et al. (2019b)	OOP_L_80	0.15	9.4	8.80	5.27	7.66	5.65	8.67	8.80	7.71	8.80	8.80	8.14	4.61	3.34
	OOP_M_80	0.28	6.7	8.80	2.22	6.68	5.65	4.80	5.12	5.02	4.96	6.68	7.57	3.66	2.46
	OOP_H_80	0.51	5.7	1.76	1.76	4.93	5.65	2.72	2.62	3.32	2.77	4.31	6.55	2.93	1.84

Note: q_{meas} = capacity measured during experiment; q_{pred} = capacity predicted

Mo.-S = Morandi et al. (2013) - Stepwise formulation; Mo.-L = Morandi et al. (2013) - Linear formulation; Ver. = Verlato et al. (2014); NZ. = NZSEE (2017); Fur. = Furtado et al. (2018a); Ri. (a) = Ricci et al. (2018a); Ri. (b) = Ricci et al. (2018b); Ak. = Akhoundi et al. (2018); Cav. = Cavaleri et al. (2019); Di Dom. = Di Domenico et al. (2021)

Table 2.8 Ratio of OoP strength predicted as in Table 2.7 to the experimental OoP strength for IP-damaged infill specimens (each ratio is equal to the ratio of the predicted reduction factor to the experimental reduction factor)

			$q_{pred} / q_{meas} = R_{pred} / R_{meas}$											
Experimental Study	Specimen	IP drift %	Mo.-S Eq. 26	Mo.-L Eq. 27	Ver.	NZ.	Fur.	Ri. (a)	Ri. (b) Eq. 35	Ri. (b) Eq. 36	Di Dom.	Ak.	Cav. Eq. 39	Cav. Eq. 40
Angel (1994)	2	0.34	*0.41*	*0.41*	**1.44**	*0.85*	*0.92*	*0.95*	*0.59*	*0.95*	*0.92*	**1.69**	*0.79*	*0.52*
	3	0.22	**1.37**	*0.56*	**1.11**	*0.57*	*0.94*	**1.04**	*0.53*	*0.97*	*0.85*	**1.22**	*0.62*	*0.43*
Flanagan & Bennett (1999b)	19	0.78	*0.25*	*0.25*	0.*49*	**1.07**	*0.25*	*0.23*	*0.91*	*0.83*	**1.12**	*0.75*	*0.35*	*0.21*
Calvi & Bolognini (2001)	6	0.40	*0.75*	*0.75*	**2.45**	**2.59**	**1.46**	**1.46**	**1.95**	**1.50**	**1.47**	**3.00**	**1.37**	*0.88*
	2	1.20	*0.00*	*0.00*	**2.25**	**3.89**	*0.77*	*0.64*	**1.37**	*0.78*	*0.99*	**2.25**	**1.37**	*0.77*
Furtado et al. (2016)	Inf_03	0.50	*0.77*	*0.77*	**2.18**	**3.04**	**1.21**	**1.17**	**2.52**	**2.75**	**2.52**	**2.88**	**1.29**	*0.81*
Spesdar (2017)	IF-D1	0.66	*0.30*	*0.30*	*0.64*	**1.32**	*0.36*	*0.33*	**1.29**	**1.21**	**1.42**	**1.00**	*0.45*	*0.27*
Wang (2017)	IF_RC_ID	1.38	*0.00*	*0.00*	*0.00*	**1.56**	*0.21*	*0.17*	*0.92*	*0.70*	*0.98*	*0.55*	*0.41*	*0.23*
Ricci et al. (2018a)	OOP_L_80	0.16	*0.94*	*0.54*	*0.81*	*0.60*	*0.87*	*0.94*	*0.79*	*0.91*	*0.88*	*0.86*	*0.48*	*0.35*
	OOP_M_80	0.37	*0.42*	*0.42*	**1.43**	**1.35**	*0.88*	*0.89*	*0.99*	*0.90*	**1.07**	**1.71**	*0.79*	*0.51*
	OOP_H_80	0.58	*0.75*	*0.75*	**1.87**	**2.40**	**1.02**	*0.96*	**1.29**	**1.04**	**1.37**	**2.65**	**1.19**	*0.73*
Ricci et al. (2018b)	OOP_L_120	0.21	**1.01**	*0.44*	*0.83*	*0.80*	*0.72*	*0.81*	**1.01**	**1.01**	**1.01**	*0.90*	*0.47*	*0.32*
	OOP_M_120	0.50	*0.30*	*0.30*	*0.86*	**1.19**	*0.47*	*0.46*	**1.00**	**1.09**	**1.25**	**1.13**	*0.50*	*0.32*
	OOP_H_120	0.89	*0.36*	*0.36*	*0.72*	**1.44**	*0.33*	*0.29*	*0.80*	*0.75*	*0.99*	**1.00**	*0.49*	*0.29*
Akhoundi et al. (2018)	SIF-IO(0.3%)-B	0.3	**1.17**	*0.23*	*0.87*	*0.81*	*0.60*	*0.63*	*0.74*	*0.62*	*0.59*	**1.00**	*0.48*	*0.32*
	SIF-IO(0.5%)-B	0.5	*0.30*	*0.30*	*0.86*	**1.05**	*0.48*	*0.46*	*0.67*	*0.49*	*0.53*	**1.13**	*0.51*	*0.32*
	SIF-IO(1%)-B	1.0	*0.39*	*0.39*	*0.79*	**1.36**	*0.32*	*0.28*	*0.54*	*0.32*	*0.41*	*0.98*	*0.51*	*0.29*
De Risi et al. (2019b)	OOP_L_80	0.15	*0.94*	*0.56*	*0.82*	*0.60*	*0.92*	*0.94*	*0.82*	*0.94*	*0.94*	*0.87*	*0.49*	*0.36*
	OOP_M_80	0.28	**1.31**	*0.33*	*0.99*	*0.84*	*0.72*	*0.76*	*0.75*	*0.74*	1.00	**1.13**	*0.55*	*0.37*

Experimental Study	Specimen	IP drift %	q_{pred} / q_{meas} = R_{pred} / R_{meas}											
			Mo.-S Eq. 26	Mo.-L Eq. 27	Ver.	NZ.	Fur.	Ri. (a)	Ri. (b) Eq. 35	Ri. (b) Eq. 36	Di Dom.	Ak.	Cav. Eq. 39	Cav. Eq. 40
	OOP_H_80	0.51	*0.31*	*0.31*	*0.86*	*0.99*	*0.47*	*0.46*	*0.58*	*0.48*	*0.75*	**1.14**	*0.51*	*0.32*
Mean			0.60	0.40	1.11	1.42	0.70	0.69	1.00	0.95	1.05	1.39	0.68	0.43
Standard deviation			0.40	0.21	0.62	0.87	0.33	0.35	0.48	0.49	0.43	0.71	0.33	0.20
COV [%]			67.12	52.27	55.54	61.32	47.10	49.83	48.20	51.56	41.00	51.14	48.35	46.42

Note: q_{meas} = capacity measured during experiment; q_{pred} = capacity predicted as in Table 7; R_{pred} = predicted reduction factor; R_{exp} = experimental reduction factor
In the cases where the predicted strength is lower than actual strength, the ratio is underlined and italicized and where higher they are bolded.
Mo.-S = Morandi et al. (2013) - Stepwise formulation; Mo.-L = Morandi et al. (2013) - Linear formulation; Ver. = Verlato et al. (2014); NZ. = NZSEE (2017); Fur. = Furtado et al. (2018a); Ri. (a) = Ricci et al. (2018a); Ri. (b) = Ricci et al. (2018b); Ak. = Akhoundi et al. (2018); Cav. = Cavaleri et al. (2019); Di Dom. = Di Domenico et al. (2021)

Table 2.9 OoP Capacity prediction for IP-damaged infill specimens by pairing two types of models

Experiments	Specimens	IDR [%]	Predicted pure OoP Strength (kPa)			
			D & S	F & B	M & G	R et al. (c)
Angel (1994)	6	0.25	13.22	12.00	12.73	19.75
Pereira et al. (2011)	Wall_REF_01	0.8	4.13	3.67	6.09	21.53
	Wall_REF_02	0.8	5.57	4.94	8.52	26.84
Da Porto (2013)	I	1.2	36.15	31.06	56.14	30.07
Hak et al. (2014)	TA1	1.5	37.54	33.64	52.43	25.57
	TA2	2.5	37.54	33.64	52.43	25.57
	TA3	1	37.54	33.64	52.43	25.57
Specimens	Reduction factor, R		Predicted reduced OoP Strength (q_{pred}) in kPa			
	Di Domenico et al. (2021)		D & S	F& B	M & G	R et al. (c)
6	1.00		13.22	12.00	12.73	19.75
Wall_REF_01	0.65		2.68	2.39	3.95	13.99
Wall_REF_02	0.73		4.05	3.60	6.21	19.55
I	0.67		24.39	20.96	37.88	20.29
TA1	0.61		22.80	20.44	31.85	15.53
TA2	0.42		15.71	14.08	21.94	10.70
TA3	0.82		30.66	27.48	42.82	20.88
Specimens	q_{meas} (kPa)		q_{pred} /q_{meas}			
			D & S	F & B	M & G	R et al. (c)
6	12.40		**1.07**	*0.97*	**1.03**	**1.59**
Wall_REF_01	2.07		**1.30**	**1.15**	**1.91**	**6.76**
Wall_REF_02	6.89		*0.59*	*0.52*	**0**.*90*	**2.84**
I	18.46		**1.32**	**1.14**	**2.05**	**1.10**
TA1	13.54		**1.68**	**1.51**	**2.35**	**1.15**
TA2	8.25		**1.90**	**1.71**	**2.66**	**1.30**
TA3	13.17		**2.33**	**2.09**	**3.25**	**1.59**
Mean			1.46	1.30	2.02	2.33
Standard deviation			0.53	0.48	0.78	1.89
COV [%]			36.39	36.76	38.72	80.98

Note: q_{meas} = capacity measured during experiment; q_{pred} = capacity predicted
In the cases where the predicted strength is lower than actual strength, the ratio is underlined and italicized and where higher bolded.
D & S = Dawe and Seah (1989); F & B = Flanagan and Bennett (1999a); M & G = Moghaddam and Goudarzi (2010); R. et al. (c) = Ricci et al. (2018c)

2.2.3.3 Models for predicting OoP capacity in case of gaps and openings

Dawe and Seah (1989) is the only model that explicitly addresses the condition of gaps between the upper beam and the infill wall. As mentioned

in section 2.1.3.4, models by Bashandy et al. (1995) and Flanagan and Bennett (1999a) can also be used by using the equations partially. Therefore, the accuracy of these equations was evaluated by comparing them with some available experimental results. In this case, since the gap is considered at the top of the infill wall, vertical arching is not considered and only horizontal arching is supposed to be effective because of which the masonry properties in the horizontal directions (e.g. compressive strength, elastic modulus) were used to calculate OoP capacity. Table 2.10 shows the predicted strength and ratio of predicted strength to the experimental strength for the models of Dawe and Seah (1989), Bashandy et al. (1995) and Flanagan and Bennett (1999a). As the number of experimental data is too less, it is difficult to decide on the reliability of such models. The gaps between the infill wall and the frames need further investigation.

Openings like doors and windows are necessary for the infill walls and they are commonly built. To understand which models can be used for the case of opening, first, the OoP capacities of the chosen infill specimens were computed by assuming a solid infill wall. For this, models showing better results in the previous calculations were taken i.e. Dawe and Seah (1989) and Flanagan and Bennett (1999a). These models were checked with 4 infill specimens from a few experiments (Table 2.11). The OoP strengths predicted by both models were higher in all cases except for a specimen by Akhoundi et al. (2016). Therefore, it was felt that a reduction factor needs to be coupled to have a reliable prediction.

Table 2.10 Prediction of the OoP strength for gapped infill

Experiment	Specimen	q_{meas} (kPa)	q_{pred} (KPa)		
			Dawe and Seah (1989)	Bashandy et al. (1995)	Flanagan & Bennett (1999a)
Dawe & Seah (1989)	WE6	10.6	12.7	36.88	11.6
Akhoundi et al. (2016)	SIF-A	8.8	0.5	0.23	0.5
Wang (2017)	IF-RC-TG	18.5	18.9	23.26	16.9
Di Domenico et al. (2018)	OOP_3E	4.1	1.4	0.05	1.3

Experiment	Specimen	q_{pred}/q_{meas}		
		Dawe & Seah (1989)	Bashandy et al. (1995)	Flanagan & Bennett (1999a)
Dawe & Seah (1989)	WE6	1.20	3.48	1.09
Akhoundi et al. (2016)	SIF-A	0.06	0.03	0.05
Wang (2017)	IF-RC-TG	1.02	1.26	0.91
Di Domenico et al. (2018)	OOP_3E	0.35	0.01	0.32
Mean		0.66	1.19	0.59
Standard deviation		0.47	1.41	0.42
COV [%]		71.18	118.37	71.29

Table 2.11 Prediction of the OoP strength for infill with opening

Experiment	Specimen	Opening type	Opening %	q_{meas} kPa	Initial q_{pred} (kPa)		R_o	
					D & S	F & B	ASCE	Lib. et al.
Dawe & Seah (1989)	WE 9	window	19.0	17.4	34.65	31.6	0.81	0.75
Akhoundi et al. (2016)	PIF-B	window	12.8	9.88	2.16	1.96	0.87	1.00
Spesdar (2017)	IF-W-ND	window	17.0	43.7	53.72	48.3	0.83	0.84
Wang (2017)	IF-RC-D0	door	17.6	36.2	47.16	42.4	0.82	0.86

Specimen	ASCE q_{pred} (kPa)		Lib et al q_{pred} (kPa)		ASCE q_{pred}/q_{meas}		Lib et al. q_{pred}/q_{meas}	
	D & S	F & B	D & S	F & B	D & S	F & B	D & S	F & B
WE 9	28.05	25.57	26.07	23.76	1.61	1.47	1.50	1.37
PIF-B	1.88	1.71	2.16	1.96	0.19	0.17	0.22	0.20
IF-W-ND	44.59	40.12	45.03	40.51	1.02	0.92	1.03	0.93
IF-RC-D0	38.86	34.96	40.34	36.29	1.07	0.97	1.11	1.00
Mean					0.97	0.88	0.97	0.87
Standard deviation					0.51	0.46	0.47	0.42
COV [%]					52.19	52.51	48.27	48.53

Note: q_{meas} = capacity measured during experiment; q_{pred} = capacity predicted
D & S = Dawe and Seah (1989); F & B = Flanagan and Bennett (1999a)
ASCE =ASCE 41 (2017); Lib. et al. = Liberatore et al. (2020)

Therefore, reduction factors for the opening were calculated as per ASCE/SEI 41-17 and Liberatore et al. (2020). After adding the effects of openings, predicted capacities were much closer to experimental strengths (Table 2.11). Although the number of infill specimens is too low to make a solid decision, it appears that the models by Dawe and Seah (1989) and Flanagan and Bennett (1999a) can be paired with the equation of ASCE/SEI 41-17 or Liberatore et al. (2020) to determine the OoP capacity of URM infill walls with openings.

2.2.3.4 Models for Predicting the OoP displacement of the infill wall at peak load

The models by FEMA 273 (1997) and Flanagan and Bennett (1999a) were used to predict the OoP displacement of the infill walls at the peak OoP load. Infill specimens from the experimental tests where displacement information is available were chosen.

The use of both models resulted in an over-prediction of the displacement at the peak load (Table 2.12). The overall prediction of FEMA 273 is better between the two models. However, it appears that these models need to be improved for obtaining acceptable results.

Table 2.12 Displacement prediction by the capacity models for IP-undamaged infill specimens

Experiment	Specimen	h/t	d_{meas} (mm)	d_{pred} (mm)		d_{pred} /d_{meas}	
				F & B	FEMA	F & B	FEMA
Angel (1994)	1	*34.2*	22.7	-	-	-	-
Flanagan & Bennett (1999b)	18	11.2	11.5	25.9	26.9	2.25	2.34
	25	*22.4*	25.3	58.8	-	2.33	-
	22	6.8	49.5	18.2	15.5	0.37	0.31
Calvi & Bolognini (2001)	10	20.4	13.0	63.4	79.3	4.88	6.10
Furtado et al. (2016)	Infill_01	15.3	21.1	37.6	40.8	1.78	1.93
	Infill_02	15.3	16.6	37.6	40.8	2.27	2.46
Akhoundi et al. (2016)	SIF-B	20.4	24.2	37.9	47.5	1.58	1.96
Spesdar (2017)	IF-ND	10.9	12.5	11.0	11.3	0.88	0.91
Wang (2017)	IF-S	10.9	15.1	11.0	11.3	0.73	0.75
Furtado et al. (2020)	M4	15.3	7.2	37.6	40.8	5.23	5.67
Ricci et al. (2018a)	80_OOP_4E	*22.9*	5.4	49.5	-	9.17	-
Ricci et al. (2018b)	120_OOP_4E	15.3	8.0	29.7	32.2	3.72	4.03
Domenico et al. (2018)	OOP_4E	*22.9*	5.4	49.5	-	9.17	-
De Risi et al. (2019b)	120_OOP_4E	*22.9*	5.9	49.5	-	8.28	-
Panto et al. (2019)	Infill Sytem_1	16.4	20.0	28.8	31.7	1.44	1.59
Koutas & Bournas (2019)	S_CON	19.2	22.5	26.8	31.8	1.19	1.41
	D_CON	8.9	10.5	11.3	11.6	1.08	1.11
Mean						3.31	2.35
Standard deviation						2.89	1.75
COV [%]						87.34	74.55

Note: d_{meas} = displacement measured during experiment; d_{pred} = displacement predicted
- sign in each columns represents the cases in which the models become invalid.
h/t values in which the model becomes invalid are italicized and underlined.
F & B = Flanagan and Bennett (1999a); FEMA = FEMA 273 (1997)

2.2.4 Effect of orthotropy of masonry in the OoP capacity infill walls

Masonry is an orthotropic material. The properties of masonry infill are different in horizontal and vertical (gravity) directions. However, in many of the available models, it is not possible to take two properties and normally the masonry properties in vertical directions are used. This makes difference in the evaluation of the OoP capacity. To understand the effect of considering

the properties of masonry in both directions, OoP capacities were re-evaluated and compared with previous results.

For this, capacity models by Dawe and Seah (1989), Bashandy et al. (1995) and Flanagan and Bennett (1999a) were used because, in these models, the total capacity is derived by summing capacities due to horizontal and vertical arching while the same is not explicitly done in other models. The mechanical characteristics of infill walls in both horizontal and vertical directions were used (i.e. considering the orthotropy of masonry). In the cases where masonry properties are not available in one direction, they are assumed equal to the values in the other direction.

The results from the calculation are given in Table 2.13. It can be observed that the prediction error is reduced in general when both the vertical and horizontal characteristics are used. Especially for models of Dawe and Seah (1989) and Flanagan and Bennett (1999a), the difference between predicted and experimental strength was reduced. No difference was encountered between the results under the hypotheses for specimens whose vertical and horizontal infill properties were assumed equal. The mean and standard deviation of the ratios between the predicted and the experimental strengths from both Dawe and Seah (1989) and Flanagan and Bennett (1999a) models are similar. However, Flanagan and Bennett's (1999a) model provides the OoP capacity lower than that provided by Dawe and Seah's (1989) model, i.e. the former model is slightly conservative.

Table 2.13 Prediction of the OoP strength for IP-undamaged infill specimens by considering the horizontal and vertical properties of masonry

Experiment	Specimen	q_{meas} (KPa)	Revised q_{pred} (KPa)			Revised q_{pred} /q_{meas}			Previous q_{pred} /q_{meas}		
			D & S	B et al.	F & B	D & S	B et al.	F & B	D & S	B et al.	F & B
Dawe & Seah (1989)	WE2	19.2	34.7	141.0	31.6	*1.80*	**7.34**	*1.64*	1.96	7.09	1.78
	WE4	11.2	18.8	53.8	17.1	*1.68*	**4.80**	*1.53*	1.82	4.46	1.66
	WE5	7.8	7.8	3.8	7.1	*1.00*	*0.49*	**0.91**	1.08	0.47	0.99
	WE8	13.4	18.8	53.8	17.1	*1.40*	**4.01**	*1.28*	1.52	3.73	1.39
Angel (1994)	1	8.18	6.2	2.6	5.3	0.75	0.32	0.64	0.75	0.32	0.64
Flanagan & Bennett (1999)	18	26.6	35.4	64.9	32.3	*1.33*	*2.44*	*1.21*	1.61	3.44	1.47
	25	8.1	8.9	9.6	8.1	*1.09*	*1.19*	*1.00*	1.32	1.75	1.21
	22	39.5	51.6	88.3	47.0	**1.31**	*2.24*	*1.19*	1.24	2.90	1.58
Calvi & Bolognini (2001)	10	2.9	2.0	2.9	1.7	0.68	*0.98*	0.58	0.68	1.08	0.58
Furtado et al. (2016)	Infill_01	7.9	2.5	3.2	2.3	0.32	0.41	0.29	0.32	0.41	0.29
	Infill_02	7.2	2.5	3.2	2.3	0.35	0.44	0.31	0.35	0.44	0.31
Akhoundi et al. (2016)	SIF-B	10.1	2.2	2.2	2.0	0.21	0.22	0.19	0.21	0.22	0.19
Spesdar (2017)	IF-ND	66.3	53.8	114.6	48.3	0.81	1.73	0.73	0.81	1.73	0.73
Wang (2017)	IF-S	34.3	63.2	109.7	57.6	1.84	3.20	1.68	1.84	3.20	1.68
Furtado et al. (2020)	M4	4.8	4.3	5.1	3.9	0.91	1.08	0.82	0.91	1.08	0.82
Ricci et al. (2018a)	80_OOP_4E	5.1	3.6	1.5	3.3	*0.70*	0.29	*0.64*	0.64	0.30	0.58
Ricci et al. (2018b)	120_OOP_4E	9.7	7.7	8.3	7.0	*0.79*	**0.85**	*0.71*	0.73	0.93	0.66
Di Domenico et al. (2018)	OOP_4E	5.1	3.5	2.2	2.6	*0.68*	**0.42**	*0.51*	0.64	0.49	0.48
De Risi et al. (2019b)	120_OOP_4E	8.8	8.0	7.0	7.2	*0.91*	*0.79*	*0.82*	0.72	0.54	0.65
Panto et al. (2019)	Infill Sytem_1	13.3	5.6	6.6	5.1	**0.42**	**0.50**	**0.39**	0.49	0.52	0.44
Koutas & Bournas (2019)	S_CON	13.4	17.3	3.9	15.7	1.29	0.29	1.17	1.29	0.29	1.17
	D_CON	26.4	80.4	139.0	72.7	3.05	5.27	2.75	3.05	5.27	2.75
Mean						1.06	1.79	0.95	1.09	1.85	1.00
Standard deviation						0.63	1.92	0.58	0.66	1.88	0.62
COV [%]						59.24	107.44	60.26	60.56	101.94	61.50

Note: q_{meas} = capacity measured during experiment; q_{pred} = capacity predicted
Italicized and underlined values indicates that error is reduced while the bolded values indicate that there is increase in error
D & S = Dawe and Seah (1989); B et al. = Bashandy et al. (1995); F & B = Flanagan and Bennett (1999a)

2.3 Numerical modelling of OoP responses of masonry infill walls

The presence of the infill wall modifies the behaviour of the infilled frame. The interaction between the infill wall and the frame is complex. Due to the variability in the behaviour of the infilled frame systems, it is challenging to develop numerical models which is computationally simple and which can capture all aspects of the interaction between the infill wall and the frames. Several authors have proposed modelling strategies for infill walls and they can be generally divided into two groups: micro-modelling approach and macro-modelling approach.

Micromodels are based on finite element representations of the frames and the infill wall. In micro-modelling, the response of the frame, masonry infill, joints and interfaces are described using proper constitutive relations. Micromodels can represent complex issues like a local frame–infill interaction, sliding of the units along mortar joints as well as crack propagation in the infill wall and reinforced concrete elements. However, such models are computationally expensive. Good results depend on proper calibration of the model, and inappropriate use can lead to a very incorrect conclusion (Shing and Mehrabi 2002; Asteris et al. 2011; Penava et al. 2016)

The macro-models are based on replacing masonry infills by means of one (or more) equivalent pin-jointed struts for each infill wall and are regarded as macro-element modelling techniques. This is the most frequently employed technique to perform nonlinear static or dynamic analysis because of its simplicity and lower computational effort. Some design codes suggest macro-models for seismic assessment of infilled framed structures (e.g. Eurocode 8).

The concept to consider the effect of masonry infill was first given by Polyakov (1960). Later Holmes (1961) proposed to replace the infill panel with an equivalent diagonal strut having a cross-section width equal to one-third of the diagonal length of the infill wall.

This concept was further developed by many other researchers (Polyakov 1960; Holmes 1961; Smith 1962; Smith and Carter 1969; Liauw 1972; Mainstone 1974; Paulay and Priestley 1992; Durrani and Luo 1994; Hendry 1998; Al-Chaar 2002). It was later identified that the use of a single diagonal strut cannot accurately address different aspects of the interaction between the frame and the infill wall (e.g. increase in shear force in the columns). Therefore, multiple diagonal struts were proposed instead of a single strut to simulate the behaviour of masonry infills (Thiruvengadam 1985; Chrysostomou 1991; Crisafulli 1997; Chrysostomou et al. 2002; El-Dakhakhni 2002; El-Dakhakhni et al. 2003; Crisafulli and Carr 2007).

Some works were done to define the stiffening effects through the use of an equivalent diagonal strut (Papia et al. 2003; Asteris et al 2015). Few others defined the inelastic behaviour of the equivalent diagonal strut to perform nonlinear analysis to capture the nonlinear behaviour of infilled frames (e.g. Panagiotakos and Fardis 1996; Žarni´c and Gostič 1997; Dolšek and Fajfar 2005). Different techniques have been implemented to perform the cyclic analysis of infilled frames with the use of the equivalent diagonal strut (Madan et al. 1997, Cavaleri et al. 2005, Rodrigues et al. 2010, Cavaleri and Di Trapani 2014).

Although the concept of the diagonal struts and its development has progressed over the years, most models were limited to IP analysis and could take into account only the IP resistance of infilled frames. The common practice in the evaluation of infilled frames in the out-of-plane direction is still limited to determining the normal forces on the infill wall using some indirect method (e.g. using an average response of the floors above and below the infill wall) and comparing those forces with the out-of-plane capacity of the infill wall which is normally computed using the analytical capacity models as discussed in section 2.2. Accordingly, the interaction between the IP and OoP

loads in determining the infill's capacity is usually neglected in evaluating the seismic responses of the infilled frame.

The first macro-element model that defined both IP and OoP resistance of infill walls, as well as the interaction between the two forces using the method of equivalent struts was given by Hashemi and Mosalam (2007). In this model, the infill wall was represented by a three-dimensional strut-and-tie (3D-SAT) system. The model had two diagonal struts (represented by dashed line) and each of them is modelled by four pin-connected compression beam elements. At the centre, these struts are joined by a tension-only elastic link element (represented by a solid line). The link (tie) is common to both diagonal struts (Fig 2.24). The tension-only link element in the model was assumed to be rigid in tension by defining a very large elastic modulus for this element.

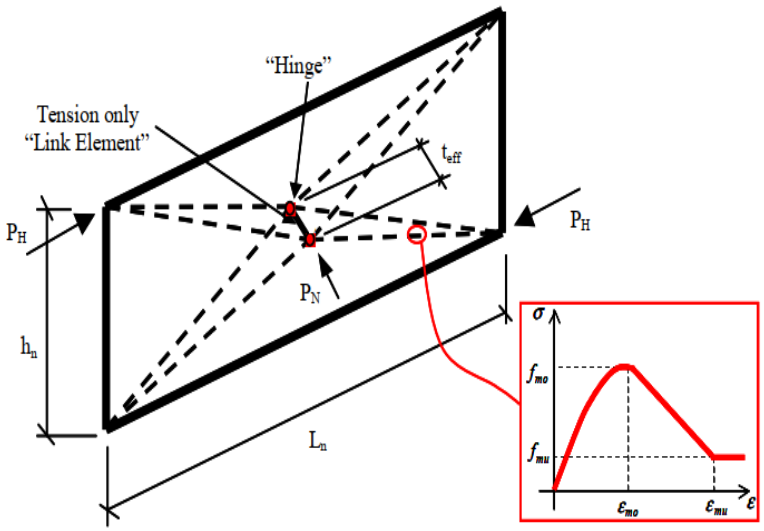

Figure 2.24 Strut and tie model (Hashemi and Mosalam, 2007)

In the model, the mechanical properties of the struts were defined by peak and ultimate stress-strain parameters as shown in Fig 2.24. These parameters were fixed by calibrating with the results of a more detailed FE analysis. The calibration process utilised a failure surface defined by an interaction diagram between the IP and OoP force capacities of the infill wall. In modelling, first, the IP and OoP capacities of infill wall from FE results were taken and the cross-section of the struts was calculated, and finally, the effective thickness of the struts was established through an iterative process until the desired capacity was reached. Although the model showed the possibility to address the problem of IP-OoP interaction, the model had some issues. For example, it was possible that the IP and OoP force path may violate the chosen interaction relationship and in some cases, it was difficult to satisfy the strength and stiffness requirement simultaneously in IP and OoP directions.

Later, Kadysiewski and Mosalam (2009) modified the model of Hamshemi and Mosalam (2007) to eliminate the problems associated with strut and tie model. The model had a single diagonal strut. The diagonal strut consisted of two beam-column elements connected at the midpoint node. The midpoint node was assigned with a lumped mass for the consideration of the response of the infill wall in the OoP direction (Fig 2.25). The diagonal strut is provided with both tensile and compressive properties. The macro-modelling was done in the open-source platform OpenSees (McKenna et al. 2000). The diagonal strut was modelled by using two "BeamWithHinges" elements. The ends of the diagonal elements (connected to the midspan node) were represented by the nonlinear fiber section available in OpenSees. The cross-section of the BeamColumn element was modelled by locating nonlinear fibers along a line in the OoP direction.

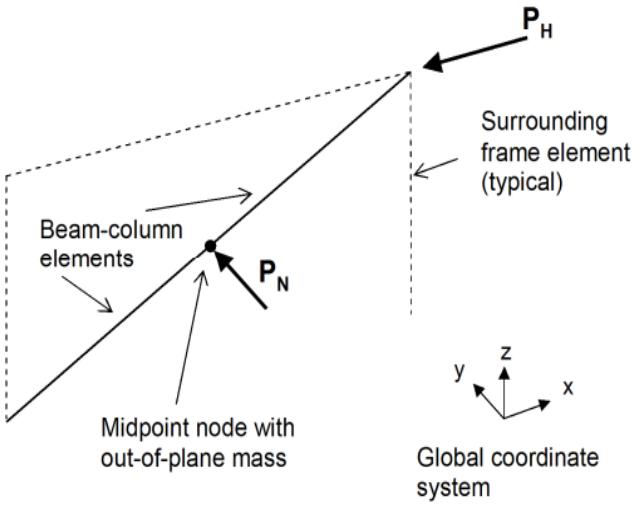

Figure 2.25 Macro-model by Kadysiewski and Mosalam (2009)

The numerical modelling involves lengthy calculations beforehand. First, the pure IP axial strength of the diagonal strut is to be defined according to FEMA 356. Then the yield point of the infill wall is to be calculated and the IP horizontal deflection at the yield point and the collapse prevention limit state needs to be fixed, and the effective cross-sectional area of the equivalent diagonal element is to be calculated. Similarly, for the OoP direction, OoP parameters like the frequency and effective weight are to be defined and the OoP capacity of the infill wall under the pure OoP load is to be determined based on FEMA 356. Then the yield moment corresponding to OoP capacity is calculated and is converted to the required yield moment for the equivalent element which is taken as a moment capacity when IP axial force is zero. Afterward, OoP displacement of the equivalent element at yield and collapse prevention limit states are defined. Using the target axial force (P)-moment (M) relationship) which is 3/2 power curve, the interactive forces and moments capacities of the equivalent numbers are defined and the number of

fibers in the cross-section is fixed. Finally, for the defined numbers of fibers, fiber area, fiber location (centroid), fiber yield stress and fiber yield strain are to be calculated. The rigorous calculation makes it complicated for the design engineers to use this model in practice.

The model can be used for static (monotonic, cyclic) and dynamic analysis and has the ability to represent the global behaviour of the structural system. However, the model has not been tested with different experimental studies. The properties of the infill wall vary a lot which influences the OoP capacity directly (also IP capacity) as discussed in section 2.1. Therefore, it is not sure how good the responses will be. Moreover, the OoP capacity is evaluated based on FEMA 356. From the detailed study (Section 2.2) it was observed that the FEMA 356 approach is very conservative. Similarly, in the model, the infill panel retains strength and stiffness after exceeding the collapse prevention limit state which is unrealistic and leads to errors in the calculated global responses of the building model. Due to this feature, collapsed panels will still be carrying the load in the analysis, which will lead to an underestimation of the load in the other panels and elements of the surrounding frame. This problem was later improved by Mosalam and Günay (2015) by integrating the progressive collapse algorithm developed previously by Talaat and Mosalam (2009). The algorithm was developed by using the element removal technique based on dynamic equilibrium and the resulting transient change in system kinematics.

Furtado et al. (2015) also proposed another simplified macro-model to simulate the integrated IP and OoP behaviour of infill walls. It is based on the model of Rodrigues et al. (2010) which was originally made to capture IP response of infilled frame. In this model, masonry infill is simulated by four diagonal struts with rigid behaviour. The diagonal struts are connected by one central element (Fig 2.26). All the non-linearity is concentrated in this central

element. To simulate the OoP behaviour, two central nodes with equal masses are assigned.

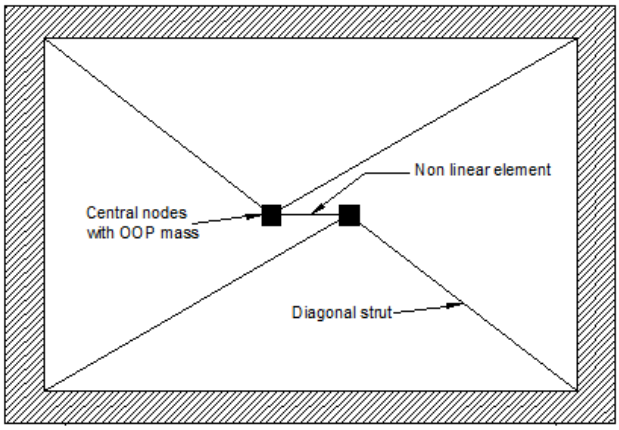

Figure 2.26 Macro model by Furtado et al. (2015)

In the model, four diagonal struts can be represented with either "BeamWithHinges" or elastic BeamColumn elements while the central element can be represented with "BeamWithHinges" or a nonlinear BeamColumn element. The non-linear IP axial behaviour of the central strut is characterized by a multi-linear curve which indicates: (i) cracking force and cracking displacement; (ii) yielding force and yielding displacement; (iii) maximum strength and the corresponding displacement; (iv) residual strength and the corresponding displacement. The hysteresis is controlled by three additional parameters: stiffness degradation—α, pinching effect—β and strength degradation—γ. The pinching 04 material available in OpenSees was used to represent the IP hysteretic behaviour of the infill wall. Although the numerical model takes into account a combination of IP failure modes like

diagonal cracking, sliding and corner crushing, it predominant represents the failure in diagonal cracking.

For the OoP response, out-of-plane behaviour is considered as following a linear elastic hysteretic curve. Mass equal to 0.81 M (M is the total mass of the infill wall) was assigned to central nodes (half on each node) and the natural period of vibration was considered as that original infill wall and OoP bending stiffness was considered as per the FEMA 356 and the suggestion of Mosalam and Günay (2015). In order to have a realistic representation of the behaviour of the infill walls, automatic removal of collapsed elements during the simulation was achieved by adopting the element removal algorithm of Mosalam and Günay (2015). When the infill model reaches the IP and OoP drift limits defined by linear interaction, the infill walls are removed. The drift limits were defined based on available experimental studies.

Though the model is relatively simple compared to the model of Kadysiewski and Mosalam (2009) because of lesser calculations, the model involves parameters which is not easy to fix, especially for the IP analysis. Moreover, the model is calibrated with respect to one experimental study and it is not obvious how the responses will be when compared to other experimental results.

More recently, a four-strut macro-element model was proposed by Di Trapani et al. (2018). The model can take into account the IP and OoP behaviour of infill walls as well as their interaction (Fig 2.27) and is relatively simpler compared to previous models. It is to be noted that the model was developed to predict the OoP capacity of the infill wall differently from the previously developed integrated IP-OoP macro-models. The macro-model had two diagonal struts, one horizontal strut and one vertical strut. Each strut is represented by two fiber-section BeamColumn elements and they are

connected by a node at the mid-span. Altogether there are four mid-span nodes at the same location and these nodes can move independently in the IP direction while they are constrained to move together in the OoP direction. The struts are pin connected to the frames.

In this model, the compressive behaviour of the struts was represented by four stress-strain parameters as shown in Fig 2.27: peak stress-strain and ultimate stress-strain values. The diagonal struts were defined by an empirical strength value as the peak stress in the fibers and ultimate stress as 60% of the peak value while both peak and ultimate strains were given empirical values. For the horizontal and vertical struts, compressive strength of the masonry was defined as peak stress and only strain values were empirical. Due to the use of fiber-section elements, the model could directly take into account the arching mechanism of infills during OoP load through the coupling of axial force and moment. The possibility of using the fiber section elements to reproduce the arching behaviour is discussed in detail in Asteris et al. (2017).

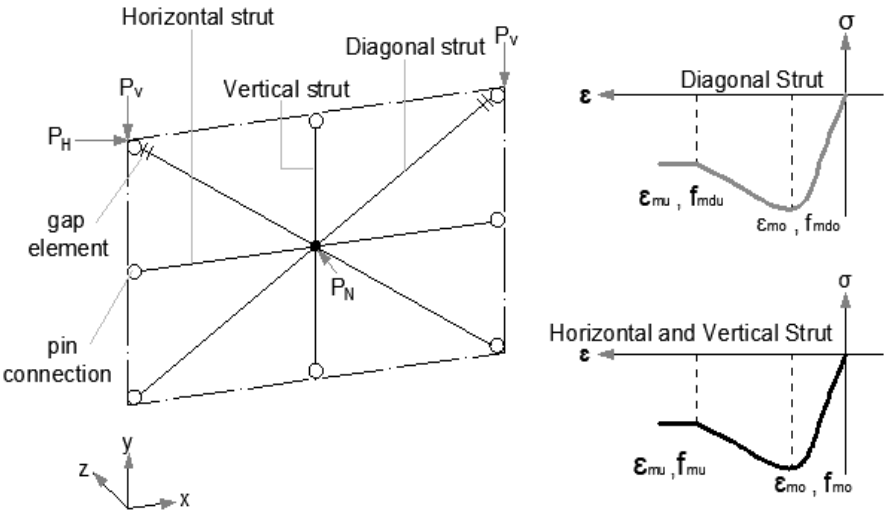

Figure 2.27 Macro model by Di Trapani et al. (2018)

For a fibre-section element, the rate of internal force increment, $\dot{s}^s(x)$, at a section can be related to the rate of increment of the section deformation, $\dot{e}^s(x)$, through the tangent stiffness matrix $k_T^s(x)$, by the following relation:

$$\dot{s}^s(x) = \begin{bmatrix} \dot{N}(x) \\ \dot{M}(x) \end{bmatrix} = k_T^s(x) \begin{bmatrix} \dot{\varepsilon}_0 \\ \dot{k} \end{bmatrix} = k_T^s(x)\dot{e}^s(x) \tag{2.43}$$

where $\dot{\varepsilon}_0$ is the axial strain rate at the centroidal axis of the beam, $\dot{k}$ is the rate of change of section curvature, $\dot{N}(x)$ is the rate of change of axial force and $\dot{M}(x)$ is the rate of change of the bending moment. After cracking in the fibre-section, the tangent stiffness matrix is non-diagonal and the change in the axial load and bending moment is related to the change in the axial centroidal strain and curvature given by:

$$\begin{aligned} \dot{N}(x) &= k_{T,11}^s \dot{\varepsilon}_0 + k_{T,12}^s \dot{k} \\ \dot{M}(x) &= k_{T,21}^s \dot{\varepsilon}_0 + k_{T,22}^s \dot{k} \end{aligned} \tag{2.44}$$

The section stiffness and resistance are derived from the uniaxial stress-strain relation specified for each fiber in the section. Cracking in flexure shifts the neutral axis of bending and introduces element elongation along the centroidal axis which induces the compressive forces at the two ends. This feature produces a three-hinge arching mechanism.

In the model of Di Trapani et al. 2018, the geometry of the equivalent struts can be defined easily without lengthy preliminary calculations. At the same time, the stress-strain parameters can be fixed in such a way that the numerical results (IP and OoP responses) are in good match with the experimental results. This has been shown by the authors. However, the

drawback of this model is the identification of the empirical stress-strain parameters. There is no standard procedure to define these parameters for the struts and this is a big challenge for the models to be used practically.

Therefore, the development of a user-friendly, practical, and effective macro-model is imperative in the present context to identify both the IP and OoP capacities of the infilled frame also considering the possible interaction between the IP and OoP forces during seismic events.

3 NEW MACRO-ELEMENT MODEL FOR INFILLED FRAMES

In this chapter, a new modified macro-element model is proposed. Given the limitation associated with the model of Di Trapani et al. (2018) as discussed in Chapter 2, it is decided to modify and further develop the model to make it usable in the case of infill wall with different mechanical and geometrical properties following standard procedures. The main objective of the proposed models are:

1. The model has to account for the arching action of the masonry infill wall due to OoP loads and capture the OoP capacity of the infill wall effectively.
2. The model has to account for the IP resistance of the infilled frame.
3. The model has to account for the interaction between the IP and OoP loads. The model should be able to account for the influence of damage caused by IP load on the OoP response and vice versa.
4. The model has to be simple enough so that it can be used in practice for the estimation of the OoP capacity of infilled with different mechanical and geometrical characteristics for seismic analysis of infilled frame structures.

The proposed macro-element model is suitable for the analysis of RC frames with URM infill walls made of solid or hollow masonry units. The

infill wall should be constituted by one leaf, without openings, and without RC bond beams and/or columns. The details of the macro-model, its calibration and validation with the experimental results are discussed in the next sections.

3.1 Details of the proposed four-strut macro model

The proposed model is a modification of the macro-element model proposed by Di Trapani et al. (2018). The modified model has a similar configuration to its predecessor i.e. it has 4-struts: two diagonal struts, one horizontal strut and one vertical strut. Each strut in the model is represented by two fibre-section BeamColumn elements and they are connected by a node at the mid-span (Fig 3.1). Altogether there are four mid-span nodes and these nodes can move independently in the plane of the infill wall (each node can exhibit different IP displacements) and they move together in the OoP direction (each node has the same value of OoP displacement). This is achieved by defining the constraints in a suitable way in OpenSees. In the model, the IP load (P_H) is applied at the top of the infilled frame while the OoP load (P_N) is applied to the centre nodes (Fig 3.1). Due to the OoP load, the struts are subjected to direct bending and the use of the fiber-section based BeamColumn elements enables struts to take bending into account.

Compared to the model of Di Trapni et al. (2018), there is a slight change in the connections of the struts to the frame. Instead of a pin connection, the struts have a moment connection with the frame. For a pin-ended strut, due to significant OoP deflection, there was an early flexural failure at the middle of the strut preventing the struts from attaining full arching effect. When rotational restraint was provided at the ends, it limited excessive deflection at the centre of the struts and also induced extra compression at the ends of the struts, thereby improving the arching action.

Therefore, the end connections of the struts were changed in the proposed model to increase the OoP capacity of the struts to match the experimental results.

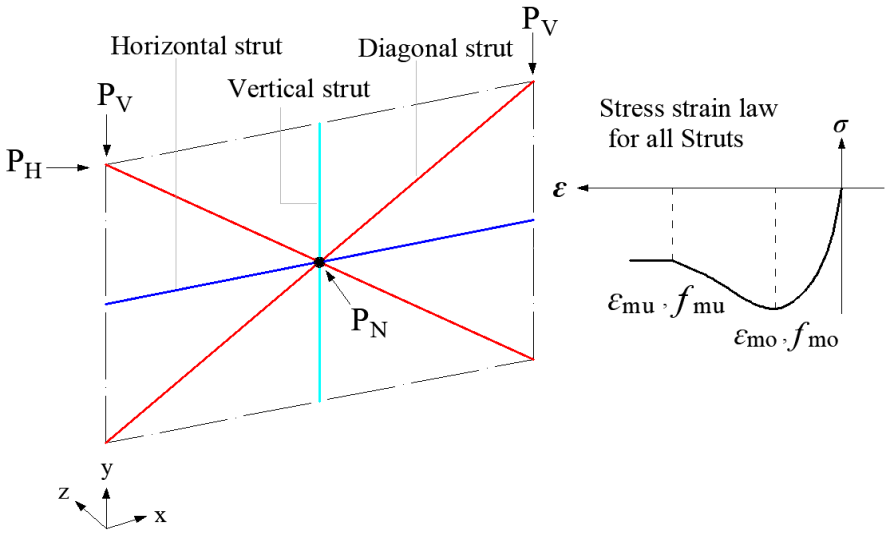

Figure 3.1 Proposed macro-element model

As in the model of Di Trapani et al. (2018), the compressive property of the fibers in the struts is represented by four stress-strain parameters, namely, f_{mo}, f_{mu}, ε_{mo} and ε_{mu} as shown in Fig 3.1. However, in the proposed model, all the struts are defined by the same parameters instead of different parameters for different types of struts. This change has further simplified the model because of the fewer parameters to be known for its use.

In the model, the width of the diagonal struts w_d, horizontal strut w_h and vertical strut w_v are calculated by the following equations:

$$w_d = d/3 \tag{3.1}$$

$$d = \sqrt{l'^2 + h'^2} \tag{3.2}$$

$$w_h = h - w_d / \cos\theta \tag{3.3}$$

$$w_v = l - w_d / \sin\theta \tag{3.4}$$

where l and h are the clear length and height of the infill wall respectively, while l' is the centre to centre distance between the columns and h' indicates the height from the top of the lower beam to the centre of top beam as shown in Fig 3.2. The Greek letter θ is the angle defining the slope of the diagonal struts.

If w_d is the width of the diagonal strut, $w_d / \cos\theta$ is the total contact length between the diagonal struts and the columns and $w_d / \sin\theta$ is the total contact length between the diagonal struts and the beams. The thickness of each strut is defined as the thickness of the infill wall (t).

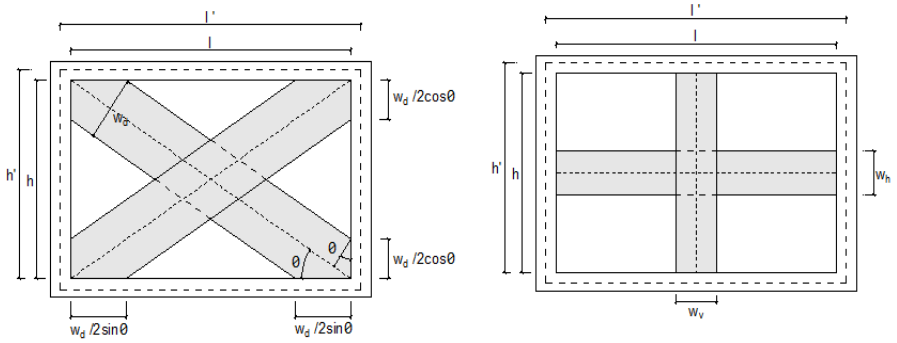

Figure 3.2 Dimensioning of the diagonal, vertical and horizontal struts

It is important to understand that the definition of struts geometry (width and thickness) according to the above equations is sufficient to derive good IP resistance. When checked with different experimental results, the IP

numerical responses were close to the experimental responses. However, the use of an actual infill thickness as a strut thickness yielded comparatively low OoP strength. Hence, to accurately represent both IP and OoP resistances of infill walls, the width and thickness of all the diagonal, vertical and horizontal struts are replaced by surrogate values in the proposed model. Surrogated struts maintain the same cross-sectional area as the original struts. This technique is also used in the model of Di Trapani et al. (2018). However, there is a small modification in the current model. In the model of Di Trapani et al. (2018), only the diagonal struts use a surrogate thickness value. The thickness of horizontal and vertical struts was not replaced with the surrogated thickness and rather the actual thickness of the infill wall was used. But, in the proposed model, all struts use the surrogated thickness.

To derive the surrogate width $\bar{w}$ and surrogate thickness $\bar{t}$ of the struts, it is assumed that the OoP resistance q of any strut is proportional to the compressive strength of the masonry f_m and the strut width w, and is inversely proportional to the square of the slenderness ratio of the strut $\frac{l_s}{t}$ as follows:

$$q \propto \frac{f_m w}{\left(\frac{l_s}{t}\right)^2} \tag{3.5}$$

In Eq. 3.5, l_s is the length of the strut. If f_m is replaced by f_{mo}, the strut width w and thickness t have to be replaced by $\bar{w}$ (surrogated width) and $\bar{t}$ (surrogated thickness) so that the OoP resistance remains the same and the area of the struts does not change. f_{mo} is the empirical compressive strength of the struts. In doing so, the Eq. (3.5) becomes,

$$\frac{f_m w}{\left(\frac{l_s}{t}\right)^2} = \frac{f_{mo}\bar{w}}{\left(\frac{l_s}{\bar{t}}\right)^2} \tag{3.6}$$

Since the cross-sectional area of the struts is not changed, the IP resistance of the infilled frame remains the same. The equivalence between the cross-sectional area of the surrogate strut and the original strut is defined by the following equation.

$$wt = \bar{w}\bar{t} \tag{3.7}$$

Substituting the expression for surrogate width $\bar{w}$ from Eq. (3.7) into Eq. (3.6), we get the following equation.

$$\frac{f_m w}{\left(\frac{l_s}{t}\right)^2} = \frac{f_{mo} wt}{\bar{t}\left(\frac{l_s}{\bar{t}}\right)^2} \tag{3.8}$$

On solving Eq. (3.8), the following relations for the surrogate thickness can be obtained as

$$\bar{t} = \frac{f_m}{f_{mo}} t \tag{3.9}$$

$$\bar{w} = \frac{f_{mo}}{f_m} w \tag{3.10}$$

As seen from the Eqs. 3.9 - 3.10, to define the geometry of the struts, it is also necessary to fix the strength peak parameter f_{mo} besides knowing the mechanical properties (compressive strength) of the masonry used in the infill wall. The derivation of the f_{mo} is discussed later in the chapter. According to the above-defined equations, the surrogate width and thickness of all the struts can be calculated. To avoid confusion, the surrogate widths of the diagonal,

vertical and horizontal struts are hereafter represented by $\overline{w_d}$, $\overline{w_v}$, and $\overline{w_h}$ respectively, while the surrogate thickness for all struts is represented by $\overline{t}$.

The model is validated with the available experimental results based on nonlinear static analysis. To be specific, first, the IP cyclic load is applied and afterward, the OoP load is applied in displacement-controlled mode. Nevertheless, the model can be used to perform the analysis also in a force-controlled environment. Due to the higher deflection of the struts, the model can become unstable. To control this, geometric nonlinearity in the model is taken into account by using BeamColumn elements formulated with Corotational coordinate transformation available in the OpenSees platform. The validation of the model is discussed in the next section.

3.2 Validation of the proposed macro model

The validation process was first aimed toward improving the capability to replicate the experimental results compared to the modelling approach provided by Di Trapani et al (2018). To this aim, an experimental test by Angel (1994) was used which was also used by Di Trapani et al (2018). Specimen 3 from the experiment was taken as a reference specimen.

Angel (1994) tested seven full-scale, single-storey, single-bay RC infilled frames with both IP and OoP loads. The design details of the infilled frame are shown in Fig 3.3. The geometrical and material properties of the infill specimen are given in Table 3.1. In the experiment, the infilled frame was first subjected to IP cyclic lateral displacements until the infills reached double the drift of first cracking (Δ_{cr}). After the completion of the IP test, the infill wall was loaded in the OoP direction using an airbag applied pressure. For example, specimen 3 taken for the validation process, was subjected to an IP drift of 0.22% before applying OoP load (IP displacement history is shown in Fig 3.4).

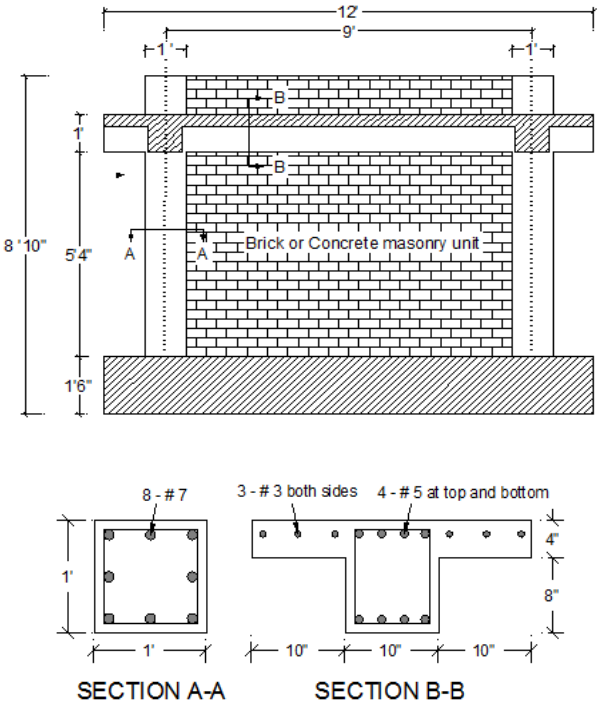

Figure 3.3 Infilled frames tested by Angel (1994)

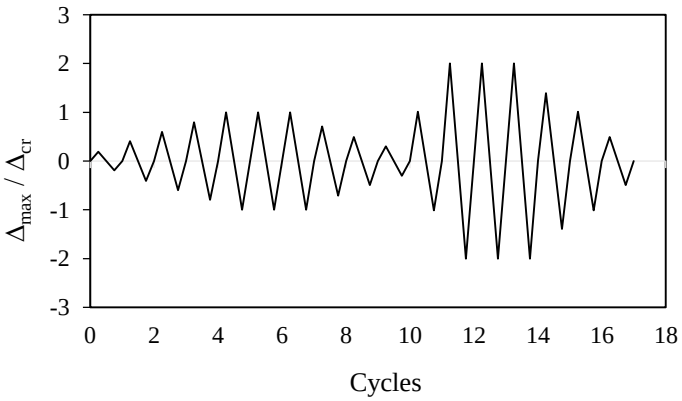

Figure 3.4 IP displacement history for Angel (1994)

Table 3.1 Geometrical and material properties of the masonry infill specimen 3 of Angel (1994)

Specimen	f_{mv} N/mm^2	f_{mh} N/mm^2	E_{mv} N/mm^2	E_{mh} N/mm^2	f_m N/mm^2	E_m N/mm^2	l mm	h *mm*	t *mm*	l' *mm*	h' *mm*	d *mm*
3	10.1	10.1	5212	5212	10.1	5212	2438	1626	47	2743	1782	3271

Table 3.2 Geometrical and mechanical properties of struts calculated for specimen 3 of Angel (1994)

Specimen	w_d mm	w_v mm	w_h mm	$\overline{w}_d$ mm	$\overline{w}_v$ mm	$\overline{w}_h$ mm	$\bar{t}$ mm	f_{mo} N/mm^2	f_{mu} N/mm^2	ε_{mo}	ε_{mu}
3	1090.4	472.6	315	387	168	112	134	3.6	2.16	0.0030	0.015

Numerical simulation was carried out in the open-source software platform OpenSees. Reinforce concrete frame elements, as well as strut elements, were modelled by fibre-section BeamColumn elements with distributed plasticity. Concrete 02 material model available in OpenSees was used to simulate the mechanical behaviour of the concrete and masonry material while reinforcement in the frames was modelled using Steel 02 material model. Concrete02 is a uniaxial stress-strain concrete material with tensile strength and linear tensile softening. In the current study, zero tensile strength has been assumed according to Mander et al. (1988). The concrete confinement due to transverse reinforcement is not taken into account. Similarly, Steel02 is a uniaxial steel material with isotropic strain hardening based on Menegotto-Pinto model (Menegotto and Pinto 1973). A distinct layer was defined in the fibers of the frame elements to model longitudinal reinforcements. Concrete02 material is combined with MinMax material available in OpenSees to simulate the failure of fibers in the struts by dropping the corresponding stress to zero when the ultimate strain was achieved. Loading was applied in a similar pattern as used in the experimental tests The IP lateral displacement was applied at the upper nodes of the frame model and

the OoP load was applied at the centre of the struts which represents the infill centre.

The geometrical properties of the diagonal, vertical, and horizontal struts required for the macro-model are presented in Table 3.2. The material properties of the strut fibers namely, f_{mo}, f_{mu}, ε_{mo} and ε_{mu} are also given in Table 3.2. The numerical results for the IP and OoP responses are shown in Fig 3.5. The correlation between the experimental and the numerical results is reasonably good despite the simplicity of the model.

The numerical results from the proposed model are also compared with the numerical results given by Di Trapani et al. (2018). It can be observed that both models yielded similar IP responses but the OoP response of the proposed model is closer to the experimental result. This shows that the proposed model accounts for OoP response comparatively better, i.e. the proposed modifications enable the model to account for both the IP and OoP responses of the URM infill wall in a more reliable way.

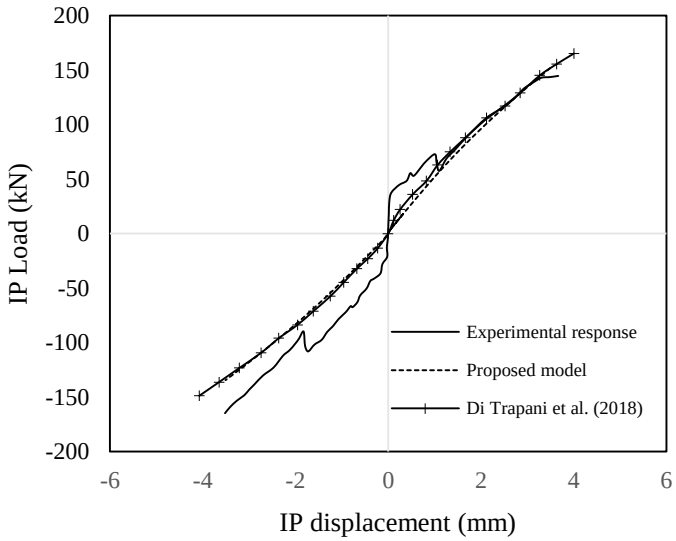

(a)

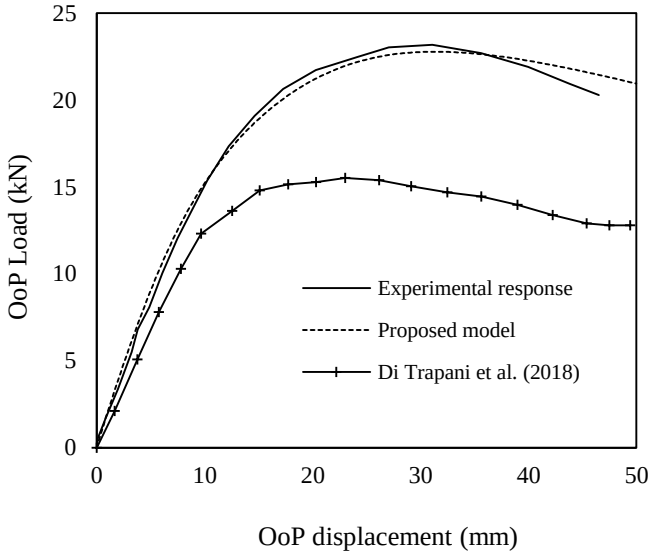

(b)

Figure 3.5 Comparison between the experimental and numerical responses for specimen 3 tested by Angel (1994): a) IP responses; b) OoP responses

After knowing that the results obtained from the proposed model are better, the model was further tested with other sets of experiments available in the literature. For this, those experimental studies in which detailed information is available were taken. Experiments with any sort of strengthening (e.g. bed joint reinforcement, horizontal or vertical bond beam) or any gaps in between the infill wall and the frames were avoided to have a clear understanding of the application of the proposed model in the case of a URM infill wall.

Different experimental studies which involved cyclic IP loading at the top of infilled frames followed by OoP loading using the uniformly distributed load (airbag) or concentrated load (4 load points at the centre) were considered: Calvi & Bolognini (2001); Ricci et al. (2018a, 2018b); De Risi et

al. (2019b); Da Porto et al. (2013). A short discussion of the important features of these experimental studies is presented here.

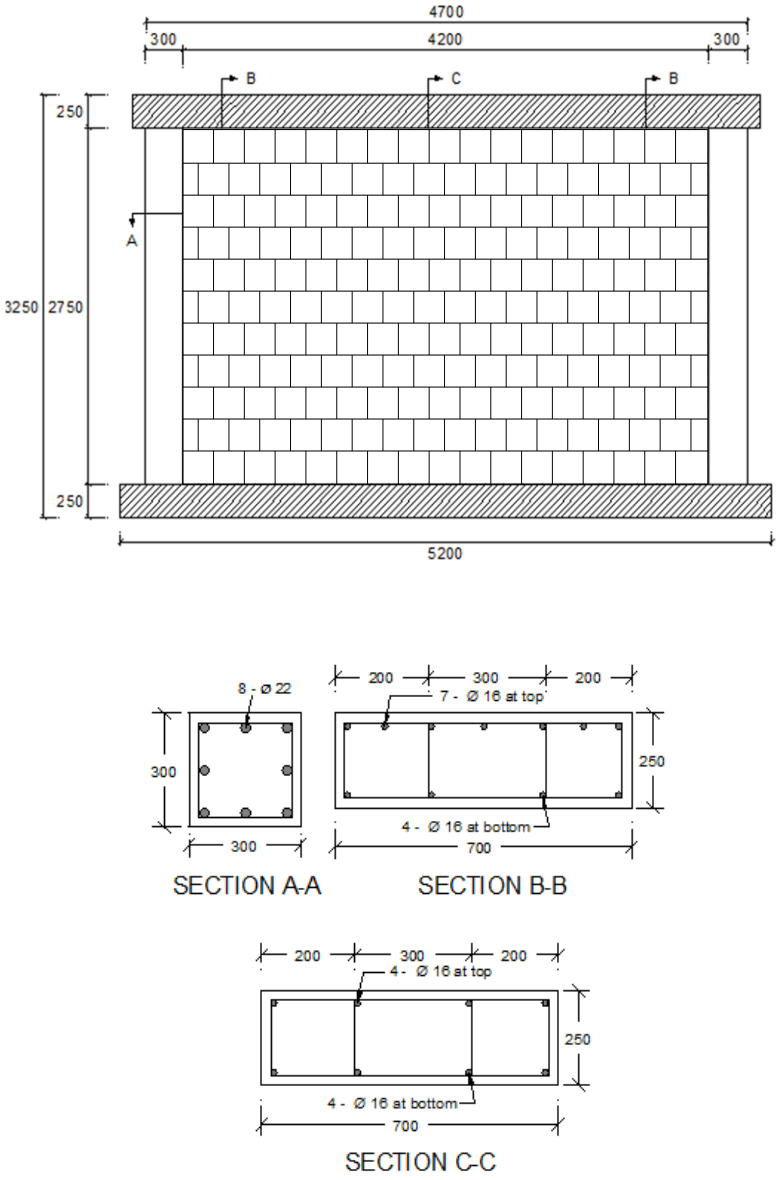

Figure 3.6 Infilled frame tested by Calvi & Bolognini (2001) (dimensions in mm – infill of clay hollow bricks)

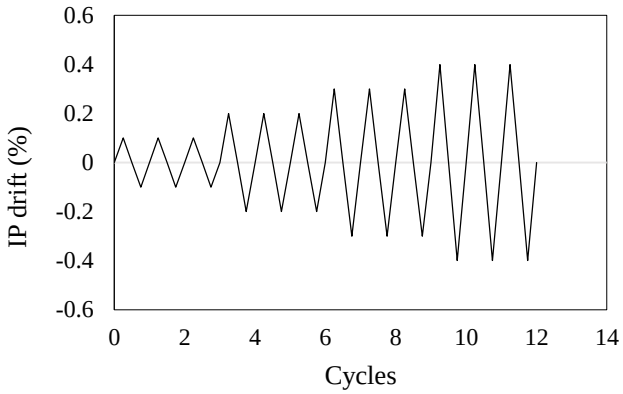

Figure 3.7 IP drift history applied during the experiment of Calvi and Bolognini (2001)

Calvi and Bolognini (2001) tested RC frames infilled with URM infill wall made of hollow clay units. Thickness of the infill wall was about 135 mm. The details of this infilled frame specimen are shown in Fig 3.6. The tests were performed under the action of vertical loads applied to the columns. Two URM infilled frames specimens were tested. The first specimen (specimen 6) was subjected to the IP cyclic drift of 0.4 % and the second specimen (specimen 2) was subjected to the IP cyclic drift of 1.2 %. After the application of the IP loads, the OoP load was applied monotonically at four load points. For the validation purpose, specimen 6 (#6) was taken into account (for specimen 2, the force-displacement curve was not provided by the authors). Three cycles of IP drift loads were applied to specimen 6 as given in Fig 3.7.

Da Porto et al. (2013) tested RC frames infilled with URM walls made up of clay hollow brick units. The thickness of the infill wall was 300 mm. The geometric details of the reference frame are shown in Fig 3.8. The experiment was conducted in the presence of a vertical load applied to each

column. In-plane quasi-static cyclic horizontal displacement was imposed at the level of the top beam to a drift of 1.2 %. Three cycles of IP drift loads were applied to the specimen. After the application of the cyclic in-plane drifts, the infill panel was subjected to monotonic out-of-plane loading at four loading points until collapse. The IP displacement history applied to the infilled specimen is given in Fig 3.9.

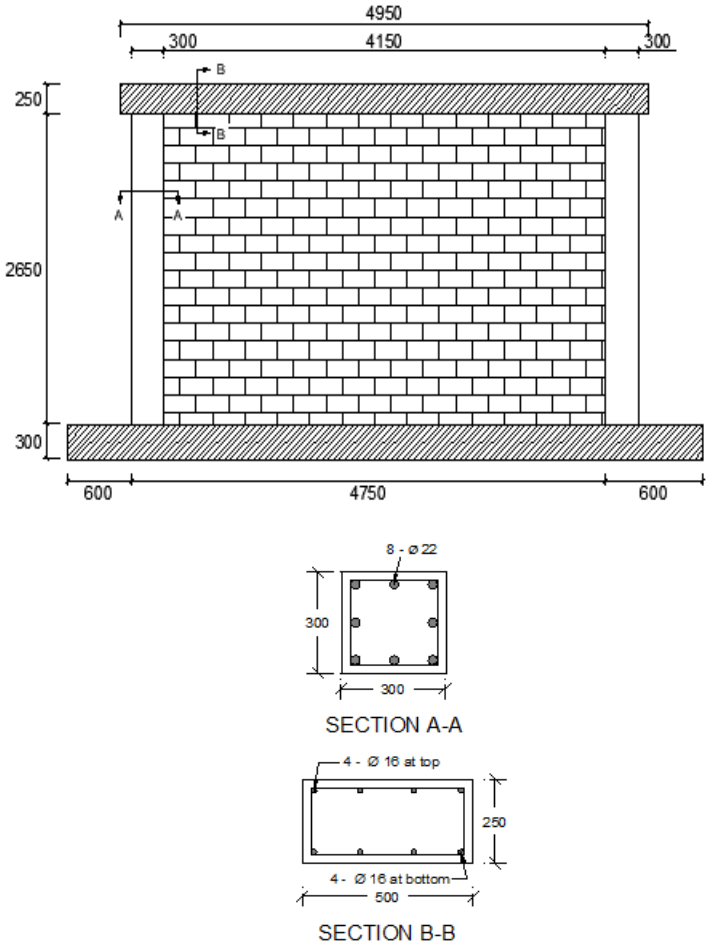

Figure 3.8 Infilled frame tested by Da Porto et al. (2013) (dimension in mm – infill of clay hollow bricks)

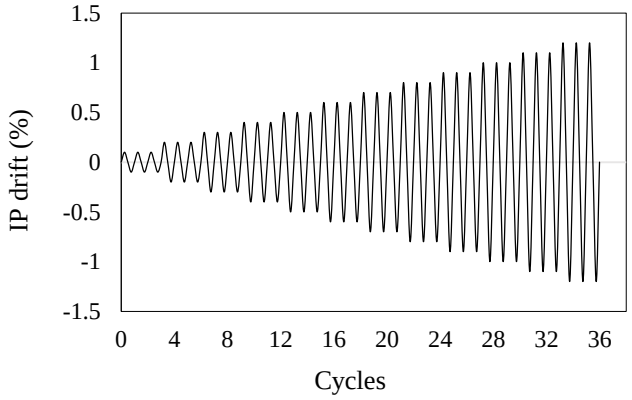

Figure 3.9 IP drift history applied during the experiment of Da Porto et al. (2013)

Ricci et al. (2018a, 2018b) experimented on two sets of infill walls in RC frames, one of thickness 80 mm (specimen #1) and the other of thickness 120 mm (specimen #2). The main purpose of using the infill wall of two thicknesses was to determine the influence of the slenderness ratio in the OoP capacity. Both infill specimens were tested with pure OoP load and also under the combination of IP and OoP load (IP load followed by OoP load). The goal of performing the tests under pure OoP load and in combined IP and OoP load was to determine the effect of IP damage on the OoP capacity of the infill wall. Infilled specimens were subjected to three different levels of IP drift before loading in the OoP direction. IP tests were performed using quasi-static cycling loading at one end of the upper beam while OoP tests were conducted using the four-point loading method at the centre of the infill. The details of the tested frame are shown in Fig 3.10. For the numerical simulation, the OoP response after the first level IP drift, i.e. 0.16% for specimen #1 and 0.21% for specimen #2, was selected. The IP displacement history is shown in Fig 3.11.

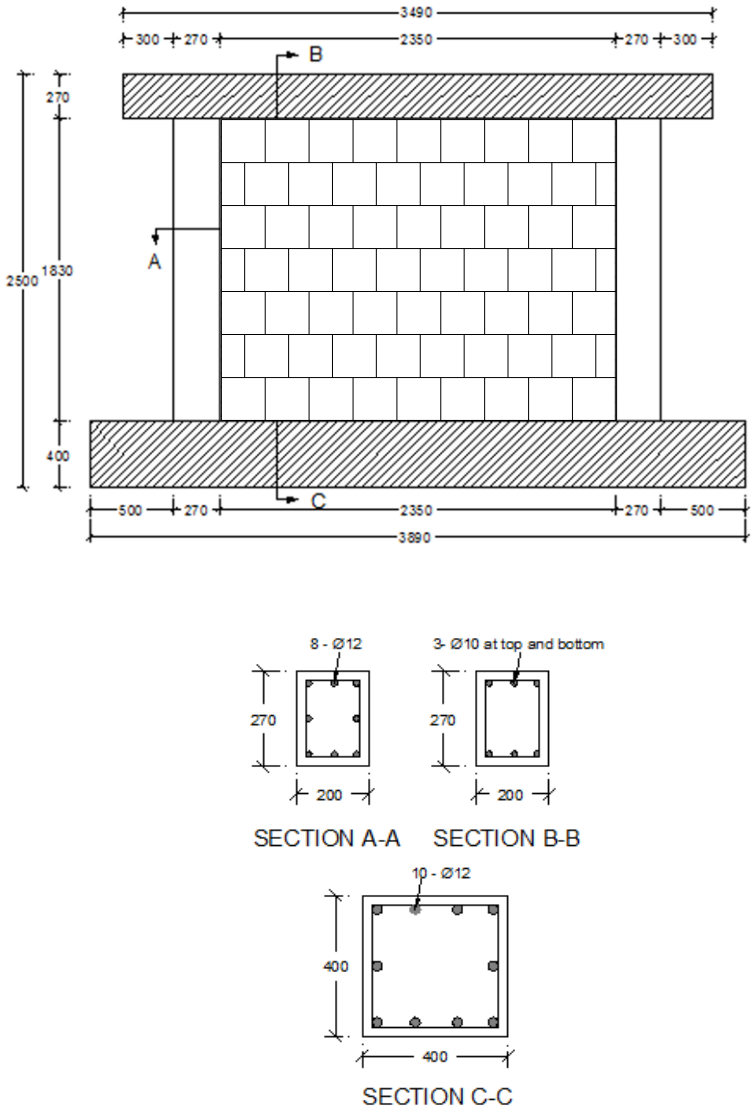

Figure 3.10 Infilled frame tested by Ricci et al. (2018a, 2018b) (dimension in mm – infill of clay hollow bricks)

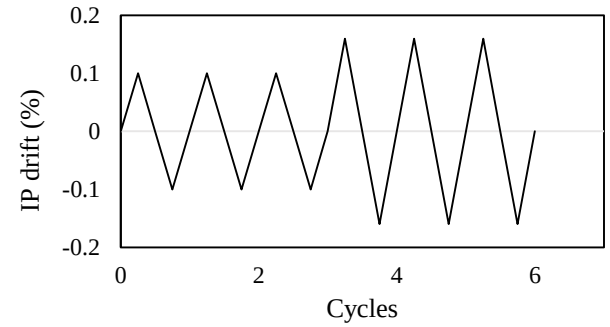

a)

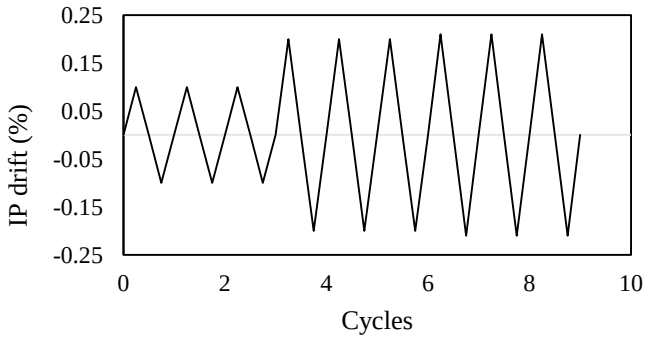

b)

Figure 3.11 IP drift history applied during the experiment of Ricci et al. (2018a, 2018b): a) 80 mm infill, b) 120 mm infill

De Risi et al. (2019b) continued the experimental campaign of Ricci et al. (2018a, 2018b). In this experiment, the effect of the aspect ratio on the OoP capacity of the infill was investigated. The tested frame was similar but the aspect ratio of the infill specimen was equal to one. An infill wall of 80 mm thickness was tested similarly as in Ricci et al. (2018a); one test was performed with a pure OoP test and three other tests were performed by applying OoP load after three different levels of IP drifts. The details of the infilled frame are shown in Fig 3.12. For the numerical simulation, the OoP

test after 0.15% IP drift was taken. The IP drift history of the selected test is shown in Fig 3.13.

The material properties of the concrete frames and masonry infills from the above-discussed four experiments are given in Table 3.3, and the geometric properties of the masonry infill walls and the struts initially calculated are given in Table 3.4.

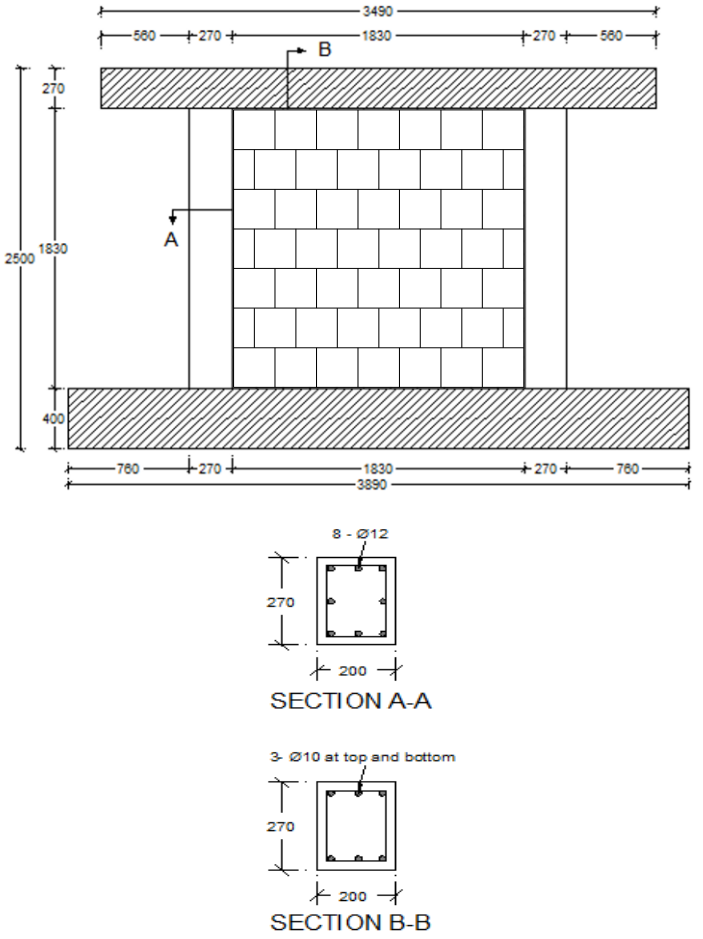

Figure 3.12 Infilled frame tested by De Risi et al. (2019b) (dimension in mm – infill of clay hollow bricks)

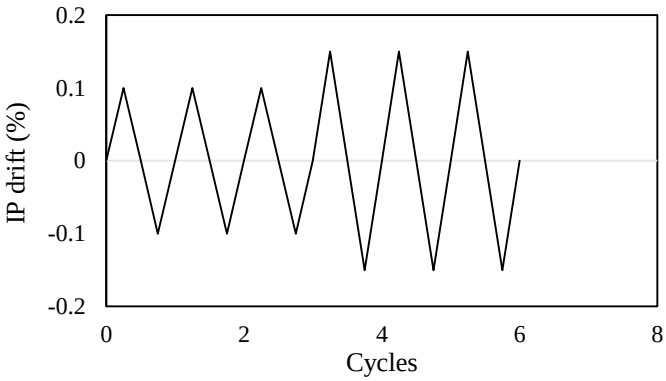

Figure 3.13 IP drift history applied during the experiment of De Risi et al. (2019b)

Table 3.3 Material Properties of the Concrete Frame and Masonry Infills for Specimens under Study

Experiment		f_c N/mm^2	f_{mv} N/mm^2	f_{mh} N/mm^2	E_{mv} N/mm^2	E_{mh} N/mm^2	f_m N/mm^2	E_m N/mm^2
Calvi & Bolognini (2011)	#6	34.6	1.11	1.10	991	1873	1.10	1362.4
Da Porto et al. (2013)		36.4	6	1.19	4312	1767	2.67	2760.3
Ricci et al. (2018a)	#1	36	2.45	1.81	1255	1090	2.11	1169.5
Ricci et al. (2018b)	#2	46.2	2.12	1.65	1262	1455	1.87	1355.0
De Risi et al. (2019b)		42.9	4.63	2.37	3452	1891	3.31	2554.9

Table 3.4 Geometric Properties of the Masonry Infills Equivalent Struts for the Specimens under Study

Experiment		l mm	h mm	t mm	l' mm	h' mm	d mm	w_d mm	w_v mm	w_h mm
Calvi & Bolognini (2011)	#6	4200	2750	135	4500	2875	5510	1836.5	847.3	554.8
Da Porto et al. (2013)		4150	2650	300	4450	2775	5244	1748.1	901.8	575.8
Ricci et al. (2018a)	#1	2350	1830	80	2620	1965	3275	1091.6	573.2	446.3
Ricci et al. (2018b)	#2	2350	1830	120	2620	1965	3275	1091.6	573.2	446.3
De Risi et al. (2019b)		1830	1830	80	2100	1965	2876	958.6	474.2	474.2

Table 3.5 Geometrical and Mechanical Properties for the diagonal, vertical and horizontal struts

Experiment	$\overline{w}_d$ mm	$\overline{w}_v$ mm	$\overline{w}_h$ mm	$\bar{t}$ mm	f_{mo} N/mm^2	f_{mu} N/mm^2	ε_{mo}	ε_{mu}
Calvi and Bolognini (2001) #6	1259.8	581.3	380.6	196.8	0.758	0.45	0.00045	0.0053
Da Porto et al. (2013)	845.9	436.4	278.7	620.0	1.293	0.78	0.00069	0.0075
Ricci et al. (2018a) #1	440.6	231.4	180.2	198.2	0.851	0.51	0.00049	0.0057
Ricci et al. (2018b) #2	500.2	262.7	204.5	261.9	0.857	0.51	0.00049	0.0057
De Risi et al. (2019b)	400.5	198.1	198.1	191.5	1.384	0.83	0.00073	0.0079

The surrogated geometrical properties of the struts and the effective stress-strain parameters of the fibers in the struts used for the numerical analyses are given in Table 3.5. The numerical results obtained from the proposed model for different cases are shown in Fig 3.14 to Fig. 3.18.

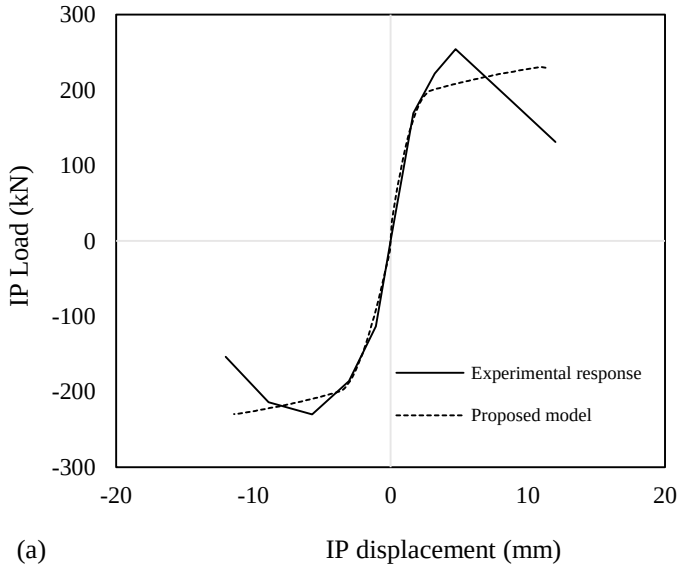

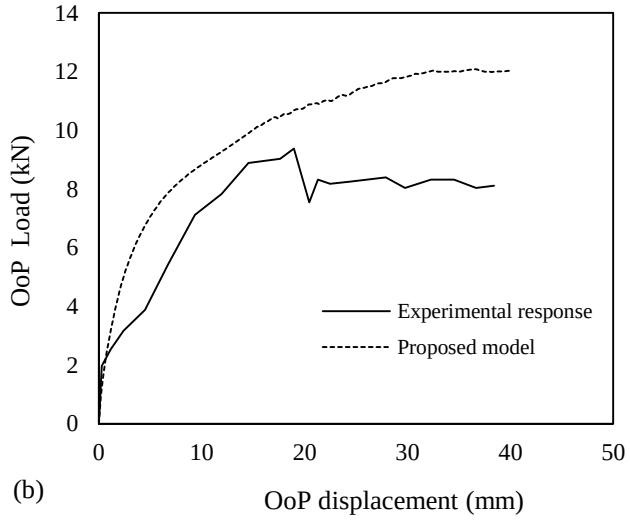

Figure 3.14 Comparison between the experimental and numerical responses for specimen #6 tested by Calvi & Bolognini (2001): a) IP responses; b) OoP responses

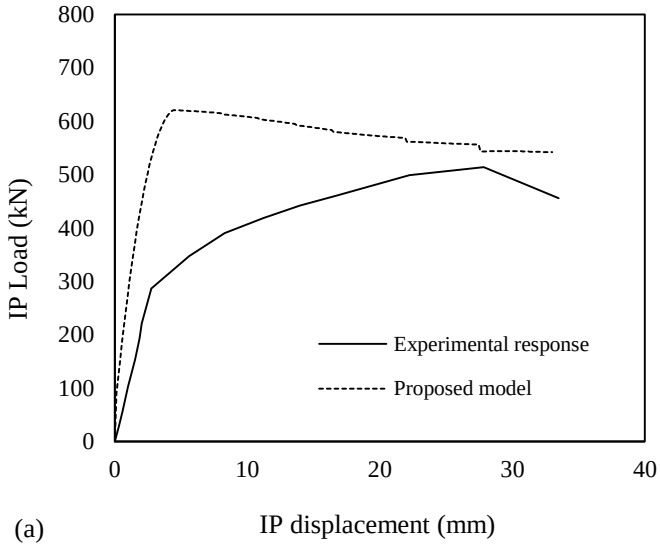

(a)

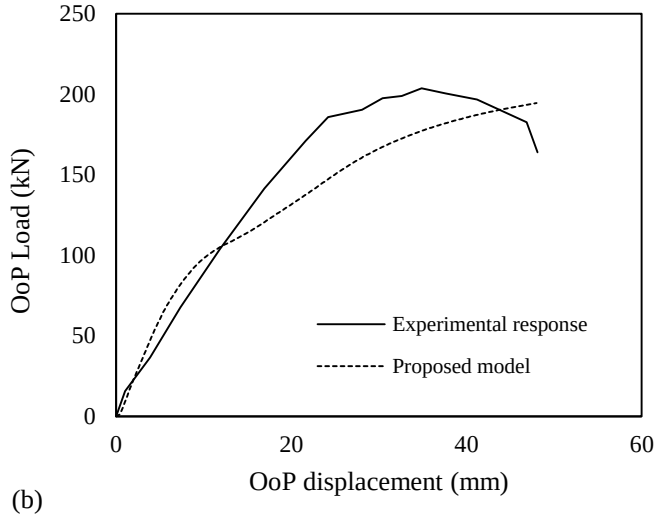

(b)

Figure 3.15 Comparison between the experimental and numerical responses for specimen tested by Da Porto et al. (2013): a) IP response; b) OoP response

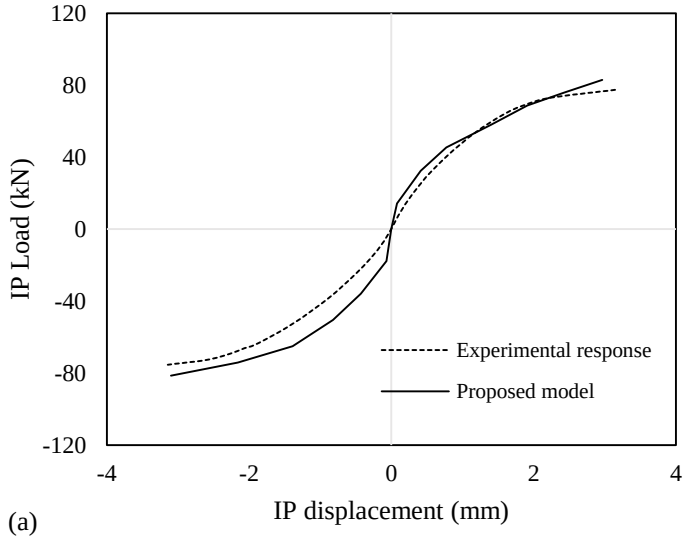

(a)

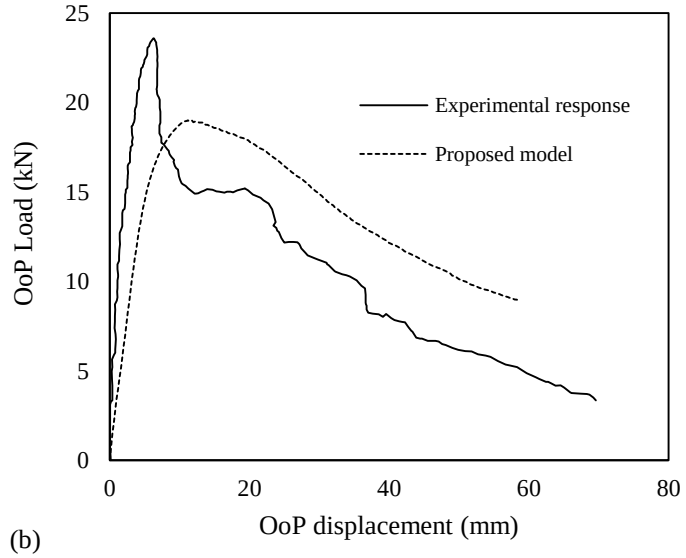

(b)

Figure 3.16 Comparison between the experimental and the numerical responses for specimen #1 (80 mm) tested by Ricci et al. (2018a): a) IP responses; b) OoP responses

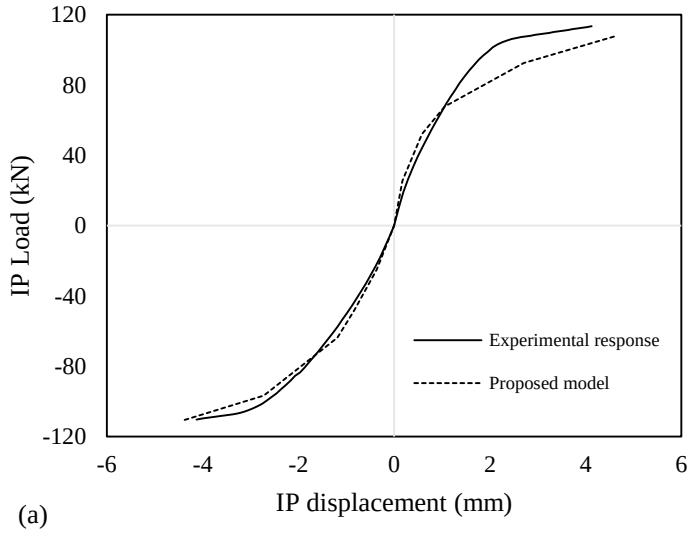

(a)

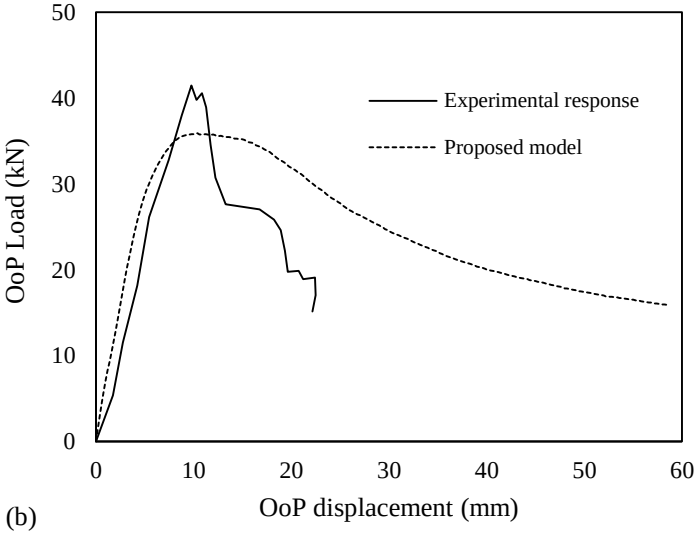

(b)

Figure 3.17 Comparison between the experimental and the numerical responses for specimen #2 tested by Ricci et al. (2018b): a) IP responses; b) OoP responses

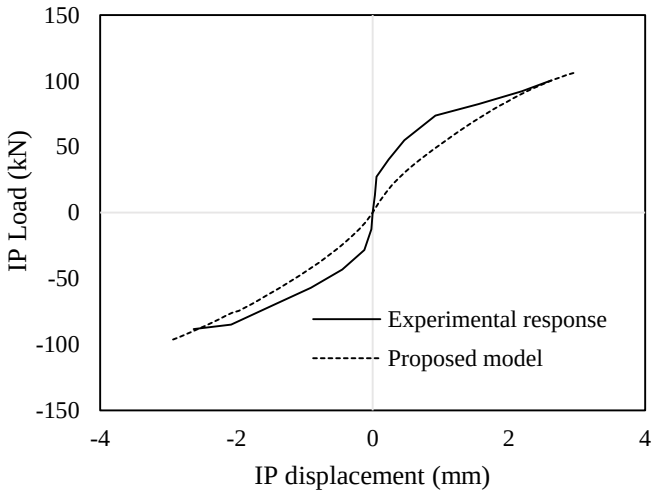

(a)

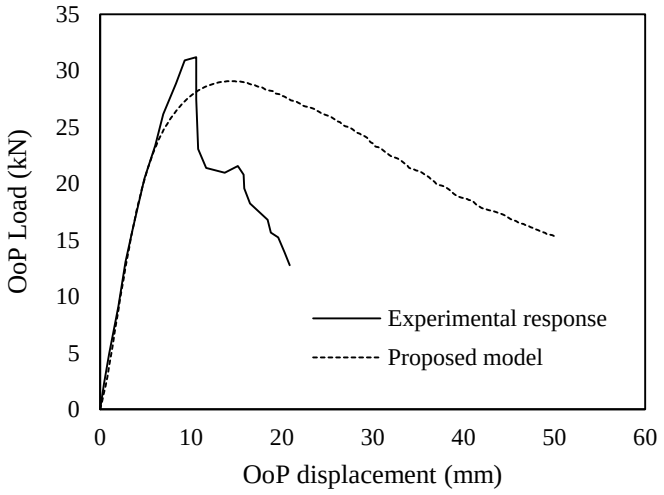

(b)

Figure 3.18 Comparison between the experimental and the numerical responses for specimen tested by De Risi et al. (2019b): a) IP responses; b) OoP responses

From the above figures, it can be seen that the numerical results obtained from the proposed model are good. Both IP and OoP responses from the numerical analyses are close to the experimental results except in a few aspects. In the case of Da Porto et al. (2013), the model provides a stiffer IP response, and the peak IP strength is also higher than the experimental one. In the case of De Risi et al. (2019b), the IP response from the model is slightly less stiff. In general, the results show that the proposed model is able to take into account the effect of prior IP damage on the OoP response of an infill wall. Moreover, the model also captures the degradation of OoP strength after attaining the peak strength. The strength decreases gradually and goes to failure with increasing OoP deflection. This was possible because of the integration of MinMax material in series with the Concrete02 material for the fibers in the struts. All these validations indicate the higher reliability of the proposed macro-model in capturing the IP and OoP behaviour of URM infill walls as well as the interaction effects due to combined IP and OoP loads.

3.3 Role of the diagonal, vertical and horizontal struts in the OoP capacity

The contribution of the horizontal, vertical and diagonal struts in OoP load resistance is different. In the model, the diagonal and vertical struts offer bigger resistance while the horizontal strut has the least role in OoP resistance. The OoP resistance due to diagonal struts is highest among the struts when the infill wall is not damaged previously by IP load. But if the infilled frame is subjected to IP drift before the application of the OoP load, the OoP resistance of the diagonal struts is affected. As the IP drift increase, the damage in the diagonal struts is higher and the OoP resistance offered by the struts decreases. Due to the orientation of the horizontal and vertical struts, they have no role

in the IP resistance. Therefore, OoP resistances of both horizontal and vertical struts are unaffected and remain the same after the IP analysis.

The contributions of the individual struts in the OoP resistance for different experiments are shown in Figs 3.19 - 3.24. The figure shows that the OoP resistance of the vertical strut can be higher than the diagonal struts for the IP damaged case.

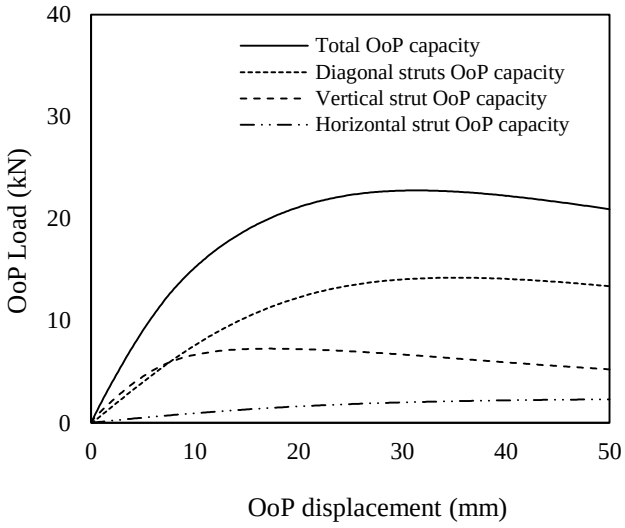

Figure 3.19 Role of horizontal, vertical and diagonal struts in resisting the OoP load (ref. to specimen #3 tested by Angel 1994)

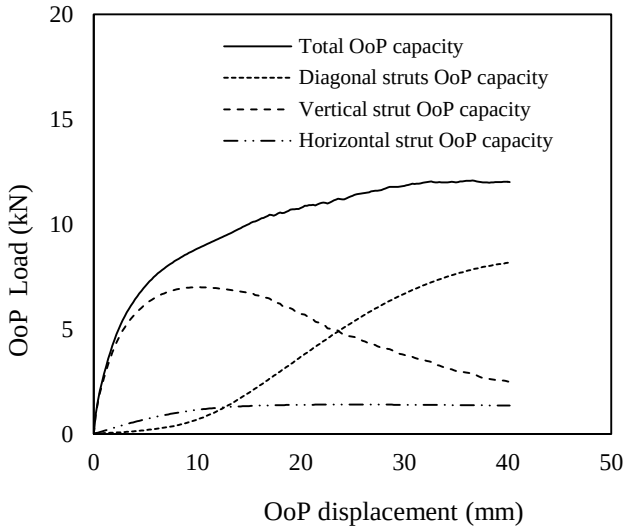

Figure 3.20 Role of horizontal, vertical and diagonal struts in resisting the OoP load (ref. to specimen #6 tested by Calvi and Bolognini 2001)

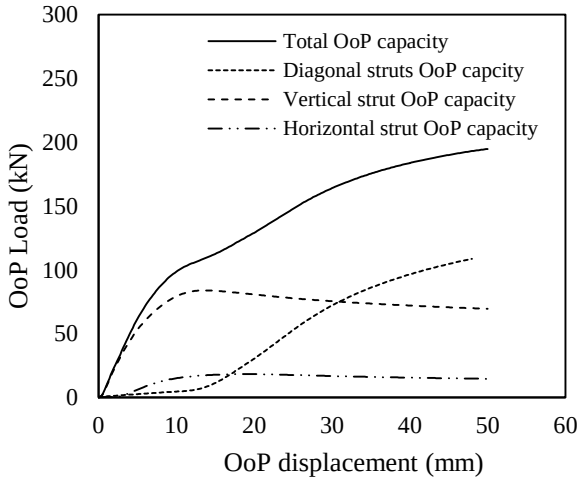

Figure 3.21 Role of horizontal, vertical and diagonal struts in resisting the OoP load (ref. to specimen tested by Da Porto et al. 2013)

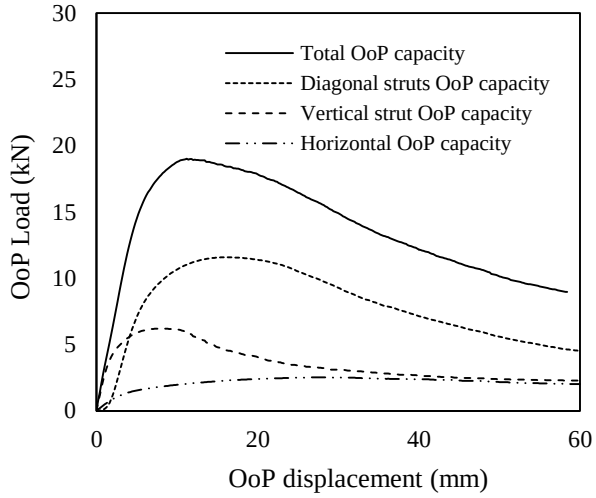

Figure 3.22 Role of horizontal, vertical and diagonal struts in resisting the OoP load (ref. to specimen #1 (80 mm) tested by Ricci et al. (2018a)

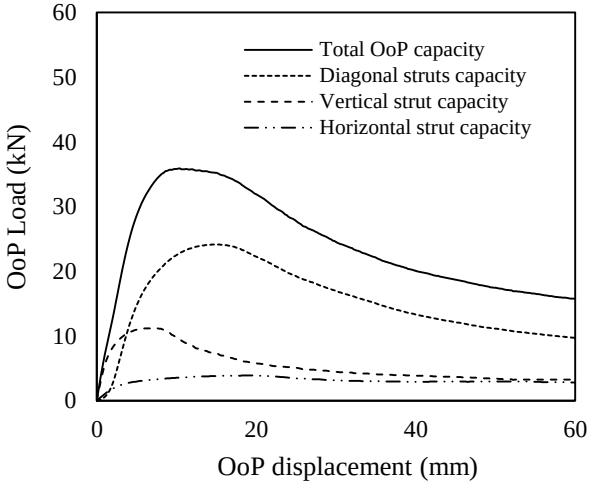

Figure 3.23 Role of horizontal, vertical and diagonal struts in resisting the OoP load (ref. to specimen #2 (120 mm) tested by Ricci et al. 2018b)

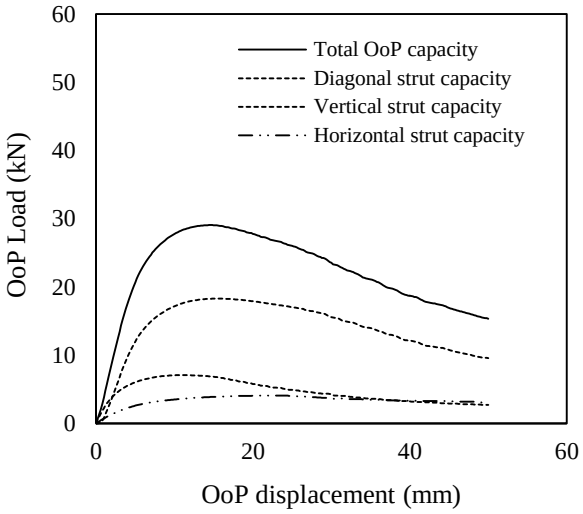

Figure 3.24 Role of horizontal, vertical and diagonal struts in resisting the OoP load (ref. to specimen tested by De Risi et al. 2019b)

3.4 Correlation between stress-strain parameters and mechanical properties of masonry

Stress-strain parameters (f_{mo}, f_{mu}, ε_{mo} and ε_{mu}) are key elements when using the fibre-section based model. These parameters define the mechanical property of the struts' fibers and in this model, they are used to describe the compressive behaviour of the struts. To make the model standard and simple and univocal to use in practical applications, these parameters need to be selected by a definitive procedure. To derive these parameters, the use of actual mechanical characteristics of masonry is an effective and simple strategy. In this section, the correlation function that connects the properties of the masonry and the stress-strain parameters is proposed.

In the beginning, for the case of Angel's (1994) experiment, numerical simulations were performed assigning the stress-strain parameters empirically. The simulations were performed by assigning the mechanical parameters (f_{mo}, f_{mu}, ε_{mo} and ε_{mu}) in order to obtain responses similar to the experimental results, in both IP and OoP directions. The main objective was to improve the response compared to the earlier model by Di Trapani et al. (2018). Therefore, the parameters were fixed in such a way that the minimum offset between the numerical and experimental response was achieved.

Afterward, for the case of infill specimens by Calvi and Bolognini (2001), Da Porto et al. (2013), Ricci et al. (2018a, 2018b) and De Risi et al. (2019b), the simulations were repeated following the similar approach i.e. the stress-strain parameters in each case was selected randomly to achieve a good correspondence between the experimental and numerical responses. It was possible to obtain very matching results. However, the challenge was to select the parameters with a standard procedure. In order to develop the correlation function, first, the best possible values of these parameters were found, thanks to multiple analyses and the quick functioning of OpenSees. While selecting the parameters, a due focus was also given to the correlation between the required parameters and the mechanical properties of a masonry infill.

After multiple analyses, at one point, a correlation was established between the effective parameters and the mechanical properties of masonries. The final stress-strain parameters were correlated with the product of the compressive strength f_m and the elastic modulus E_m of the masonry infill. These two parameters are not the only ones influencing the infill's response (as discussed in Chapter 2) but the analyses proved them to be the ones having the most influence. The best-fitting curves that give the required parameters are plotted in Fig 3.25 and are represented by the following equations (Eq. 3.11 - Eq. 3.14).

$$f_{mo} = \begin{cases} 0.61 + 0.0001 f_m E_m - 10^{-9} (f_m E_m)^2, & f_m E_m < 40000 \\ 3, & f_m E_m > 40000 \end{cases} \quad (3.11)$$

$$\varepsilon_{mo} = 4 \times 10^{-8} f_m E_m + 0.00039 \quad (3.12)$$

$$f_{mu} = 0.6 \times f_{mo} \quad (3.13)$$

$$\varepsilon_{mu} = \begin{cases} 0.0047 + 4 \times 10^{-7} f_m E_m - 3 \times 10^{-12} (f_m E_m)^2, & f_m E_m < 48000 \\ 0.017, & f_m E_m > 48000 \end{cases} \quad (3.14)$$

The ultimate strain calculated according to Eq. (3.14) has a value close to $10 \times \varepsilon_{mo}$. Therefore, ε_{mu} can be defined simply by the following equation.

$$\varepsilon_{mu} = 10 \times \varepsilon_{mo} \quad (3.15)$$

Using the above equations, the stress-strain parameters required for the struts can be calculated if the properties of masonry (f_m and E_m) are known. While calculating, the mean values of the properties are to be used following the Eqs. 3.16 and 3.17.

$$f_m = \sqrt{f_{mh} \times f_{mv}} \quad (3.16)$$

$$E_m = \sqrt{E_{mh} \times E_{mv}} \quad (3.17)$$

where f_{mv} and f_{mh} represent the compressive strength of masonry in the vertical and horizontal directions, E_{mv} and E_{mh} are the elastic modulus of masonry in the vertical and horizontal directions respectively.

This provision (Eqs. 3.16 and 3.17) facilitates the proposed model to consider the orthotropic nature of masonry. This is a very important consideration for infill walls with hollow masonry units. For hollow units, these mechanical properties can be very different in the direction parallel and perpendicular to the holes in the unit. Design engineers often face difficulty in considering the strength of the masonry in such conditions. For infill walls with solid masonry units, the properties can be considered equal in both vertical and horizontal directions if the data is unavailable.

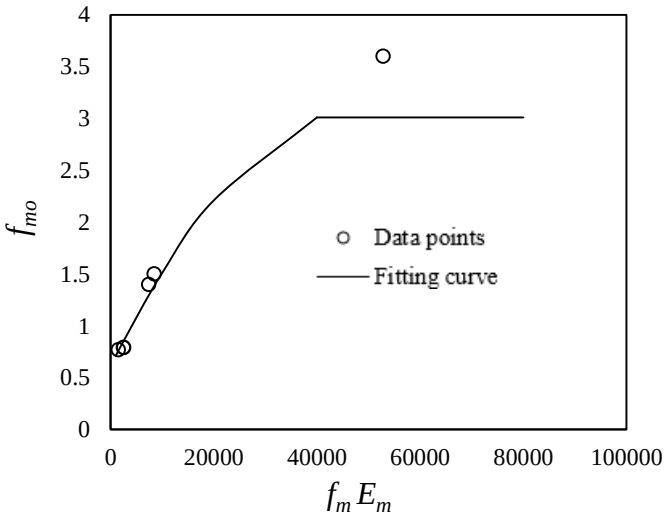

(a)

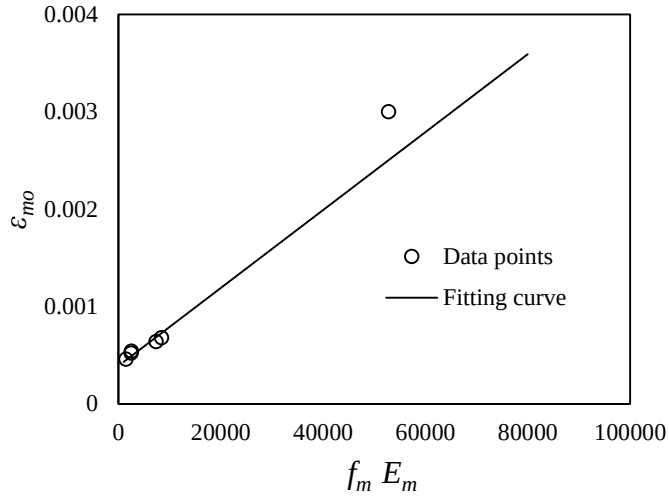

(b)

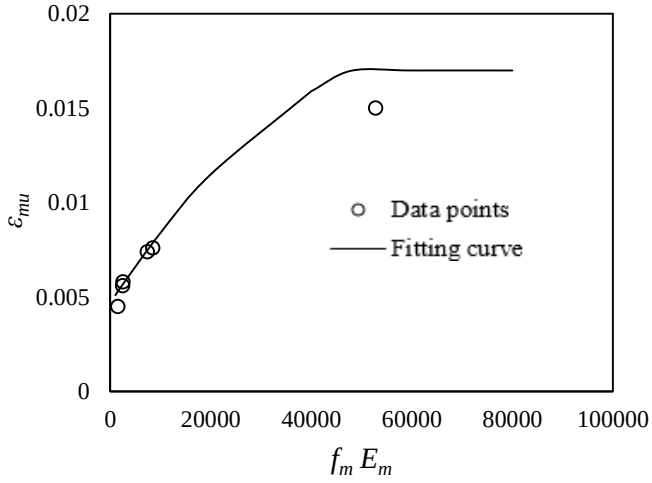

(c)

Figure 3.25 Plot between the stress-strain parameters and the product of f_m and E_m : a) f_{mo} , b) ε_{mo} , c) ε_{mu}

It is to be noted that the above equations are established by fitting a not very large number of data. Especially for the higher values of $f_m E_m$ the data points are not sufficient due to the unavailability of experimental results. The values of f_{mo} and ε_{mu} in the higher range of $f_m E_m$ proposed to be constant after observing the numerical results for Angel's (1994) specimens. It was found that a variation in the value of these two parameters does not influence the numerical response significantly. The value of ε_{mu} can also be defined as 10 times the value of ε_{mo} even for the constant part (Fig 3.25c) as stated earlier. The result will not be affected much. Nevertheless, these equations can be further updated with the availability of more experimental data.

From the above discussion, it is evident that the mechanical characterization of the equivalent struts in the proposed approach is simple and shows the possibility of using it for practical applications. The infill model here proposed can be used with any structural analysis software that provides the possibility of fibre modelling of beam element cross-section. This possibility is now more and more diffused and available in commercial software.

Further, the proposed model maintains the simplicity typical of the replacement of two-dimensional elements (infill wall) into two or more one-dimensional elements (equivalent struts) for practical cases, and in the reduction of computational efforts. In the case of a single infilled frame like those analyzed during the validation process and acted by the loading patterns as discussed before, the analysis time for this model is very low, unlike the case of the micro-modelling approach, like that proposed by Cavaleri et al (2019), which requires several hours for each analysis under the same loading patterns.

3.5 Further remarks on the proposed model

In the proposed macro-model, the OoP resistance of any strut is proportional to the compressive strength of masonry and the strut width. Further, OoP resistance reduces when the slenderness ratio of the strut increases. This makes the OoP resistance of the diagonal, vertical, and horizontal struts different. More specifically, diagonal struts have the biggest role while the horizontal strut has the least contribution to OoP resistance. The scenario can be different for an IP-damaged infill wall because the OoP resistance of diagonal struts decreases gradually with increasing levels of IP damage as shown before.

In the validation process, the thicknesses of the infill specimens in the selected experiments were small in most of the cases. In the case of low thickness infill walls, the OoP strength is small and, although the role of horizontal and vertical struts in the OoP strength is comparatively lower than that of the diagonal struts, they were necessary to derive the full OoP strength as proved by a comparison with experimental tests. On the other hand, as the thickness of the infill wall becomes big, OoP strength provided by horizontal and vertical struts also increases. Particularly, OoP resistance due to vertical strut also becomes significant in such cases, and numerically obtained OoP strength may be overestimated. It was confirmed after the comparison with some available experimental results on thick infill wall specimens (e.g. Flanagan and Bennett 1999b, Hak et al. 2014) as shown in the figure below.

The easiest way to address this condition is to eliminate the vertical strut from the model, as this strut (like the horizontal one) contributes only to OoP resistance and not to the IP resistance of infilled frames. Figs 3.26 & 3.27 show the numerical response obtained by using the macro-element model for such cases, with and without the keeping vertical strut (related experimental

data are in Table 3.6 and the geometrical and mechanical parameters for the struts identified following the procedure described above are provided in Table 3.7).

Table 3.6 Geometrical and mechanical properties of the infill wall obtained from the experiments

Experiments	l mm	h mm	t mm	f_{mh} MPa	f_{mv} MPa	E_{mh} MPa	E_{mv} MPa
Flanagan and Bennett (1999b)	2240	2240	200	3	5.6	2300	5300
Hak et al. (2014)	4222	2950	350	1.08	4.64	499	5299

Table 3.7 Geometrical and mechanical properties of struts used for numerical simulations

Experiments	$\overline{w}_d$ mm	$\overline{w}_v$ mm	$\overline{w}_h$ mm	$\overline{t}$ mm	f_{mo}	f_{mu}	ε_{mo}	ε_{mu}
Flanagan and Bennett (1999b)	490	310	310	446	1.84	1.10	0.00096	0.0096
Hak et al. (2014)	791	428	299	816	0.96	0.58	0.00054	0.0054

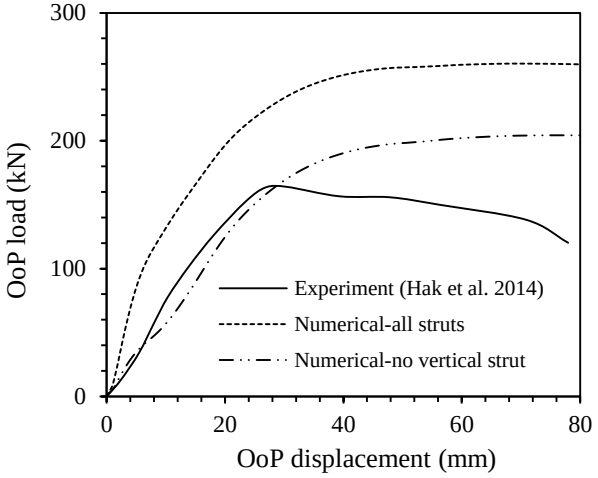

(a)

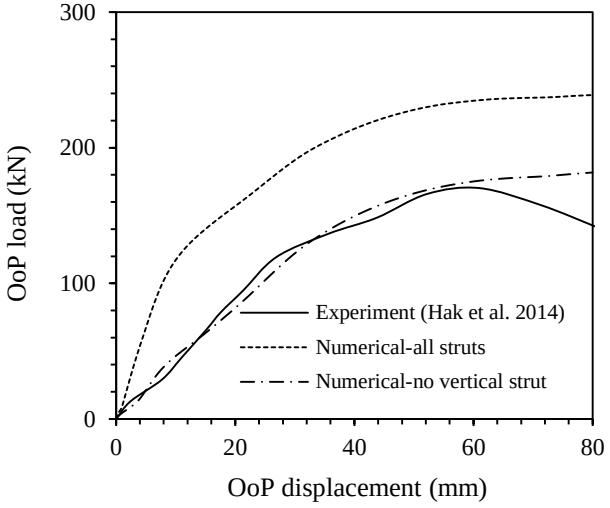

(b)

Figure 3.26 OoP response with and without vertical strut for Hak et al. (2014) infill wall specimens of thickness 350 mm: (a) OoP load after 1% of IP drift; (b) OoP load after 1.5% of IP drift

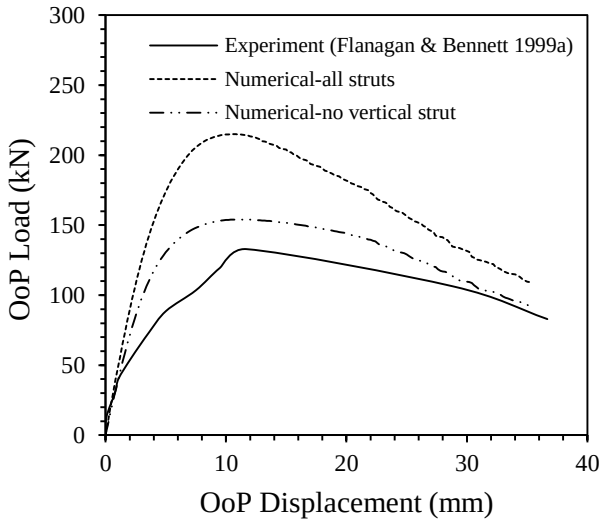

Figure 3.27 OoP response with and without the vertical strut for Flanagan and Bennett (1999b) infill wall specimen 18 of thickness 200 mm loaded only in OoP

Although the model is simple and has the potential to calculate the OoP capacity for any type of URM infill wall, the proposed model has the following limitations:

a. The model is applicable for a single-leaf infill wall of any thickness: it is not suitable to determine the OoP capacity of an infill wall with double leaves having a gap in-between.
b. The model is validated for taking into account the effect of prior IP damage on OoP behaviour but not yet vice versa due to a lack of a suitable experiment to simulate. Nevertheless, the model is able to take into account the effect of prior OoP damage on the IP capacity of the infill wall.
c. The effectiveness of the model for the analysis of infilled steel frames needs to be verified further.

d. The model is proposed for the case of URM infills walls. It cannot be applied to any infill wall having an interior RC tie beam or column. Further work is necessary to see how the model can be used when additional elements like the bond beam or reinforcement are present in the infill wall.
e. The proposed model is validated with infill walls without openings. For the case of opening, a necessary reduction of the OoP capacity is to be done as discussed in chapter 2.

4 PARAMETRIC ANALYSIS AND PROPOSAL OF PREDICTION EQUATIONS

In the previous chapters, different parameters that have a direct influence on the OoP capacity of the infill wall were discussed. It was identified that the OoP strength of infill walls is related to the development of an arching action which depends heavily on the compressive strength of masonry and the slenderness ratio of infill walls. Likewise, separately, different available analytical capacity models which can be used to estimate the OoP capacity of the infill wall were investigated. The results from the capacity models were scattered, one giving better results than the others when compared with the available experimental results (see chapter 2). In this chapter, the proposed macro-model (see chapter 3) has been applied to understand the effect of more important parameters that govern the OoP capacity of the infill wall.

As already known, several parameters have to be considered to describe the OoP capacity of infill walls. However, the influence of each parameter is not easy to be defined. Although parameters like the compressive strength of masonry and the slenderness ratio of infill walls are more important, there is great uncertainty about them. For example, infill walls made with hollow masonry units usually have differences in their mechanical

properties in horizontal and vertical directions. Even in many experimental tests, property in only one direction is reported. Likewise, the variation in the thickness of the infill wall is huge which changes the slenderness ratio and affects the arching action significantly. Additionally, the aspect ratio of the wall is also different depending upon the use and function of the infill wall. The increase in the aspect ratio increases the slenderness ratio in the horizontal direction and consequently decreases the OoP capacity (refer to chapter 2 for details).

To analyse the effect of each parameter in detail, rigorous experimental campaigns have to be achieved which is costly and time-consuming. At the moment, this cannot be done. The main difficulty is the lack of experimental tests on a wide range of geometrical and mechanical properties of masonry infill walls (discussed in chapter 2). In this context, a systematic study of the influence of the key parameters is possible only through numerical investigations.

In the past, FE-based micro-models have been used partially to deepen the understanding of the OoP behaviour of URM infill walls and the aspect of the IP-OoP interaction (Agnihotri et al. 2013; Cavaleri et al. 2019; Liberatore et al. 2020; Wang et al. 2020). For example, Agnihotri et al. (2013) investigated the influence of slenderness ratio and aspect ratio on OoP capacity. Moreover, the authors also investigated the influence of slenderness ratio and aspect ratio on strength reduction due to the previous IP damage. They concluded that the variation in the rate of strength decay is higher due to a change in the aspect ratio rather than the change in the slenderness ratio. According to the authors, infill walls with a higher aspect ratio can have a higher strength decay rate with increasing IP damage. Additionally, the authors proposed a high reduction of OoP strength even at a small IP drift (e.g. more than 50% strength reduction due to an IP drift of 0.15% for a wall with

a slenderness ratio of 16) which is not convincing when compared to experimental results.

Likewise, Wang et al. (2020) concluded that the reduction of OoP strength due to IP damage is influenced by slenderness ratio, aspect ratio, and additionally by masonry strength which was not previously considered by other researchers. The strength reduction was found lower for masonry infills with higher compressive strength but the stiffness decay was not affected by the masonry strength. According to the authors, infill walls with a higher slenderness ratio are affected by a higher reduction of strength/stiffness at the same level of IP damage. Additionally, the rate of strength decay was lower for masonry infills with a higher aspect ratio in contrast to the idea of Agnihotri et al. (2013). Therefore, this aspect needs further investigation.

In this chapter, with the aim to understand more about the parameters and their influence, the proposed macro-element model (described in chapter 3) was used and, a parametric analysis was performed to investigate the OoP strength of infill walls bounded closely by frames on all sides. The reason is simple, the model can take into account the variation in the geometrical and mechanical properties of masonry easily, and at the same time, and the model is much faster in computation compared to micro-models which are normally used when detailed parametric investigation like this has to be carried out (in all examples discussed above, micro-models were used). Different lengths, heights, and thicknesses of infill walls were considered along with variations in the mechanical properties of masonry. OoP capacity was determined with or without considering the IP damage. To consider the IP damage, OoP load was applied after the application of IP load. Two loads were not applied simultaneously because the model is found to be reliable with respect to the available tests characterized by a sequential application of IP and OoP loads.

The details of the parameters considered in this study are discussed in the next section.

4.1 Ranges for the parameters investigated

For the parametric analysis, three different heights of infill walls were considered i.e. 2400 mm, 2600 mm, and 2800 mm. For each infill wall height, five different aspect ratios were assumed i.e. 1.0, 1.25, 1.5, 1.75, and 2. To vary the aspect ratio, the length of the infill wall was changed by keeping the height constant for each height of the infill considered. The thicknesses of infill walls were varied from 80 mm to 300 mm (with an increment of 20 mm) thus making a big variation in the slenderness ratios (i.e. 8 to 35). It has to be noted that different thicknesses of infill walls considered in this study may not correspond to the typical values in practical applications. Nevertheless, different ranges were taken to understand the effect of the slenderness ratio more precisely through numerical analysis.

Similarly, the mechanical characteristics of the masonry were also varied. As the definition of the struts in the proposed model depends upon the two properties (compressive strength and elastic modulus), these properties were taken in a suitable range. The equivalent compressive strength (defined by Eq. 3.16) was taken in the range from 1 to 6 MPa (in the step of 0.5 MPa) and the elastic modulus was assumed as 1000 times the compressive strength of masonry, as shown in Table 4.1.

Additionally, the stiffness of the bounding frames was varied by changing the dimension of the columns. Different sizes of beams and columns were taken as shown in Table 4.1. The investigated frames were representative of framed structures complying with the seismic requirements of the contemporary building design codes.

Table 4.1 Parameters considered for numerical modelling

Frame measures		Concrete		IP drift	Infill wall measures			Masonry	
Column size (width×depth) mm×mm	Beam size mm×mm	f_c MPa	E_c MPa	IDR %	height h mm	Aspect ratio l/h	thickness t mm	f_m MPa	E_m MPa
300 ×300, 450×300, 600×300, 750×300, 300×450, 300×600, 300×750	300×400	30	27500	0 to 2 step (0.25)	2400 2600 2800	1, 1.25, 1.5, 1.75, 2	80 – 300 step (20)	1 to 6 step (0.5)	1000 $\times f_m$
Reinforcement content in columns	2% of the cross-section area with minimum 3 rebars in the shorter side and uniformly distributed along the longer side -Transverse ties with 8 mm rebars @ 100 mm c/c							Yield strength of rebar = 500 MPa	
Reinforcement content in beams	1% of the cross-section area with 3 rebars at the top and bottom -Transverse ties with 8 mm rebars @ 100 mm c/c								

Two different cases of infill walls were considered: i) IP-damaged, ii) IP-undamaged. The IP drift was taken as a measure of the IP damage and was defined by different values of inter-storey drift ratio (IDR). The range of IDR was taken from 0 to 2% (step of 0.25%). 0% IDR indicates the IP-undamaged case. To cause the IP damage, a single cycle of IP load was applied to each masonry infilled frame before the application of the OoP load. The details of the different parameters considered in the study are summarised in Table 4.1.

4.2 Effect of infill wall thickness and masonry strength in the OoP capacity

The OoP capacity of infill walls was highly influenced by the variation of both the infill thickness and the strength of masonry. Upon increasing the thickness of the infill wall from 100 to 300 mm, the OoP capacity increased by almost 8 folds, independent of the masonry compressive strength f_m. In other words, as the slenderness ratio (h/t) becomes lower, the OoP capacity

becomes higher. Likewise, for the same thickness of the infill wall, the OoP capacity was higher when the masonry was strong i.e. when the compressive strength of masonry was higher. The OoP capacity increased by almost 5 times higher when masonry strength was increased from 1 MPa to 6 MPa for any infill thickness considered.

In Fig 4.1a-c, the numerical outputs for some specific thicknesses of infill walls at specific values of masonry strengths are shown. These results shown in the figure are for the case of aspect ratio l/h equal to 1. The curves in the figures clearly highlight the effect of masonry strength and thickness of infill walls. These figures also indicate that with the increase in the infill surface area (i.e. increase in height and length of infill walls), the OoP capacity decreases. This is due to the increase in the slenderness ratio in both the vertical and the horizontal directions. From this discussion, it is also obvious that with the increase in the infill aspect ratio, OoP capacity decreases.

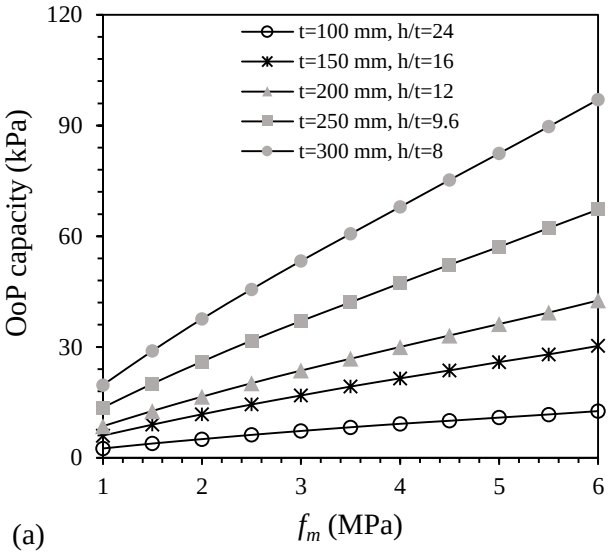

(a)

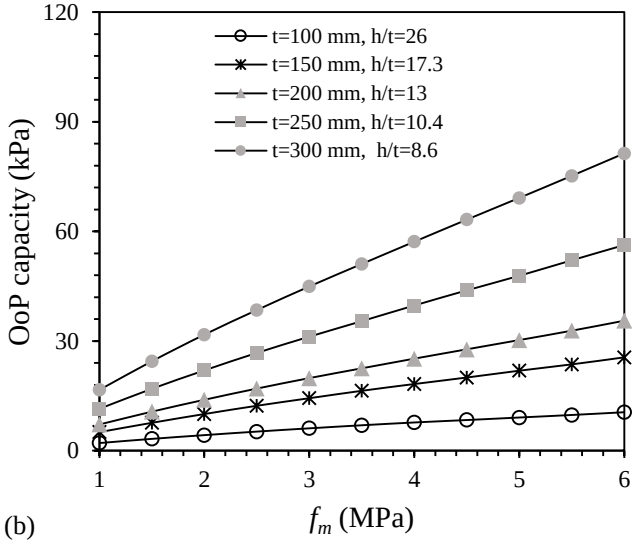

(b)

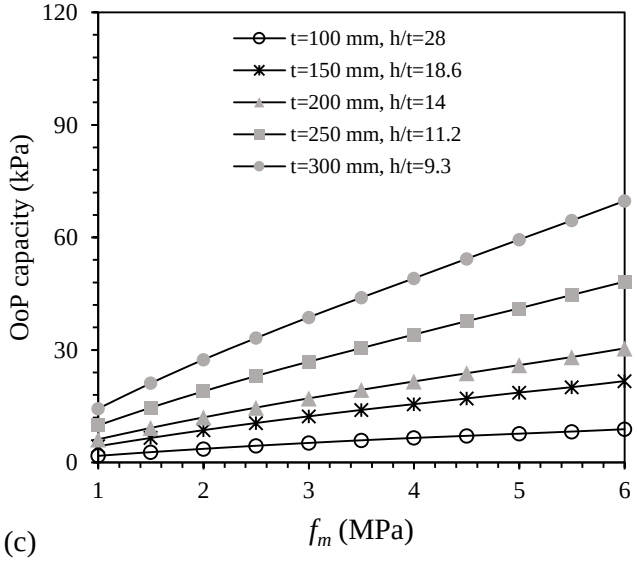

(c)

Figure 4.1 OoP capacity of infill walls depending upon masonry strength and infill wall thickness, slenderness ratio and size: a) $l = h = 2400$ mm; b) $l = h = 2600$ mm; and c) $l = h = 2800$ mm

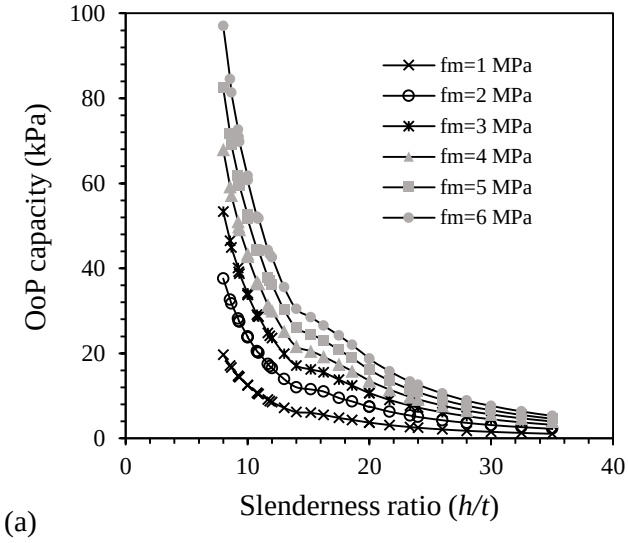

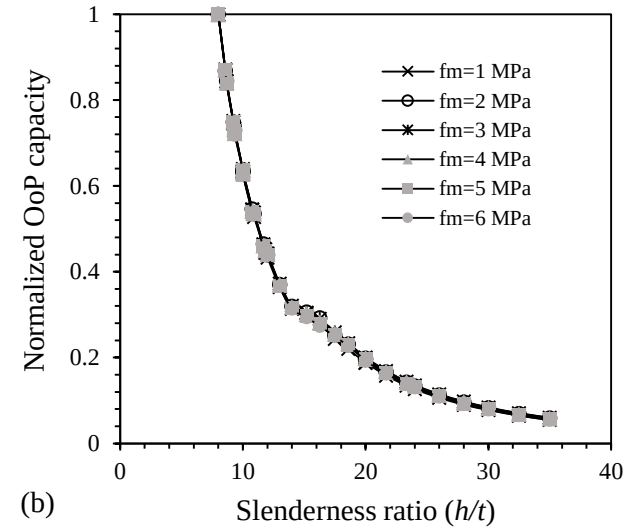

Figure 4.2 (a) OoP capacity of infill walls depending upon slenderness ratio and masonry strength; (b) OoP capacity normalized with respect to the maximum one corresponding to the minimum slenderness ratio

In Fig 4.2-a, results are plotted in terms of the slenderness ratio of infill walls. It can be observed that the OoP strength is very low when the slenderness ratio increases beyond 20 (EC8 limit is 15). The results indicate that the OoP capacity is proportional to the strength of masonry. The results are consistent with the original concept of arching provided by McDowell et al. (1956). Additionally, Fig 4.2-b highlights that the rate of reduction of OoP strength due to the increasing slenderness ratio is not influenced by the strength of masonry. For a better understanding, a 3D representation of the results is shown in Fig 4.3.

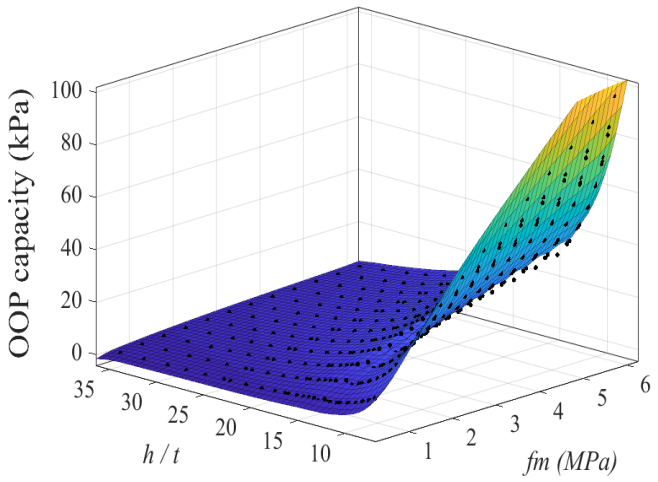

Figure 4.3 OoP capacity of infill walls versus masonry strength f_m and slenderness ratio h/t

4.3 Effect of aspect ratio in the OoP capacity

As indicated earlier, five different aspect ratios were considered and OoP capacities were evaluated using the proposed macro-model. In Figs 4.4 – 4.6, the variation of OoP capacity due to the change in the aspect ratios of

infill walls is shown for different thicknesses and strengths of masonry. The results are plotted for the case of infill walls having a height of 2600 mm. Upon increasing the aspect ratio from 1 to 1.5, the OoP capacity decreased to about 60% and, when the aspect ratio was equal to 2, the OoP capacity dropped to almost 40% on average. The trend was similar for the infill walls with other heights (i.e. 2400 mm and 2800 mm). From Figs 4.4b, 4.5b & 4.6b, it is highlighted that the reduction of the OoP strength of infill walls due to increasing aspect ratio is not influenced by the masonry strength and the thickness (or slenderness ratio) of infill walls.

For the comparison, OoP capacities at different aspect ratios for infill walls of different heights, thicknesses, and masonry strengths are included in Fig 4.7.

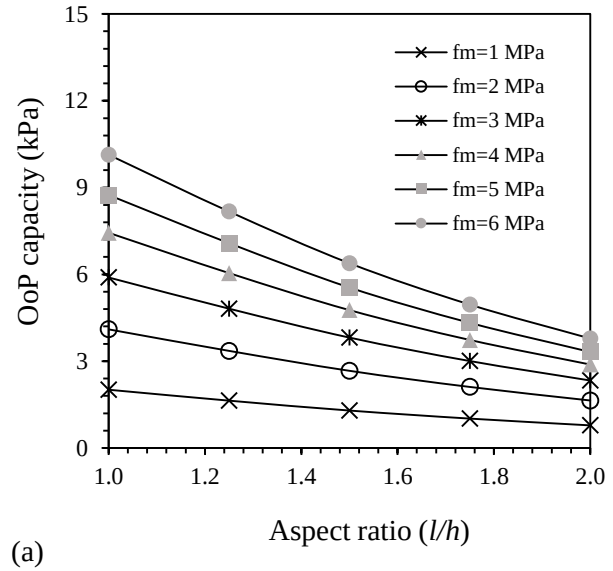

(a)

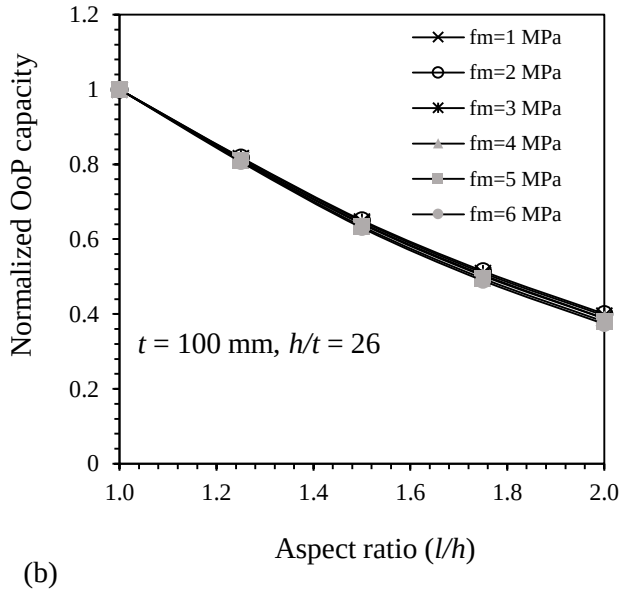

(b)

Figure 4.4 (a) OoP strength vs aspect ratio for different values of masonry strength - t = 100 mm, h = 2600 mm, h/t = 26 ; (b) OoP capacity normalized with respect to the maximum one corresponding to the minimum aspect ratio

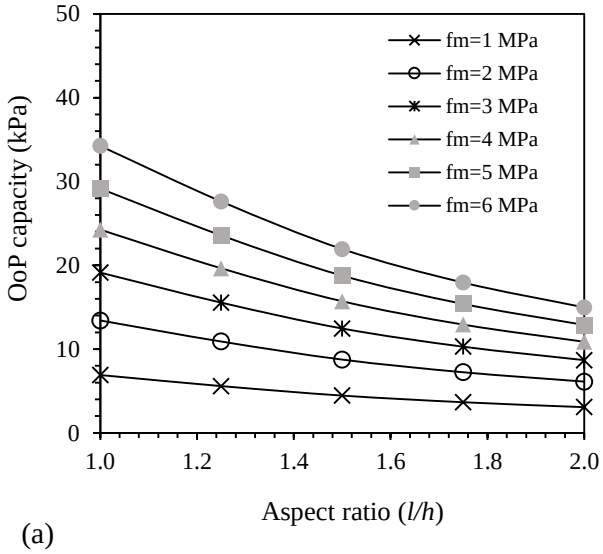

(a)

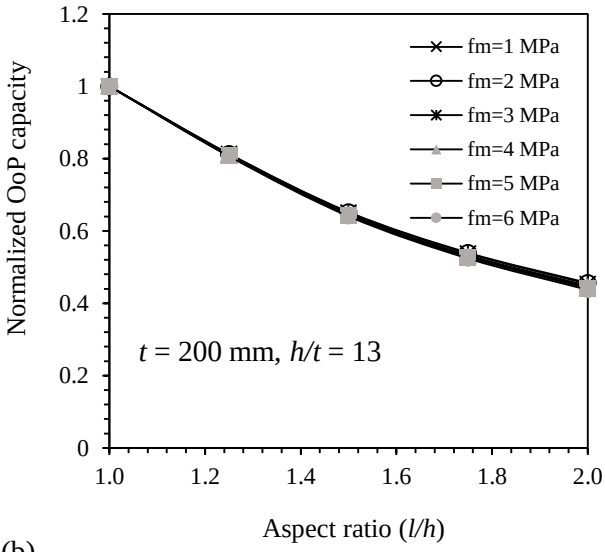

(b)

Figure 4.5 (a) OoP strength vs infill's aspect ratio for different values of masonry strength - t = 200 mm, h = 2600 mm, h/t = 13; (b) OoP capacity normalized with respect to the maximum one corresponding to the minimum aspect ratio

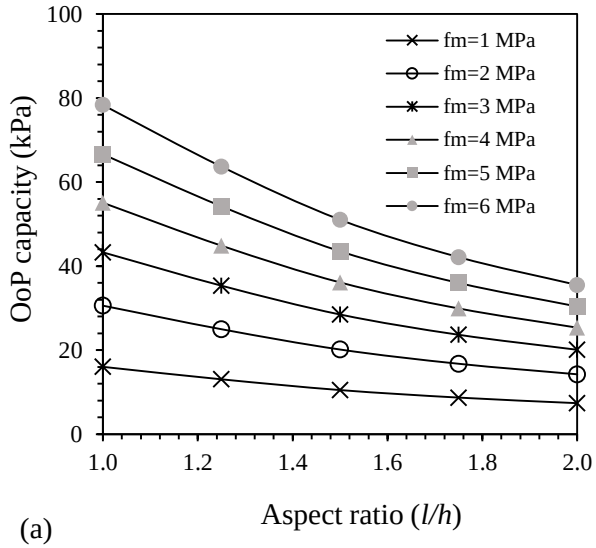

(a)

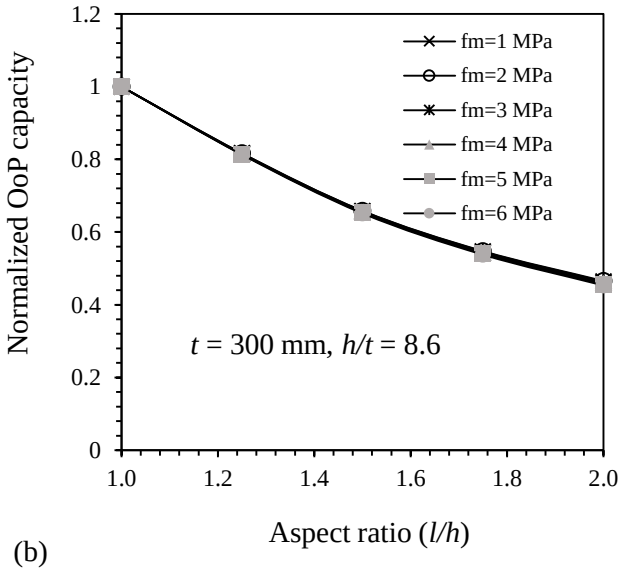

(b)

Figure 4.6 (a) OoP strength vs infill's aspect ratio - t = 300 mm, h = 2600 mm, h/t = 8.6; (b) OoP capacity normalized with respect to the maximum one corresponding to the minimum aspect ratio

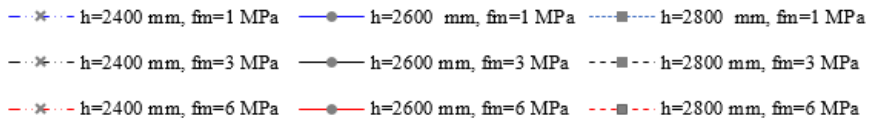
h=2400 mm, fm=1 MPa
h=2600 mm, fm=1 MPa
h=2800 mm, fm=1 MPa
h=2400 mm, fm=3 MPa
h=2600 mm, fm=3 MPa
h=2800 mm, fm=3 MPa
h=2400 mm, fm=6 MPa
h=2600 mm, fm=6 MPa
h=2800 mm, fm=6 MPa

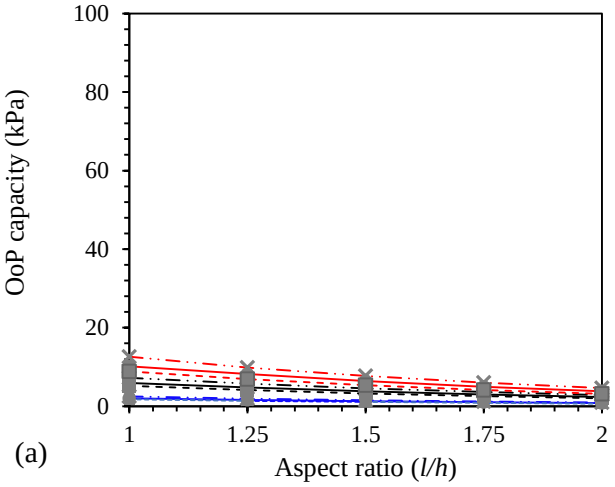
OoP capacity (kPa)
100
80
60
40
20
0
1
1.25
1.5
1.75
2
Aspect ratio (l/h)

(a)

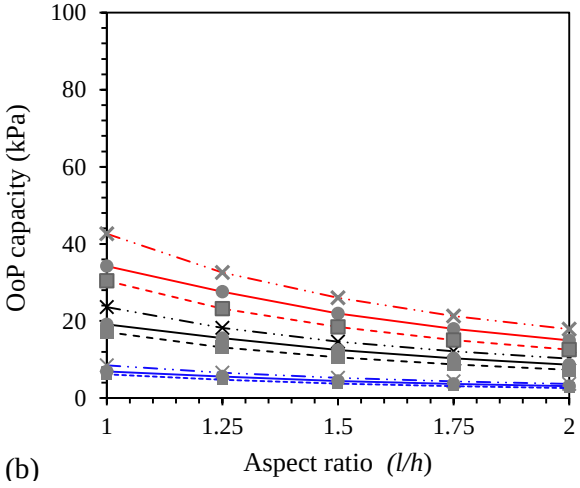
OoP capacity (kPa)
100
80
60
40
20
0
1
1.25
1.5
1.75
2
Aspect ratio (l/h)

(b)

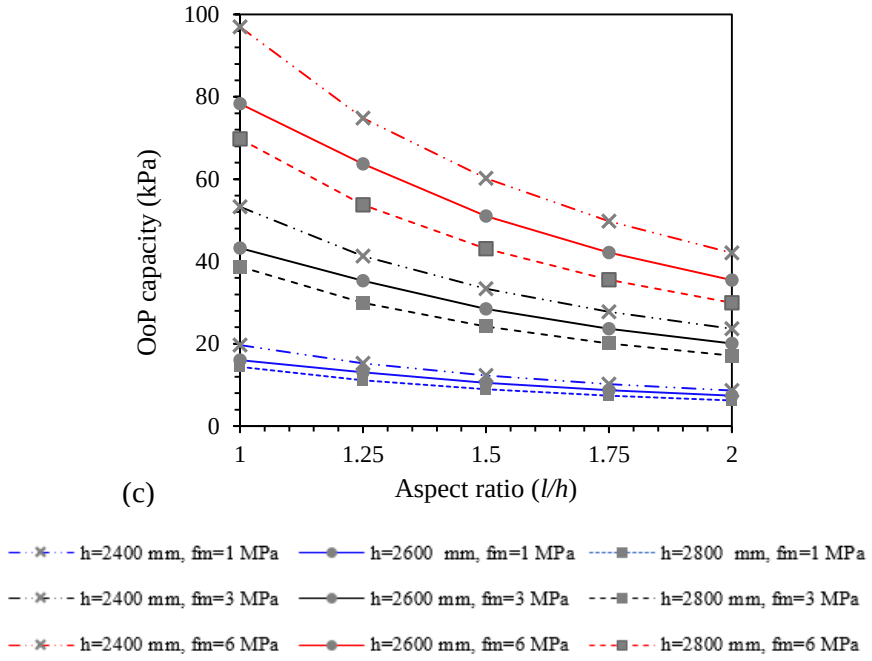

Figure 4.7 Comparative OoP strength vs infill's aspect ratio for different infill heights and strength of masonry: a) t = 100 mm; b) t = 200 mm; c) t = 300 mm

4.4 Influence of the frames' stiffness in the OoP capacity

To study the effect of columns' stiffness, the column cross-section size was increased in both directions i.e. the direction contained in the infill plane and, in the direction orthogonal to the infill plane, but not at the same time. Upon increasing the stiffness, the OoP capacity of the infill wall was slightly increased. Comparatively, the influence of the increase in frames' stiffness was higher when the dimension of columns contained in the plane of the infill wall was increased. To measure the change in the OoP capacity, the reference column size was taken as 300 mm × 300 mm (synthetically indicated as 300*300. Fig 4.8 shows the average increase (average from two directions) in

the OoP capacity of the infill walls when the columns' dimension was made higher than the reference column size.

The contribution of the columns' stiffness starts to decrease as the column's size gets bigger i.e. when the column becomes less flexible. For example, the OoP strength of the 100 mm thick infill wall with a compressive strength of 6 MPa was increased by 1.19%, 1.71%, and 2.0%, when the column size was changed from 300 mm×300 mm to 450 mm×300 mm, 600mm×300 mm and 750mm×300 mm, respectively. The relative increase in the OoP capacity, in these cases with the increase in column size, was 1.19%, 0.52%, and 0.29%, respectively. This behaviour was also similar in the infill wall of other thicknesses. Cases of 200 mm and 300 mm thick infill walls are also shown in Fig 4.8 (Fig 4.8b and Fig 4.8c respectively).

The higher stiffness of columns contributed more in the case of thicker infill walls, compared to thinner ones, and for the cases of higher masonry strengths. Nevertheless, the increase in capacity was not very significant. A similar conclusion was also made by Liberatore et al. (2020) from the results obtained from the micro-model simulations.

It is to be noted that in the current study, the flexural stiffness *EI* of the columns, corresponding to the minimum cross-sectional area 300×300 mm^2, for a concrete strength of 30 MPa and elastic modulus of 27500 MPa was 18.56×10^{12} Nmm^2. This is a minimum size of columns in the case of masonry-infilled RC frame buildings defined by many contemporary seismic codes. From the current numerical investigations, this size of the column was found sufficient for infill walls to gain full OoP strength. In this regard, Angel's (1994) and Abrams et al.'s (1996) recommendation for the stiffness of frames ($EI = 25.83\times10^{12}$ Nmm^2) appears as a sufficient requirement for the activation of the arching effect in the infill walls.

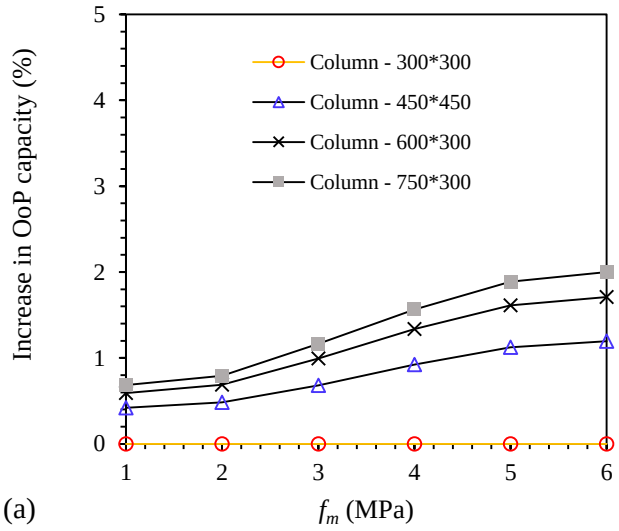
Increase in OoP capacity (%)
Column - 300*300
Column - 450*450
Column - 600*300
Column - 750*300
0
1
2
3
4
5
1
2
3
4
5
6
f_m (MPa)

(a)

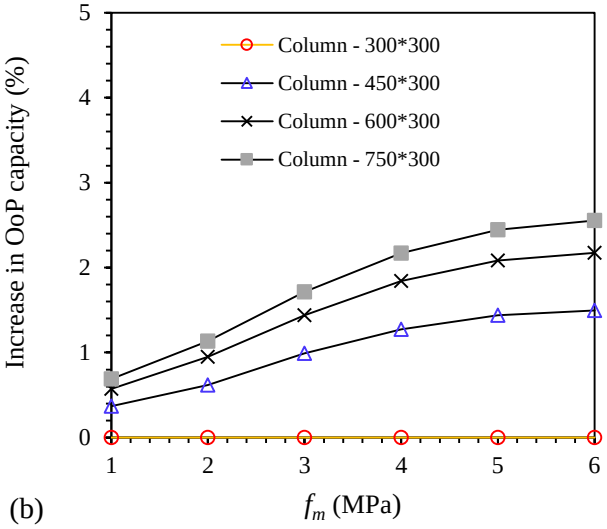
Increase in OoP capacity (%)
Column - 300*300
Column - 450*300
Column - 600*300
Column - 750*300
0
1
2
3
4
5
1
2
3
4
5
6
f_m (MPa)

(b)

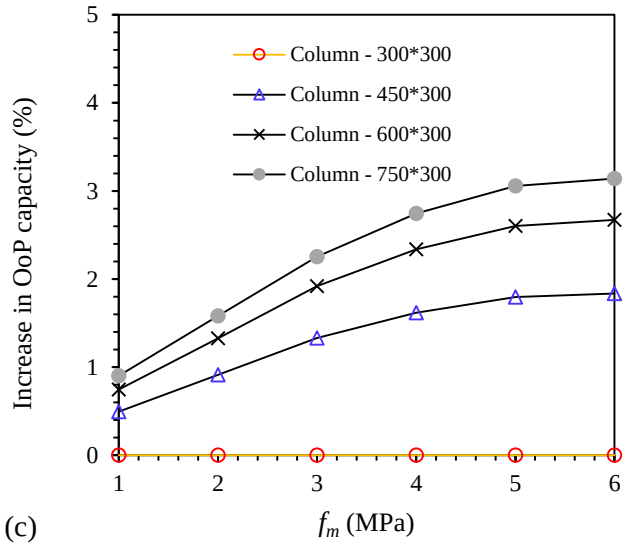

Figure 4.8 Increase in OoP capacity of infill walls according to the size of columns: a) t = 100 mm; b) t = 200 mm; c) t = 300 mm

4.5 Decay of OoP strength and stiffness

The numerical results showed that the reduction of OoP strength due to prior IP damage can vary according to the strength of masonry and the thickness (or slenderness ratio) of infill walls. This shows why the experimental results are very scattered owing to a limited number of data. The decay of OoP strength with increasing IP drift was lower for thicker and stronger masonry. Such findings were also reached by Wang et al (2020) based on their numerical study.

As an example, the particular case of an infill wall (height =2600 mm) having an aspect ratio of 1.0 is shown in Figs 4.9 - 4.12. These figures clearly show that at the same level of IP damage, strength decay is lower when the strength of masonry is higher.

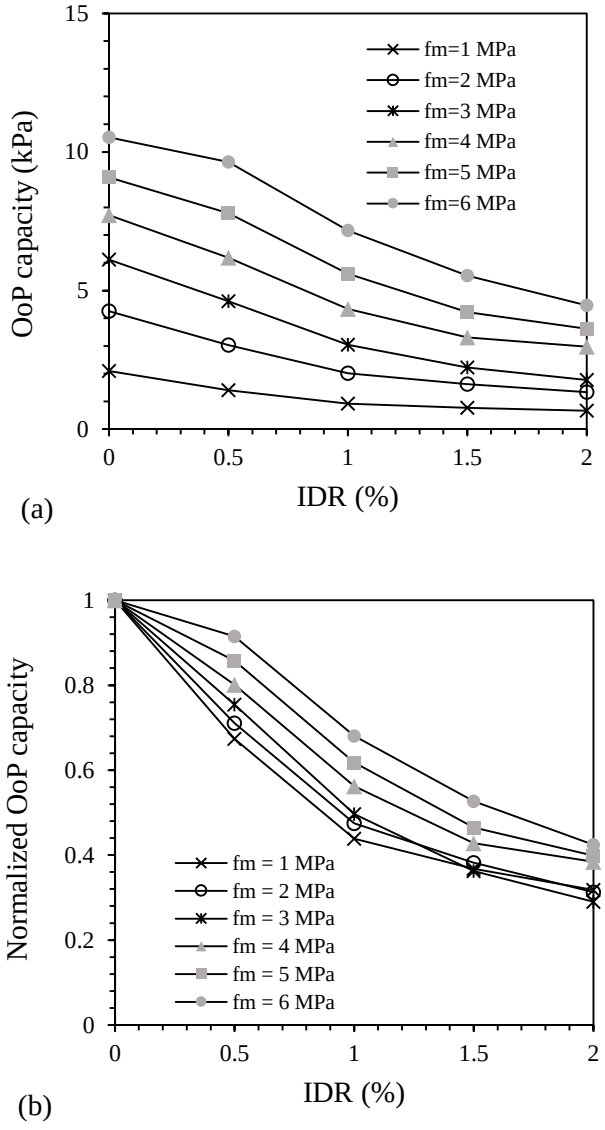

Figure 4.9 (a) Decay of OoP capacity of infill walls vs IP drift – $l = h$ = 2600 mm, t = 100 mm (h/t= 26); (b) normalized OoP capacity

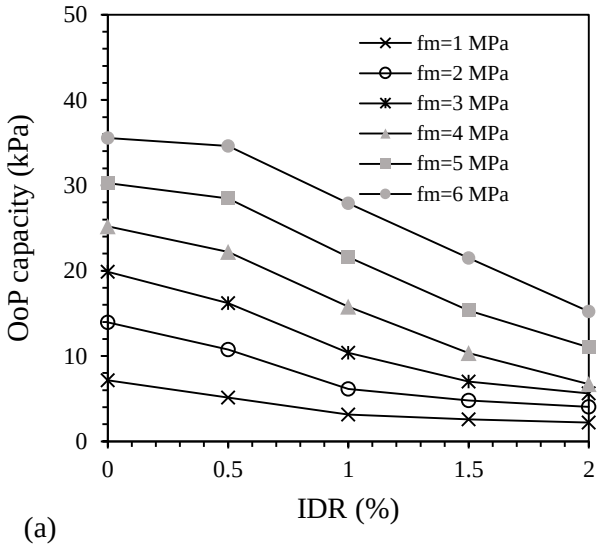

(a)

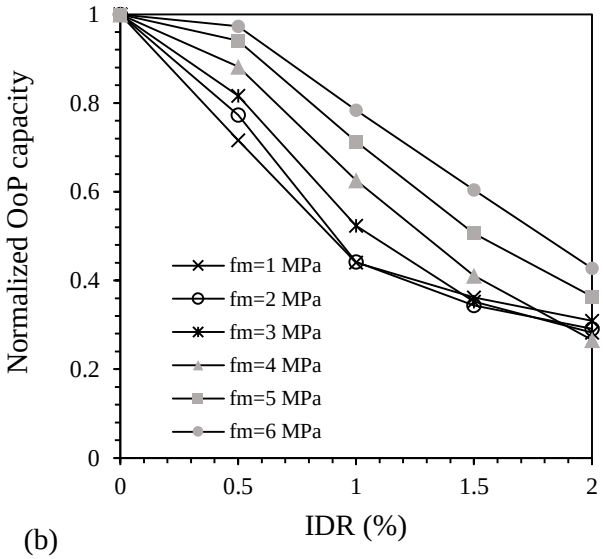

(b)

Figure 4.10 (a) Decay of OoP capacity of infill walls vs IP drift – l = h = 2600 mm, t = 200 mm (h/t = 13); (b) normalized OoP capacity

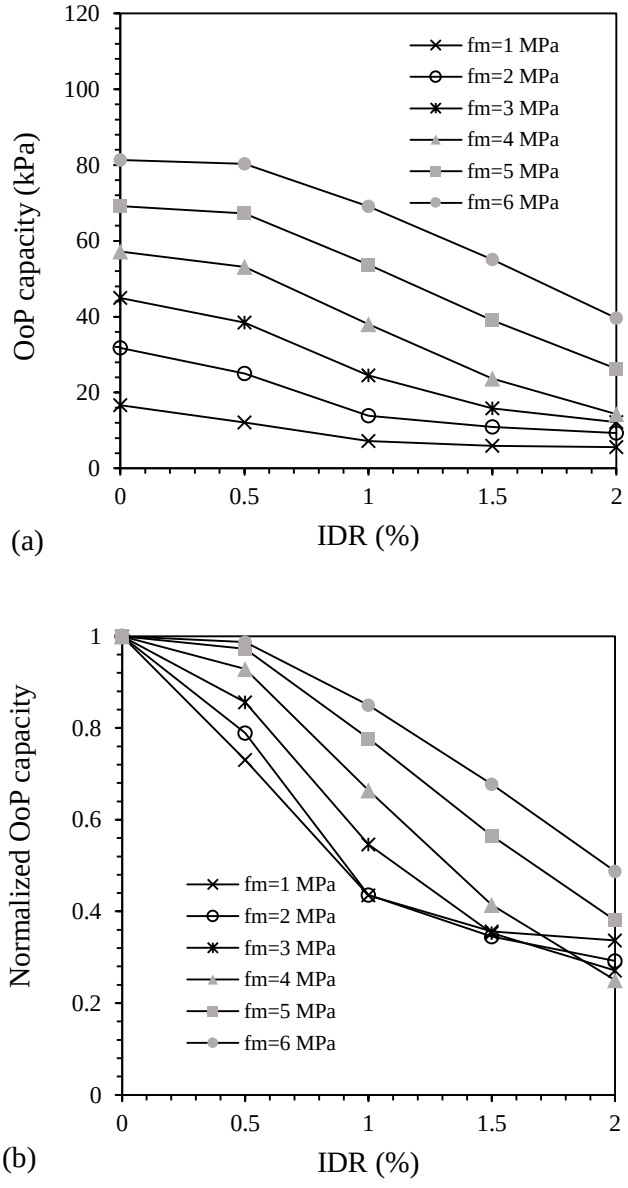

Figure 4.11 (a) Decay of OoP capacity of infill walls vs IP drift – $l = h = 2600$ mm, $t = 300$ mm ($h/t = 8.6$); (b) normalized OoP capacity

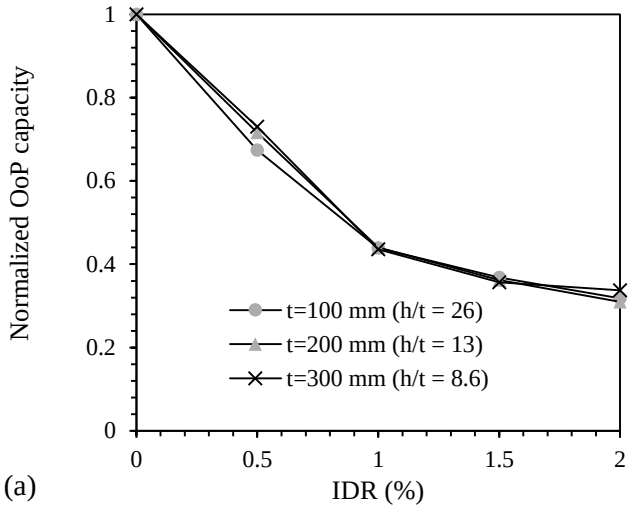
Normalized OoP capacity
IDR (%)
t=100 mm (h/t = 26)
t=200 mm (h/t = 13)
t=300 mm (h/t = 8.6)
0
0.2
0.4
0.6
0.8
1
0
0.5
1
1.5
2

(a)

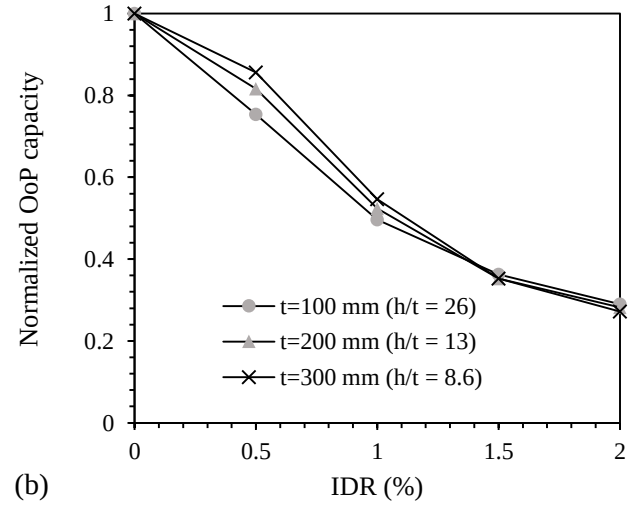
Normalized OoP capacity
IDR (%)
t=100 mm (h/t = 26)
t=200 mm (h/t = 13)
t=300 mm (h/t = 8.6)
0
0.2
0.4
0.6
0.8
1
0
0.5
1
1.5
2

(b)

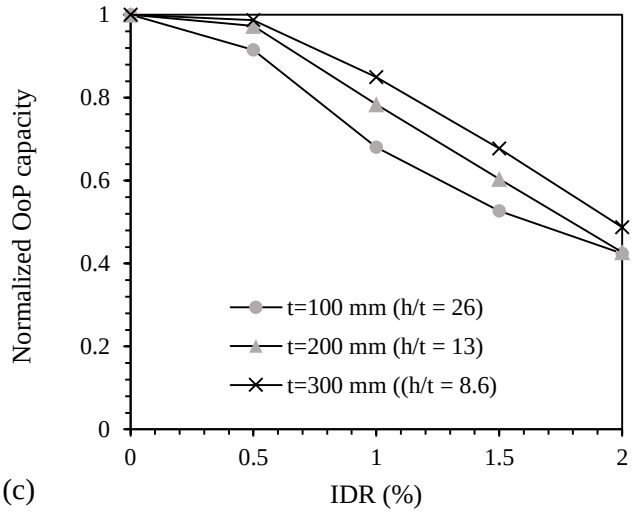

(c)

Figure 4.12 Comparison of decay of the OoP capacity of infill walls for l = h = 2600 mm according to infill thickness (or slenderness ratio): a) f_m = 1 MPa; b) f_m =3 MPa; c) f_m = 6 MPa

Specifically in Fig 4.12, the decay of OoP strength according to infill wall thickness (or h/t), at different strengths of masonry, is compared. The figure shows that the decay of OoP strength is higher when the slenderness ratio is higher.

Fig 4.12a also indicates that for a low strength of masonry, the reduction of OoP capacity is less influenced by h/t values. In summary, the strength decay of infill walls characterized by any h/t values, for an assigned level of IP damage, is lower in the case of higher strength of masonry.

In Fig 4.13, the OoP capacities of infill walls having different heights and having an aspect ratio of 1 at various levels of IP drifts are kept together for comparison.

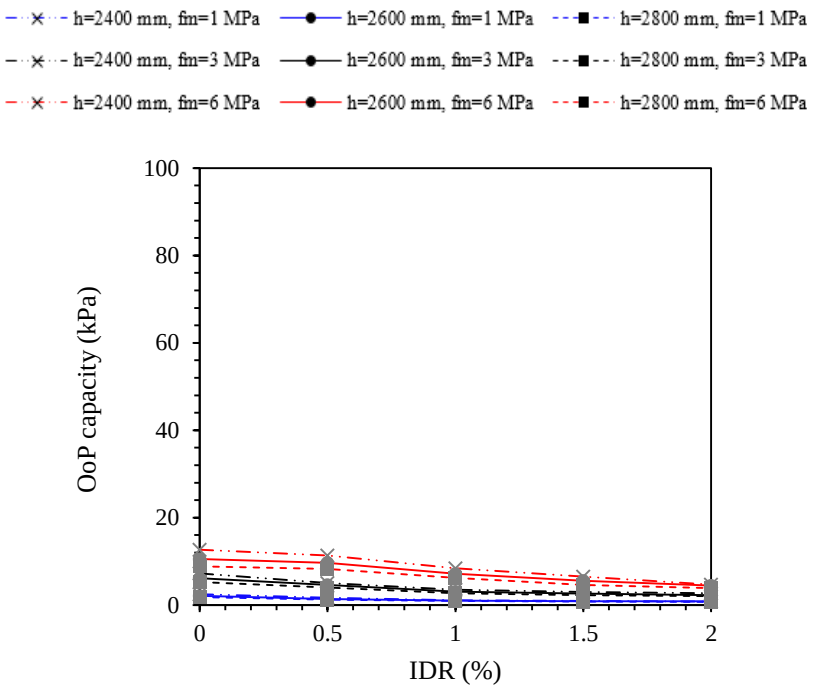
h=2400 mm, fm=1 MPa
h=2600 mm, fm=1 MPa
h=2800 mm, fm=1 MPa
h=2400 mm, fm=3 MPa
h=2600 mm, fm=3 MPa
h=2800 mm, fm=3 MPa
h=2400 mm, fm=6 MPa
h=2600 mm, fm=6 MPa
h=2800 mm, fm=6 MPa
OoP capacity (kPa)
IDR (%)
0
20
40
60
80
100
0
0.5
1
1.5
2

a)

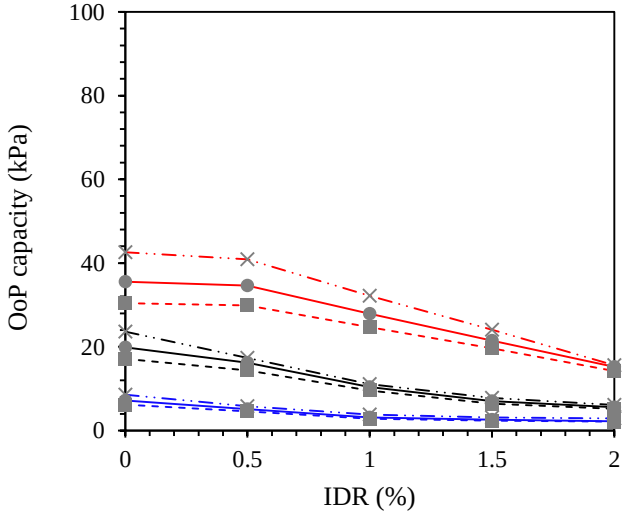
OoP capacity (kPa)
IDR (%)
0
20
40
60
80
100
0
0.5
1
1.5
2

b)

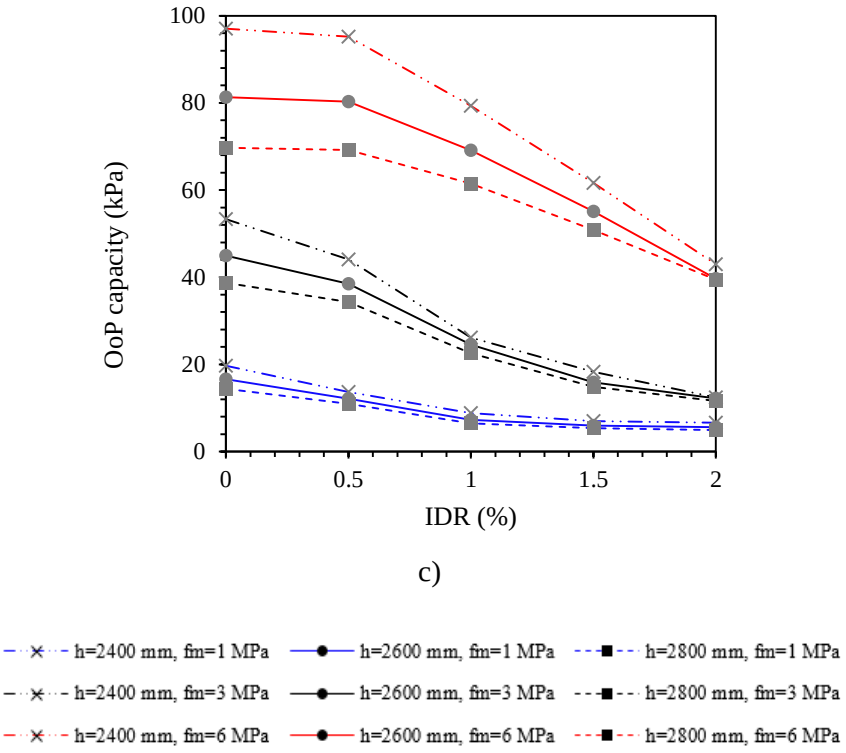

Figure 4.13 Comparative decay of OoP strength for infills of different size having aspect ratio 1: a) t = 100 mm; b) t = 200 mm; c) t = 300 mm

Upon investigating the effect of aspect ratio on strength decay due to IP damage, it was found that it has very little influence. It is different from what is shown by Wang et al. (2020), where the authors indicated a lesser reduction in the OoP strength at the same level of IP damage when the aspect ratio was higher. As an example, a particular case of infill wall (height =2600 mm) for two different values of masonry strengths (1 and 6 MPa) is shown in Figs 4.14 - 4.16. It can be observed that the increase in aspect ratio slightly accelerated the strength decay process, especially in the case of infill walls of higher slenderness (compare Fig 4.14b and Fig 4.15b) but the difference in the

decay rate was negligible when the slenderness ratio was smaller (Fig 4.15b & Fig 4.16b).

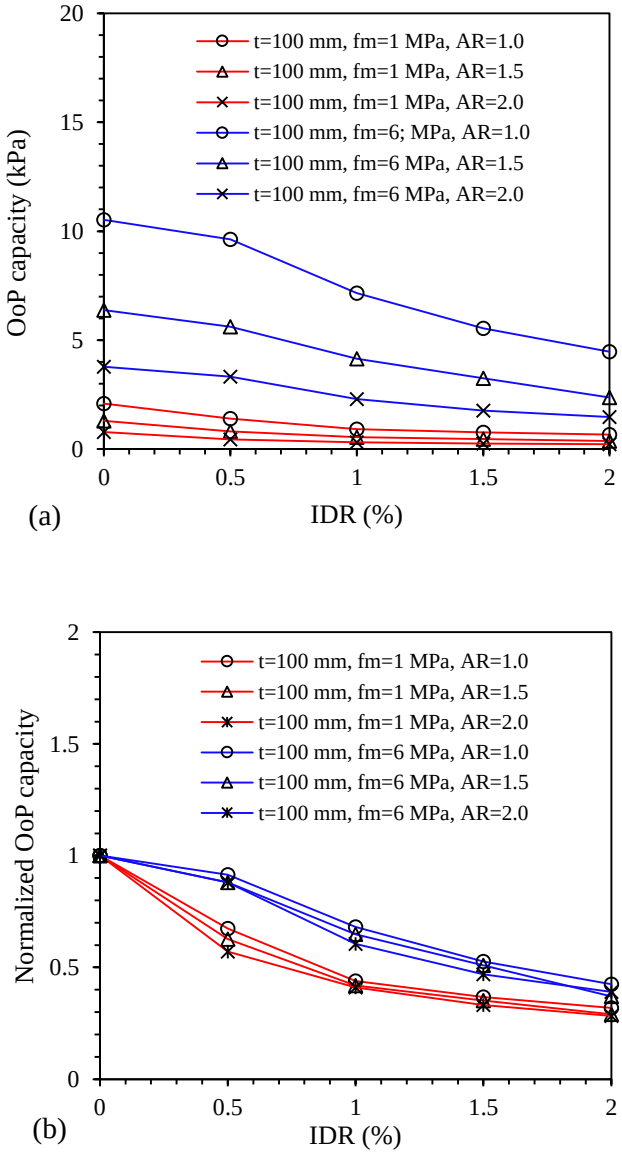

Figure 4.14 (a) Decay of OoP capacity of infill walls vs IP damage according to the aspect ratio (AR) – h =2600 mm, t =100 mm (h/t =26); (b) normalized OoP capacity

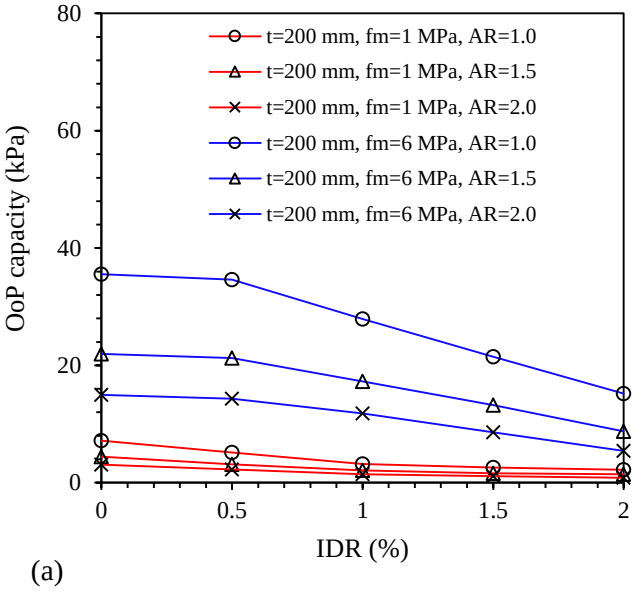

(a)

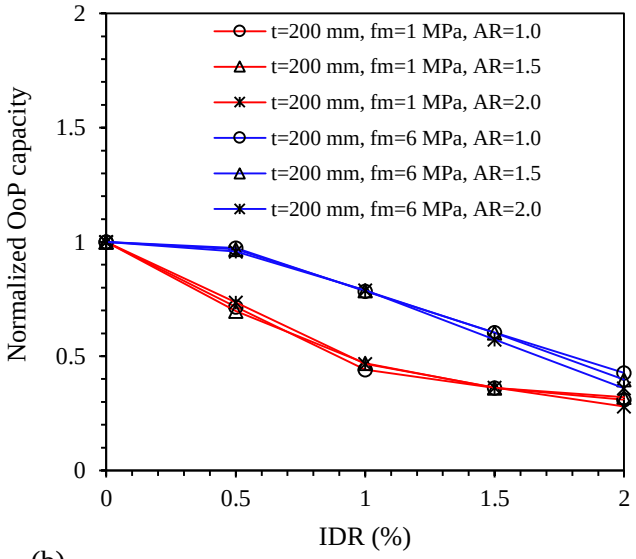

(b)

Figure 4.15 (a) Decay of OoP capacity of infill walls vs IP damage according to the aspect ratio (AR) – h =2600 mm, t =200 mm (h/t =13); (b) normalized OoP capacity

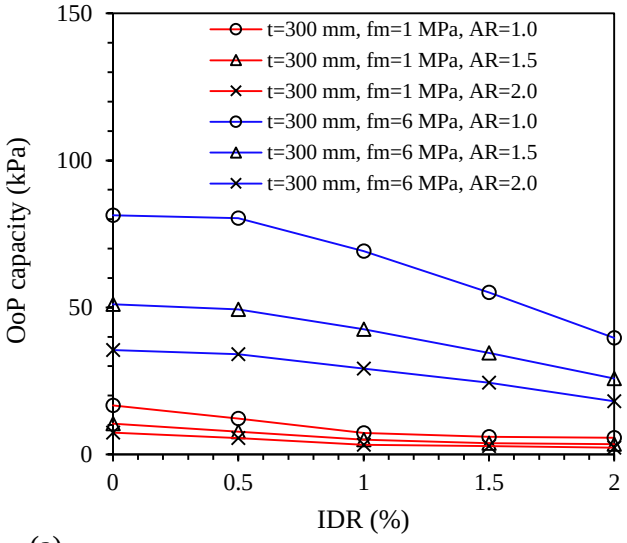

(a)

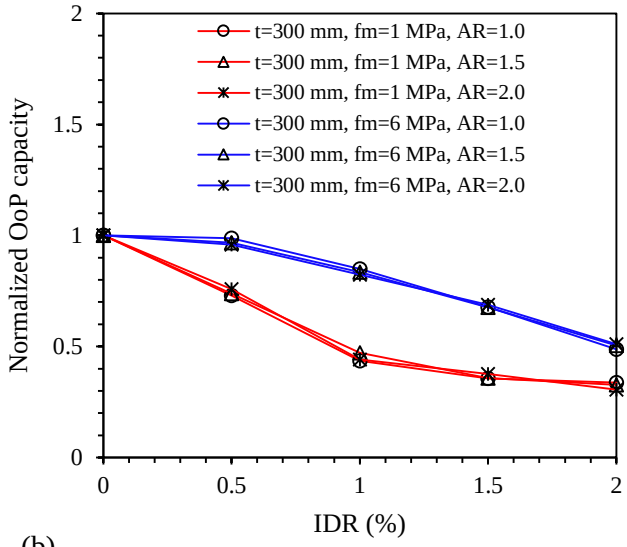

(b)

Figure 4.16 (a) Decay of OoP capacity of infill walls vs IP damage according to the aspect ratio (AR) – h =2600 mm, t =300 mm (h/t =8.6); (b) normalized OoP capacity

The complex nature of the OoP strength decay is easy to be understood from Fig 4.17 & 4.18. The reduction factors, numerically evaluated, fixing the values of f_m and *IDR* for infill walls of different h/t ratios, are less scattered compared to the other ones calculated by fixing the values of h/t and *IDR* for different values of f_m. This indicates that the large variation in the OoP capacity of infills can be brought about by differences in f_m.

Regarding the OoP stiffness, an initial stiffness was evaluated by estimating a secant stiffness using the point on the OoP load-displacement curves corresponding to one-third of the maximum strength. Such an approach has been taken in other studies as well (e.g. Cavaleri et al. 2019). To calculate the decay of the stiffness, the OoP stiffness was evaluated after each increasing level of IP damage as shown in Fig 4.19. As in the case of the OoP strength, the numerical results showed the dependence of OoP stiffness decay on masonry strength and thickness (or $\boldsymbol{h/t}$) of infill walls. But the decay of stiffness was not as scattered as the decay of strength. Some examples are shown in Figs 4.20- 4.22 for a case of infill wall of $h = l$ =2600 mm. Unlike the strength, the OoP stiffness decays rapidly when the infill wall is damaged previously in IP even by a small amount of drift. This is because the prior IP-damaged infill wall goes through a stiffness recovery process and gains the OoP strength peak at a larger displacement compared to the IP-undamaged cases. The sensitivity of f_m and h/t on the decay of OoP stiffness becomes lesser when the infill is prior damaged in IP by a drift of more than 1%.

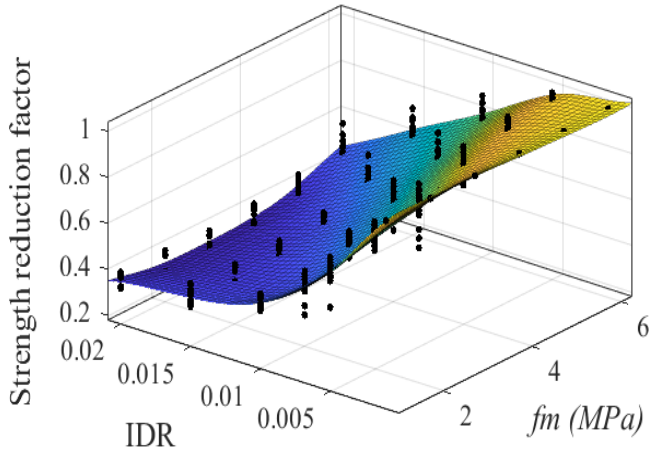

Figure 4.17 Strength reduction factor according to masonry strength and IP drift for various slenderness ratios

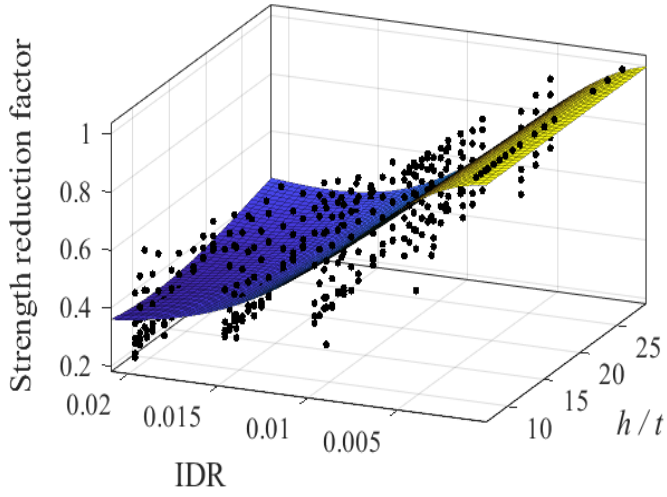

Figure 4.18 Strength reduction factor according to slenderness ratio and IP drift for various masonry strengths

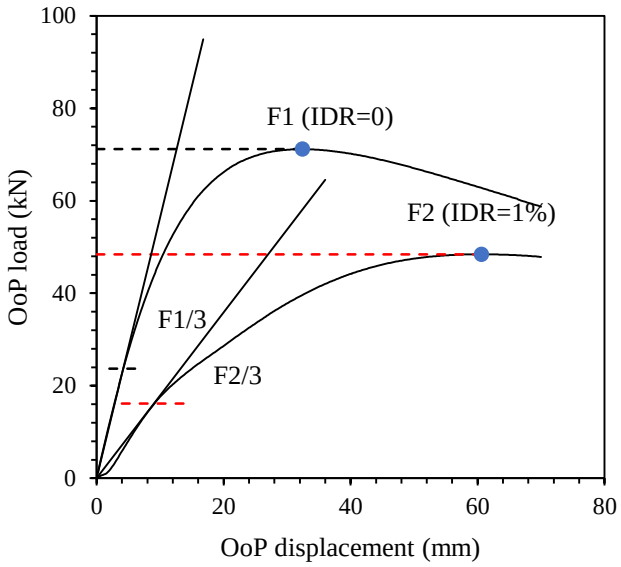

Figure 4.19 Example of evaluation of the OoP stiffness (infill with l =h =2600 mm, t =100 mm, f_m =6 MPa)

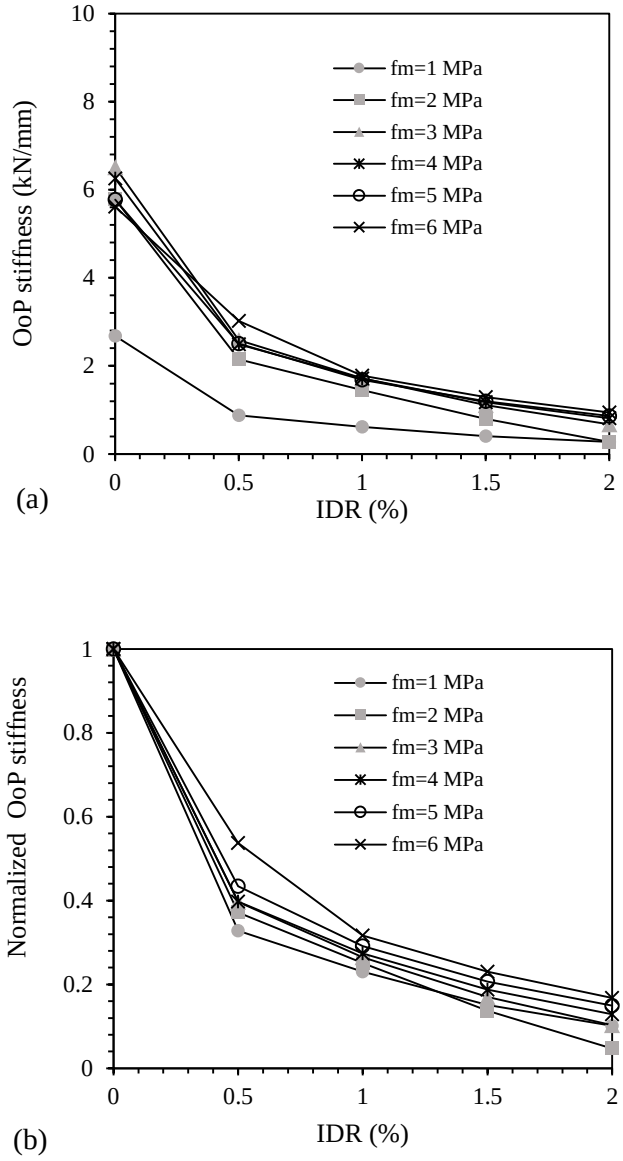

Figure 4.20 (a) OoP stiffness decay - *l*=*h* =2600 mm, *t* =100 mm (*h*/*t*=26); (b) OoP normalized stiffness

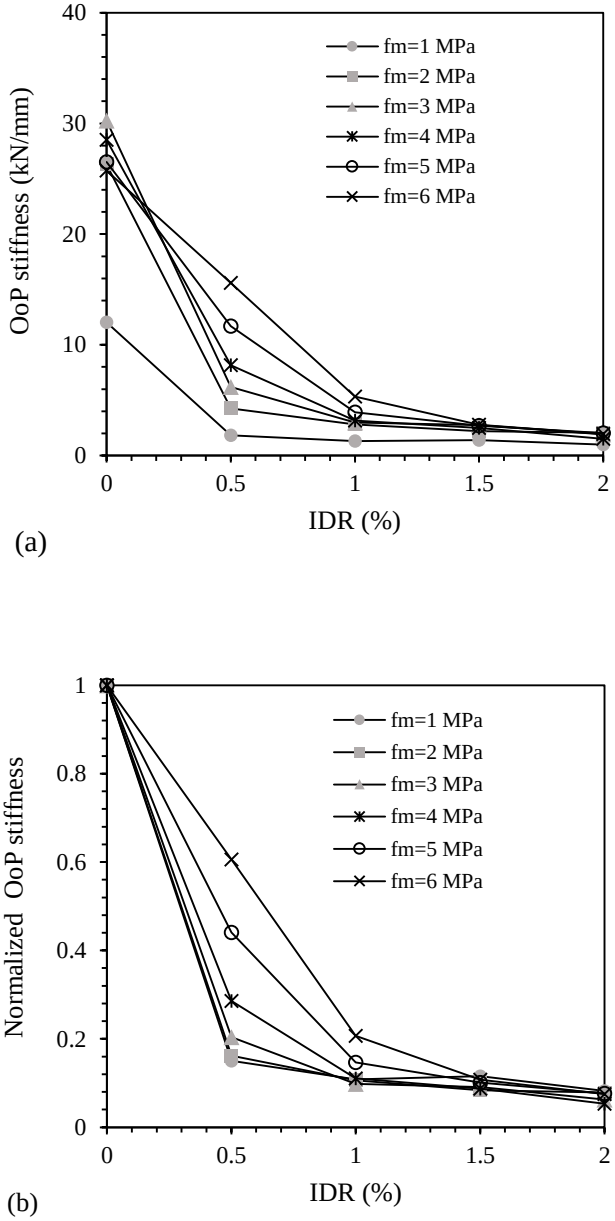

Figure 4.21 (a) OoP stiffness decay - *l*=*h*=2600 mm, *t* =200 mm (*h*/*t*=13); (b) OoP normalized stiffness

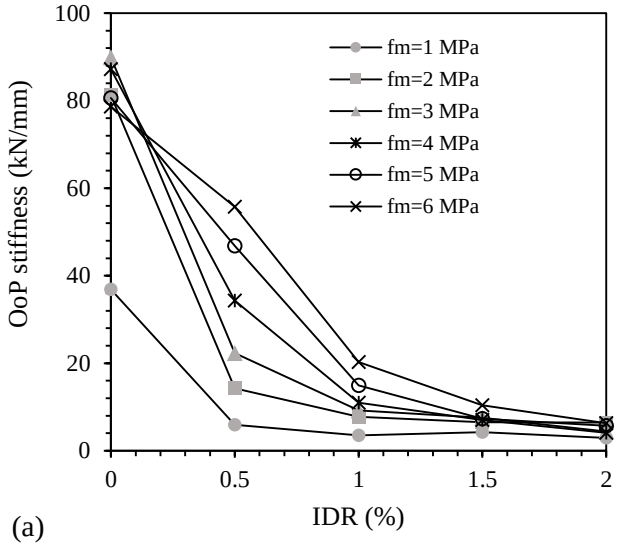

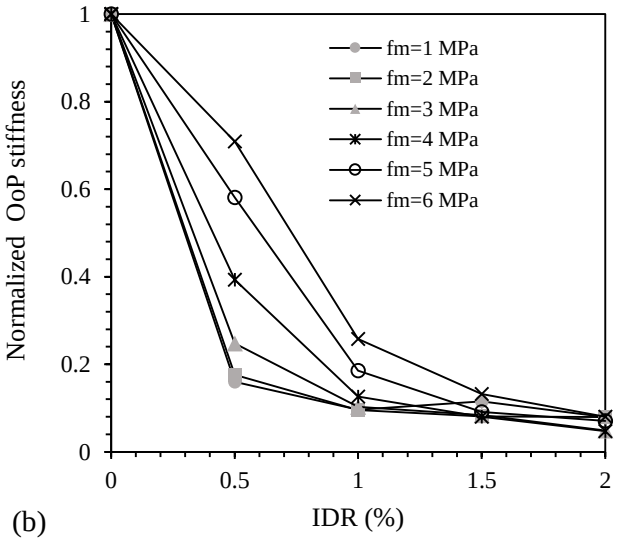

Figure 4.22 (a) OoP stiffness decay – l=h =2600 mm, t =300 mm (h/ t=8.6); (b) OoP normalized stiffness

4.6 OoP capacity prediction equations and validations

Based on the numerical results of the extensive parametric analysis conducted, empirical equations have been proposed to estimate the OoP strength of the infill wall considering the influence of masonry strength, slenderness ratio, aspect ratio, and IP damage. Additionally, a decay law has been proposed for OoP stiffness.

4.6.1 Case of IP undamaged infill walls

To describe the OoP capacity of a URM infill wall in IP-undamaged conditions, the focus was given to two important parameters: the masonry compressive strength and the slenderness ratio. After fitting the numerical results, the OoP capacity of an infill wall was best expressed by the following equation

$$q = 800 \frac{f_m^{1.1}}{(h/t)^{1.9}} \tag{4.1}$$

The above equation is valid for an infill wall with an aspect ratio of 1. In the above equation, the compressive strength of masonry f_m has to be expressed in MPa. The correlation between the numerical results and the predicted OoP capacities (using Eq. 4.1) is shown in Fig 4.23. The dispersion between the numerical and estimated results is very low with a very high degree of the correlation coefficient ($R^2 = 0.985$). The average ratio between estimated and numerical capacity was about 0.95 with the coefficient of variation (COV) as low as 0.15.

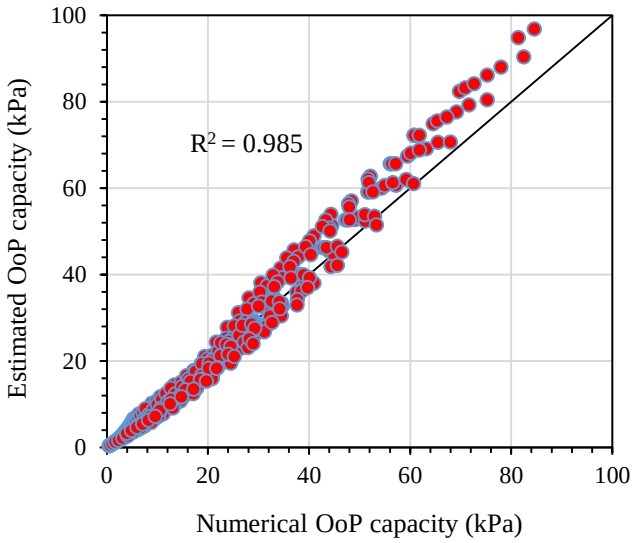

Figure 4.23 Scatter plot of the numerical and estimated OoP capacity

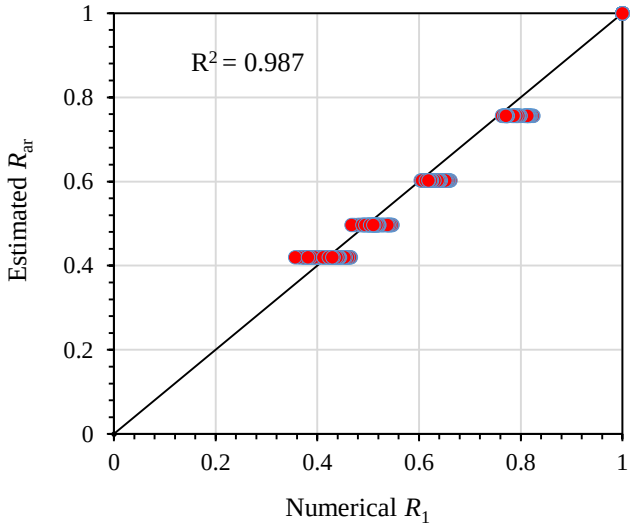

Figure 4.24 Scatter plot of the numerical and estimated reduction factor R_{ar}

Further, to consider the reduction of OoP capacity due to the increase in the aspect ratio of an infill wall, an empirical equation to calculate the reduction factor R_{ar} was derived based on all numerical results. The reduction factor R_{ar} for aspect ratio can be expressed as follows:

$$R_{ar} = (l/h)^{-1.25} \tag{4.2}$$

Eq. 4.2 is valid for the infill walls with $l \geq h$ and for infill walls bounded on all sides by the frames. It correlates with the numerical data very well. The correlation between the numerical and the estimated values of R_{ar} is shown in Fig 4.24. The strength reduction path due to increasing aspect ratio represented by Eq. 4.2 is shown in Fig 4.25.

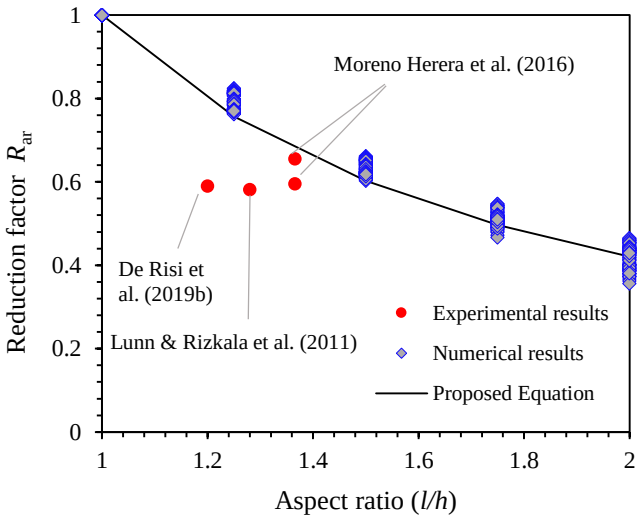

Figure 4.25 Comparison of the strength reduction factor according to the aspect ratio

For a better comparison of the proposed equation, the numerical results and some available experimental results are also inserted in Fig 4.25.

Combining Eq. 4.1 and Eq. 4.2, a new equation (Eq. 4.3) was derived to estimate the OoP capacity of infill walls of any aspect ratio, not IP-damaged previously. The equation is valid for infill walls bounded on all four edges, for $l \geq h$ and f_m not larger than 11 MPa. The upper bound value of f_m equal to 11 MPa is kept because the proposed model was validated with experimental data only up to this range.

$$q = 800 \frac{f_m^{1.1}}{(h/t)^{1.9}} \times (l/h)^{-1.25} \tag{4.3}$$

Eq. 4.3 was checked with available experimental results (Table 4.2). Although the equation is solely derived from a regression analysis of the numerical results, it estimated OoP capacity with good accuracy (mean ratio 0.81, COV 0.30). The correlation between the experimental and estimated capacity can also be observed in Fig 4.26.

Table 4.2 Comparison of the experimental OoP strength and estimated strength

Author	Specimen	Experimental Strength (kPa)	Estimated Strength (kPa)	$\frac{Estimated}{Experimental}$
Angel (1994)	1	8.18	8.64	1.06
Flanagan & Bennett (1999b)	18	26.60	38.33	1.44
	25	8.10	10.27	1.27
Calvi & Bolognini (2001)	10	2.92	1.71	0.59
Moreno-Herera et al. (2016)	W1	8.81	5.30	0.60
	W2	10.49	10.10	0.96
	W3	11.06	10.37	0.94
	W4	7.33	6.08	0.83
	W5	13.44	7.21	0.54
	W6	17.61	13.72	0.78
	W7	18.06	14.09	0.78
	W8	14.24	8.26	0.58
Spesdar (2017)	IF-ND	66.30	67.51	1.02
Furtado et al. (2020)	M4	4.76	2.34	0.49
Ricci et al. (2018a)	80_OOP_4E	5.12	3.47	0.68
Ricci et al. (2018b)	120_OOP_4E	9.74	6.58	0.68
Di Domenico et al. (2018)	OOP_4E	5.12	3.27	0.64
De Risi et al. (2019b)	OOP	8.80	8.34	0.95
Di Domenico et al. (2019a)	OOP_4E	9.74	6.58	0.68
mean				0.81
standard deviation				0.25
COV[%]				30.5

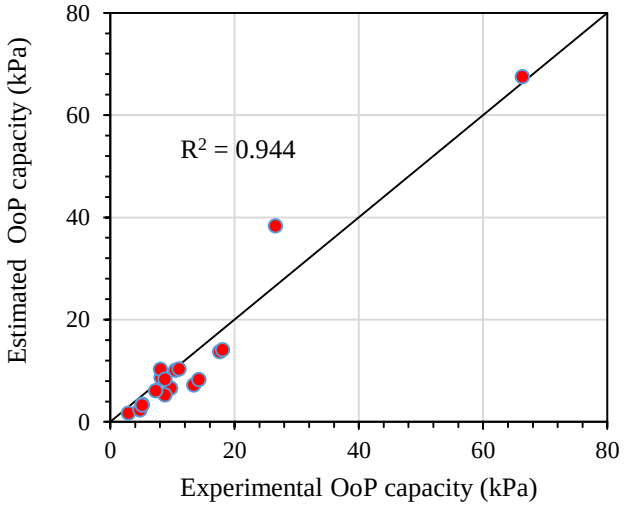

Figure 4.26 Scatter plot between the experimental and estimated OoP strength

4.6.2 Case of previously IP damaged infill walls

From the previous discussions, it is clear that the amount of strength reduction due to IP damage is determined by the strength of masonry, slenderness ratio, level of IP drift, and, very less by the aspect ratio. In this section, the numerical results are analysed separately to determine the ratio of the IP-damaged capacity P_{dam} to the IP-undamaged capacity P_{undam} i.e. the OoP capacity reduction factor R_1 considering different factors.

Depending upon the level of IP damage and the strength of masonry, the strength reduction factor R_1 can be expressed as

$$R_1 = \frac{P_{dam}}{P_{undam}} = \min\left(0.5 \times f_m^{0.09} \times IDR^{-0.27}; 1\right) \tag{4.4}$$

Similarly, depending upon the level of IP damage and the slenderness ratio, the fitting equation of the following form was obtained.

$$R_1 = \frac{P_{dam}}{P_{undam}} = \min\left(0.69 \times \left(\frac{h}{t}\right)^{-0.08} \times IDR^{-0.27}; 1\right) \tag{4.5}$$

Finally, by integrating the strength of masonry, slenderness ratio, and IP drift level (aspect ratio is ignored as it has the lowest impact), the strength reduction factor can be expressed as:

$$R_1 = \frac{P_{dam}}{P_{undam}} = \min\left(0.662 \times f_m^{0.22} \times \left(\frac{h}{t}\right)^{-0.18} \times IDR^{-0.26}; 1\right) \tag{4.6}$$

In the above Eqs. 4.4 - 4.6, the IDR is expressed in percentage and f_m is in MPa. The factor R_1 takes the value 1 when IDR is equal to zero i.e. no IP damage. The correlation between the numerical results and estimated values by using Eqs. 4.4 - 4.6 can be seen in Fig 4.27.

Eq. 4.4 and Eq. 4.5 cover a small band of the numerical data relatively while Eq. 4.6 satisfy a wide range (Fig 4.28). The strength reduction factors computed by using Eq. 4.6 for particular values of f_m and h/t for different levels of *IDR* are further shown in Fig 4.29. Moreover, the strength reduction factors estimated by the proposed equations and the strength reduction factors obtained during the experiments available in the literature are kept in Fig 4.30. R_1 calculated according to Eq. 4.6 matches closely the variability shown by the experimental results (the related data are provided in Table 4.3).

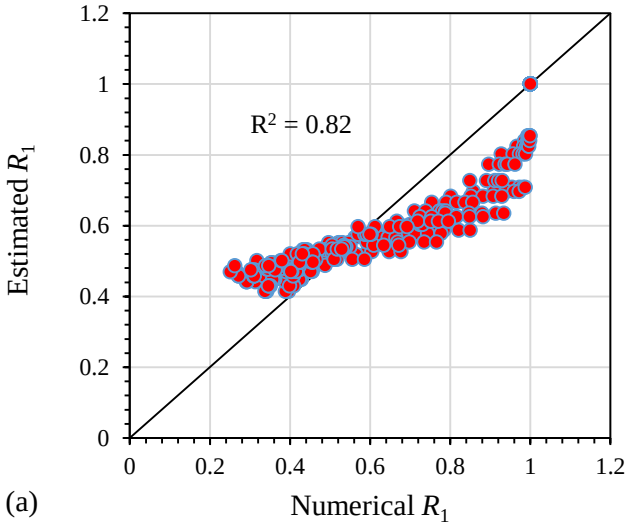

(a)

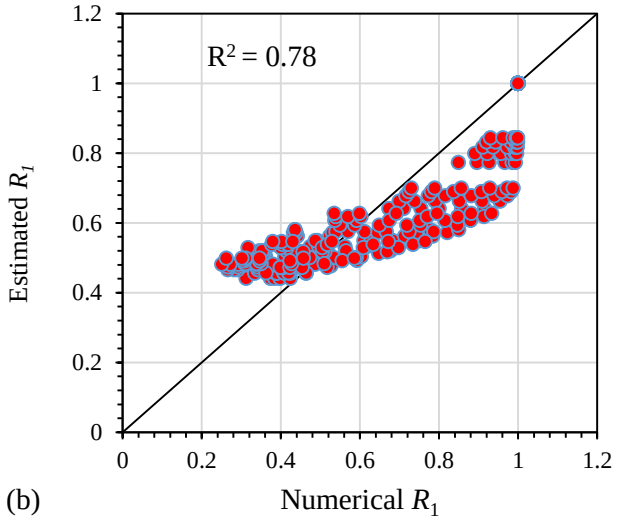

(b)

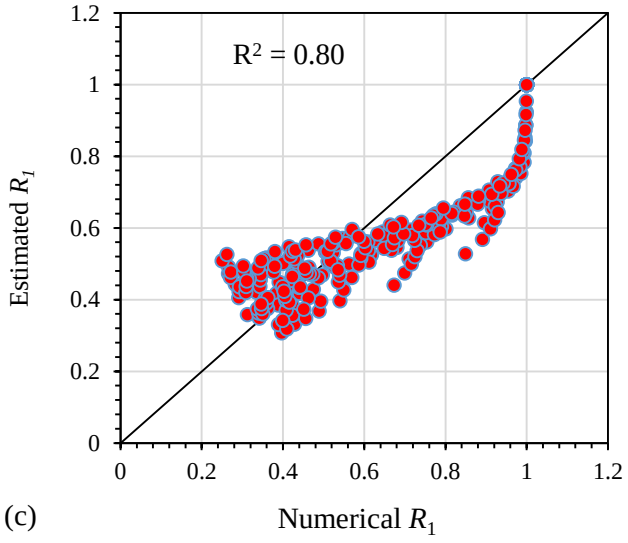

(c)

Figure 4.27 Scatter plot of the numerical and estimated values of the reduction factor R_2 using a) Eq. 4.4; b) Eq. 4.5; c) Eq. 4.6

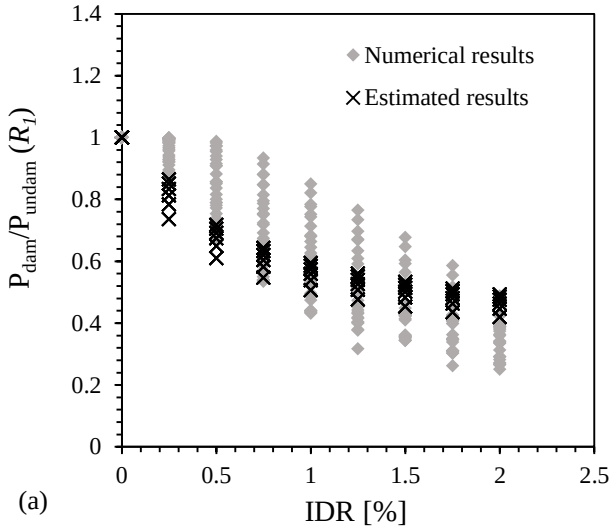
Numerical results
Estimated results
P_{dam}/P_{undam} (R_1)
IDR [%]
0
0.2
0.4
0.6
0.8
1
1.2
1.4
0
0.5
1
1.5
2
2.5

(a)

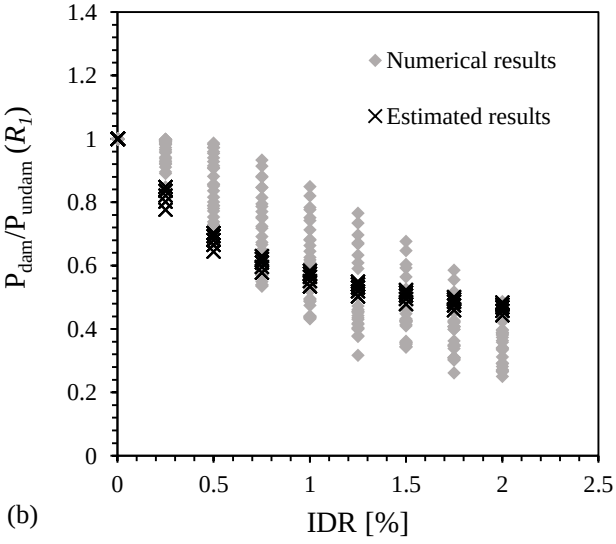
Numerical results
Estimated results
P_{dam}/P_{undam} (R_1)
IDR [%]
0
0.2
0.4
0.6
0.8
1
1.2
1.4
0
0.5
1
1.5
2
2.5

(b)

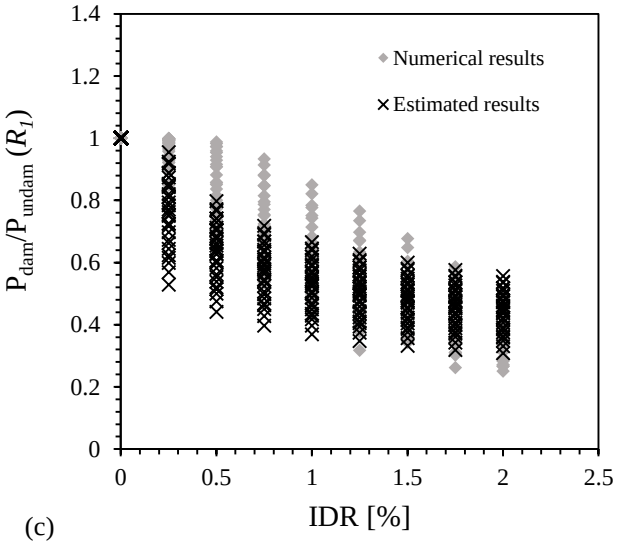

(c)

Figure 4.28 Comparison of the numerical and the estimated values of the reduction factor R_2: a) Eq. 4.4; b) Eq. 4.5; c) Eq. 4.6

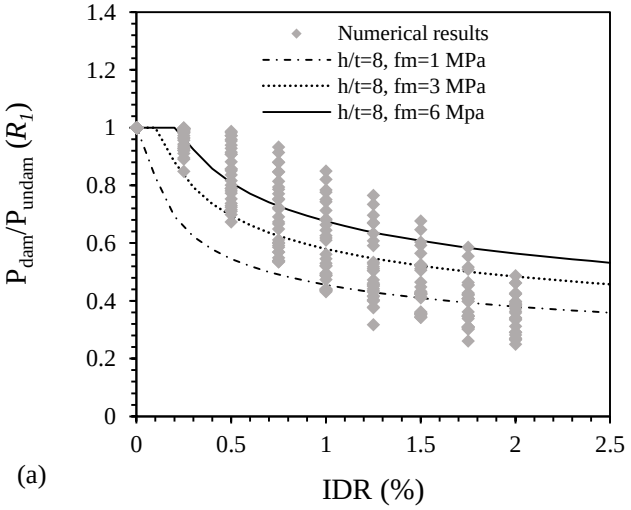

(a)

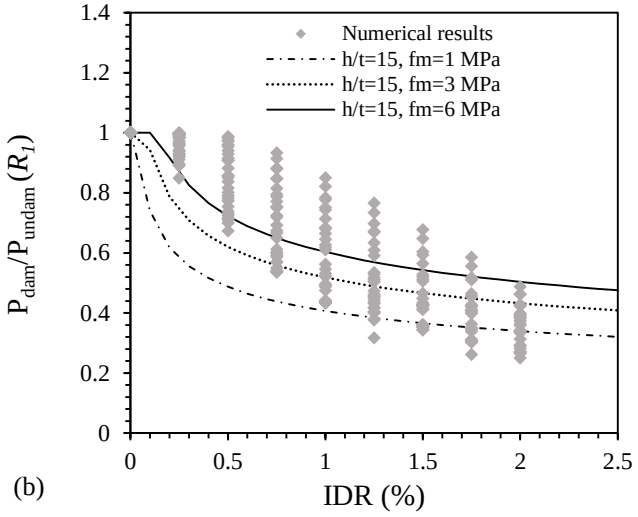

(b)

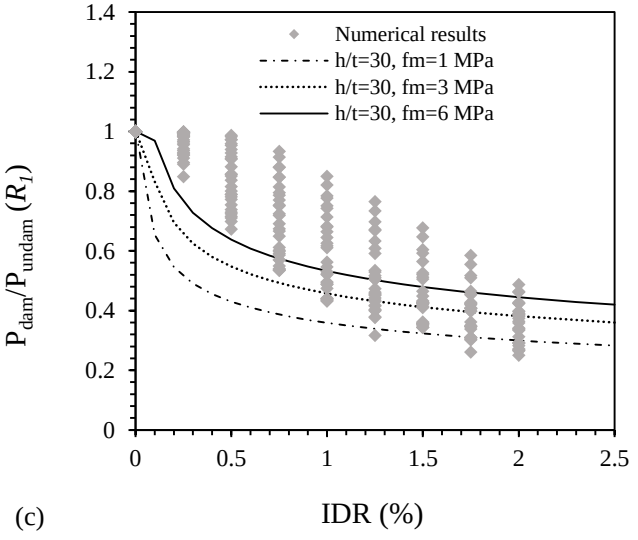

(c)

Figure 4.29 Comparison of the OoP strength numerical decay and the estimated decay by using Eq. 4.6: a) *h/t* = 8; b) *h/t* =15; c) *h/t* =30

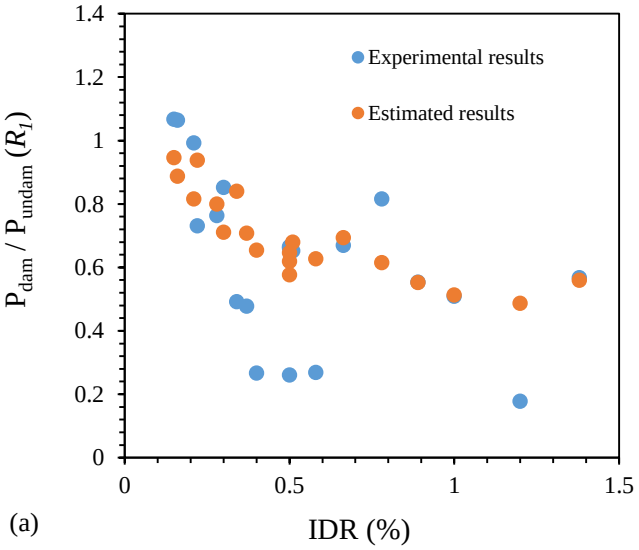
Experimental results
Estimated results
P_{dam} / P_{undam} (R_1)
IDR (%)
0
0.2
0.4
0.6
0.8
1
1.2
1.4
0
0.5
1
1.5

(a)

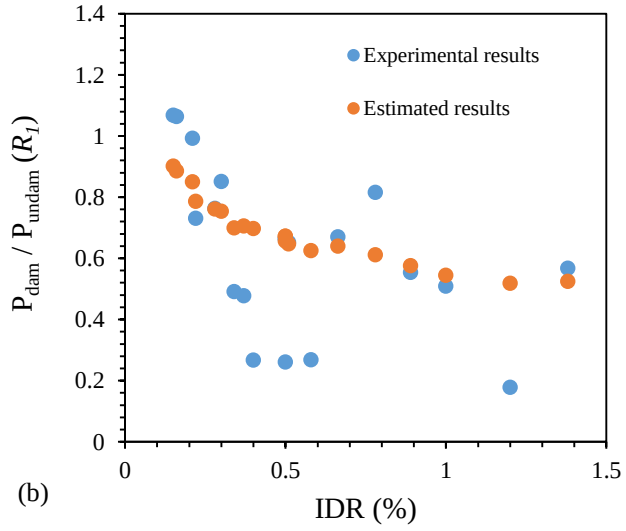
Experimental results
Estimated results
P_{dam} / P_{undam} (R_1)
IDR (%)
0
0.2
0.4
0.6
0.8
1
1.2
1.4
0
0.5
1
1.5

(b)

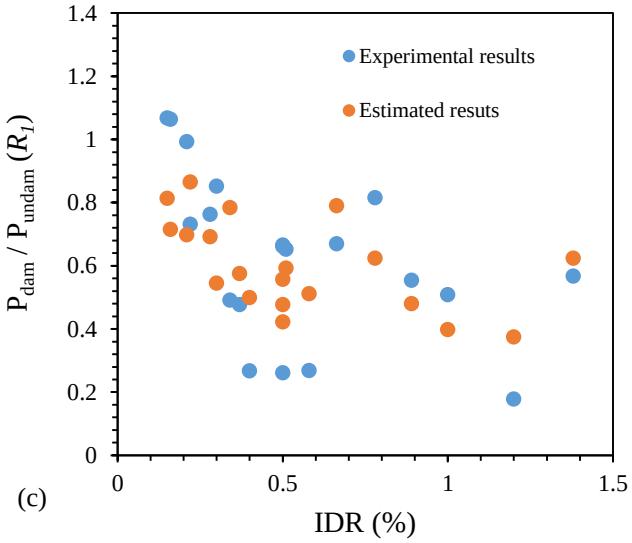

Figure 4.30 Comparison of the strength reduction factor obtained from experiments in the literature and those estimated by using the proposed equations: (a) Eq. 4.4, (b) Eq. 4.5, (c) Eq. 4.6

For further comparisons, strength reduction factors calculated from a few recent proposals available in the literature (Furtado et al. 2018a; Ricci et al. 2018a; and Cavaleri et al. 2019) are also kept in Fig 4.31. The proposal of Furtado et al. (2018a) and Ricci et al. (2018a) give similar results as both equations were proposed based on the same test results. Additionally, results obtained from a new model by Di Domenico et al. (2021) (Eq. 4.7) including the effect of aspect ratio in the strength decay, are shown in Fig 4.31b. The before mentioned model for the reduction factor is expressed as

$$R_1 = \frac{P_{dam}}{P_{undam}} = \min\left\{1; \left(1.438 - 0.245\frac{l}{h} - 0.042 \times \min\left(\frac{h}{t}; 20.4\right)\right) \times IDR^{-0.719}\right\} \qquad (4.7)$$

The calculated strength reduction factors from the equation provided by Di Domenico et al. (2021) are also kept in Table 4.3. In Table 4.3, Est. indicates the estimated values from analytical equations while Exp. Indicates the values obtained during the experiments.

Table 4.3 Comparison of experimental and estimated [Eq. 4.4 - Eq. 4.7] values of P_{dam} / P_{undam}

Author	Specimen	$R_{Exp.}$	$R_{Est.}$ Eq. 4.4	$R_{Est.}$ Eq. 4.5	$R_{Est.}$ Eq. 4.6	$R_{Est.}$ Eq. 4.7	$\frac{Est.[Eq.4.4]}{Exp.}$	$\frac{Est.[Eq.4.5]}{Exp.}$	$\frac{Est.[Eq.4.6]}{Exp.}$	$\frac{Est.[Eq.4.7]}{Exp.}$
Angel (1994)	2	0.49	0.84	0.70	0.78	0.46	1.71	1.42	1.60	0.94
	3	0.73	0.94	0.79	0.87	0.63	1.28	1.08	1.18	0.87
Flanagan & Bennett (1999a)	19	0.82	0.61	0.61	0.62	0.86	0.75	0.75	0.76	1.06
Calvi & Bolognini (2001)	6	0.27	0.65	0.70	0.50	0.40	2.45	2.61	1.87	1.50
	2	0.18	0.49	0.52	0.38	0.18	2.73	2.91	2.11	1.02
Furtado et al. (2016)	Inf_03	0.26	0.58	0.67	0.42	0.57	2.21	2.58	1.62	2.18
Spesdar (2017)	IF-D1	0.67	0.69	0.64	0.79	0.86	1.04	0.96	1.18	1.29
Wang (2017)	IF_RC_ID	0.57	0.56	0.53	0.62	0.51	0.99	0.93	1.10	0.90
Ricci et al. (2018a)	OOP_L_80	1.06	0.89	0.89	0.72	1.00	0.83	0.83	0.67	0.94
	OOP_M_80	0.48	0.71	0.71	0.58	0.55	1.48	1.48	1.21	1.15
	OOP_H_80	0.27	0.63	0.63	0.51	0.40	2.34	2.33	1.91	1.48
Ricci et al. (2018b)	OOP_L_120	0.99	0.82	0.85	0.70	1.00	0.82	0.86	0.70	1.01
	OOP_M_ 120	0.67	0.65	0.67	0.56	0.80	0.97	1.01	0.84	1.20
	OOP_H_120	0.55	0.55	0.58	0.48	0.53	1.00	1.04	0.87	0.95
Akhoundi et al. (2018)	SIF-0.3%-B	0.85	0.71	0.75	0.54	0.52	0.83	0.89	0.64	0.61
	SIF-0.5%-B	0.66	0.62	0.66	0.48	0.36	0.94	0.99	0.72	0.54
	SIF-1.0%-B	0.51	0.51	0.54	0.40	0.22	1.01	1.07	0.78	0.43
De Risi et al. (2019b)	OOP_L_80	1.07	0.95	0.90	0.81	1.00	0.89	0.84	0.76	0.94
	OOP_M_80	0.76	0.80	0.76	0.69	0.84	1.05	1.00	0.91	1.10
	OOP_H_80	0.65	0.68	0.65	0.59	0.55	1.04	0.99	0.91	0.84
Mean							1.32	1.33	1.12	1.05
Standard deviation							0.60	0.67	0.45	0.37
COV [%]							46%	50%	40%	35.36%

Relatively, Eq. 4.7 by Di Domenico et al. (2021) gave a better prediction since the equation itself was derived from the regression analysis of experimental results included in Table 4.3 (except Flanagan and Bennett 1999b; Furtado et al. 2016; Spesdar 2017; Wang 2017; Akhoundi et al. 2018). Nevertheless, considering that the proposed equation (Eq. 4.6) was derived based on the numerical results alone, it is equally effective. It is to be remembered that the proposed Eq. 4.6 considers the masonry strength while Eq. 4.7 does not consider it in the reduction of OoP capacity due to prior IP damage.

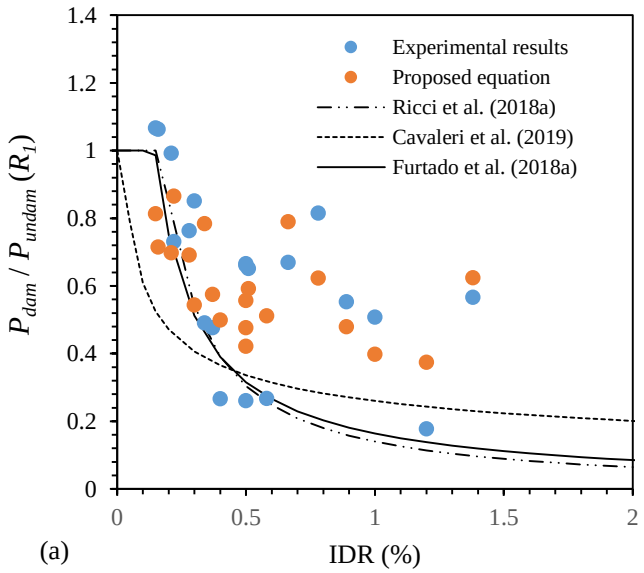

(a)

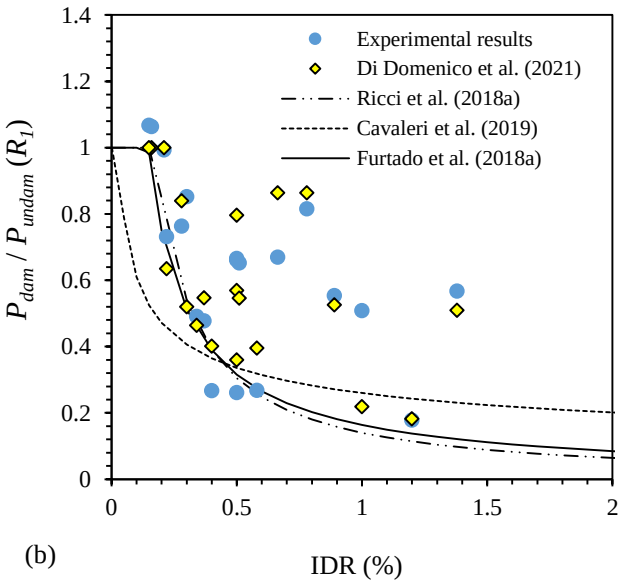

Figure 4.31 Comparison of OoP capacity decay from experimental results, numerical results and some available proposals: a) focusing on proposed equation (Eq. 4.6); b) focusing on proposals of Di Domenico et al. (2021)

It is not to be forgotten that the experimented infill specimens have variations also in loadings besides the variations in geometrical (h/t, l/h) and mechanical (f_m, E_m) properties. Some specimens were subjected to monotonic load in IP and OoP directions while others were subjected to cyclic or half cyclic loads. This has an impact on the level of OoP strength reduction. A true comparison among these experimental results is therefore not possible. Nevertheless, experimental results show the variability and highlight the uncertainties in OoP strength decay, and the proposed equation (Eq. 4.6) was able to consider the effect of such variations in a good way.

Finally, considering the strength reduction factor R_1 due to IP damage from Eq. 4.6, a new equation (Eq. 4.8) is proposed to estimate the OoP capacity of the URM infills in IP-damaged conditions, that is

$$q = 800\frac{f_m^{\,1.1}}{(h/t)^{1.9}} \times (l/h)^{-1.25} \times \min(0.662 \times f_m^{\,0.22} \times \left(\frac{h}{t}\right)^{-0.18} \times IDR^{-0.26}; 1) \qquad (4.8)$$

The above equation can be used as well for the IP-undamaged condition, the part of reduction factor according to Eq. 4.6 is equal to 1 in such a case. The proposed equation facilitates the calculation and comparison of OoP strength with those experimental tests where reference undamaged specimens are unavailable like in the case of Da Porto et al. (2013), Hak et al. (2014) as shown in Table 4.4. The comparison between the estimated capacities (using Eq. 4.8) and experimental results shows a good agreement with the mean of the ratio between estimated and experimental strengths equal to 0.9 and COV equal to 31.6% (Table 4.4). The correlation between the estimated and experimental results is shown in Fig 4.32.

Table 4.4 Comparison of the experimental and estimated OoP strengths for IP damaged infills

Author	Specimen	Experimental Strength (kPa)	Estimated Strength (kPa)	$\frac{Estimated}{Experimental}$
Angel (1994)	2b	4.02	6.35	1.58
	3b	5.98	6.50	1.09
	6b	12.39	9.99	0.81
Calvi & Bolognini (2001)	2	0.52	0.64	1.24
	6	0.78	0.86	1.10
Pereira et al. (2011)	Wall_REF_01	2.07	1.98	0.96
Da Porto et al. (2013)	URM_U	18.46	11.36	0.62
Hak et al. (2014)	TA1	13.54	10.48	0.77
	TA2	8.25	9.18	1.11
	TA3	13.17	11.65	0.88
Spesdar R. (2017)	IF-D1	44.40	55.75	1.26
Wang C. (2017)	IF-RC-ID	37.60	34.88	0.93
Ricci et al. (2018a)	80_IP+OOP_L	5.44	2.48	0.46
	80_IP+OOP_M	2.44	2.00	0.82
	80_IP+OOP_H	1.37	1.78	1.29
Ricci et al. (2018b)	120_IP+OOP_L	9.67	4.60	0.48
	120_IP+OOP_M	6.49	3.67	0.57
	120_IP+OOP_H	5.37	3.16	0.59
De Risi et al. (2019b)	IP_L-OOP	9.39	6.79	0.72
	IP_M-OOP	6.72	5.77	0.86
	IP_H-OOP	5.74	4.94	0.86
mean				0.9
Standard deviation				0.29
COV [%]				31.6

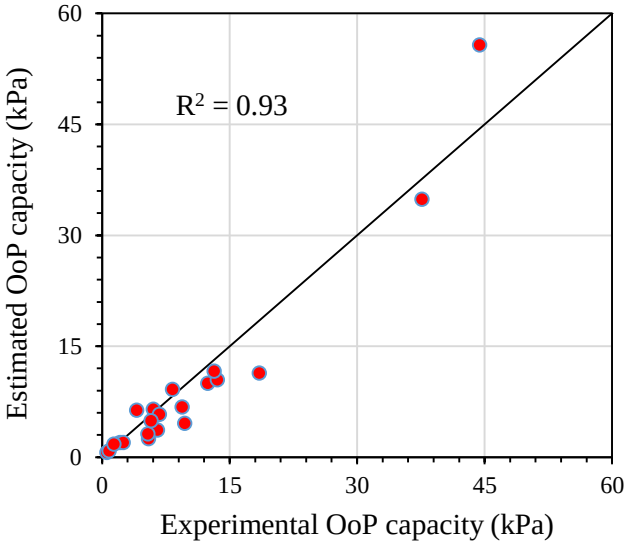

Figure 4.32 Scatter plot between the experimental OoP strength and estimated strength by using Eq. 4.8 for IP damaged specimens

Like a residual OoP strength after IP damage, it is important to know the residual OoP stiffness for a given level of IP damage. To determine the decay of initial stiffness, an equation was fitted to best represent the numerical results. The residual initial stiffness $K_{r,ini}$ expressed as a ratio of damaged stiffness $K_{ini,dam}$ to undamaged stiffness $K_{ini,undam}$ can be represented as:

$$K_{r,ini} = \frac{K_{ini,dam}}{K_{ini,undam}} = \min(0.17 \times IDR^{-0.8};\ 1) \tag{4.9}$$

In the above equation, reduction of stiffness is considered only due to IP drift. The influence of other parameters like masonry strength and

slenderness ratio was not much significant unlike in the case of the decay of OoP strength.

Eq. 4.9 is similar to the one proposed by Cavaleri et al. (2019) as shown in Fig 4.33a. In the same figure, the models proposed by Furtado et al. (2018a) and Ricci et al. (2018a) for the reduction of the secant stiffness, are also included for comparison. Furtado et al. (2018a) and Ricci et al. (2018a) evaluated the initial OoP stiffness corresponding to the first infill wall macro-cracking. However, it is to be noted that it is not easy to identify the value of the force and the displacement corresponding to the first macro-cracking even during the experiments. In their experiments, Furtado et al. (2018a) and Ricci et al. (2018a) assumed a point in the load-displacement curve where significant yielding started. Stiffness evaluated with this approach cannot be related directly to one adopted in this study. Since the idea is to recognize the decay of OoP stiffness, the comparison serves the purpose. The correlation between the estimated results (using Eq. 4. 9) and numerical results can be observed in Fig 4.33b.

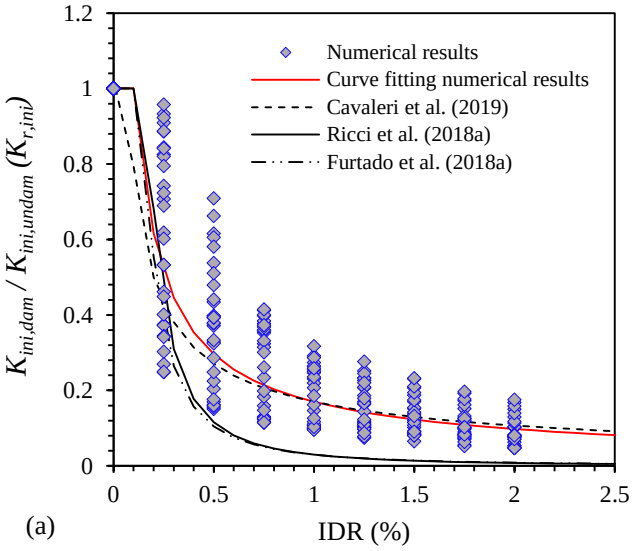

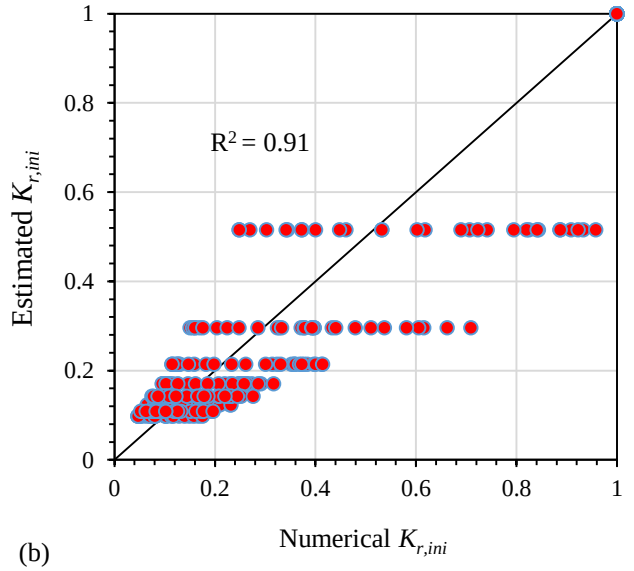

Figure 4.33 a) Decay of initial OoP stiffness; b) Scatter plot between the numerical and estimated (using Eq. 4.9) stiffness decay ratio

5 OUT-OF-PLANE FRAGILITY ANALYSIS OF URM INFILL WALLS

Fragility functions are important tools to know the probability of OoP collapse of infill walls during an earthquake. To derive the appropriate fragility functions, damage data from past earthquakes are the primary and reliable resources. Based on real earthquake data, few empirical fragility functions for RC buildings corresponding to different damage states of infill walls (especially for damage in IP) have been proposed (e.g. De Luca et al. 2015, Del Gaudio et al. 2017). But fragility functions specific to OoP collapse of infill walls are very rare.

Cardone and Perrone (2015) were one of the few to propose the OoP fragility function for masonry infill walls based on the results of experimental data. The median collapse level Peak Ground Acceleration (PGA) was about 0.6g (g indicates acceleration due to gravity). Likewise, Gautam et al. (2021) proposed the OoP fragility of infill walls for RC buildings in Nepal based on damage data after the 2015 Gorkha Earthquake. According to them, a median value of 0.4g PGA was obtained for severe OoP damage in the infill walls.

Although the damage data-based empirical fragility curves represent the vulnerability in a true sense, empirical fragility functions are many times limited to the data on which they are derived (Del Gaudio et al. 2019). Moreover, they often suffer from inaccurate knowledge of seismic demands like PGA (Gautam et al. 2021). The PGA differs from place to place and for

a good estimate of the empirical fragility, the information about the ground motion has to be proper.

Therefore, to derive seismic vulnerability information for any type of infill wall with different geometrical and mechanical characteristics, numerical model-based analytical fragility curves can be more insightful. Nevertheless, it is not to be forgotten that the numerical models are also affected by various uncertainties (Celarec and Dolšek 2013; Holický et al. 2016; Castaldo et al. 2020).

In very few studies, numerical models have been used to derive OoP fragility. This was often limited by computational effort in analysing a huge number of cases due to variations in the properties of the infills as well as due to the lack of a proper numerical model to capture IP-OoP interaction. In recent years, macro-element models that capture IP-OoP interaction have also advanced (as discussed in Chapter 2), and some of these models have been used to derive OoP fragility functions of masonry infill walls in seismic loads.

For example, Gesualdi et al. (2020) used the model of Di Domenico et al. (2017), Ricci et al. (2018c) to propose fragility curves for multi-storey buildings (gravity design, and low-seismic design) featuring two-leaf infills (100 mm +100 mm with a cavity in between) based on their possible IP and OoP failures. Fragility was proposed also considering IP-OoP interaction. Fragility curves were derived considering two performance levels of masonry infill walls (limited damage and life safety) by performing incremental nonlinear time history analysis. The OoP fragility of infill walls was comparatively higher when IP-OoP interaction was considered. The fragility was also higher with the increase in the number of storeys in the buildings. Moreover, the authors remarked that the most important parameter that governs fragility is the type of infill and its characteristics. The fragility was

not much influenced by the frame types; whether gravity design or low-seismic design.

Similarly, Ricci et al. (2020) proposed OoP fragility curves for three different infill layouts (single leaf: 300 mm 'strong layout', two-leaf: 80+120 mm 'weak layout' and two-leaf: 120+200 mm 'intermediate layout') by using the empirical modelling approach of Ricci et al. (2018c). Incremental nonlinear time history analyses were performed to determine the probability of collapse of infill walls on 16 case-study buildings (4 buildings with each of 2, 4, 6 & 8 storey) for each infill layout. Their study also showed that the fragility was higher when considering IP-OoP interaction and the fragility increased with an increase in the height of the building. Fragility was also affected by the infill's properties. Weak infill walls showed an average collapse PGA of 0.23g (0.6g) with (without) IP-OoP interaction. For intermediate infill walls layout, it was 0.33g (0.88g) and for strong infill walls, it was 0.69g (1.25g). Masonry strength of weak and intermediate infill was assumed 1.1 MPa in horizontal and vertical directions while strong infill walls were assumed strength of 6 (1.2) MPa in vertical (horizontal) directions.

Both Gesualdi et al. (2020) and Ricci et al. (2020) proposed the fragility functions for double-leaf (two-leaf) infill walls. They used the empirical approach of Ricci et al. (2018c) to model the IP-OoP interaction. From the investigation of the available experiments, it was found that there is only one experiment by Furtado et al. (2016) where infilled frame with double-leaf infill was tested. In the experiment, IP load was applied first with a double leaf infill and then an interior leaf was removed and OoP load was applied to a remaining single leaf. Ricci et al. (2018c) used the result of this experiment to define the reduction of the ultimate OoP displacement due to IP damage. However, no comparison of force-displacement response with the experimental result was provided. In fact, Ricci et al. (2018c) used their model

to identify the first OoP collapse PGA also for the case of double-leaf infill walls in RC buildings. Although the same approach was used by both Gesualdi et al. (2020) and Ricci et al. (2020) the fragility proposed by Gesualdi et al. (2020) and Ricci et al. (2020) for two-leaf infill walls raises doubts, considering that there are not sufficient experiments to verify the numerical results.

Di Trapani et al. (2020) also derived OoP fragility functions for infill specimens tested by Angel (1994) by using a macro-element model proposed previously by the authors (Di Trapani et al. 2018). In their study, one storey infilled frame was first subjected to various levels of IP drifts and then OoP incremental dynamic analyses were performed. The OoP fragility was higher when prior IP damage (IP drift) was higher. The fragility also depended upon the relative stiffness of the frames and the infill wall.

Furtado et al. (2018b) also derived fragility curves for infilled RC buildings through incremental dynamic analysis. The fragility was higher when infills' failure due to IP-OoP interaction was considered compared to when infills' failure only due to damage in IP direction was assumed. For the collapse of the infill wall, the median PGA required was greater than 0.5g. Kadysiewski and Mosalam (2009) also proposed fragility functions with a higher probability of infill wall's collapse when considering the IP-OoP interaction compared to the collapse of infill wall due to damage in IP or OoP independently.

In the aforementioned examples, fragility functions were derived by considering the variability in the ground motions and the variability in the properties of the infill walls was almost ignored. Kadysiewski and Mosalam (2009) had investigated the effect of variation in masonry strength. The authors did not find a worthy difference in the fragility of infill walls. However, as we have discussed before, the influence of infill's mechanical

and geometrical and mechanical properties on the OoP capacity is higher and this should make a significant impact also on the OoP fragility of the infill walls.

From the above discussion, it is clear that the investigation of the modification of the OoP fragility of infill walls by taking into account the uncertainty of infill's mechanical and geometrical properties, and at the same time, the IP-OoP interaction, is still lagging. Therefore, in this chapter, the OoP fragility of the infill walls is derived considering the uncertainties in the mechanical and geometrical properties of infill walls. A probabilistic approach has been used, based on a Monte Carlo simulation, to capture the uncertainty in the infills' strength and geometric features as well as the uncertainty in the IP drift (inter-storey drift ratio) during an earthquake. Single leaf masonry infill walls without openings have been considered for the study. Fragility curves have been derived for infill walls built with two types of masonry units, i.e. hollow and solid. A further subdivision of the infill walls with hollow blocks has been made identifying hollow strong units and hollow weak units. All the assumed categories were interested by three different levels of IP damage: low, medium and high corresponding to three ranges of IP drifts (it will be better discussed later in this chapter). The fragility curves proposed in this study refer to infill walls placed at the bottom and top floors of a low-rise RC building. For the numerical analysis, the proposed macro-element model (chapter 3) has been used.

5.1 Proposed approach to derive fragility curves

Fragility curves are cumulative distribution functions that represent the probability of exceedance of a certain damage state (DS) for a given type of building/structural element over a range of an intensity measure IM. In this study, the capacity Peak Ground Acceleration "PGA" has been taken as an

intensity measure. A log-normal distribution function can be used and is here assumed for the fragility associated with the OoP collapse state according to the following expression:

$$P[DS / IM] = \varphi\left(\frac{\ln(IM) - \ln(\overline{IM})}{\beta}\right) \quad (5.1)$$

where ϕ is the standard normal cumulative distribution function, $\overline{IM}$ refers to a median value and β is the log-standard deviation that accounts for the uncertainties in the capacity of the building's /structural element's fragilities for the collapse damage state.

The use of Monte Carlo simulation is popular in fragility analysis (e.g. Kadysiewski and Mosalam 2009; Nanayakkara and Dias 2016; Giordano et al. 2019). In this study too, for the derivation of OoP fragility curves of masonry infill walls, Monte Carlo simulation was used which takes into account the variability of the input parameters directly in the model. Consequently, the outputs are affected by the casual assumptions defined over a range of representative input cases.

To reproduce the physical process using a probabilistic approach, first, a cycle of IP drift demand randomly assigned was applied to an infilled frame. The geometrical and mechanical characteristics of the infill wall were also assigned randomly. After the IP analysis, the infill wall was pushed in the OoP direction to determine the capacity (Fig 5.1). Monte Carlo methodology includes the following steps:

1) Random generation of input variables: thickness and strength of masonry, IP displacement demand, etc.;
2) Calculation of OoP capacity by using a macro-element model in OpenSees;

3) Determination of the equivalent OoP pseudo (spectral) acceleration;
4) Derivation of the capacity Peak Ground Acceleration (PGA) associated to the pseudo acceleration;
5) Determination of the probability of exceedance of OoP collapse, and finally obtaining the fragility for a given case study.

The above procedure was implemented first in MATLAB for the generation of a random input variables' matrix (MATLAB code is provided in Appendix B). In the present study, the uncertainties were assigned for (i) the strength of concrete in the reinforced concrete frame surrounding an infill wall, (ii) level of IP damage, (iii) thickness of the infill wall, and (iv) compressive strength of masonry. Input variables were generated employing different distributions of variables. Since the input variables were generated randomly, it allowed the evaluation of the median and the log-standard deviation in the results. The input variables are described in the next section. Then, the random matrix was linked to OpenSees to perform numerical analyses, getting the matrix of the results corresponding to each case of analysis (The MATLAB code for linking random variables to OpenSees is available in Appendix B). The results obtained by OpenSees were the maximum OoP forces and the corresponding OoP displacements. Additionally, one-third of the maximum OoP forces and the corresponding OoP displacements were also extracted after each analysis to derive the OoP stiffness of the infill walls (refer to Chapter 4 for the OoP stiffness calculation).

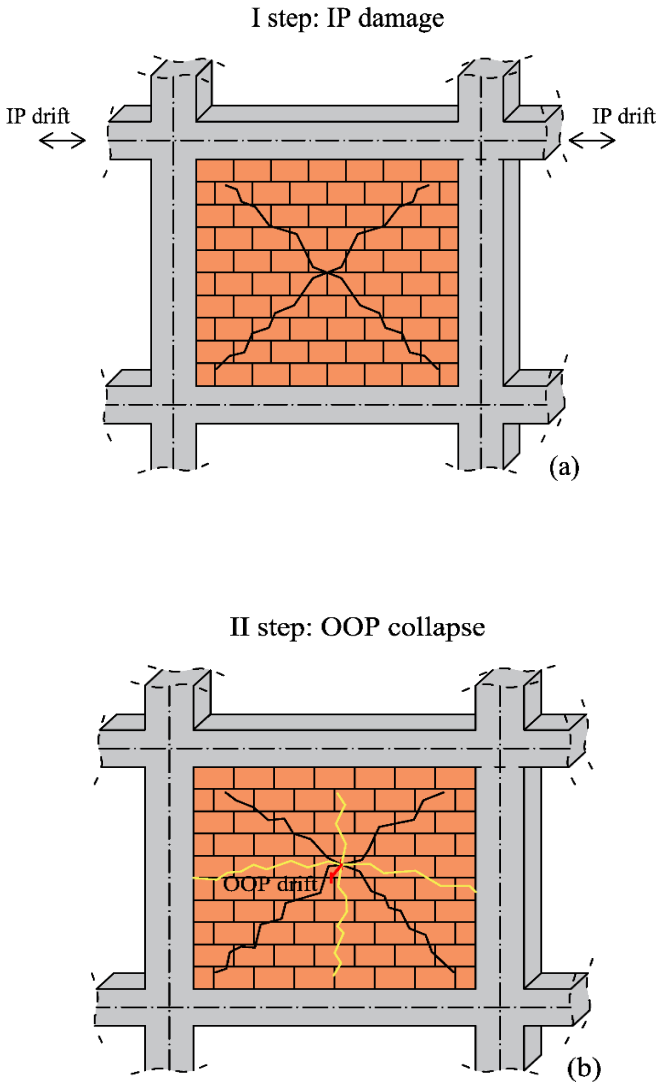

Figure 5.1 a) IP damage; b) OoP collapse

5.2 Evaluation of PGA from the response spectrum

For a given case, in evaluating the approximate capacity in terms of pseudo (spectral) acceleration, the OoP strength is divided by the mass of the infill wall. In calculating the mass of the infill, the density of solid masonry is assumed to be 1900 kg/m3 on average while for hollow masonry it is assumed as 900 kg/m^3. These density values were assumed considering average values among representative units in the common practical materials and construction techniques. Being assumed input parameters, they can be changed to meet specific requirements in specific areas where large-scale risk analysis is required.

Each pseudo (spectral) acceleration can be associated with one PGA value by using the demand spectra. Demand spectra for non-structural elements like infill walls depend upon their position along the height of a building, the fundamental period of the infill wall and the fundamental period of the building (NTC 2018, Eucocode 8). For the present study, demand spectra according to the Italian Building Code 2018 (NTC 2018) and the commentary to the Italian Building Code 2018 (Circolare C.S.LL.PP. n.7 – 21/01/2019), has been used, and the expression of the demand spectrum $S_a(T_a, T_1, Z/H)$ is given as:

$$S_a = \begin{cases} PGA\left(1+\frac{Z}{H}\right)\left[\frac{a_p}{1+\left(a_p-1\right)\left(1-\frac{T_a}{aT_1}\right)^2}\right] \geq PGA & for \quad T_a \leq aT_1 \\ PGA\left(1+\frac{Z}{H}\right)a_p & for \quad aT_1 \leq T_a < bT_1 \\ PGA\left(1+\frac{Z}{H}\right)\left[\frac{a_p}{1+\left(a_p-1\right)\left(1-\frac{T_a}{bT_1}\right)^2}\right] \geq PGA & for \quad T_a \geq bT_1 \end{cases} \tag{5.2}$$

In the above expression, T_a is the fundamental vibration period of the infill wall, while T_1 is the fundamental vibration period of the building. H is the height of the building (expressed in meters) and Z is the level at which the infill is located (in meters). In Eq. 5.2, PGA is expressed in terms of g (gravity acceleration). In the present work, the fundamental period of the building is evaluated using a simplified equation as follows:

$$T_1 = c \cdot H^{3/4} \tag{5.3}$$

In Eq. 5.3, c is a coefficient equal to 0.075 in the case of RC structures (NTC 2018, Eurocode 8). In general, this equation, as well as the number of other similar equations proposed to calculate the fundamental period of the structure (with or without taking into account the presence of the infill walls), are semi-empirical equations obtained by regression analysis on the periods of vibration measured during earthquakes or ambient vibration tests. More in detail, the equation used in this study was theoretically derived using Rayleigh's method with the following assumptions: the equivalent static lateral forces are distributed linearly over the height of the building, the distribution of stiffness with height produces a uniform storey drift under the linearly distributed lateral forces, and the deformations are controlled by the drift limit-state (Goel and Chopra 1997; Arlekar and Murty 2000; Crowley and Pinho 2006).

The numerical value of the constant "c" was obtained from the measured periods of buildings during the 1971 San Fernando earthquake. In doing so, stiffness of cracked infill walls was considered as well. This equation was first employed in seismic design codes such as ATC3-06 (1978), expressing the height of the building in feet and c=0.03 for reinforced concrete moment-resisting frame buildings. Later, Eurocode 8, Italian Building Code

(NTC 2018) adopted this equation by expressing the height in meters and assuming c=0.075.

In Eq. 5.2, the parameters a, b and a_p are defined depending on the fundamental period T_1 of the structure according to Table 5.1 (Tab. C7.2.II Circ. 2019). These parameters help better capture the amplification of ground acceleration at the level of non-structural components (Petrone et al. 2015).

In correlating the OoP seismic force acting in the infill wall and the corresponding pseudo acceleration, behaviour factor of infill walls was assumed to be equal to 1 as recommended by a number of sources (e.g. NZS 1170 (2004), NTC 2018).

Table 5.1 Parameters for the response spectrum interaction

	a	*b*	a_p
T_1<0.5 s	0.8	1.4	5.0
0.5 s ≤ T_1 <1.0 s	0.3	1.2	4.0
T_1≥0.5 s	0.3	1.0	2.5

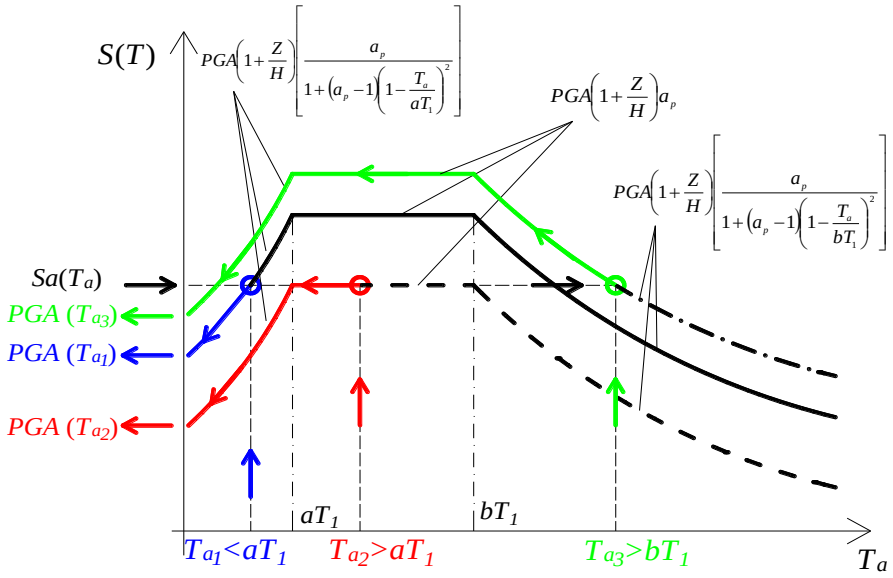

Figure 5.2 Evaluation of the PGA from the response spectrum for two different conditions

Once the period of the panel T_a and the fundamental period of the structure T_1 are obtained, by imposing the equivalence between the spectral acceleration $S_a(T_a, T_1, Z/H)$ and the pseudo-acceleration obtained numerically (that is the infill OoP capacity), it is possible to use Eq. 5.2 to derive the capacity PGA associated with the infill OoP capacity (Fig 5.2). By referring to Fig 5.2, it can be seen that by using this approach (involving Eq. 5.2 and Eq. 5.3), one can use the value of the OoP pseudo-acceleration to use the equation of the spectrum in the specific interval depending on T_a and T_1. According to Eq. 5.2, it is considered the possibility that T_a is lower than $a.T_1$, between $a.T_1$ and $b.T_1$ or higher than $b.T_1$. In doing so, one can use the equation corresponding to the right interval and calculate the capacity PGA

that corresponds to three different positioning of the spectrum and thereby obtaining different values of capacity PGA (Fig 5.2).

In the present study, two different approaches were made in calculating the fundamental period of the panel in the OoP direction, i.e. (i) an analytical approach and (ii) a numerical approach based on the results of the numerical analyses in terms of stiffness. Considerations of the differences obtained by the following two approaches are described in the section of the paper dealing with the results.

Regarding the analytical approach, the fundamental period T_a of the masonry infill in the out-of-plane direction is calculated by the expression given in Eq. 5.4, where m_w is the mass of the infill per unit height *h*, E_{mv} is the vertical modulus of elasticity of masonry and I_w is the moment of inertia of the infill cross-section corresponding to the vertical bending. Eq. 5.4 is:

$$T_a = \frac{2h^2}{\pi}\sqrt{\frac{m_w}{K_{red}\cdot E_{mv}\cdot I_w}} \tag{5.4}$$

It is to be noted that, in evaluating the period of the panel, the reduction in the flexural stiffness due to the IP damage has been considered to obtain a more realistic prediction. For this, the OoP stiffness reduction factor K_{red} proposed by Cavaleri et al. (2019) was used, that is:

$$K_{red} = [\min(1; 0.17 IDR^{-0.67})] \tag{5.5}$$

IDR being the inter-storey drift ratio in percentage experienced by the panel in IP direction. The above equation was validated by the authors against a range of experimental and numerical data.

The second approach is based on the results provided by the numerical analysis depending on the effective stiffness evaluated at one-third of the maximum OoP force $F_{\max,OoP}/3$ and the corresponding displacement $\partial\left(F_{\max,OoP}/3\right)$. In detail, the numerical period is calculated by using the well-known formula for one degree of freedom (dof) system (the equivalent one dof system is that described by the OoP displacement in the center of an infill wall and the corresponding restoring force) given as follows:

$$T_a^* = 2\pi\sqrt{\frac{M^*}{K_{num}}}, \qquad K_{num} = \frac{\left(\frac{F_{\max,OOP}}{3}\right)}{\delta\left(\frac{F_{\max,OOP}}{3}\right)} \tag{5.6}$$

In calculating the vibration period, the participating mass M^* corresponding to the first OoP mode of vibration of the infill wall was taken as 50% of the total mass of the infill wall.

Regarding the choice of mass participation, different values have been adopted in the literature. Normally, to define mass participation, micro-modelling is employed so that the numerically obtained vibration period of the infill wall matches with the experimentally obtained period. Afterward, the equivalency between the results of micro-model and macro-model is established. For example, Di Domenico et al. (2017) used 81% of the total mass based on the recommendation of Kadysiewski and Mosalam (2009). Kadysiewski and Mosalam (2009) derived this value from a modal analysis by considering the OoP motion of an infill wall equivalent to that of a beam element simply supported at two ends. Ricci et al. (2020) used 66% mass as an effective mass considering the OoP mode of an infill wall equivalent to an elastic homogeneous plate whose first vibration mode is described by a sinusoidal shape function. In the same way, Di Trapani et al. (2020)

determined around 55% mass as an effective first mode mass based on a comparison of the stiffness of the elastic plate from a finite element model with the OoP stiffness obtained from the macro-model given by Di Trapani et al. 2018. Likewise, Gesualdi et al. (2020) assumed 80% mass participation to determine the fragility of infill walls in OoP acceleration. The developed macro-model which is used in the current study has a close affinity with the study of Di Trapani et al (2020). Therefore, 50% first mode mass is assumed in this study.

5.3 Range of parameters and base assumptions

In this study, fragility groups have been defined for two groups of URM infill walls: a) infill with solid masonry units, and b) infill with hollow masonry units. Infill wall with solid masonry units has been assumed to have an isotropic property while infill wall with hollow masonry units are considered to have an orthotropic property for simplicity although solid units are also not isotropic truly. The hollow masonry units were further subdivided into two sub-groups with two categories of masonry strength identified: b-1) strong masonry, and b-2) weak masonry. Please refer to Table 5.2 for more details on the classification of masonry.

Additionally, the fragility has been sub-grouped according to the level of IP damage according to IP drift: low (0-0.7%), medium (0.7-1.4%), and high (1.4-2%) respectively. Further categorisation of the fragility is done as per the aspect ratios of infill walls (1.0, 1.25, 1.50 and 1.75).

The range of IP drift for three different levels of IP damage was defined based on the results of extensive parametric analyses performed using the developed macro-element model (Chapter 3). The reduction of OoP strength due to IP damage is largely influenced by the geometrical and mechanical properties of the infill walls. On average, for infill walls of different

characteristics, a low IP damage level corresponds to a loss in OoP strength by no more than 30%, and the medium IP damage level indicates a reduction by almost 60%, while the high IP damage level induces higher loss of OoP strength. The level of OoP strength reduction obtained numerically agrees with experimental results and has been discussed in the previous chapters.

To derive the fragility, only one damage state has been considered in the OoP direction i.e. the damage state of collapse, and consequently, the fragility for OoP collapse is obtained. The infill wall is assumed to collapse conventionally after attaining the peak strength in the OoP direction. Although the infill wall is not likely to collapse when it attains its maximum OoP capacity this is a typical technique in the force-based assessment approach. The collapse is identified by the OoP pseudo acceleration equal to the ratio between the OoP strength and mass. However, as before-mentioned, the Peak ground Acceleration (PGA) has been taken as an Engineering Demand Parameter for the fragility assessment in this study.

Regarding the assumption of the conventional collapse state at the attainment of the maximum OoP strength it has to be said that it is preferred with respect to the safety assessment based on displacement capacity because the prediction of the ultimate OoP displacement is yet difficult and not reliable (discussed in Chapter 2). In different experiments, IP-damaged infill shows higher OoP displacement compared to the case of IP-undamaged infill (e.g. Flanagan and Bennett 1999b; Calvi and Bolognini 2001; Ricci et al. 2018b; De Risi et al. 2019b, etc.), while in many other experiments ultimate displacement capacity is almost same for IP-damaged and undamaged infill wall (e.g. Angel 1994; Akhoundi et al. 2018). However, it is true for all experimental findings that the OoP strength begins to reduce gradually after attaining peak strength. Therefore, maximum OoP strength can be used as a sufficient benchmark to define the safety criteria. Such an approach to

evaluate the safety of the infill wall by using the maximum OoP strength obtained from quasi-static tests against OoP collapse due to seismic forces has been suggested by other researchers too (e.g. Calvi and Bolognini 2001; Da Porto et al. 2015). However, in doing so, it is not to be forgotten that the amplification effect due to the interaction between the infill wall and the frame or due to the position of the infill wall in the structure has to be taken into account.

For the current study, infill walls were assumed to be laterally bounded by square columns of size 300 mm×300 mm and 300 mm×400 mm beams at the top and bottom. Columns are provided with 8 @18 mm longitudinal steel reinforcements while the beams have 3 @16 mm steel reinforcements at the top and bottom. The concrete in the frame members is confined by rectangular stirrups (@ 8 mm) kept at a spacing of 75 mm centre to centre. The effect of confinement, provided by the steel reinforcement, as suggested in Campione et al. (2016), Cavaleri et al. (2017), has been taken into account according to Mander's model (Mander et al. 1988). The yield strength of reinforcement steel is taken as 500 MPa.

It is to be noted that the material and geometrical properties of the RC frames should also be treated as random variables. Practically they can differ a lot. However, for simplicity, the geometric properties of the frames were treated in this study as deterministic because recognized as not influencing the results from the parametric analysis (Chapter 4), and only the strength of concrete was assumed as a random variable. The size of columns used in this study is defined as a minimum size in the case of RC frame buildings by contemporary seismic codes. Also, the minimum stiffness of the frames used in this study is in the range defined by Angel (1994), and taking a higher value (i.e. bigger size of frames) would not change the OoP capacity of the infill

wall which is shown in the last chapter and has also been indicated by other researchers (e.g. Liberatore et al. 2020).

For the solid masonry (case of isotropic), the minimum thickness of infill has been kept as 100 mm while the maximum thickness is assumed to be 200 mm, and for the hollow masonry (case of orthotropic), the thickness varies from 100 mm to 300 mm. The elastic modulus of masonry material is assumed to be 1000 times the value of compressive strength in both isotropic and orthotropic cases according to Eurocode 6 (2005). The main characteristics of the random variables assumed in this study are shown in Table 5.2. Examples of distribution of the compressive strength of masonry for isotropic and orthotropic (both strong and weak masonry) cases are shown in Fig 5.3a-c.

For each case of low, medium and high IP damage, and for each different case of the aspect ratio of the infill wall, 400 different random samples were generated. Inter-storey drift ratio (IDR) which is randomly imposed on the infill wall, is taken as a measure of IP damage. In Fig 5.4a, a sample distribution of IDR to consider three different levels of IP damage is shown while in Fig 5.4b, the distribution of the masonry thickness for the case of solid and hollow unit masonry is shown.

Table 5.2 Distribution of input parameters

Variable	Property	Distribution features
Strength of concrete	Uniform distribution	
	Min (MPa)	20
	Max (MPa)	30
IP damage	Uniform distribution	
	Low level (%)	IDR 0 to 0.7
	Medium level (%)	IDR 0.7 to 1.4
	High Level (%)	IDR 1.4 to 2
Thickness of solid masonry	Uniform distribution	
	Min (mm)	100
	Max (mm)	200
Thickness of hollow masonry	Uniform distribution	
	Min (mm)	100
	Max (mm)	300
Strength of solid masonry a) (Isotropic behavior)	Gaussian distribution	
	Min (MPa)	3.0
	Max (MPa)	7.0
	Mean (μ)	5.0
	Standard deviation (σ)	1.0
Strength of hollow masonry – strong panels b-1) (Orthotropic behavior)	Gaussian distribution	
	Min (MPa)	1.0
	Max (MPa)	6.0
	Mean (μ)	3.5
	Standard deviation (σ)	1.0
Strength of hollow masonry – weak panels b-2) (Orthotropic behavior)	Gaussian distribution	
	Min (MPa)	1.0
	Max (MPa)	3.0
	Mean (μ)	2.0
	Standard deviation (σ)	1.0

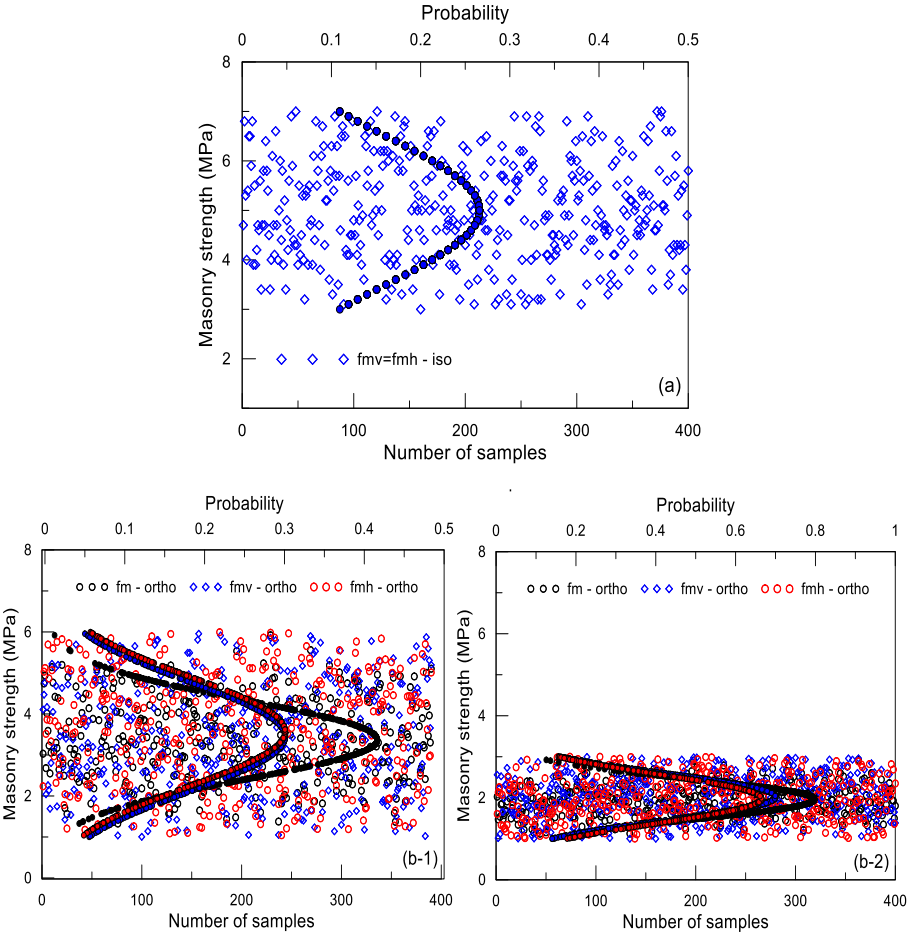

*fmh - ortho, fmv - ortho = Compressive strength of masonry in the horizontal and vertical direction for hollow units

**fm - ortho = Equivalent compressive strength of masonry for hollow units (orthotropic behavior)

***fm - iso = Equivalent compressive strength of masonry for solid units (isotropic behavior)

Figure 5.3 Distribution of the compressive strength of the masonry: a) isotropic case (solid units), b-1) orthotropic case (hollow strong units) and b-2) orthotropic case (hollow weak units)

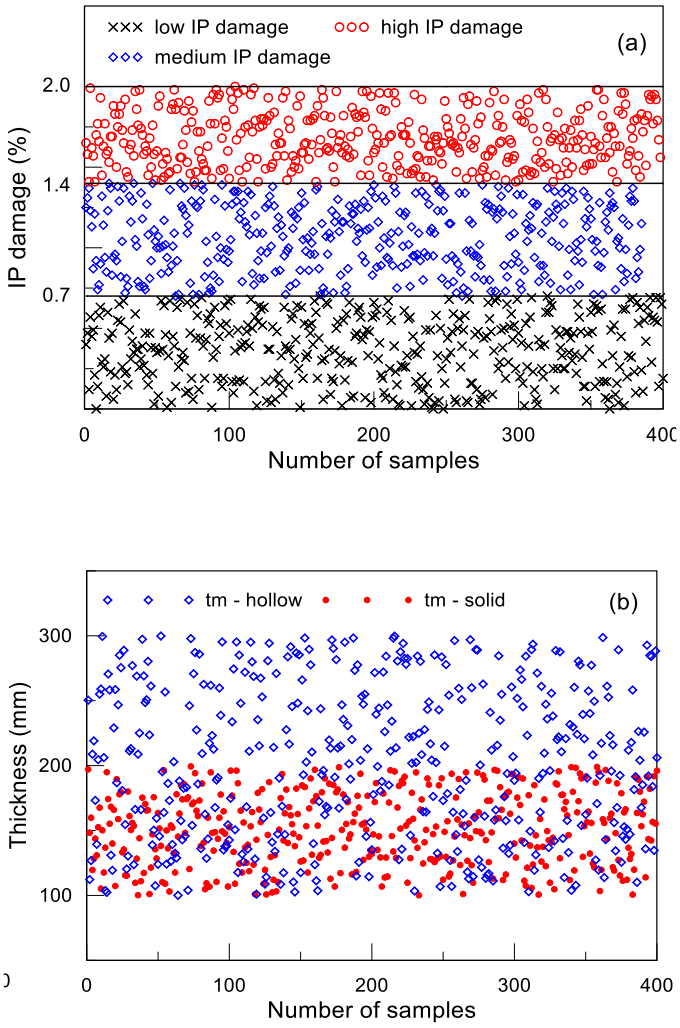

Figure 5.4 Distribution of the a) IP damage, b) thickness for solid and hollow masonry

5.4 Discussion of the results

In this section, the results of the fragility analysis are discussed for all the significant assumptions made. It was assumed a 3-storey moment-resisting RC frame structure with an inter-storey height of 3 m (total height of the

building was 9 m). The fundamental period of the building was 0.39 sec. In this context, the fragility was evaluated considering also the influence of the position of the panel with respect to the floors of the structure, evaluating the PGA at the state of OoP collapse of infill walls placed at the ground storey (first floor) and, at the top storey (third floor) of the reference structure.

In the description of the fragility, the analyses and results were labelled depending upon the type of masonry (i.e. iso and ortho for solid and hollow masonry respectively), the level of IP damage (i.e. ld, md, and hd for low, medium, and high damage respectively), the aspect ratio of infill walls in terms of length-to-height ratio (1.0, 1.25, 1.5, 1.75) and the positioning of the infill panel with respect to the structure (I and III for the first and the third floor respectively). For the case of hollow masonry units, the symbols "s" and "w" indicate strong and weak masonry units respectively. Definitely, as an example, the fragility curve iso_ld_1.0_I indicates the fragility of an infill wall made with solid masonry units, subjected to low IP damage having an aspect ratio 1.0, and placed on the first floor, while, the fragility curve ortho_w_hd_1.5_III indicates the fragility for an infill wall made with hollow masonry weak units subjected to high IP damage for a panel with aspect ratio 1.5, placed on the third floor, and so on. In addition, I or I* and III or III* are used respectively to give distinction between results calculated by using the vibration period calculated by Eq. 5.4 (analytical evaluation) or Eq. 5.6 (by numerical results).

5.4.1 Influence of the fundamental period in the evaluation of the PGA

The PGAs obtained by using the two different approaches before mentioned for the evaluation of the vibration period of infill walls in the OoP direction were compared highlighting the sensitivity to the interaction with the

response spectrum. In this comparison, the infills placed on the third floor of the low-rise reference structure were considered.

First, it has to be noticed that, as expected, the OoP pseudo acceleration, as well as the PGA, decreased with the increasing level of IP damage and the increasing of the aspect ratio. For a given level of IP damage, infill panels with an aspect ratio 1.0 provided higher OoP capacity than panels with aspect ratios of 1.25, 1.5 and 1.75. At the same time, for a given value of aspect ratio, infill panels experiencing low levels of IP damage (0.0-0.7%) showed higher capacity compared to that obtained by increasing the level of IP damage (medium and high – drift in the ranges 0.7-1.4% and 1.4-2.0% respectively).

Another consideration has to be done regarding the different responses obtained depending on the type of masonry walls. Overall, it was noticed that hollow masonry showed PGA values higher than solid masonry. This is due to the higher thickness coupled with a low mass of the panels that provided higher pseudo-accelerations and lower vibration periods. To give an overall frame about the values obtained from the analyses, Table 5.3 shows the results for each case of analysis in terms of median values of the PGA and mean values for the vibration period for the two approaches. It is reminded that T_a and T_a^* refers to the vibration period calculated by Eq. 5.4 and Eq. 5.6 respectively.

At the same time, the vibration period of the infill panels was affected by the IP damage and aspect ratio. The increasing of the vibration period leads to a different positioning in the response spectrum. It was noticed that with the increasing level of IP damage and the increase of the aspect ratio, the vibration period of the panel in some cases changes from the first branch of the response spectrum (T<aT1) to the second (aT1<T<bT1). This requires to use a different equation in the evaluation of PGA as shown in Fig 5.2. This was observed in

most of the cases of analysis. Having said this, by using Eq. 5.4, the period of vibration was not much affected by the aspect ratio but only by the level of IP damage (it can be seen in Table 5.3). But while using Eq. 5.6, the vibration period was significantly influenced both by aspect ratio and IP damage level because the numerical model takes into account the change in stiffness directly.

This causes high scatter between T_a and T_a^* that can make the former up to two times the latter. These variations are clearly highlighted in Fig 5.5 and Fig 5.6 for hollow strong and weak masonry units and Fig 5.7 for solid masonry units.

Table 5.3 Results of the Monte Carlo simulations for infill walls placed at the third floor of the reference structure

Solid masonry – iso (isotropic)												
	low IP damage				medium IP damage				high IP damage			
	Analytical		Numerical		Analytical		Numerical		Analytical		Numerical	
Aspect ratio	PGA (g)	Ta (sec)	PGA (g)	T_a^* (sec)	PGA (g)	Ta (sec)	PGA (g)	T_a^* (sec)	PGA (g)	Ta (sec)	PGA (g)	T_a^* (sec)
1	2.32	0.11	2.70	0.06	1.11	0.16	1.68	0.09	0.67	0.19	0.92	0.12
1.25	1.78	0.11	2.29	0.08	0.96	0.15	1.25	0.11	0.48	0.19	0.59	0.13
1.5	1.59	0.10	1.57	0.09	0.69	0.16	0.67	0.13	0.43	0.19	0.45	0.15
1.75	1.25	0.10	1.11	0.10	0.51	0.16	0.46	0.15	0.32	0.19	0.32	0.19
Hollow masonry - ortho (orthotropic) strong masonry units												
1	3.96	0.08	4.78	0.04	1.96	0.11	2.49	0.07	1.22	0.13	1.56	0.09
1.25	3.59	0.07	3.98	0.05	1.50	0.11	1.79	0.08	1.03	0.12	1.14	0.10
1.5	2.64	0.07	2.79	0.06	1.22	0.11	1.29	0.10	0.80	0.13	0.81	0.13
1.75	2.37	0.07	2.30	0.08	1.00	0.11	1.03	0.12	0.63	0.13	0.55	0.15
Hollow masonry - ortho (orthotropic) weak masonry units												
1	1.73	0.09	2.02	0.07	0.70	0.14	0.92	0.10	0.50	0.16	0.68	0.12
1.25	1.62	0.09	1.81	0.07	0.66	0.14	0.82	0.10	0.45	0.16	0.57	0.13
1.5	1.41	0.09	1.56	0.08	0.55	0.14	0.68	0.11	0.38	0.17	0.44	0.14
1.75	1.37	0.10	1.47	0.08	0.51	0.14	0.65	0.12	0.33	0.17	0.37	0.14

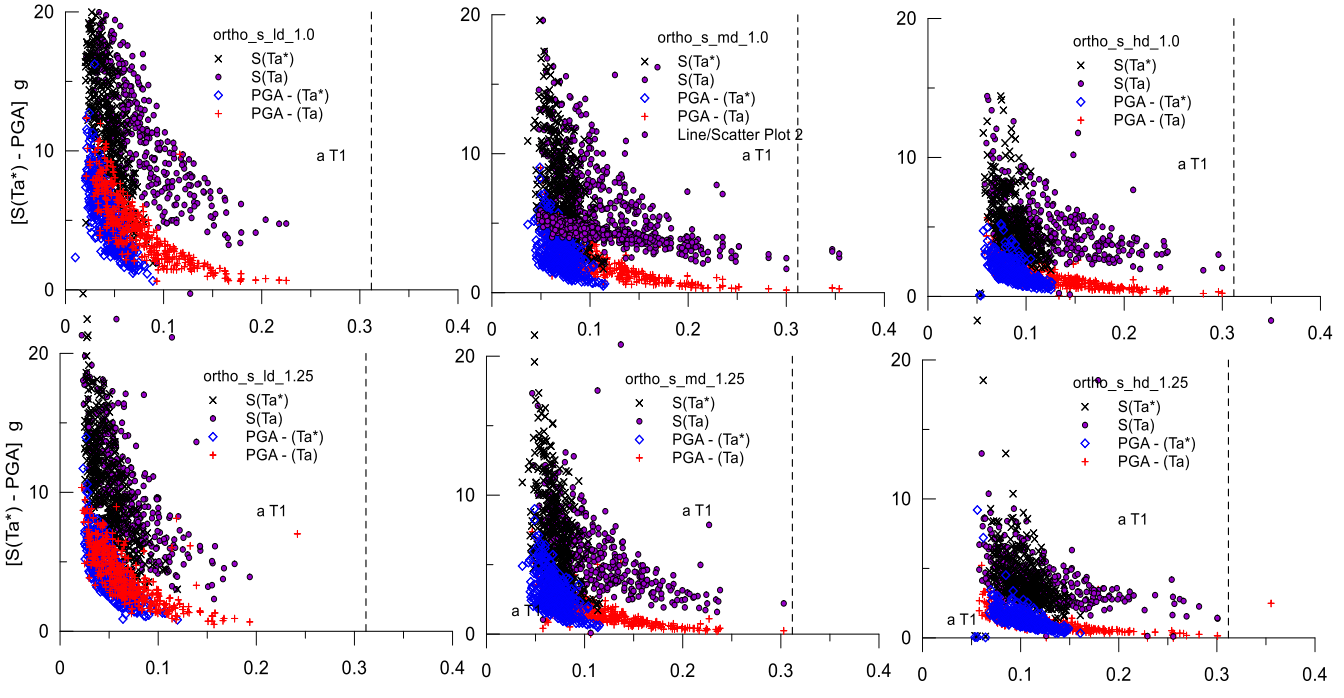
ortho_s_ld_1.0
ortho_s_md_1.0
ortho_s_hd_1.0
ortho_s_ld_1.25
ortho_s_md_1.25
ortho_s_hd_1.25
S(Ta*)
S(Ta)
PGA - (Ta*)
PGA - (Ta)
Line/Scatter Plot 2
a T1
[S(Ta*) - PGA] g
Vibration period of infill (sec)

a)

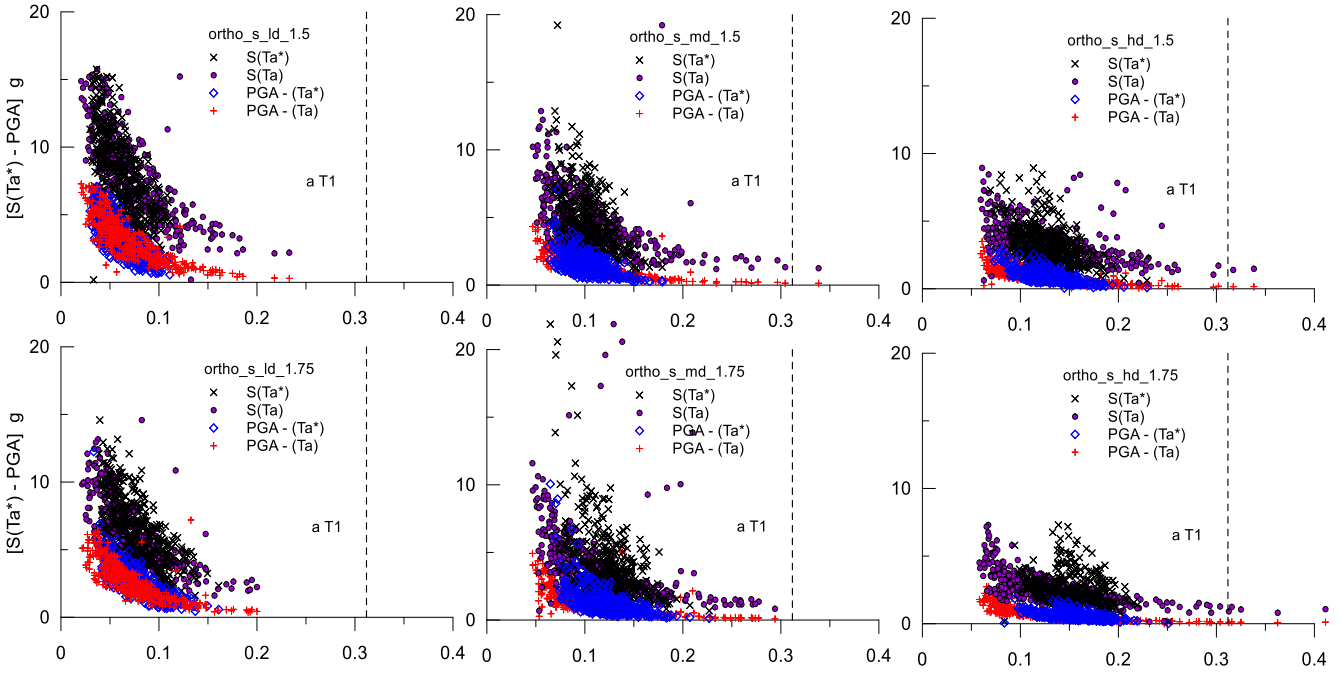

b)

Figure 5.5 Results of the Monte Carlo simulations: pseudo-acceleration and PGA depending on the vibration period of the infill walls for the case of orthotropic - strong masonry units: a) for aspect ratio 1.0 and 1.25; b) for aspect ratio 1.5 and 1.75

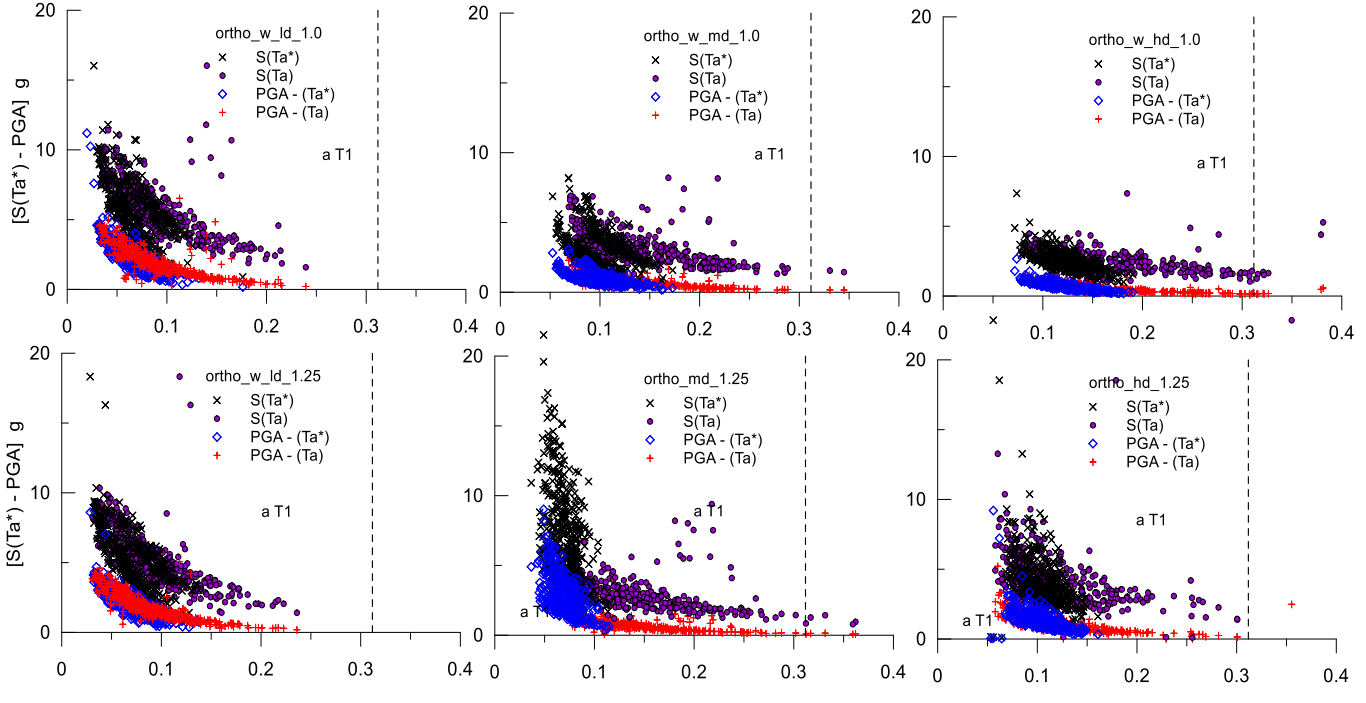
ortho_w_ld_1.0
ortho_w_md_1.0
ortho_w_hd_1.0
ortho_w_ld_1.25
ortho_md_1.25
ortho_hd_1.25
S(Ta*)
S(Ta)
PGA - (Ta*)
PGA - (Ta)
a T1
[S(Ta*) - PGA] g
Vibration period of infill (sec)

a)

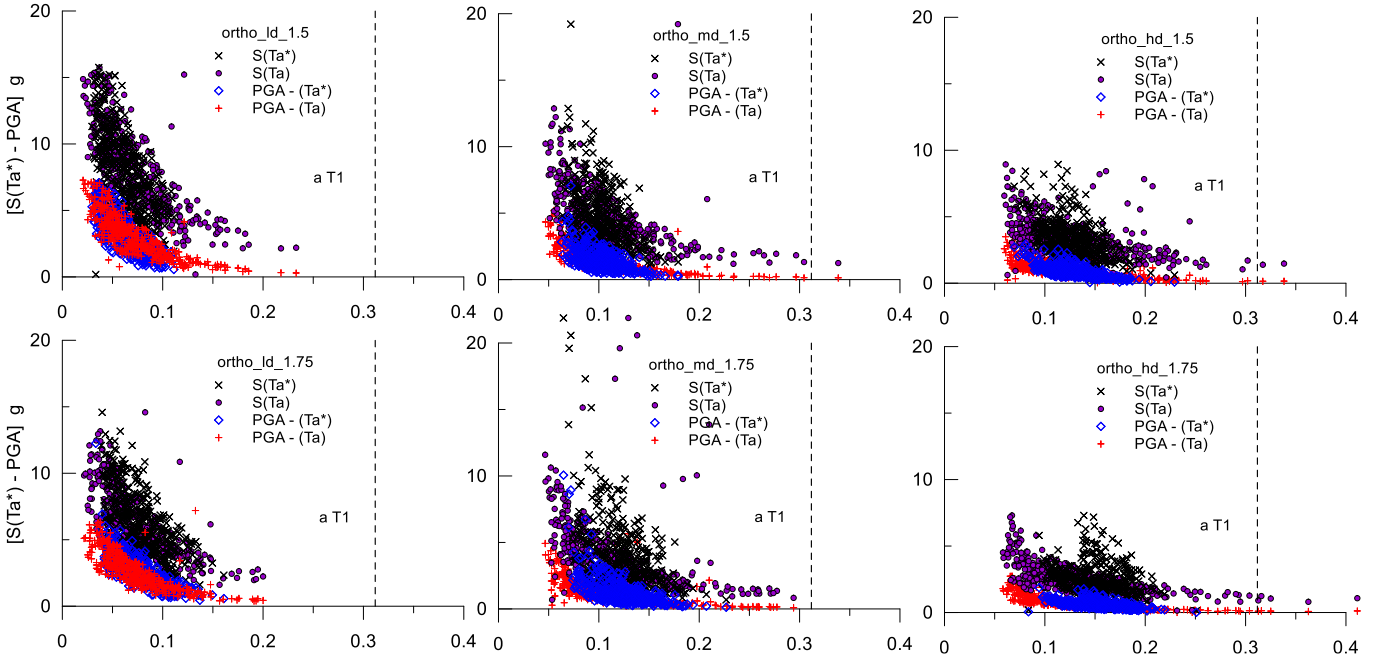

b)

Figure 5.6 Results of the Monte Carlo simulations: pseudo-acceleration and PGA depending on the vibration period of the infill walls for the case of orthotropic - weak masonry units: a) for aspect ratio 1.0 and 1.25; b) for aspect ratio 1.5 and 1.75

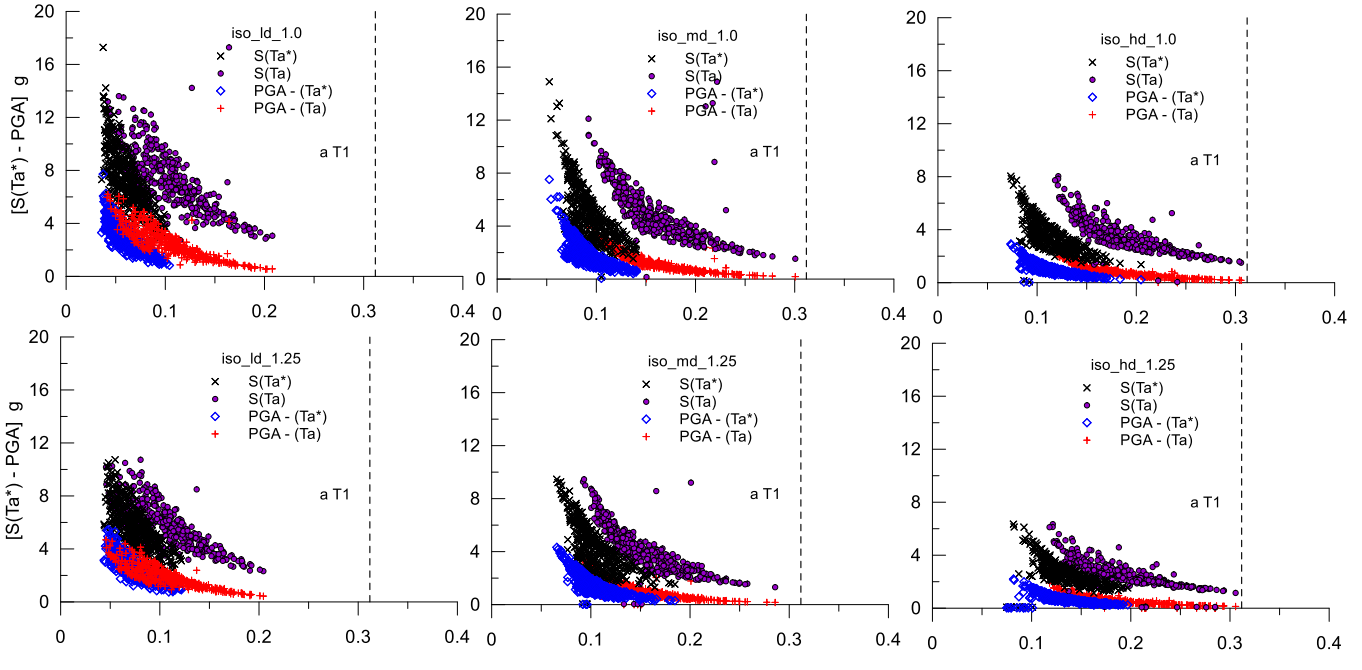
iso_ld_1.0
iso_md_1.0
iso_hd_1.0
iso_ld_1.25
iso_md_1.25
iso_hd_1.25
S(Ta*)
S(Ta)
PGA - (Ta*)
PGA - (Ta)
a T1
[S(Ta*) - PGA] g
Vibration period of infill (sec)

a)

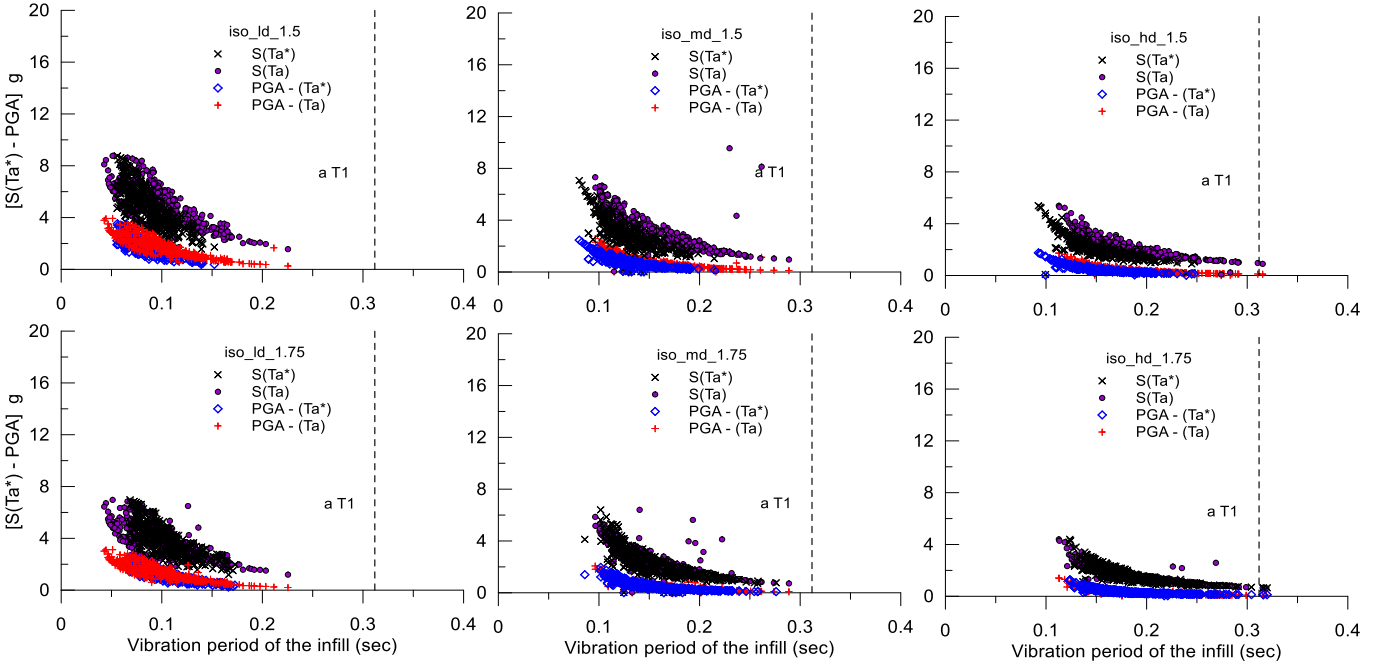

b)

Figure 5.7 Results of the Monte Carlo simulations: pseudo-acceleration and PGA depending on the vibration period of the infill walls for the case of isotropic masonry: a) for aspect ratio 1.0 and 1.25; b) for aspect ratio 1.5 and 1.75

To focus more on the variation of the vibration period, they are plotted in Fig 5.8 and Fig 5.9 for the cases of hollow (strong and weak masonry units respectively) and Fig 5.10 for solid masonry units. In the figures, the vibration periods are shown for each case of analysis and are also related to the different branches of the response spectrum.

Unfortunately, there are not many experiments where the OoP vibration period of the infill wall is measured. In one experiment by Onat et al. (2018) where the infilled frame was tested in a shake table under bidirectional motions, an infill wall of length 5600 mm and height of 2250 mm (aspect ratio of 2.5) made of hollow clay brick units (thickness = 220 mm) showed a period of 0.11s in a forced -vibration test at IP-undamaged condition. The period increased gradually with progressive damage with the application of high-intensity motions. When IP drift experienced by the infilled frame was almost 1.2%, the period increased to 0.32s. This shows that the change in the vibration period is significantly affected by the level of IP damage. Although the aspect ratio of infill used in this experiment is not investigated in the current study, the observed period is in the range obtained from the numerical analyses.

Few other cases of measurements of the OoP vibration period in the strip of infill walls (especially partition walls not surrounded by frames completely) can be found in Rabinovitch and Madah (2011) and Petrone et al. (2014). Ta = 0.125s and Ta = 0.03s were observed in the former and later case. However, the comparison may not be suitable for cases of infill walls investigated in this study. In another test, Furtado et al. (2016) determined a fundamental period of about 0.04s and 0.032s for infill walls of thickness 150 mm and 100 mm respectively. The infill had a length of 4200 mm and a height of 2300 mm (aspect ratio of 1.83) and was made with hollow clay brick. This represents a much stiffer wall compared to Onat et al. (2018).

For the above discussion, it is clear that the vibration period of the infill wall is still a subject of further investigation. Nevertheless, it can be said that the variation in the properties of the infill wall makes a significant difference in their values and this is captured more by the numerical models rather than the analytical approach. Therefore, in the subsequent results regarding the evaluation of the fragility curves, it was assumed to evaluate the PGA by using the vibration period calculated from the numerical data.

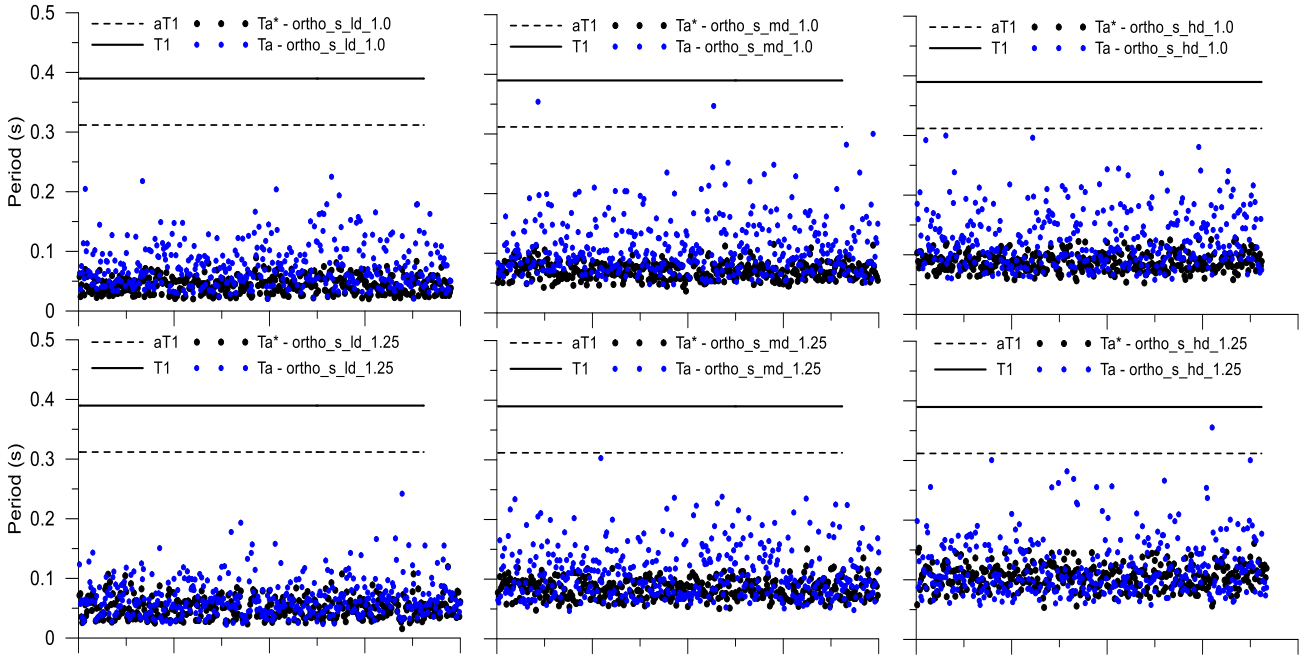
aT1
T1
Ta* - ortho_s_ld_1.0
Ta - ortho_s_ld_1.0
aT1
T1
Ta* - ortho_s_md_1.0
Ta - ortho_s_md_1.0
aT1
T1
Ta* - ortho_s_hd_1.0
Ta - ortho_s_hd_1.0
aT1
T1
Ta* - ortho_s_ld_1.25
Ta - ortho_s_ld_1.25
aT1
T1
Ta* - ortho_s_md_1.25
Ta - ortho_s_md_1.25
aT1
T1
Ta* - ortho_s_hd_1.25
Ta - ortho_s_hd_1.25
Period (s)
Period (s)
0
0.1
0.2
0.3
0.4
0.5
Number of samples

a)

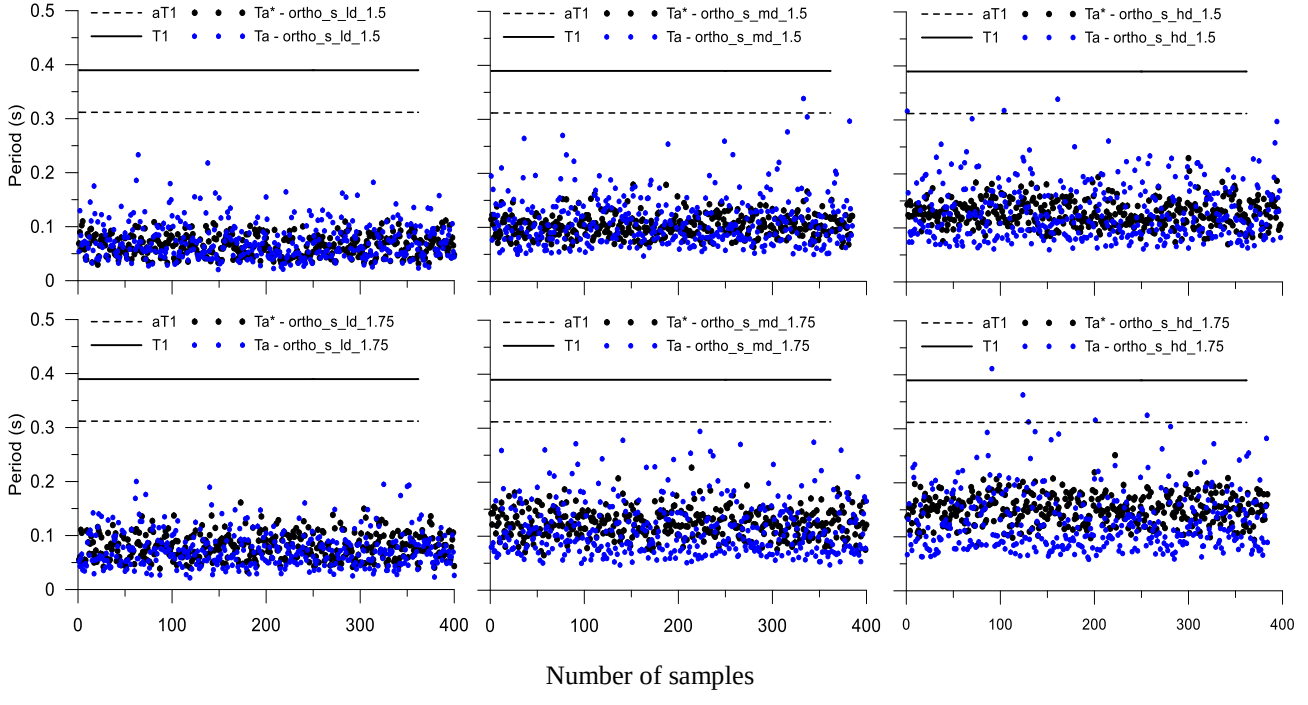

b)

Figure 5.8 Vibration period of the infill walls for all the cases of orthotropic - strong masonry units: a) for aspect ratio 1.0 and 1.25; b) for aspect ratio 1.5 and 1.75

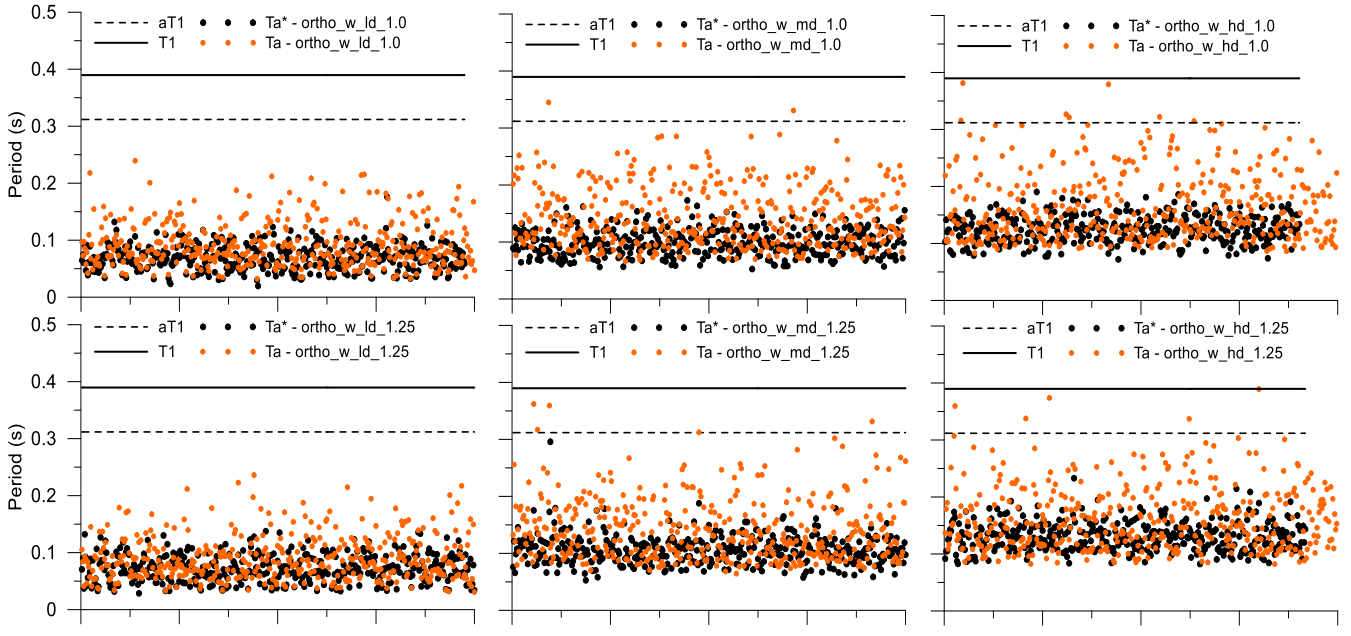
aT1
T1
Ta* - ortho_w_ld_1.0
Ta - ortho_w_ld_1.0
aT1
T1
Ta* - ortho_w_md_1.0
Ta - ortho_w_md_1.0
aT1
T1
Ta* - ortho_w_hd_1.0
Ta - ortho_w_hd_1.0
aT1
T1
Ta* - ortho_w_ld_1.25
Ta - ortho_w_ld_1.25
aT1
T1
Ta* - ortho_w_md_1.25
Ta - ortho_w_md_1.25
aT1
T1
Ta* - ortho_w_hd_1.25
Ta - ortho_w_hd_1.25
Period (s)
0.5
0.4
0.3
0.2
0.1
0
Number of samples

a)

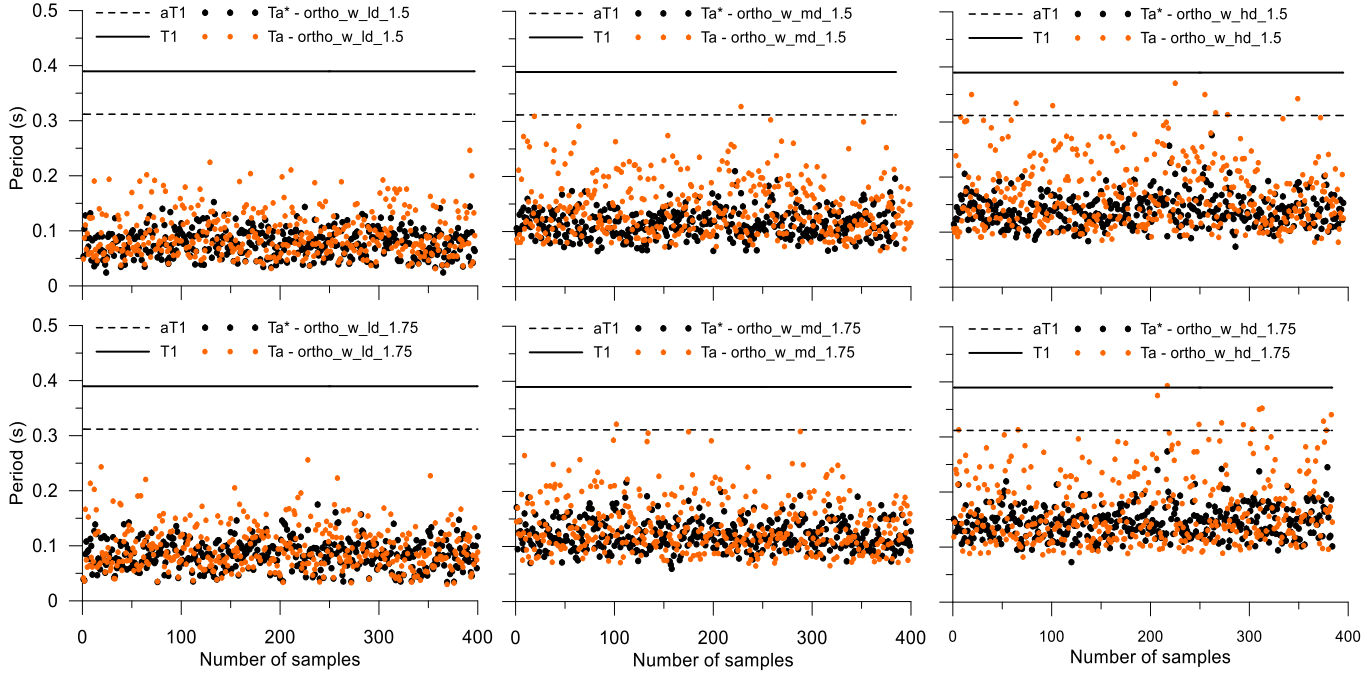

b)

Figure 5.9 Vibration period of the infill walls for all the cases of orthotropic - weak masonry units: a) for aspect ratio 1.0 and 1.25; b) for aspect ratio 1.5 and 1.75

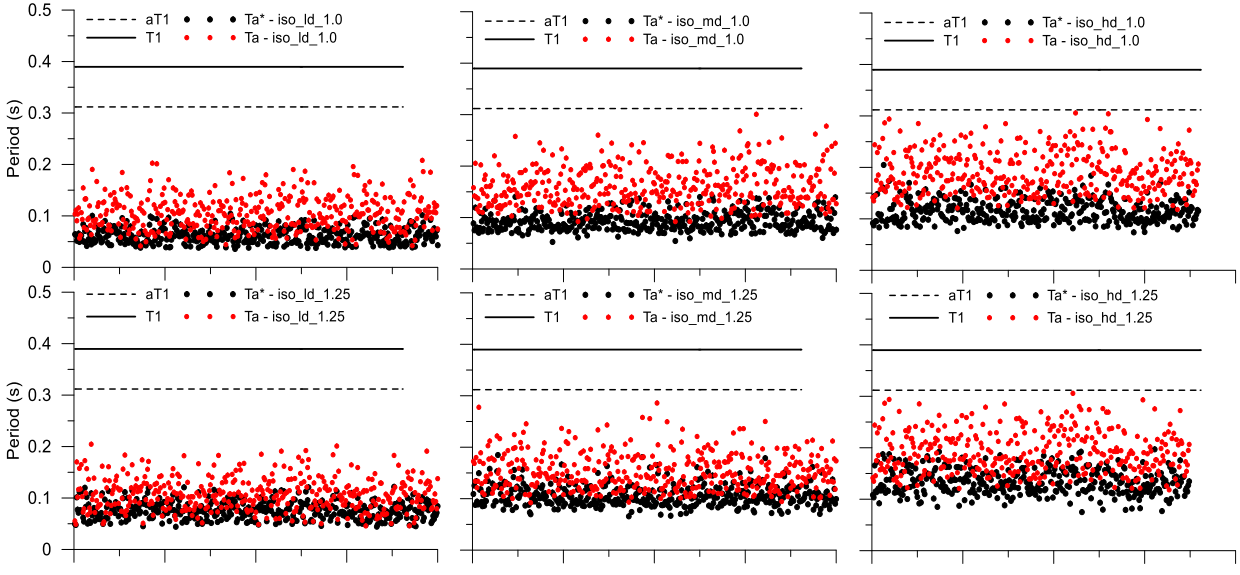
aT1
T1
Ta* - iso_ld_1.0
Ta - iso_ld_1.0
aT1
T1
Ta* - iso_md_1.0
Ta - iso_md_1.0
aT1
T1
Ta* - iso_hd_1.0
Ta - iso_hd_1.0
aT1
T1
Ta* - iso_ld_1.25
Ta - iso_ld_1.25
aT1
T1
Ta* - iso_md_1.25
Ta - iso_md_1.25
aT1
T1
Ta* - iso_hd_1.25
Ta - iso_hd_1.25
Period (s)
0
0.1
0.2
0.3
0.4
0.5
Number of samples

a)

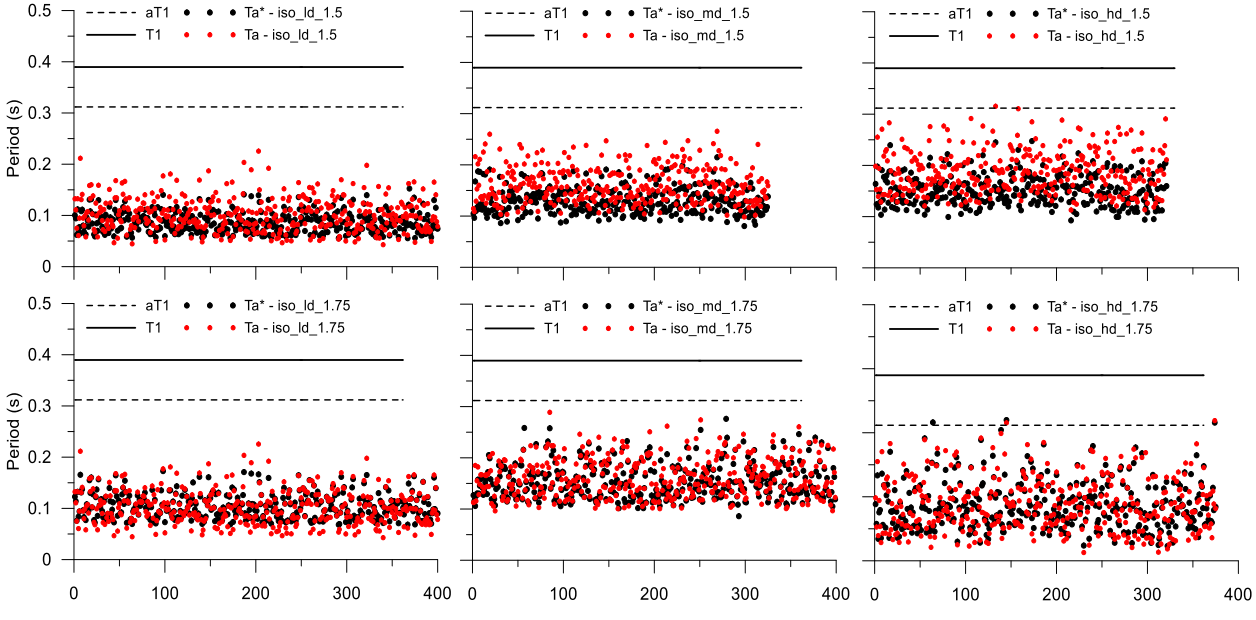

b)

Figure 5.10 Vibration period of the infill walls for all the cases of isotropic masonry: a) for aspect ratio 1.0 and 1.25; b) for aspect ratio 1.5 and 1.75

5.4.2 OoP fragility curves

In this section, the OoP fragility curves obtained by employing the proposed procedure, are discussed focusing on the influence of the different assumptions made during the investigation, which are as follows:

1. aspect ratio;
2. level of IP damage;
3. positioning of the infill panel with respect to the structure;
4. type of masonry (solid and hollow units).

The results in terms of fragility curves obtained for solid and hollow units are shown in Figs 5.11-5.13. In these figures, the fragility curves are shown for panels placed on both the first floor and the third floor, considering all the three levels of IP damage (low, medium, high), depending on the aspect ratio of the infill walls. The fragility curves are obtained based on the median and the log-standard deviation evaluated as described in the previous sections. The values obtained for each case of analysis are shown in Table 5.4.

The fragility for the panels placed at the top of the reference structure (third floor) resulted to be higher compared to that at the base (first floor) for the same level of IP damage considered. This is due to higher amplification of the ground acceleration at the top level than at the bottom. Although it is likely to have less IP damage on the top floor than at the bottom due to smaller inter-story drift, this serves for comparison with respect to the position of the infill wall in the building for equal IP damage. OoP collapse depends upon the combined effect of IP drift and OoP acceleration demands at the level of the infill wall. At the same time, the fragility appeared higher when the aspect ratio increased. Overall, what was described above was observed for both types of infills made with hollow and solid masonry units.

In detail, for aspect ratio 1.0, the PGA (median) values at the first and the third floor resulted in 4.24 g and 2.70 g for the infills made with solid units,

while for the case of hollow masonry units, the PGA resulted in 7.52 g and 4.78 g respectively in the case of strong masonry units and 3.12 g and 2.02 g respectively in the case of weak masonry units. By increasing the aspect ratio from 1.0 to 1.75 and by increasing the level of IP damage from low to high, it was observed that the PGA values dropped to 0.40 g and 0.32 g for the solid masonry units, 0.86 g and 0.55 g for the hollow strong masonry units and 0.59 g and 0.37 g for the hollow weak masonry units. This means that the fragility of infill with an aspect ratio of 2.0 or larger is even higher. These results are very important in the view of showing the high variability depending upon different assumptions.

Table 5.4 Results of the Monte Carlo simulations for infill walls placed on the third floor of the reference structure

PGA iso (g)									
	ld I	ld III		md I	md III		hd I	hd III	
Aspect ratio	median		std dev	median		std dev	median		std dev
1	4.24	2.70	1.49	2.13	1.68	1.72	1.44	0.92	1.70
1.25	2.90	2.29	1.50	1.59	1.25	2.00	0.92	0.59	2.01
1.5	2.46	1.57	1.53	1.06	0.67	2.15	0.71	0.45	1.81
1.75	1.74	1.11	1.58	0.73	0.46	2.24	0.40	0.32	1.65
PGA ortho (g) – strong panels									
1	7.52	4.78	1.63	3.92	2.49	1.66	2.45	1.56	1.63
1.25	6.25	3.98	1.64	2.81	1.79	1.73	1.79	1.14	1.77
1.5	4.38	2.79	1.67	2.02	1.29	1.73	1.27	0.81	1.73
1.75	3.48	2.30	1.67	1.31	1.03	1.97	0.86	0.55	1.70
PGA ortho (g) – weak panels									
1	3.18	2.02	1.66	1.44	0.91	1.58	1.07	0.67	1.57
1.25	2.84	1.81	1.65	1.29	0.82	1.65	0.90	0.57	1.62
1.5	2.45	1.56	1.63	1.07	0.68	1.63	0.70	0.45	1.59
1.75	2.22	1.47	1.62	0.82	0.65	1.65	0.59	0.37	1.62

The influence of the aspect ratio is much evidenced in Figs 5.14–5.16 for both types of masonry i.e. solid and hollow. The figures show the curves for the same level of IP damage and the same floor level, by varying only the aspect ratio. It can be noticed that fragility increases with the increase of the aspect ratio from 1.0 to 1.75. To give an example, in the case of solid masonry units and for a medium level of IP damage, the medium values of the PGA at collapse varied from 2.13 g and 1.68 g to 0.73 g and 0.46 g for the infill panels placed at the first and the third floor respectively. Similarly, for hollow strong masonry units, the variation of the PGA was from 3.92 g and 2.49 g to 1.31 g and 1.03 g respectively, while for hollow weak masonry units, the PGA dropped from 1.44 g and 0.91 g to 0.82 g and 0.65 g with increasing aspect ratio for infill panels placed at the first and the third floor respectively.

Finally, the comparisons of the fragility obtained for solid and hollow unit masonries are shown in Figs 5.17–5.19 highlighting the performances of different types of infills for a given level of IP damage. The results indicate that the probability of collapse is lower in all the cases of hollow strong masonry units. The reason, as described in the previous section, is due to the lower weight of the panels and the corresponding high pseudo-acceleration that provides also the highest values of PGA. This can be observed from the results available in Table 5.4. Different considerations can be done in the case of hollow weak masonry units, in which the fragility resulted comparable to that obtained for masonry walls with solid units due to the lower strength of the masonry itself.

Based on the results, it can be stated that, in the absence of previous IP damage, the infilled frames provide high strength and high PGA in the out-of-plane direction. Consequently, lower vulnerability is obtained. On the other hand, in the presence of previous IP damage, regardless of whether it is medium or high, the strength in the OoP direction drops to critical values,

providing the infilled frames very high vulnerability for low values of PGA, especially on higher floors and, for the high values of aspect ratio.

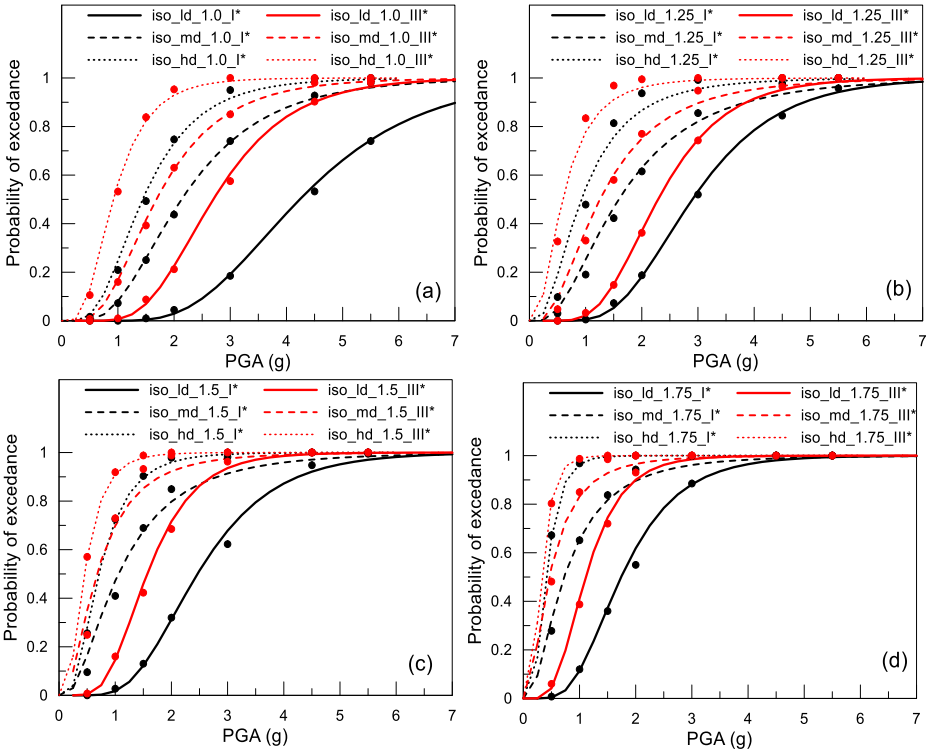

Figure 5.11 Fragility curves for solid masonry including low, medium and high IP damage for different aspect ratio: a) 1.0, b) 1.25, c) 1.5, d) 1.75

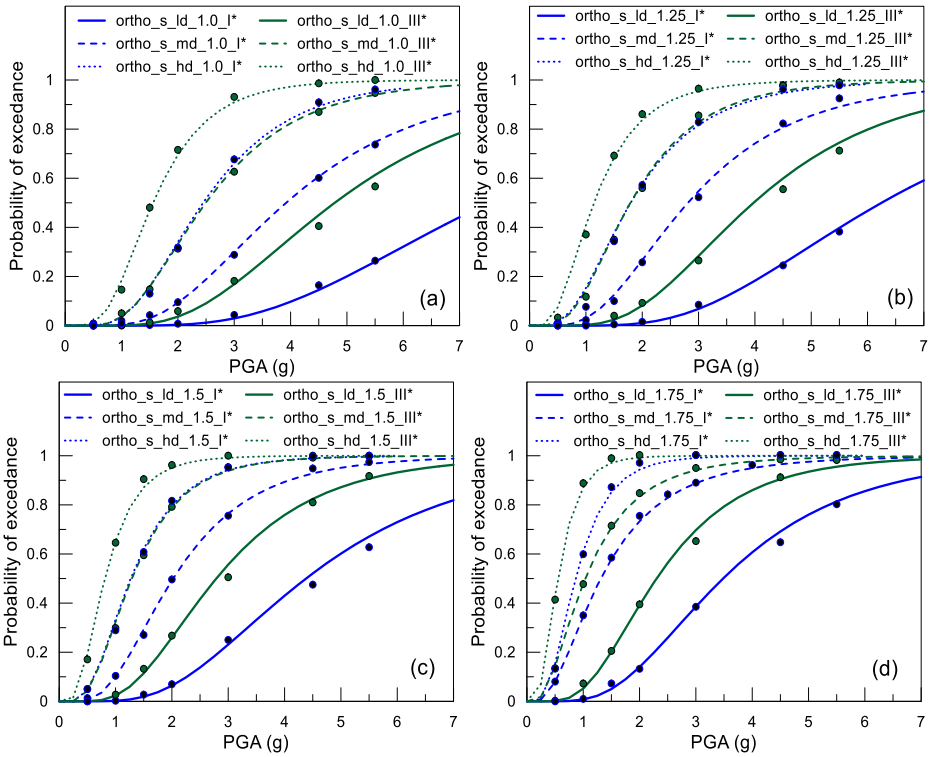

Figure 5.12 Fragility curves for hollow strong masonry units including low, medium and high IP damage for different aspect ratio: a) 1.0, b) 1.25, c) 1.5, d) 1.75

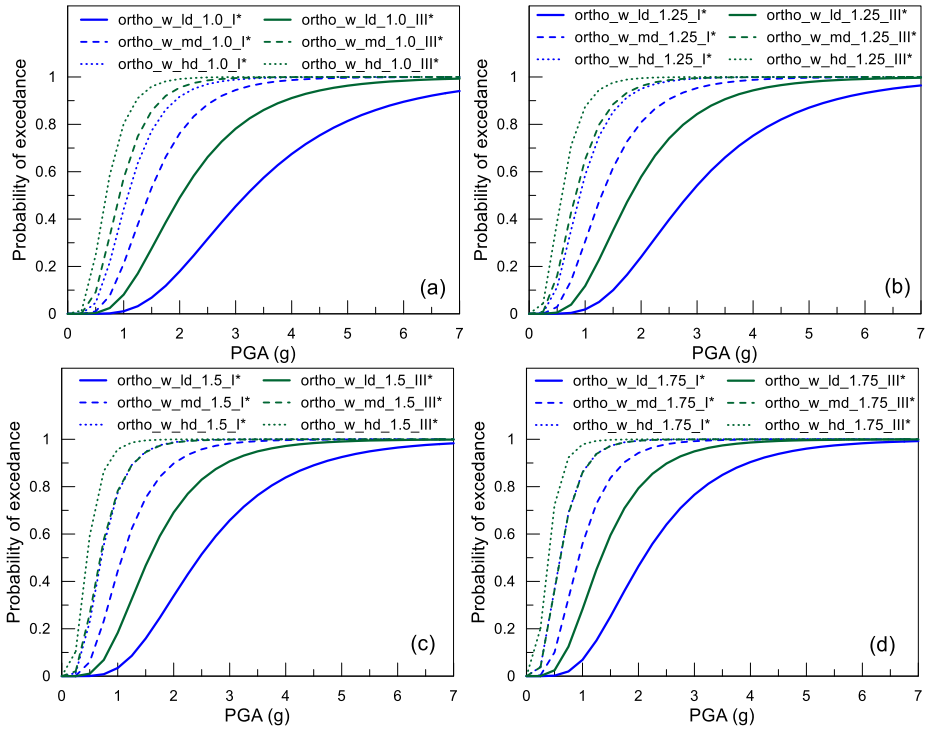

Figure 5.13 Fragility curves for hollow weak masonry units including low, medium and high IP damage for different aspect ratio: a) 1.0, b) 1.25, c) 1.5, d) 1.75

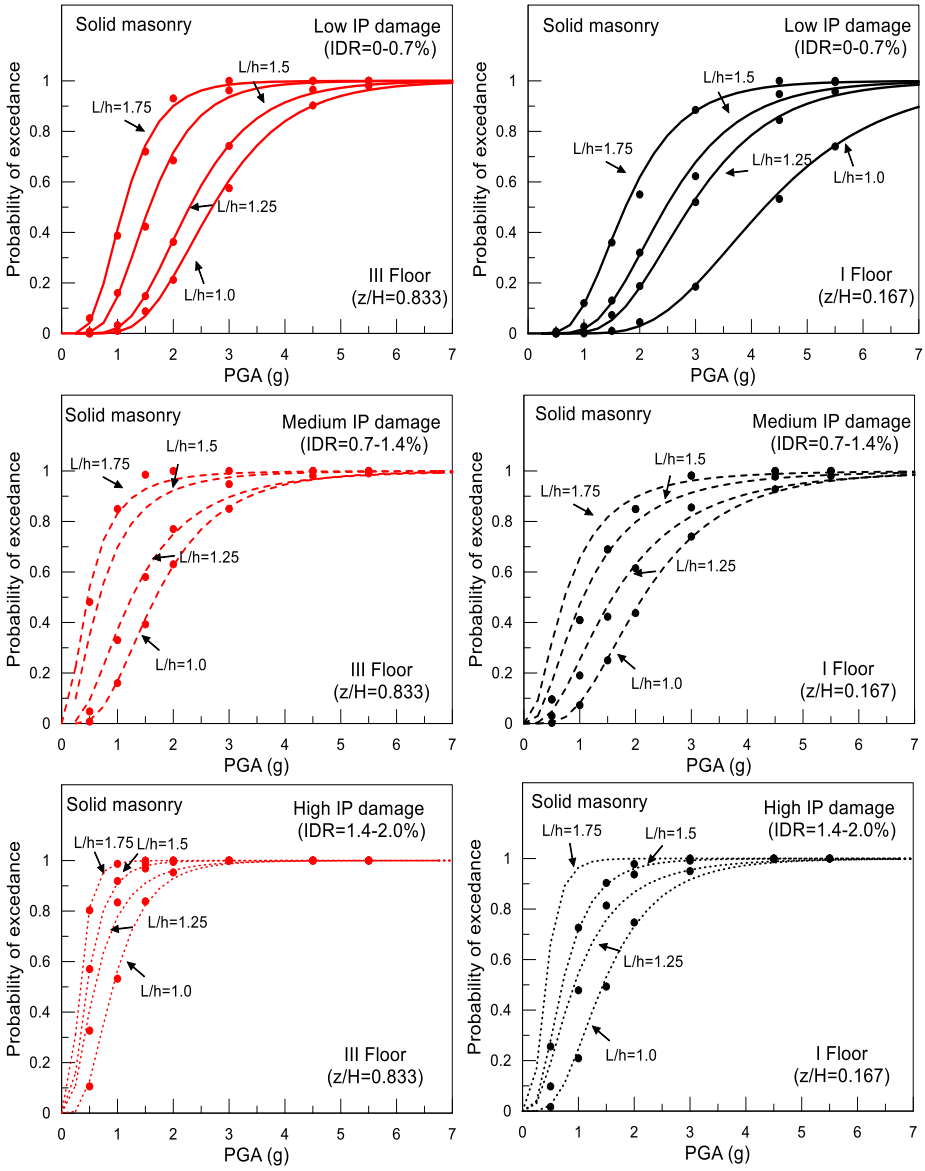

Figure 5.14 Fragility curves for solid masonry: influence of the aspect ratio for a given level of IP damage

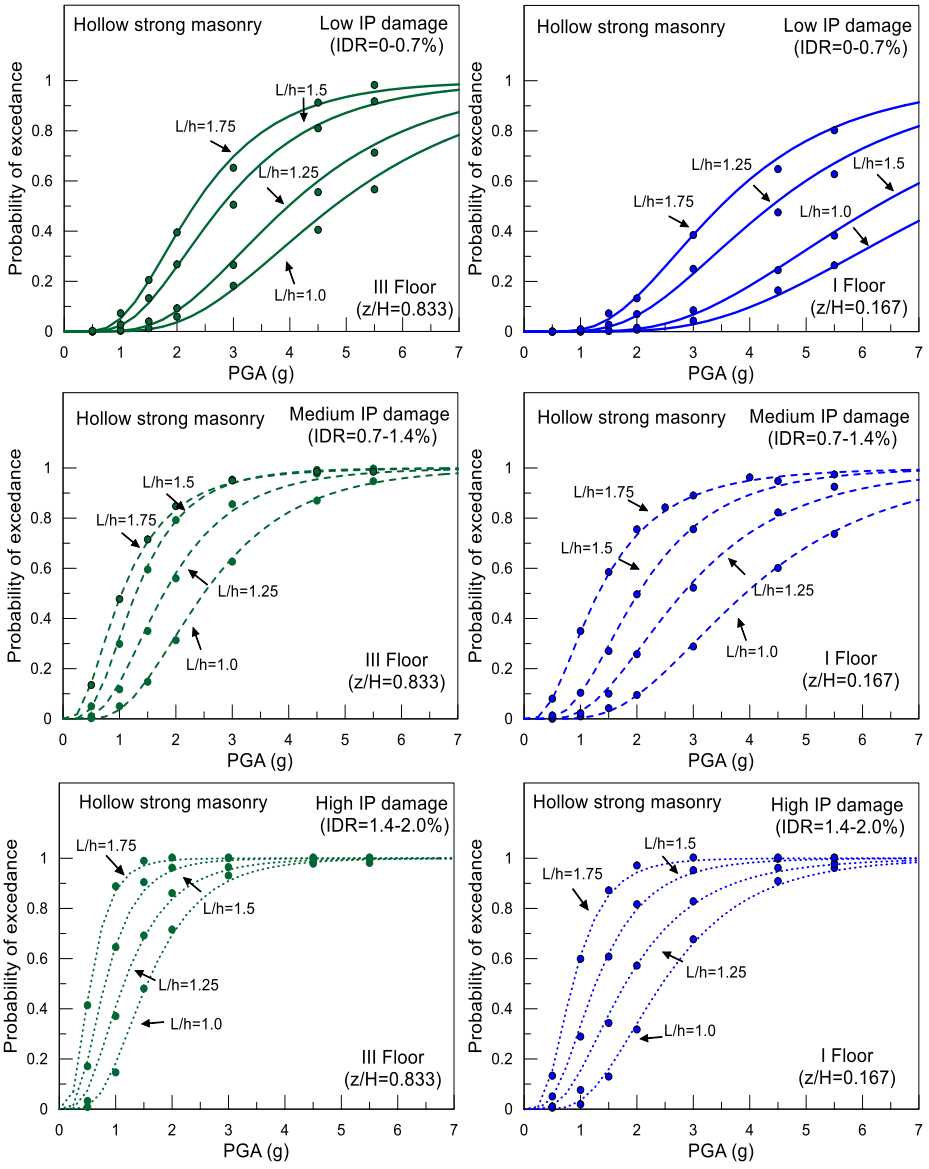

Figure 5.15 Fragility curves for hollow strong masonry units: influence of the aspect ratio for a given level of IP damage

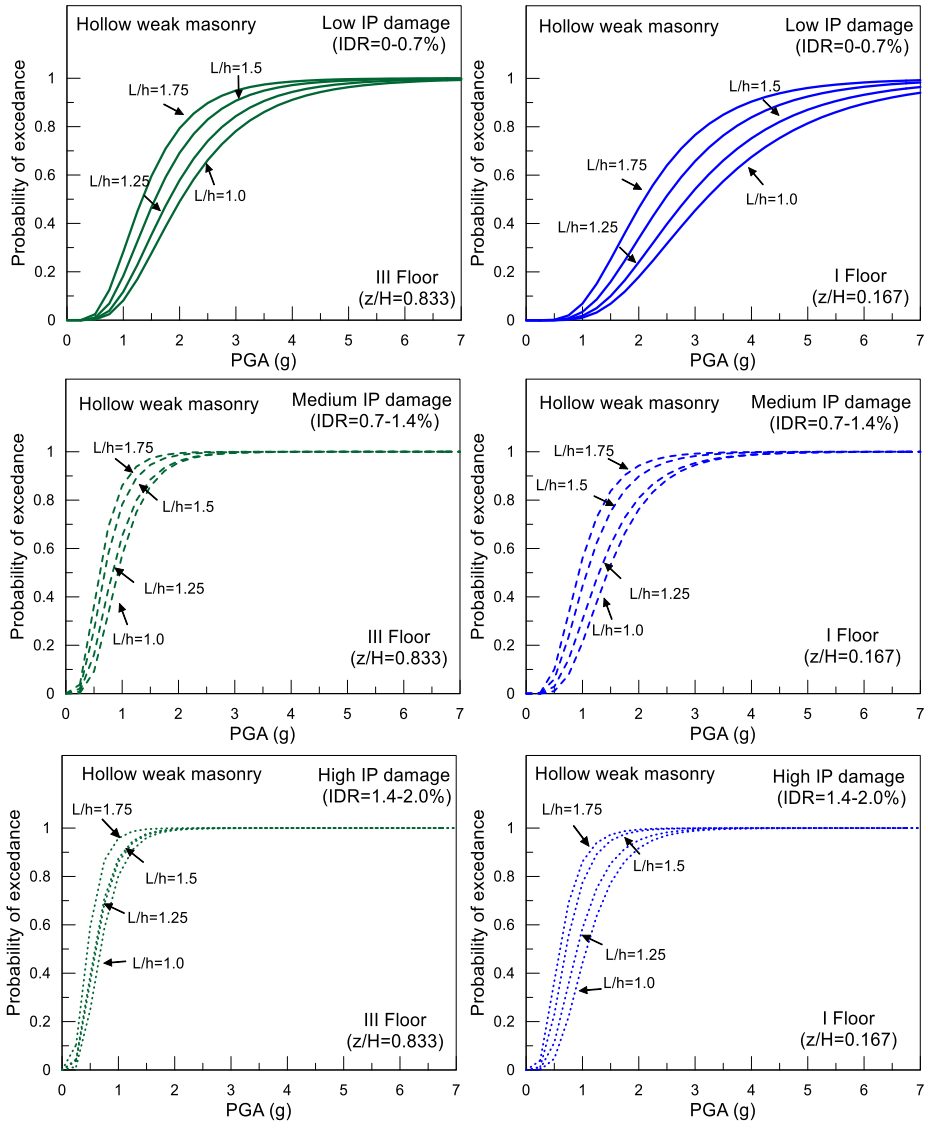

Figure 5.16 Fragility curves for hollow weak masonry units: influence of the aspect ratio for a given level of IP damage

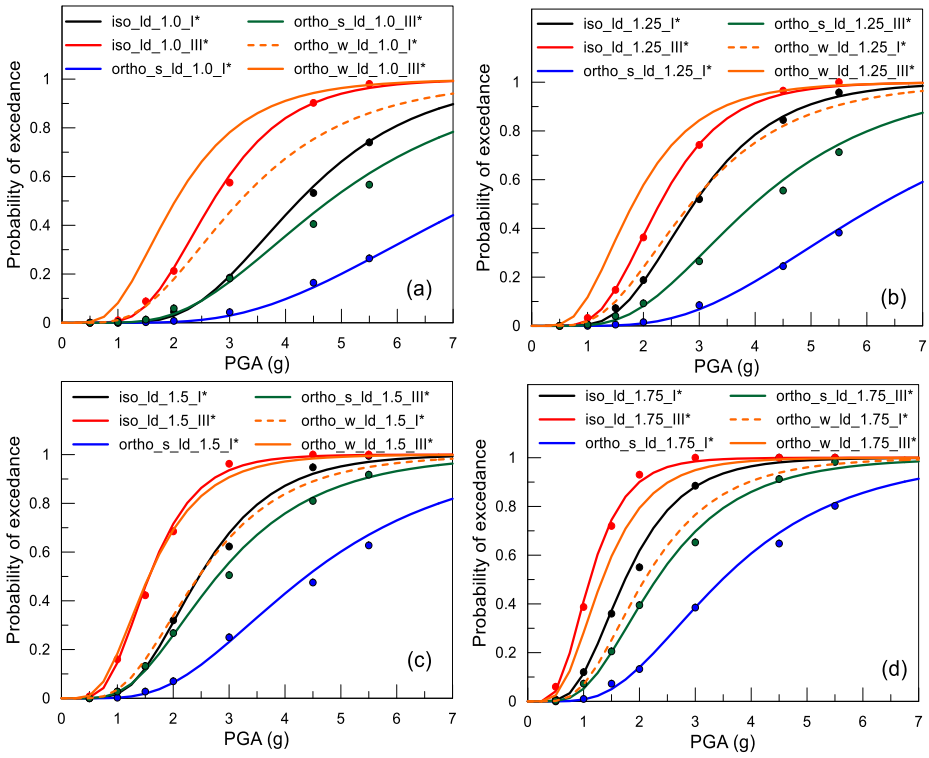

Figure 5.17 Influence on the fragility of the type of masonry for low level of IP damage (f_m of 5 MPa, 3.5 MPa and 2 MPa for solid and hollow strong and weak masonry respectively)

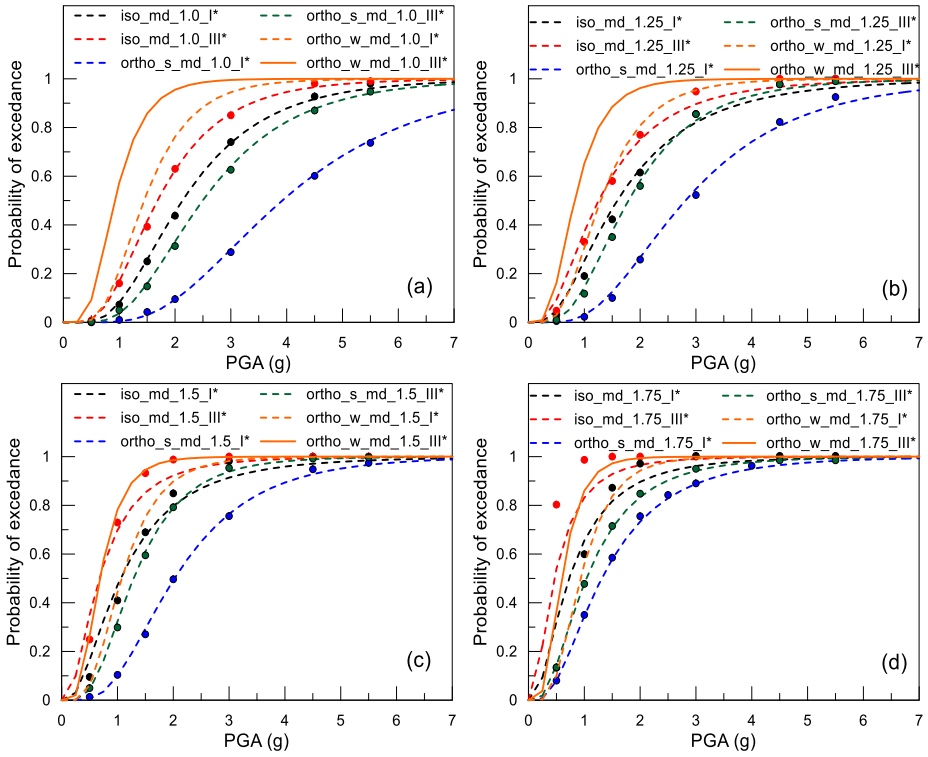

Figure 5.18 Influence on the fragility of the type of masonry for medium level of IP damage (f_m of 5 MPa, 3.5 MPa and 2 MPa for solid and hollow strong and weak masonry respectively)

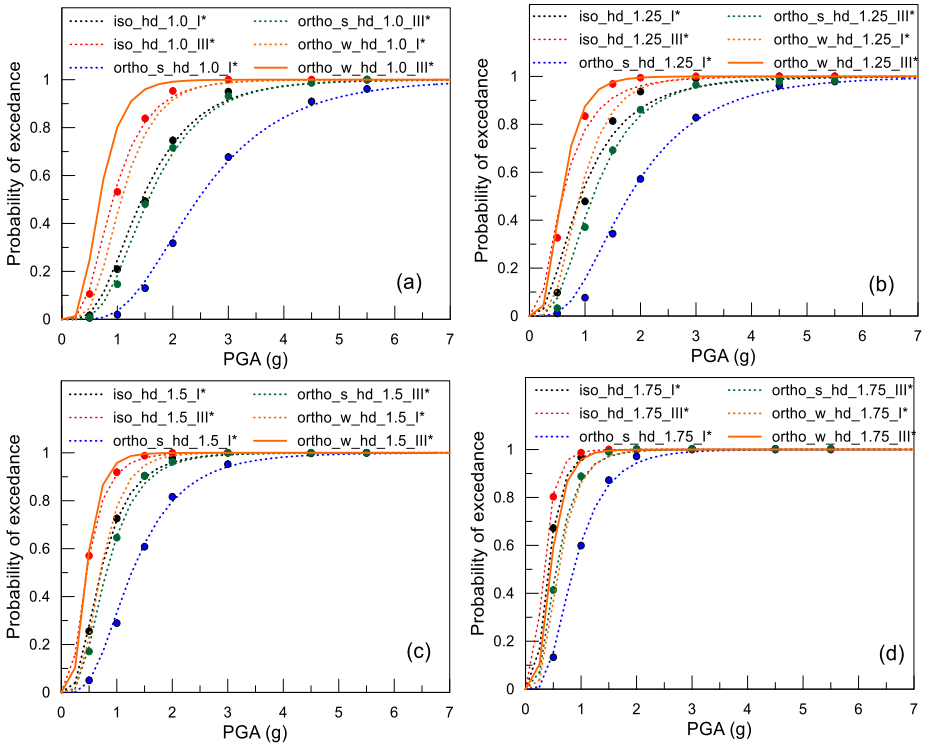

Figure 5.19 Influence on the fragility of the type of masonry for high level of IP damage (f_m of 5 MPa, 3.5 MPa and 2 MPa for solid and hollow strong and weak masonry respectively)

5.5 Comparisons with available experimental data

In this section, to confirm the reliability of the results obtained by the proposed procedure in the context of evaluating the OoP fragility of infill walls, comparisons are done with available experimental data on masonry infill specimens tested in the OoP direction with (or without) prior IP damage. In doing so, an experimental database of infill specimens having geometrical and mechanical characteristics within the range of that used to perform the numerical analyses in this study was selected from the investigated

experimental studies (Chapter 2). To be specific, experimental data by Dawe and Seah (1989), Angel (1994), Flanagan and Bennett (1999b), Pereira et al. (2011), Da Porto et al. (2013), Hak et al. (2014), Da Porto et al. (2015), Furtado et al. (2016), Moreno-Herrera et al. (2016), Furtado et al. (2020), Ricci et al. (2018a), Ricci et al. (2018b), Pantò et al. (2019), etc. were used for the comparisons.

It has to be noted that, in most cases, the available data refer to masonry panels made by hollow units, and the majority of the data were found regarding the infills subjected to low IP damage (Table 5.5). To the best knowledge of the author, only a few data can be found for solid masonry units with aspect ratios in the range of 1.0 and 1.5. No data were found for OoP tested infilled frames constituting solid masonry units and the medium and high IP damage to make compatible comparisons.

Although the details of the geometry of tested infill specimens were available in most of the experiments, the information regarding the density of the masonry was not always available. Therefore, to derive the mass of the infill wall, the density of solid masonry was assumed to be 1900 kg/m3. For the case of hollow masonry units, the percentage of voids is known for many cases and on average lies between 50% - 60%. Based on this information, the density of hollow masonry was considered 900 kg/m3 (slightly less than 50% of solid masonry) and was also used accordingly to calculate the analytical fragility curves. This value is slightly less for the masonry with hollow concrete units but since there are only a few cases it is used so, this facilitates the comparison with the analytical fragility obtained assuming the same density.

The comparisons were performed, from the experimental data, evaluating the capacity PGA in the OoP direction (Eqs. 5.2-5.5) starting from the calculation of OoP pseudo (spectral) acceleration and considering the

panel placed at the bottom of a three-storey reference low-rise RC building (i.e. z/H=0.167). The OoP pseudo (spectral) acceleration for the experimented infill specimens was derived by dividing the OoP strength of the infill specimens by the mass of the infill wall as described in section 5.2. Moreover, as in the case of fragility from numerical results, fragility groups were differentiated also for comparison based on:

1. Range of aspect ratio
2. Range of In-Plane damage
3. Type of masonry units (hollow and solid)

It is important to state that, in the fragility curves presented in this study, the aspect ratio was defined by a deterministic variable, while the IP damage was defined as a random variable within a specific range. Therefore, the compatibility of the comparisons with available data can be considered reliable being the infills sub-grouped with similar values of aspect ratio independently from the absolute dimensions of the infilled frames. In doing so, the scale factor of the experimental specimens is not considered (specimens with aspect ratios of 1 or near to 1 are used, see Table 5.5) making possible the comparison with the numerical data. Regarding the variability of the other characteristics, the thickness and the strength of the masonry are included in the uncertainties defined for the fragility analysis.

Table 5.5 Experimental database

Exp. Study	Scale	Type of OOP load	Specimen	Masonry type	*L/h*	f_{mv}	f_{mh}	OoP strength	Mass	OoP acc.	IP drift	PGA
						(MPa)	(MPa)	(kN)	(kg)	(g)	(%)	(g)
Dawe & Seah (1989)	1:1	M (AB)	WE2	HCONBL	1.29	24.3	18.4	193.54	1723.68	11.45	0.00	8.88
		M (AB)	WE4	HCONBL	1.29	24.3	18.4	112.90	1270.08	9.06	0.00	6.78
		M (AB)	WE5	HCONBL	1.29	24.3	18.4	78.62	816.48	9.82	0.00	6.79
Angel (1994)	1:1	M (AB)	1	SCB	1.50	11.51	11.51	32.43	358.49	9.22	0.00	6.03
		M (AB)	2b	SCB	1.50	10.85	10.85	15.93	358.49	4.53	0.34	2.38
		M (AB)	3b	SCB	1.50	10.13	10.13	23.70	358.49	6.74	0.22	3.74
		M (AB)	6b	SCB	1.50	4.58	4.58	49.12	741.08	6.76	0.25	4.21
Flanagan & Bennett (1999b)	1:1	UC (AB)	19	HCBL	1.00	5.6	3	108.88	903.17	12.29	0.78	7.67
		UC (AB)	18	HCBL	1.00	5.6	3	133.47	903.17	15.06	0.00	11.24
		UC (AB)	25	HCBL	1.00	5.6	3	40.64	451.58	9.17	0.00	5.92
		UC (AB)	22	HCBL	1.00	2.29	2.6	198.20	1490.23	13.56	0.00	10.43
Pereira et al. (2011)	2:3	C (AB)	Wall_REF_01	HCB	2.06	1.26	-	12.30	803.25	1.56	0.80	0.85
		C (AB)	Wall_REF_02	HCB	2.06	1.34	-	41.60	910.35	4.66	0.50	2.88
Da Porto et al. (2013)	1:1	M (CL)	URM_U	HCB	1.57	6	1.19	203.00	2969.33	6.97	1.20	3.88
Da Porto et al. (2015)	1:1	M (CL)	1-GP-UR	HCB	1.57	1.19	6	18.60	1484.66	1.28	1.20	0.43
		M (CL)	7-BC-UR	HCB	1.57	1.19	6	47.40	1484.66	3.25	1.20	1.11
Hak et al. (2014)	1:1	UC (CL)	TA1	HCB	1.43	4.64	1.08	168.50	3921.44	4.38	1.50	2.16
		UC (CL)	TA2	HCB	1.43	4.64	1.08	102.70	3921.44	2.67	2.50	1.18
		UC (CL)	TA3	HCB	1.43	4.64	1.08	163.90	3921.44	4.26	1.00	2.27
Furtado et al. (2016)	1:1	M (AB)	Inf_01	HCB	1.83	0.531	-	75.90	1304.10	5.93	0.00	2.85
		UC (AB)	Inf_02	HCB	1.83	0.531	-	69.80	1304.10	5.46	0.00	2.62
		UC (AB)	Inf_03	HCB	1.83	0.531	-	17.90	1304.10	1.40	0.50	0.37
Moreno-Herrera et al. (2016)	1:1	M (AB)	W1	HCONBL	1.37	3.72	-	91.67	1058.21	8.83	0.00	5.04
		M (AB)	W2	HCB	1.37	6.48	-	109.15	1076.94	10.33	0.00	6.57
		M (AB)	W3	HCB	1.37	6.17	-	115.08	1123.76	10.44	0.00	6.68

Exp. Study	Scale	Type of OOP load	Specimen	Masonry type	*L/h*	f_{mv}	f_{mh}	OoP strength	Mass	OoP acc.	IP drift	PGA
						(MPa)	(MPa)	(kN)	(kg)	(g)	(%)	(g)
		M (AB)	W4	SCB	1.37	4.15	4.15	76.27	2253.77	3.45	0.00	1.67
		M (AB)	W5	HCONBL	1.07	3.72	-	109.43	828.04	13.47	0.00	7.69
		M (AB)	W6	HCB	1.07	6.48	-	143.38	842.70	17.34	0.00	11.04
		M (AB)	W7	HCB	1.07	6.17	-	147.04	879.34	17.05	0.00	10.91
		M (AB)	W8	SCB	1.07	4.15	4.15	115.94	1763.56	6.70	0.00	3.25
Furtado et al. (2020)	1:1	UC (AB	M4	HCB	1.83	1.1	-	46.00	1304.10	3.60	0.00	2.08
Ricci et al. (2018a)	2:3	M (CL)	80_OOP_4E	HCB	1.28	1.81	2.45	22.00	309.64	7.24	0.00	4.45
		M (CL)	80_IP+OOP_L	HCB	1.28	1.81	2.45	23.40	309.64	7.70	0.16	4.24
		M (CL)	80_IP+OOP_M	HCB	1.28	1.81	2.45	10.50	309.64	3.46	0.37	1.62
		M (CL)	80_IP+OOP_H	HCB	1.28	1.81	2.45	5.90	309.64	1.94	0.58	0.82
Ricci et al. (2018b)	2:3	M (CL)	120_OOP_4E	HCB	1.28	1.65	2.12	41.90	464.45	9.20	0.00	6.25
		M (CL)	120_IP+OOP_L	HCB	1.28	1.65	2.12	41.60	464.45	9.13	0.21	5.58
		M (CL)	120_IP+OOP_M	HCB	1.28	1.65	2.12	27.90	464.45	6.12	0.50	3.31
		M (CL)	120_IP+OOP_H	HCB	1.28	1.65	2.12	23.10	464.45	5.07	0.89	2.46
Pantò et al. (2019)	2:3	UC (AB)	Infill Sytem_1	HCB	1.48	3	1	52.50	355.37	15.06	0.00	10.26

Note: M = Monotonic load; UC = Unidirectional cyclic load (Load-unload-reload); C = Cyclic load (two directional); AB = Airbag (uniform load); CL = Concentrated load (point load or line load), HCONBL = Hollow concrete block; HCBL = Hollow clay block; SCB = solid clay brick; HCB = Hollow clay brick

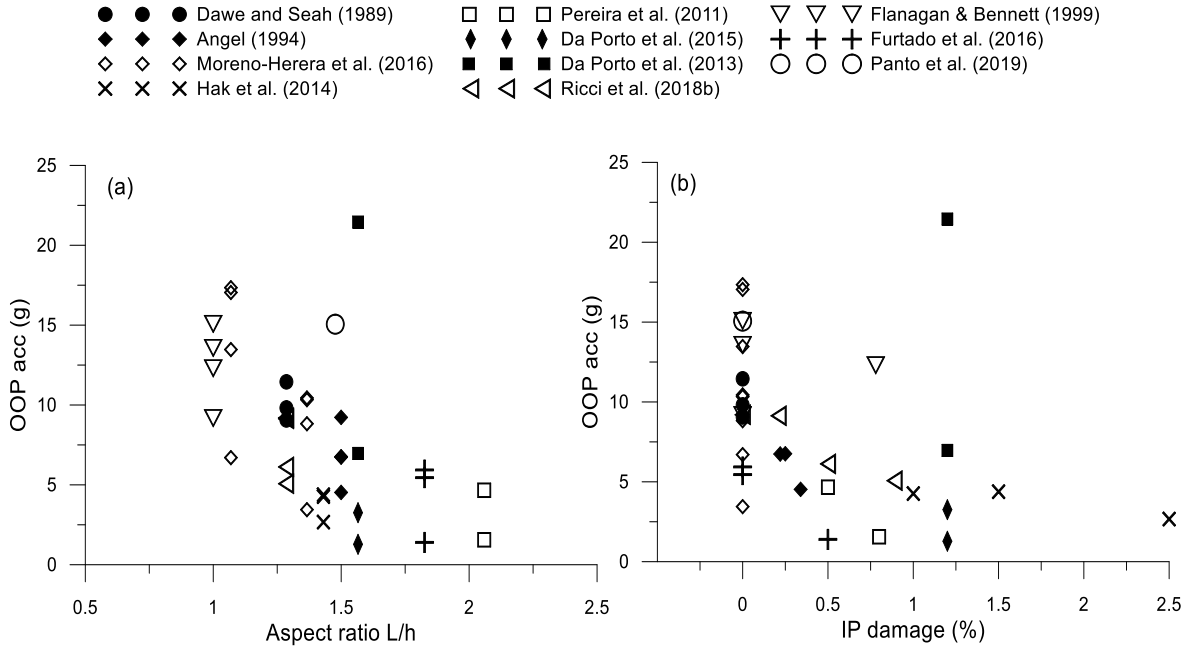

Figure 5.20 Experimental OoP acceleration depending on: a) aspect ratio; and b) IP damage

Some of the details of the infill specimens from different experiments used for comparison of fragility are summarized in Table 5.5. More detailed information on the infill specimens can be obtained also from the original papers by the authors. In addition, the results in terms of experimental OoP acceleration (OoP strength/mass) are shown in Fig 5.20a-b depending on the aspect ratio and the IP damage respectively.

In Fig 5.21, the results of the comparisons between experimental data and fragility curves are shown for out-of-plane PGA of infilled frames depending on the type of masonry, aspect ratio and IP damage. The results need to be read with a specific consideration which is described below.

Every single experimental data is shown by vertical lines (not including a specific value of the probability of exceedance) in terms of PGA. This assumption indicates the probability depending on the intersection with the fragility curves. In other words, when the intersection between the vertical lines and the fragility curves occurs at a higher probability of exceedance, the reliability of the data is higher and vice-versa. The above description is valid when the geometrical and mechanical characteristics of the experimental data match as closely as possible the range of definition of the fragility curves. Otherwise, the intersection at lower values of probability of exceedance does not indicate poor reliability in the prediction, but on the contrary, the range of validity is violated. At the same time, if the intersection is far over the full probability (around 100%) the comparisons indicate that the capacity is underestimated. Some examples of the interpretation of the results are given in the following paragraphs.

Fragility curve obtained for infilled frames made by hollow masonry units, with aspect ratio L/h =1.75 and for medium levels of IP damage was used to compare experimental results by Perreira et al. (2011) obtained for infills with an aspect ratio of 2.06, obtaining, consistently, an intersection at a

low probability of exceedance of 30% and 42% for strong and weak masonry units respectively. To discuss the motivations for these differences, it can be stated that the capacity of infills with an aspect ratio higher than 1.75 (2.06 for Perreira et al. 2011) is lower compared to that obtained for infills with an aspect ratio of 1.75. The fragility curve obtained from a median value of PGA associated with an aspect ratio of 2.06 should be positioned obviously on the left side (lower median value of PGA) with respect to the fragility curve obtained for specimens with an aspect ratio of 1.75 (higher median value of PGA). In that case, the intersection with the experimental data would be at a higher probability indicating higher reliability of the proposed fragility curve.

Similarly, the fragility curve for infilled frames made by hollow strong masonry units, with an aspect ratio L/h =1.50 and for high levels of IP damage was compared with experimental results by Hak et al. (2014) for infill walls with an aspect ratio of 1.43. Consistently, intersections at a high probability of exceedance of 95% and 75% for levels of IP damage of 1.5% and 2.5% respectively were obtained, indicating higher reliability of the defined fragility. At the same time, if the comparisons are made with fragility obtained for infilled frames made by hollow weak masonry units, the intersection is far away over the 100% of probability of exceedance, indicating that the fragility curve is not suitable due to the underestimation of the capacity. An additional consideration in this direction is further confirmed by considering that the strength of the masonry units is more suitable for the category of strong masonry instead of weak masonry.

Further, the fragility curve for infilled frames made by hollow strong masonry units, with aspect ratio L/h = 1.25 and for medium levels of IP damage was used to compare with experimental results by Ricci et al. (2018b) for infills with an aspect ratio of 1.28, obtaining, consistently, an intersection at a (low) probability of exceedance of 40%, while, the intersection at high

probability (around 90%) was obtained for the fragility curves made by hollow weak masonry units. It has to be noted also in this case the goodness of the results because the strength of the masonry used by the authors to build the infilled frame is very low (equivalent strength of around 1.8 MPa), belonging to the lower range of the strength adopted in this study (the mean strength for hollow weak units is 2 MPa).

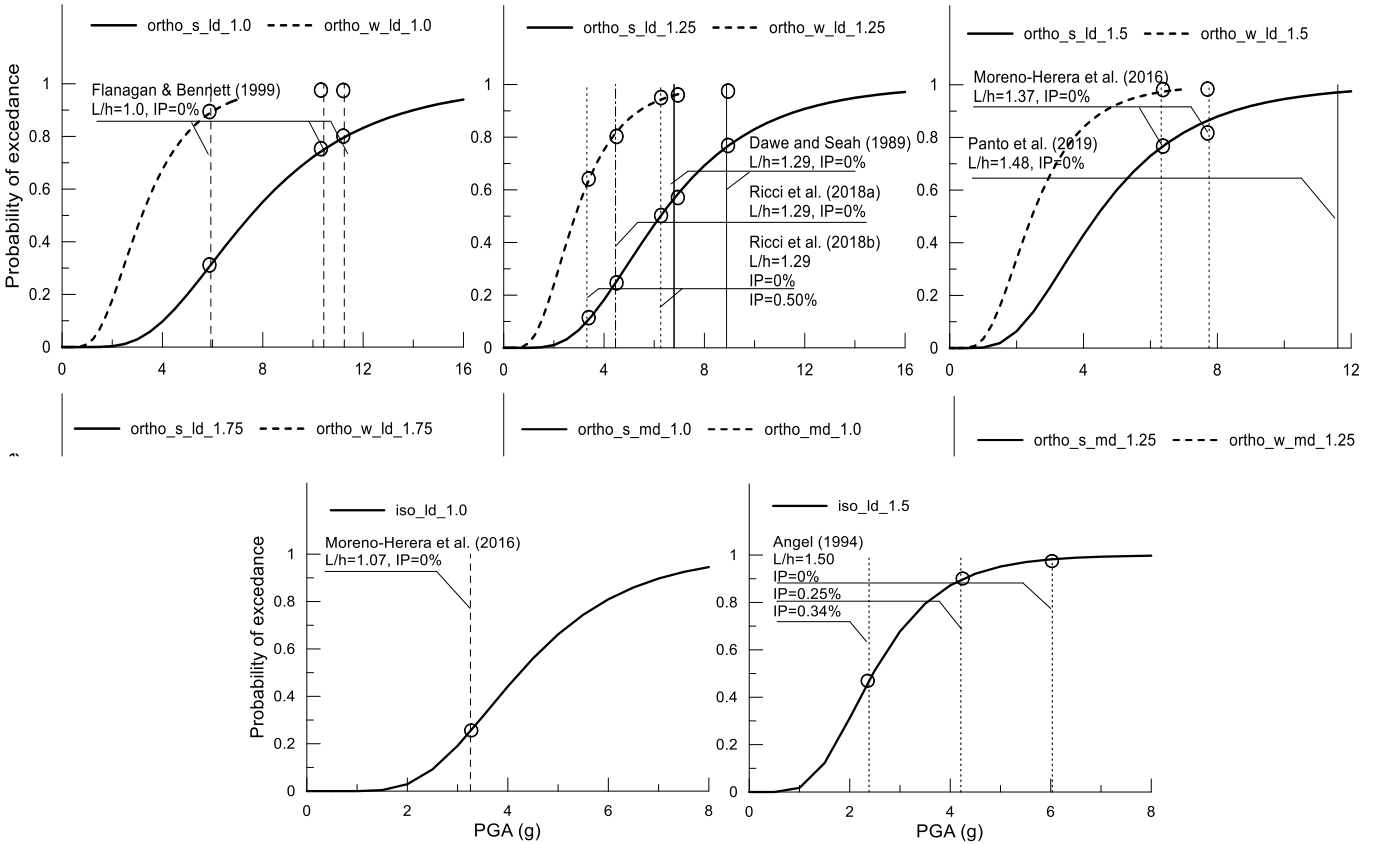
ortho_s_ld_1.0
ortho_w_ld_1.0
Flanagan & Bennett (1999)
L/h=1.0, IP=0%
ortho_s_ld_1.25
ortho_w_ld_1.25
Dawe and Seah (1989)
L/h=1.29, IP=0%
Ricci et al. (2018a)
L/h=1.29, IP=0%
Ricci et al. (2018b)
L/h=1.29
IP=0%
IP=0.50%
ortho_s_ld_1.5
ortho_w_ld_1.5
Moreno-Herera et al. (2016)
L/h=1.37, IP=0%
Panto et al. (2019)
L/h=1.48, IP=0%
ortho_s_ld_1.75
ortho_w_ld_1.75
ortho_s_md_1.0
ortho_md_1.0
ortho_s_md_1.25
ortho_w_md_1.25
iso_ld_1.0
Moreno-Herera et al. (2016)
L/h=1.07, IP=0%
iso_ld_1.5
Angel (1994)
L/h=1.50
IP=0%
IP=0.25%
IP=0.34%
Probability of excedance
PGA (g)

a)

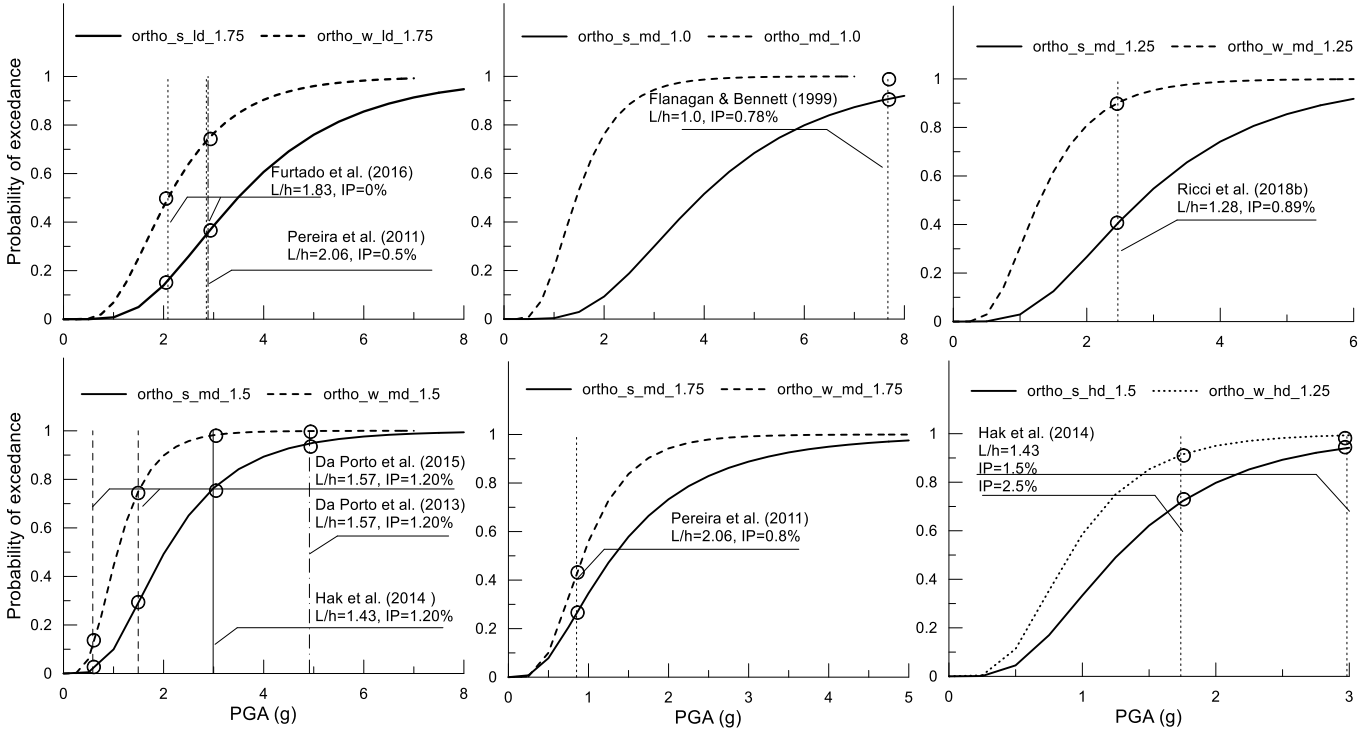

b)

Figure 5.21 Comparisons of the fragility curves with experimental OoP PGA capacity of infilled frames depending on the type of masonry, aspect ratio and IP damage: a) case of low IP damage; b) case of mild and high IP damage

Finally, the fragility curve obtained for infilled frames made by hollow strong masonry units, with aspect ratio L/h=1.5 and for low levels of IP damage were used to compare experimental results by Moreno-Herrera et al. (2016) and Pantò et al. (2019) obtained for infill walls with the aspect ratios of 1.37 and 1.48 respectively. In this case, an intersection at a high probability of exceedance of 80%, 90% (Moreno-Herrera et al., 2016) and 98% (Pantò et al., 2019) was obtained, confirming the reliability and the goodness of the results in the case of strong masonry units. While, the fragility curve obtained for infills with hollow weak masonry units is considered not suitable, for the same reasons discussed above in other cases.

6 CONCLUSION AND RECOMMENDATION

URM infill walls are important non-structural elements of modern multi-storey frame buildings. The OoP seismic vulnerability of such infill wall remains also in the modern structures complying with the recent seismic codes which can result in huge economic losses besides safety threats to the people. The OoP behaviour of infills during the earthquake is still difficult to predict. Therefore, in this study, attention was given to understanding the response of infill walls to earthquake-induced OoP seismic forces.

First of all, available OoP experimental studies on the masonry infill walls were investigated. It has to be said that the OoP experimental research is very limited in comparison to the extensive experimental research regarding the IP behaviour of the infilled frame. It was observed that the newer investigations were directed toward filling this gap.

During the review of the available experimental research, due attention was given to finding the affinity and differences between the available tests. About 80% of the tests were performed in infilled RC frames and almost 60% of them were tested in full scale. In the majority of the tests (about 85%), infill specimens were built with clay units. In three-fourths of the tests, specimens were built with hollow masonry units, while in the other one-fourth, solid masonry units were used. The strength of masonry used for the infill walls was highly scattered in the case of solid masonry units while in the case of hollow masonry units, low strength masonry (0 to 4 MPa) was adopted by the researchers in most of the experimental campaigns.

In the available experimental campaigns, the quasi-static method of testing was used more than the dynamic method (three-fourths of experiments with the former approach while the other one-fourth with the latter). Although the shaking table-based dynamic tests are more representative of the earthquake-induced seismic forces and their effect, they are rarely used because of the high costs of experimentation. Within the quasi-static approach, different methods were used for testing the infill specimens in the OoP direction. In more than 85% of the tests, infill walls were loaded in OoP by applying the airbag pressure or concentrated loads distributed at different points. While loading the infill wall directly with such loads, the damage was primarily observed in the infill walls. In a few other tests, the OoP inter-story drift load was used where the frames were loaded with point loads instead of loading infill wall, and in such cases, the damage was primarily concentrated in the frames.

Damage to the frames decreases the OoP capacity of infill walls. If the OoP drift applied to the frames is larger, the IP capacity of infilled frames is compromised significantly. Therefore, experiments conducted with a quasi-static approach do not reveal the true behavior of infilled frames subjected to seismic forces because damage occurs to both the frames and the infill wall during the earthquake and there is a big interaction between them which has been verified also from available dynamic tests. Nevertheless, static tests help to understand the OoP force capacity of infill walls which are useful while making a force-based assessment. To investigate the IP/OoP interaction effect, usually, the loading in one direction was followed by the loading in the other direction, and this is more relevant in the case of testing under quasi-static settings. In dynamic tests, shaking in both directions was applied simultaneously in a few cases while in the other few, the infill plane was

rotated perpendicularly and subjected to a specified ground motion after shaking in one direction.

In the experimental studies, it was found that several parameters like slenderness ratio, aspect ratio, boundary conditions between the frames and the infill wall, masonry strength, gravity load, openings, surface finish, frame stiffness, etc., were investigated. These parameters influence the arching effect and consequently the OoP behaviour of the URM infill walls. From the review of each experiment, it was found that some of these parameters have received good attention while others need to be deepened.

For example, newer experimental research is focusing on the effect of boundary conditions between the infill wall and the frames. Particularly, three different boundary conditions were found to be investigated: no gap (tight contact) between the infill and frames on all sides; the gap between the infill and beam at the top; and gaps with columns on the sides. Experiments showed that the arching action was delayed or not activated at all due to the presence of gaps and decreased the overall OoP capacity. Nevertheless, the boundary condition is yet to be explored in-depth, particularly in determining which type of gap is more detrimental, i.e. the gap between infill wall and beam or the gap between infill wall and columns.

Similarly, the other parameter that has received good attention is the slenderness ratio of the infill wall. The higher the slenderness ratio, the smaller is the contribution of arching and the lower is the OoP strength of the infill wall. However, there are still very few experiments conducted on thick infill walls (200 mm or higher), and the OoP behaviour of such infill walls is not understood fully. The OoP capacity of thick infill walls needs further experimental investigation. While doing so, the practical thickness of infill walls has to be considered.

Likewise, the effect of prior IP damage on the OoP strength and stiffness of infill walls have got a priority in experimental research. However, due to large variability in the geometrical and mechanical properties of the tested infilled frames, the comparison of the results is difficult. The reduction of OoP strength due to prior IP damage is not consistent among the results. Nevertheless, experiments have shown it to be dependent on several factors including the strength of masonry, slenderness ratio, etc.

Although OoP strength is heavily dependent on the compressive strength of the masonry, which is related to the type and strength of the masonry units and mortar used for the infill walls, there is a huge gap in experimental research on different ranges of infills' compressive strength. Similarly, experimental research on the effect of openings on the OoP capacity of infill walls is seriously lacking. But, openings like doors and windows are an important part of infill wall constructions. More experiments with systematic variation in mechanical properties of masonry are necessary to be focused on these directions.

In the same way, there are limited studies on the influence of surface finishes like plasters on the OoP capacity of infill walls. At the moment, a few experimental studies show a greater improvement in infill's OoP behaviour than expected. This opens up a research line on the effect of plasters with different characteristics. The stiffness of the frame members is also an important parameter to induce an arching action in the infill walls. However, a direct correlation between frames' stiffness and arching is not available so far. Considering that the stiffness of RC and steel frame members can be very different, this should be one of the aims to be reached.

In a few experiments conducted with gravity loads applied on the top of columns, the strength and stiffness of infills in the OoP direction were not significantly influenced. On the other hand, a few other experiments with

loads applied directly over the top beam of the infilled frame showed enhancement of the OoP capacity. Therefore, more research in this area is needed to determine the exact contribution of a gravity load on the OoP capacity of URM infill walls.

In general, it seems that different aspects need to be further investigated to properly understand the OoP behaviour of infill walls. But, priority should be given to two major parameters: the compressive strength of masonry and infill's slenderness ratio. Therefore, tests, possibly in full scale, involving pure OoP load or combined IP and OoP loads, both static and dynamic, should be increased on URM infill walls having various thicknesses (based on construction practices), involving appropriate ranges for the mechanical properties of masonry.

After the detailed investigation of the available experiments, analytical capacity models available to predict the OoP capacity of URM infill walls were evaluated. In the past, researchers have checked analytical models formulated for determining the OoP capacity in the IP-undamaged state, and only partially, the reliability of the capacity models to predict the reduction of OoP strength (when infills are damaged by IP actions) was checked. However, the holistic approach to checking the combined result of these two types of models was missing. Moreover, it was found that the accuracy of analytical models is affected by the number of experiments taken and the types of masonry walls considered (i.e. with or without frames). For example, Anić et al. (2020) observed the models by Ricci et al. (2018b) and Moghadam and Goudarzi (2010) relatively better for the case of infilled frames, and Liberatore et al. (2020) found the equation in Eurocode 6 (2005) on an average better for the estimation of OoP capacity of masonry walls without frames, confined masonry walls or infill walls in RC frames.

Therefore, in this study, analytical checks were done including only the cases of the URM infill wall specimens for both types of models i.e. models for predicting the OoP strength in IP-undamaged state, and models for determining OoP strength reduction factor when damaged by IP load. Moreover, the possibility of connecting two types of models was checked. To do this, suitable experiments and their results were used. In addition, the reliability of the available models to address the problem of a beam-infill gap was also checked. Further, the possibility of using them in the case of infills with openings was also examined.

Based on the detailed calculation and comparison of the analytical results with the experimental results, the accuracy of different models for different cases was identified. The analytical models of Flanagan and Bennett (1999a) or Dawe and Seah (1989) were found to predict the OoP capacity of IP-undamaged infill walls with better accuracy. Similarly, strength reduction due to IP damage was better captured by the model of Di Domenico et al. (2021). In the case of the infill-beam gap, it is possible to use the models by Flanagan and Bennett (1999a) or Dawe and Seah (1989). However, due to a few experiments, it is difficult to decide on their accuracy.

To predict the OoP strength of URM infill walls with openings, it appeared better to couple the models of Dawe and Seah (1989) or Flanagan and Bennett (1999a) with the models of ASCE/SEI 41-17 or Liberatore et al. (2020) that gives reduction factor for openings. The decrease in the OoP strength in the case of openings and the development of a suitable prediction model for such a case is still a subject of further research.

To accurately characterize the OoP behavior of infill walls, the prediction of the displacement at the peak load and also the ultimate displacement capacity is necessary. The available models resulted in a very

high error in the prediction of displacement at peak load. Therefore, this needs to be improved with a suitable prediction model.

Furthermore, it was found that the prediction of the OoP capacity by the models of Dawe and Seah (1989) or Flanagan and Bennett (1999a) can be improved by considering the orthotropic nature of masonry (using both the horizontal and vertical properties of masonry rather than using only vertical properties). This makes a big difference, particularly in the case of hollow masonry units.

The equivalent struts-based macro-models have been on the highlights for several years due to faster computation and the possibility of using them in practical applications. However, most of the available macro-models were limited to capturing the IP response of the infilled frames. In the last decades, few macro models developed for OoP analysis of infilled frames, but most of them are not easy to put into practice. The limitation is usually imposed by the use of several parameters in the models and the difficulty to choose these parameters. While some models require higher efforts for calculation, their reliability when used for varying properties of infill walls is not known. Therefore, in this study, a suitable macro-model that can be used to simulate both the IP and the OoP capacity of URM infill walls was developed.

The proposed model has four struts configurations and is a modification and development of the model proposed by Di Trapani et al. (2018). In the model, the struts were represented by fiber-section beam-column elements which enable them to directly take into account the arching mechanism of infill walls under the action of OoP loads. One of the major modifications in the model was the change in the connection of struts with the frames. It was identified that the macro model captures the OoP capacity better when the struts were connected to the frames with moment-end connections compared to when they were joined by pinned-end connections. The other

major change in the model was the use of the stress-strain parameters for diagonal, vertical and horizontal struts. While in the model of Di Trapani et al. (2018), separate stress-strain parameters were used for diagonal struts from the horizontal and vertical struts, in the proposed model, the same parameters were used for all struts. This provision simplified the model and increased the possibility of using them in a practice by decreasing the number of parameters to be fixed.

In this study, one of the main works done was the formulation of empirical equations which can be used to determine the stress-strain parameters necessary to define the compressive behaviour of the struts while building a numerical model. The use of the proposed equations requires the knowledge of only two mechanical properties of the masonry (compressive strength and elastic modulus). Thus, in this study, a standard procedure to define the geometrical and mechanical properties of the equivalent struts required for numerical modelling of infill walls was obtained.

The proposed model was validated with the experimental data available in the literature. Infill specimens with different geometrical and mechanical characteristics were used and overall, both the IP and OoP response obtained from the model was very reasonable. The model not only captured the OoP capacity in case of IP- undamaged infill wall but, it could also take into account the decrease of strength due to prior IP damage. Since there are not sufficient experimental studies to cover different aspects related to the OoP behaviour of infill walls, the use of models in different cases can still be not ascertained fully. For example, the model is proposed for the case of solid infill wall i.e. infill without an opening. Therefore, a suitable strategy needs to be developed when the model has to be applied for the case of infill walls with openings. Similarly, the model is applicable for infill walls having only single-leaf. It is not suitable to determine the OoP capacity of an infill

wall with double leaves having a gap in-between. Likewise, the model is proposed for the case of URM infills and it cannot be used for any infill having an interior RC tie beam or column. Further work is necessary to investigate this matter.

It was identified that for the use of the developed model in the case of a thick infill wall, the vertical strut has to be removed from the model. It was true when compared with two available experiments on thick infill specimens. However, the lack of sufficient experiments on thick infill specimens made it difficult to fully investigate this aspect. This needs further verification which can be done when more experiments on thick infill walls are available.

The model was validated by taking into account the effect of prior IP damage on the OoP capacity. But the model can also take into account the decrease in the IP capacity of the infill wall and the infilled frames due to prior OoP damage of infill walls. This makes it possible for the model to address the problem of IP/OoP interaction. Although the model can consider the effect of prior OoP damage in the IP capacity of the infilled frames, experiments conducted to investigate this effect are too few and due to a lack of suitable experiments, validation is still lagging. Therefore, the effectiveness of the model to be used in such cases needs further verification. Furthermore, the effectiveness of the model to capture the OoP capacity of infill walls in infilled steel frames is validated only in one case and is the subject of further investigation.

Afterward, for the first time, the macro-model was used to perform the parametric study to understand the OoP capacity of URM infill walls bounded by frames on all sides (before only through micro-models). The proposed macro-model is very useful for such a study due to its capability to capture the OoP capacity of infill walls having varying geometrical and mechanical characteristics in addition to being faster in computation. Therefore, in

evaluating the OoP capacities, different parameters were investigated in detail such as the masonry strength f_m, slenderness ratio (h/t), aspect ratio (l/h), previous IP damage, and stiffness of the bounding frames.

From the numerical experimentation, it was found that the OoP capacity of URM infill walls was heavily dependent on masonry strength and infill wall thickness (or slenderness ratio). The OoP strength was proportional to masonry strength and it decreased when the slenderness ratio and the aspect ratio of the infill wall increased. For any infill wall, the OoP strength was found to be significantly reduced when the infill's slenderness ratio was greater than 20. Similarly, the OoP strength decreased by almost 60% when the aspect ratio was doubled i.e. length two times the height. The reduction of OoP capacity due to the increasing slenderness or aspect ratio was found not to be affected by the compressive strength of masonry used in the infills.

Further, it was found that upon increasing the stiffness of the frames by increasing the column size, the OoP capacity of the infill wall can increase. However, the increase in the OoP strength was limited only to a certain size of columns beyond which the effect was insignificant. Comparatively, the influence of the increase in frames' stiffness was higher when the stiffness was increased in the IP direction of the infill wall compared to when the stiffness was increased in its OoP direction. Also, it was observed that the higher stiffness of columns contributed to the OoP strength of infill walls more in the case of thicker infill walls than the thinner infills, and for the cases of higher compressive strength of masonry. From the detailed numerical investigation, it was also found that Angel's (1994) and Abrams et al.'s (1996) recommendation for the stiffness of frames (EI = 25.83 $\times 10^{12}$ Nmm^2) is sufficient for the activation of the full arching effect in the infill walls.

The decay of OoP strength due to prior IP damage was significantly affected by both the masonry strength and the thickness (or the slenderness

ratio) of infill walls. The decay of OoP strength was lower when the infill walls were thicker (lower slenderness ratio) and when the masonry was stronger (higher compressive strength). The OoP strength decay was less influenced by the aspect ratio of infill walls. Likewise, the OoP stiffness decay was also found to be affected by the masonry strength and the slenderness ratio of infill walls. However, the scattering of the numerical results in the case of OoP stiffness was lower in comparison to the case of OoP strength.

Based on the detailed parametric study conducted with the proposed macro model, empirical equations were derived to predict the OoP strength of the infill walls in both IP-damaged or IP-undamaged states. It was found that the equation proposed by considering the influence of masonry strength and slenderness ratio in addition to IP drift level showed more affinity with the experimental findings compared to the equations (which integrate only the effect of IP drift level and masonry strength or IP drift level and slenderness ratio) when the decay of the OoP strength due to previous IP damage needs to be determined. The proposed equations provided reliable results when compared with experimental results in both IP-damaged and IP-undamaged cases.

Finally, in this study, a procedure for the evaluation of OoP fragility for infill masonry walls was proposed. The fragility was expressed in terms of capacity PGA at the collapse in the OoP direction for a reference low-rise RC building. While evaluating the fragility results, uncertainties in the capacity, considering the variation of geometrical and mechanical characteristics of the infill panels and for random conditions of in-plane damage, were assumed. Uncertainty in the strength of the concrete of the frame members was also considered. The proposed procedure followed a probabilistic approach employing a Monte Carlo simulation which is defined by the assessment of the infills' OoP responses at randomly generated input variables.

In determining the fragility, different aspects were investigated such as the influence of the aspect ratio, the influence of the level of IP damage, the influence of the positioning of the infill panel with respect to the structure, and the influence of the type of masonry and their strength i.e. solid and hollow units with different ranges of strength.

The fragility results indicated that, in the absence of previous IP damage, the infilled frames provide high strength and high PGA capacity in the OoP direction. Consequently, a lower vulnerability was obtained. On the other hand, in the presence of previous IP damage, regardless of whether it was medium or high, the strength in the OoP direction dropped to critical values, providing very high vulnerability for small values of PGA. The results were confirmed by comparisons between numerical results and experimental data available in the literature.

It was found that, for a given level of IP damage and the aspect ratio remaining the same at all floor levels from bottom to the top, the probability of OoP collapse resulted to be higher for panels placed at the top of the structure than those placed at the base of the structure. This confirmed, in the case of IP-damaged infills, the high vulnerability of the panels on higher floors of the structures where the spectral acceleration of the structure is also higher. Further, the analysis indicated that a higher fragility can be expected for infill walls with a bigger aspect ratio.

Moreover, according to the assumptions made in this study, high PGA at collapse (lower fragility) was observed for infill walls made with hollow strong masonry units compared to infills made with solid masonry units because of the lower weight and the interaction with the response spectrum influenced by lower values of the vibration periods of infills. At the same time, for the fragility group obtained for the weak hollow masonry units, higher

fragility was observed (lower values of PGA at collapse) for all the cases analyzed due to the lower strength range.

The advantage of the proposed procedure to derive fragility is that it is simple and requires the use of the code-based response spectrum to calculate the capacity in terms of PGA, besides determining the OoP capacity of infill walls either through the numerical model or a suitable analytical equation (both proposed in this study). The proposed procedure can be extended and applied to other types of infill walls depending on the construction technique of the site of interest, strengths of the materials, geometries, etc, obtaining different and specific fragility curves. In doing so, strong and weak infill walls can be analyzed in terms of vulnerability for different structures. Definitely, this is a starting point for possible future studies as well as the investigation of the influence of the vulnerability of the infill walls for medium and high-rise RC structures. Nevertheless, it has to be remembered that in such cases, especially high-rise buildings not regular in nature, they can have a very different dynamic response, and the proposed code-based procedure may not be valid.

It has to be noted that the macro-element model developed and used in this study is based on the results of the quasi-static experimental tests. The fragility results obtained by using the model were also determined by nonlinear static analysis and not through nonlinear time history analysis. Therefore, future research work can be concentrated to check the suitability of the model in the seismic evaluation of infilled frame buildings on the basis of nonlinear time history calculations.

References

1. Abrams, D.P., Angel, R., and Uzarski, J. (1996). Out-of-plane strength of unreinforced masonry infill panels. Earthquake Spectra, 12(4), 825–44.
2. Abrahamczyk, L., Penava, D., Markušić, S., Stanko, D., Luqman Hasan, P., Haweyou, M., and Schwarz, J. (2021). Die Magnitude 6,4 – Erdbeben in Albanien und Kroatien – Ingenieuranalyse der Erdbebenschäden und Erfahrungswerte für die Baunormung. Bautechnik. https://doi.org/10.1002/bate.202100070
3. Agnihotri, P., Singhal, V., and Rai, D. C. (2013). Effect of in-plane damage on out-of-plane strength of unreinforced masonry walls. Engineering Structures, 57, 1–11.
4. Akhoundi, F., Vasconcelos, G., Lourenco, P., & Silva, L. (2016). Out-of-plane response of masonry infilled RC frames: Effect of workmanship and opening. In C. Modena, F. da Porto, & M. R. Valluzzi (Eds.), Brick and Block Masonry (0 ed., pp. 1147–1154). CRC Press. https://doi.org/10.1201/b21889-143
5. Akhoundi, Farhad, Vasconcelos, G., & Lourenço, P. (2018). Experimental Out-Of-Plane Behavior of Brick Masonry Infilled Frames. International Journal of Architectural Heritage, 14(2), 221–237. https://doi.org/10.1080/15583058.2018.1529207
6. Al-Chaar, G. (2002). Evaluating Strength and Stiffness of Unreinforced Masonry Infill Structures: Defense Technical Information Cente, Fort Belvoir, VA.
7. Angel, R. (1994). Behavior of reinforced concrete frames with masonry infill walls (doctoral dissertation). University of Illinois at Urbana-Champaign.

8. Anić, F., Penava, D., Abrahamczyk, L., & Sarhosis, V. (2020). A review of experimental and analytical studies on the out-of-plane behaviour of masonry infilled frames. Bulletin of Earthquake Engineering, 18(5), 2191–2246. https://doi.org/10.1007/s10518-019-00771-5
9. Anić, F., Penava, D., Guljaš, I., Sarhosis, V., & Abrahamczyk, L. (2021). Out-of-plane cyclic response of masonry infilled RC frames: An experimental study. Engineering Structures, 238, 112258.
10. Arlekar, J.N., & Murthy, C.V.R. (2000). Ambient vibration survevy of RC-frame building having brick masonry infill walls. The Indian Concrete Journal, 74(10):588.
11. ASCE (American Society of Civil Engineers). (2017). *Seismic Evaluation and Retrofit of Existing Buildings*. ASCE/SEI 41-17, Reston, VA: ASCE.
12. Asteris P.G., Cavaleri, L., Di Trapani, F., & Sarhosis, V. (2015). A macro-modelling approach for the analysis of infilled frame structures considering the effects of openings and vertical loads. Struct. Infrastruct. Eng., 12(5), 551–566.
13. Asteris, P.G., Antoniou, S.T., Sophianopoulos, D.S., & Chrysostomou, C.Z., (2011). Mathematical Macromodeling of Infilled Frames: State of the Art. Journal of Structural Engineering 137, 1508–1517.
14. Asteris, P.G., Cavaleri, L., Di Trapani, F., & Tsaris, A.K. (2017). Numerical modelling of out-of-plane response of infilled frames: State of the art and future challenges for the equivalent strut macromodels. Eng Struct., 132:110–22.
15. ATC (Applied Technology Council) (1978). *Tentative provisions for the development of seismic regulations for buildings*, *Report No. ATC3-06*, Applied Technology Council, Palo Alto, California.

16. Bashandy T., Rubiano N., & Klingner R. 1995. Evaluation and analytical verification of infilled frame test data. P.M. Ferguson Struct. Engrg. Laboratory, Report No.95-1, Depart. of Civil Eng., Uni. of Texas at Austin, Austin, Tx.
17. Braga, F., Manfredi, V., Masi, A., Salvatori, A., & Vona, M. (2011). Performance of non-structural elements in RC buildings during the L'Aquila, 2009 earthquake. Bulletin of Earthquake Engineering, 9(1), 307–324.
18. Butenweg, C., Marinković, M., & Salatić, R. (2019). Experimental results of reinforced concrete frames with masonry infills under combined quasi-static in-plane and out-of-plane seismic loading. Bulletin of Earthquake Engineering, 17(6), 3397–3422. https://doi.org/10.1007/s10518-019-00602-7
19. Calvi, G. M., & Bolognini, D. (2001). Seismic response of reinforced concrete frames infilled with weakly reinforced masonry panels. Journal of Earthquake Engineering, 5(2), 153–185. https://doi.org/10.1080/13632460109350390.
20. Campione, G., Cavaleri, L., Ferrotto, M.F. Macaluso, G. & Papia, M. (2016). Efficiency of Stress-Strain Models of Confined Concrete With and Without Steel Jacketing to Reproduce Experimental Results. The Open Construction and Building Technology Journal, 2016, 10, (Suppl 1: M4) 65-86.
21. Cardone, D., and Perrone, G. (2015). Developing fragility curves and loss functions for masonry infill walls. Earthquakes and Structures, 9(1), 257–279.

22. Castaldo, P., Gino, D., Bertagnoli, G., & Mancini, G. (2020). Resistance model uncertainty in non-linear finite element analyses of cyclically loaded reinforced concrete systems. Engineering Structures, 211, 110496.
23. Cavaleri, L., & Di Trapani, F. (2014). Cyclic response of masonry infilled RC frames: Experimental results and simplified modeling. Soil Dynamics and Earthquake Engineering, 65: 224-42.
24. Cavaleri, L., Di Trapani, F. Ferrotto, M.F., & Davì, L. (2017). Stress-Strain Models for Normal and High Strength Confined Concrete: Test and Comparisons of Literature Models Reliability in Reproducing Experimental Results. Ingegneria Sismica, 34, Special Issue B (2017) 114-137.
25. Cavaleri, L., Zizzo, M., & Asteris, P.G. (2019). Residual out-of-plane capacity of infills damaged by in-plane cyclic loads. Engineering Structures, 109957.
26. Cavaleri, L., Fossetti, M., & Papia, M. (2005). Infilled frames: Developments in the evaluation of cyclic behaviour under lateral loads. Structural Engineering and Mechanics, 21(4), 469–494.
27. Celarec, D., & Dolšek, M. (2013). The impact of modelling uncertainties on the seismic performance assessment of reinforced concrete frame buildings. Engineering Structures, 52, 340–354.
28. Chrysostomou, C.Z. (1991). Effects of Degrading Infill Walls on the Nonlinear Seismic Response of Two-Dimensional Steel Frames (PhD). Cornell University, New York, USA.
29. Chrysostomou, C.Z., Gergely, P., & Abel, J.F. (2002). A Six-Strut Model for Nonlinear Dynamic Analysis of Steel Infilled Frames. International Journal of Structural Stability and Dynamics 2002; 2, 335–353.

30. Circolare 21 gennaio 2019, n. 7 C.S.LL.PP. Istruzioni per l'applicazione dell'«Aggiornamento delle "Norme tecniche per le costruzioni"» di cui al decreto ministeriale 17 gennaio 2018.
31. Corte, D.G., Fiorino, L., & Mazzolani, F. (2008). Lateral-loading tests on a real RC building including masonry infill panels with and without FRP strengthening. Journal of Materials in Civil Engineering, 20, 419–431.
32. Crisafulli, F.J. (1997). Seismic Behavior of Reinforced Concrete Structures with Masonry Infills (PhD). University of Canterbury, New Zealand.
33. Crisafulli, F.J., & Carr, A.J. (2007). Proposed Macro-Model For The Analysis Of Infilled Frame Structures. Bulletin of New Zealand National Society for Earthquake Engineering, 40, 9.
34. Crowley H., & Pinho R. (2006). Simplified equations for estimating the period of vibration of existing buildings. First European Conference on Earthquake Engineering and Seismology (a joint event of the 13th ECEE & 30th General Assembly of the ESC) Geneva, Switzerland, 3-8 September 2006 Paper Number: 1122.
35. da Porto, .F, Guidi, G., Benetta, M.D., & Verlato, N. (2013). Combined In-Plane/Out-of-Plane Experimental Behaviour of Reinforced and Strengthened Infill Masonry Walls. The Masonry Society, ed. 12th Canadian Masonry Symposium.
36. da Porto, F., Donà, M., Verlato, N., & Guidi, G. (2020). "Experimental Testing and Numerical Modeling of Robust Unreinforced and Reinforced Clay Masonry Infill Walls, With and Without Openings." Frontiers in Built Environment, 6, 591985.

37. da Porto, F., Guidi, G., Verlato, N., & Modena, C. (2015). Effectiveness of plasters and textile reinforced mortars for strengthening clay masonry infill walls subjected to combined in-plane/out-of-plane actions / Wirksamkeit von Putz und textilbewehrtem Mörtel bei der Verstärkung von Ausfachungswänden aus Ziegel: Effectiveness of plasters and textile reinforced mortars for strengthening clay masonry infill walls subjected to combined in-plane/out-of-plane actio. Mauerwerk, 19(5), 334–354. https://doi.org/10.1002/dama.201500673
38. Dawe, J. L., & Seah, C. K. (1989). Out-of-plane resistance of concrete masonry infilled panels. Canadian Journal of Civil Engineering, 16(6), 854–864. https://doi.org/10.1139/l89-128.
39. De Luca, F., Verderame, G. M., and Manfredi, G. (2015). Analytical versus observational fragilities: the case of Pettino (L'Aquila) damage data database. Bulletin of Earthquake Engineering, 13(4), 1161–1181.
40. De Martino, G., Di Ludovico, M., Prota, A., Moroni, C., Manfredi, G., & Dolce, M. (2017). Estimation of repair costs for RC and masonry residential buildings based on damage data collected by post-earthquake visual inspection. Bulletin of Earthquake Engineering, 15(4), 1681–1706.
41. De Risi, M. T., Di Domenico, M., Ricci, P., Verderame, G. M., & Manfredi, G. (2019b). Experimental investigation on the influence of the aspect ratio on the in-plane/out-of-plane interaction for masonry infills in RC frames. Engineering Structures, 189, 523–540.
42. De Risi, M., Del Gaudio, C., & Verderame, G. (2019a). Evaluation of Repair Costs for Masonry Infills in RC Buildings from Observed Damage Data: the Case-Study of the 2009 L'Aquila Earthquake. Buildings, 9(5), 122.

43. Del Gaudio, C., De Martino, G., Di Ludovico, M., Manfredi, G., Prota, A., Ricci, P., & Verderame, G. M. (2017). Empirical fragility curves from damage data on RC buildings after the 2009 L'Aquila earthquake. Bulletin of Earthquake Engineering, 15(4), 1425–1450.
44. Del Gaudio, C., De Risi, M. T., Ricci, P., & Verderame, G. M. (2019). Empirical drift-fragility functions and loss estimation for infills in reinforced concrete frames under seismic loading. Bulletin of Earthquake Engineering, 17(3), 1285–1330.
45. Del Vecchio, C., Di Ludovico, M., Pampanin, S., & Prota, A. (2018). Repair Costs of Existing RC Buildings Damaged by the L'Aquila Earthquake and Comparison with FEMA P-58 Predictions. Earthquake Spectra, 34(1), 237–263.
46. Di Domenico, M., De Risi, M. T., Ricci, P., Verderame, G. M., & Manfredi, G. (2021). Empirical prediction of the in-plane/out-of-plane interaction effects in clay brick unreinforced masonry infill walls. Engineering Structures, 227, 111438.
47. Di Domenico, M., Ricci, P., & Verderame, G. M. (2018). Experimental Assessment of the Influence of Boundary Conditions on the Out-of-Plane Response of Unreinforced Masonry Infill Walls. Journal of Earthquake Engineering, 24(6), 881–919. https://doi.org/10.1080/13632469.2018.1453411
48. Di Domenico, M., Ricci, P., & Verderame, G. M. (2019a). Experimental assessment of the out-of-plane strength of URM infill walls with different slenderness and boundary conditions. Bulletin of Earthquake Engineering, 17(7), 3959–3993. https://doi.org/10.1007/s10518-019-00604-5

49. Di Domenico, M., Ricci, P., & Verderame, G. M. (2019b). Predicting the Out-Of-Plane Seismic Strength of Unreinforced Masonry Infill Walls. Journal of Earthquake Engineering, 1–38. https://doi.org/10.1080/13632469.2019.1604453
50. Di Domenico, M., Ricci, P., and Verderame, G. M. (2017). Empirical unreinforced masonry infill macro-model accounting for in-plane/out-of-plane interaction. Proceedings of the 6th International Conference on Computational Methods in Structural Dynamics and Earthquake Engineering (COMPDYN 2017), Institute of Structural Analysis and Antiseismic Research School of Civil Engineering National Technical University of Athens (NTUA) Greece, Rhodes Island, Greece, 1606–1624.
51. Di Trapani, F., Macaluso, G., Cavaleri, L., & Papia, M. (2015). Masonry infills and RC frames interaction: Literature overview and state of the art of macromodeling approach. European Journal of Environmental and Civil Engineering, 19 (9), 1059–1095.
52. Di Trapani, F., Malavisi, M., Shing, P. B., and Cavaleri, L. (2020). Definition of out-of-plane fragility curves for masonry infills subject to combined in-plane and out-of-plane damage. Brick and Block Masonry - From Historical to Sustainable Masonry, J. Kubica, A. Kwiecień, and Ł. Bednarz, eds., CRC Press, 943–951.
53. Di Trapani, F., Shing, P.B., & Cavaleri, L. (2018). A macro-element model for in-plane and out-of-plane responses of masonry infills in frame structures. J. Struct. Eng., 144 (2): 04017198.
54. Dolšek, M., & Fajfar, P. (2005). Simplified non-linear seismic analysis of infilled reinforced concrete frames. Earthq Eng Struct Dyn, 34:49–66.

55. Durrani, A.J., & Luo, Y.H. (1994). Seismic Retrofit of Flat-Slab Buildings with Masonry Infills, in: NCEER Workshop on Seismic Response of Masonry Infills. National Center for Earthquake Engineering Research (NCEER), 1994; Buffalo, NY.
56. El-Dakhakhni, W.W. (2002). Experimental and Analytical Seismic Evaluation of Concrete Masonry-Infilled Steel Frames Retrofitted Using GFRP Laminates (PhD). Drexel University, Philadelphia, USA.
57. El-Dakhakhni, W.W., Elgaaly, M., & Hamid, A.A. (2003). Three-Strut Model for Concrete Masonry-Infilled Steel Frames. Journal of Structural Engineering, 2003; 129, 177–185.
58. Eurocode 6 (2005). *Design of masonry structures, Part 1-1: Common rules for reinforced and unreinforced masonry structures*, European Committee for Standardization Brussels.
59. Eurocode 8 (2004). *Design of structures for Earthquake Resistance, Part 1-1: General Rules, Seismic Actions and Rules for Buildings*, European Committee for Standardization, Brussels.
60. Fardis, M. N., Bousias, S. N., Franchioni, G., & Panagiotakos, T. B. (1999). Seismic response and design of RC structures with plan-eccentric masonry infills. 19.
61. FEMA (Federal Emergency Management Agency). (1997). *Guidelines for the seismic rehabilitation of buildings*. FEMA 273, Washington DC: FEMA.
62. FEMA (Federal Emergency Management Agency). (2000). *Prestandard and commentary for the seismic rehabilitation of buildings*. FEMA 356, Washington DC: FEMA.

63. Flanagan, R. D., & Bennett, R. M. (1999a). Arching of Masonry Infilled Frames: Comparison of Analytical Methods. Practice Periodical on Structural Design and Construction, 4(3), 105–110. https://doi.org/10.1061/(ASCE)1084-0680(1999)4:3(105).
64. Flanagan, R. D., & Bennett, R. M. (1999b). Bidirectional Behavior of Structural Clay Tile Infilled Frames. Journal of Structural Engineering, 125(3), 236–244.
65. Fowler, J.J. (1994). *Analysis of dynamic testing performed on structural clay tile infilled frames (Doctoral dissertation) Oak Ridge National Lab*. (ORNL), Oak Ridge, TN (United States).
66. Frederiksen, V. (1992). Membrane effect in laterally loaded masonary walls. A second order phenomenon. in Proceedings of the 6th Canadian Masonry Symposium. University of Saskatchewan, Saskatoon, Canada.
67. Furtado, A., Rodrigues, H., Arede, A., & Varum, H. (2015). Simplified macro-model for infill masonry walls considering the out-of-plane behavior. Earthquake Engineering & Structural Dynamics, 45(4), 507–524.
68. Furtado, A., Rodrigues, H., Arêde, A., & Varum, H. (2016). Experimental evaluation of out-of-plane capacity of masonry infill walls. Engineering Structures, 111, 48–63. https://doi.org/10.1016/j.engstruct.2015.12.013.
69. Furtado, A., Rodrigues, H., Arêde, A., & Varum, H. (2018a). Out-of-plane behavior of masonry infilled RC frames based on the experimental tests available: A systematic review. Construction and Building Materials, 168, 831–848. https://doi.org/10.1016/j.conbuildmat.2018.02.129

70. Furtado, A., Rodrigues, H., Arêde, A., & Varum, H. (2020). Effect of the Panel Width Support and Columns Axial Load on the Infill Masonry Walls Out-Of-Plane Behavior. Journal of Earthquake Engineering, 24(4), 653–681. https://doi.org/10.1080/13632469.2018.1453400
71. Furtado, A., Rodrigues, H., Varum, H., and Arêde, A. (2018b). Mainshock-aftershock damage assessment of infilled RC structures. Engineering Structures, 175, 645–660.
72. Gautam, D., Adhikari, R., & Rupakhety, R. (2021). Seismic fragility of structural and non-structural elements of Nepali RC buildings. Engineering Structures, 232, 111879.
73. Gesualdi, G., Viggiani, L. R. S., and Cardone, D. (2020). Seismic performance of RC frame buildings accounting for the out-of-plane behavior of masonry infills. Bulletin of Earthquake Engineering, 18(11), 5343–5381.
74. Giordano, N., De Luca, F., Sextos, A., and Maskey, P. N. (2019). Derivation of fragility curves for URM school buildings in Nepal. Proceedings of the 13th International Conference on Applications of Statistics and Probability in Civil Engineering (ICASP13), Korean Institute of Bridge and Structural Engineers, 1581–1588.
75. Goel, R.K., Chopra A.K. (1997). Period Formulas for Moment-Resisting Frame Buildings. Journal of Structural Engineering, 123 (11). https://doi.org/10.1061/(ASCE)0733-9445(1997)123:11(1454).
76. Hak, S., Morandi, P., & Magenes, G. (2014.). Out-of-plane experimental response of strong masonry infills. In: 2nd European conference on earthquake engineering and seismology, 12.
77. Haseltine B.A. (1976). Design of laterally loaded wall panels. Proceedings of the British Ceramic Society, 5(24). UK: Load Bearing Brickwork. Stoke-on-Trent, p. 115–26.

78. Hashemi, S.A., & Mosalam, K.M. (2007). Seismic evaluation of reinforced concrete buildings including effects of infill masonry walls. PEER 2007/100 2007; Univ. of California, Berkeley, CA.
79. Henderson, R., Jones, W., Burdette, E., & Porter, M. (1993). The effect of prior out-of-plane damage on the in-plane behavior of unreinforced masonry infilled frames. In: The Fourth DOE Natural Phenomena Hazards Mitigation Conference.
80. Hendry A.W. (1973). The lateral strength of unreinforced brickwork. The Institution of Structural Engineers, 51(2):43–50.
81. Hendry, A.W. (1998). Structural Masonry, II. ed., Palgrave.
82. Holický, M., Retief, J. V., & Sýkora, M. (2016). Assessment of model uncertainties for structural resistance. Probabilistic Engineering Mechanics, 45, 188–197.
83. Holmes, M. (1961). Steel Frames with Brickwork and Concrete Infilling, in: Proceedings of the Institution of Civil Engineers 473–478.
84. Ingham, J., Walsh, K., Dizhur, D., & Shafaei, J. (2014). Out-of-plane testing of unreinforced brick infill walls within structural frames. (Final Report – LR0441) https://doi.org/10.13140/RG.2.1.4750.0245
85. IS (Indian Standards). 2000. *Plain and reinforced concrete - code of practice* (fourth revision). IS 456. New Delhi: IS.
86. Kadysiewski, S., & Mosalam, K.M. (2009). Modeling of unreinforced masonry infill walls considering in-plane and out-of-plane interaction. PEER 2008/102 2009; Univ. of California, Berkeley, CA.
87. Klingner, R.E., Rubiano N.R., Bashandy, T.R., & Sweeney, S.C. (1996). Evaluation and analytical verification of shaking table data from infilled frames, part 2: Out-of-plane behavior. In: Proceedings of the 7th North American Masonry Conference (pp. 521-532), Colorado: Elsevier Science Ltd.

88. Komaraneni, S., Rai, D. C., & Singhal, V. (2011). Seismic Behavior of Framed Masonry Panels with Prior Damage When Subjected to Out-of-Plane Loading. Earthquake Spectra, 27(4), 1077–1103. https://doi.org/10.1193/1.3651624
89. Koutas, L. N., & Bournas, D. A. (2019). Out-of-Plane Strengthening of Masonry-Infilled RC Frames with Textile-Reinforced Mortar Jackets. Journal of Composites for Construction, 23(1), 04018079. https://doi.org/10.1061/(ASCE)CC.1943-5614.0000911
90. Liauw, T.C. (1972). An Approximate Method of Analysis for Infilled Frames with or without Opening. Building Science, 7(4):233-238.
91. Liberatore, L., AlShawa, O., Marson, C., Pasca, M., & Sorrentino, L. (2020). Out-of-plane capacity equations for masonry infill walls accounting for openings and boundary conditions. Engineering Structures, 207, 110198.
92. Lunn, D. S., & Rizkalla, S. H. (2011). Strengthening of Infill Masonry Walls with FRP Materials. Journal of Composites for Construction, 15(2), 206–214. https://doi.org/10.1061/(ASCE)CC.1943-5614.0000088.
93. Madan, A., Reinhorn, A.M., Mander, J.B., & Valles, R.E. (1997). Modeling of masonry infill panels for structural analysis. Journal of structural engineering, 123:10(1295), 1295-1302.
94. Mainstone, R.J. (1974). Supplementary Note on the Stiffness and Strengths of Infilled Frames. Presented at the Building Research Station, Garston, UK.
95. Mander, J.B., Priestley, M.J.N., & Park, R (1988). Theoretical stress-strain model for confined concrete. Journal of structural engineering, 114(8), 1804–26.

96. McDowell, E.L., McKee, K.E. & Sevin. E. (1956). Arching action theory of masonry walls. Journal of Structural Division 82 (2): 15–18. https://doi.org/10.1061/JSDEAG.0000019
97. McKenna, F., Fenves, G., Scott, M., & Jeremic, B. (2000). Open System for Earthquake Engineering Simulation (OpenSees), Berkeley.
98. Mehrabi, A.B., Shing, P.B., Schuller, M.P., & Noland, J.L. (1996). Experimental evaluation of masonry-infilled RC frames. Journal of Structural Engineering, 122(3), 228–237.
99. Menegotto, M., & P. E. Pinto. (1973). Method of analysis for cyclically loaded RC plane fames including changes in geometry and non-elastic behavior of elements under combined normal force and bending. In Proc., IABSE Symp. on the Resistance and Ultimate Deformability of Structures Acted on by Well Defined Repeated Loads, 15–22. Zürich, Switzerland: International Association for Bridge and Structural Engineering.
100. Milanesi, R. R., Morandi, P., Manzini, C. F., Albanesi, L., & Magenes, G. (2020). Out-of-plane Response of an Innovative Masonry Infill with Sliding Joints from Shaking Table Tests. Journal of Earthquake Engineering, 1–35. https://doi.org/10.1080/13632469.2020.1739173
101. Misir, I. S., Ozcelik, O., Girgin, S. C., & Yucel, U. (2016). The Behavior of Infill Walls in RC Frames Under Combined Bidirectional Loading. Journal of Earthquake Engineering, 20(4), 559–586. https://doi.org/10.1080/13632469.2015.1104748
102. Moghadam, H., & Goudarzi, N. (2010). Transverse Resistance of Masonry Infills. ACI Structural Journal, 7.
103. Moghaddam H., Dowling P., & Ambraseys N. (1988). Shaking table study of brick masonry infilled frames subjected to seismic actions. in 9th World Conference on Earthquake Engineering. Tokyo.

104. Morandi P., Hak S., & Magenes G. (2013). Simplified out-of-plane resistance verification for slender clay masonry infills in RC frames. Proceedings of the XV ANIDIS, L'Ingegneria Sismica in Italia, Padua, Italy.
105. Moreno-Herrera, J., Varela-Rivera, J., & Fernandez-Baqueiro, L. (2016). Out-of-Plane Design Procedure for Confined Masonry Walls. Journal of Structural Engineering, 142(2), 04015126.
106. Mosalam, K.M., & Günay, S. (2015). Progressive collapse analysis of RC frames with URM infill walls considering in-plane/out-of-plane interaction. Earthquake Spectra, 31(2), 921–943.
107. Moșoarcă, M., Petrus, C., Stoian, V., & Anastasiadis, A. (2016). Behaviour of masonry infills subjected to out of plane seismic actions. Part 2: Experimental testing. In: Modena C, da Porto F, Valluzzi MR (Eds), Brick Block Mason. 0 ed., CRC Press, (pp. 1293–300).
108. Nanayakkara, K. I. U., and Dias, W. P. S. (2016). Fragility curves for structures under tsunami loading. Natural Hazards, 80(1), 471–486.
109. NTC 2018. *Decreto Ministeriale delle Infrastrutture e dei Trasporti 17 gennaio 2018, Aggiornamento delle* «Norme tecniche per le costruzioni».
110. NZS (New Zealand Standard). (2004). Structural Design Actions, Part 5: Earthquake Actions – New Zealand. NZS 1170.
111. NZSEE (New Zealand Society for Earthquake Engineering Structural Engineering Society). 2017. *The Seismic Assessment of Existing Buildings (the Guidelines), Part C – Detailed Seismic Assessment: NZSEE*.

112. Onat, O., Correia, A. A., Lourenço, P. B., & Koçak, A. (2018). Assessment of the combined in-plane and out-of-plane behavior of brick infill walls within reinforced concrete frames under seismic loading. Earthquake Engineering & Structural Dynamics, 47(14), 2821–2839. https://doi.org/10.1002/eqe.3111
113. Palieraki V., Zeris C., Vintzileou E., and Adami C-E. 2018. “In-plane and out-of-plane response of currently constructed masonry infills.” Eng Struct., 177, 103–16.
114. Palieraki, V., Zeris, C., Vintzileou, E., & Adami, C.-E. (2018). In-plane and out-of plane response of currently constructed masonry infills. Engineering Structures, 177, 103–116. https://doi.org/10.1016/j.engstruct.2018.09.047
115. Panagiotakos, T.B., Fardis, M.N. (1996). Seismic response of infilled RC frames structures. Proc., XXI World Conf. of Earthquake Engineering, Acapulco, Mexico.
116. Pantò, B., Silva, L., Vasconcelos, G., & Lourenço, P. B. (2019). Macro-modelling approach for assessment of out-of-plane behavior of brick masonry infill walls. Engineering Structures, 181, 529–549. https://doi.org/10.1016/j.engstruct.2018.12.019
117. Papia, M., L. Cavaleri, & M. Fossetti. (2003). Infilled frames: Developments in the evaluation of the stiffening effect of infills. Structural Engineering and Mechanics, 16 (6), 675–693.
118. Pasca M., Liberatore L., & Masiani R. (2017). Reliability of analytical models for the prediction of out-of-plane capacity of masonry infills. Struct Eng Mech., 64(6), 765–781.

119. Paulay, T., & Priestley, M.J.N. (1992). Seismic Design of Reinforced Concrete and Masonry Buildings. Wiley, c, 1992; New York.
120. Penava, D., Sigmund, V., & Kožar, I. (2016). Validation of A Simplified Micromodel for Analysis of Infilled RC Frames Exposed To Cyclic Lateral Loads. Bulletin of Earthquake Engineering 14, 2779–2804.
121. Pereira, M.F.P., Pereira, M.F.N., Ferreira, J.E.D., & Lourenço, P.B. (2011). Behaviour of masonry infill panels in RC frames subjected to in plane and out of plane loads. in: 7th International Conference on Analytical Models and New Concepts in Concrete and Masonry Structures.
122. Petrone, C., Magliulo, G., & Manfredi, G. (2014). Shake table tests for the seismic assessment of hollow brick internal partitions. Engineering Structures, 72, 203–214.
123. Petrone, C., Magliulo, G., and Manfredi, G. (2015). Seismic demand on light acceleration-sensitive nonstructural components in European reinforced concrete buildings: Seismic demand on acceleration-sensitive nonstructural components. Earthquake Engineering & Structural Dynamics, 44(8), 1203–1217
124. Petrus, C., Stoian, V., Moșoarcă, M., & Anastasiadis, A. (2015). Reinforced Concrete Frames with Masonry Infills. Out of Plane Experimental Investigation. Civil Engineering, 11.
125. Polyakov, S.V. (1960). On the Interaction between Masonry Filler Walls and Enclosing Frame When Loading in the Plane of the Wall. Translation in Earthquake Engineering. Earthquake Engineering Research Institute 36–42.

126. Preti, M., Migliorati, L., & Giuriani, E. (2015). Experimental testing of engineered masonry infill walls for post-earthquake structural damage control. Bulletin of Earthquake Engineering, 13(7), 2029–2049. https://doi.org/10.1007/s10518-014-9701-2
127. Rabinovitch, O., & Madah, H. (2011). Finite element modeling and shake-table testing of unidirectional infill masonry walls under out-of-plane dynamic loads. Engineering Structures, 33(9), 2683–2696. https://doi.org/10.1016/j.engstruct.2011.05.019
128. Ricci, P., De Luca, F., & Verderame, G. M. (2011). 6th April 2009 L'Aquila earthquake, Italy: reinforced concrete building performance. Bulletin of Earthquake Engineering, 9(1), 285–305.
129. Ricci, P., Di Domenico, M., & Verderame, G. M. (2018a). Experimental assessment of the in-plane/out-of-plane interaction in unreinforced masonry infill walls. Engineering Structures, 173, 960–978.
130. Ricci, P., Di Domenico, M., & Verderame, G. M. (2018b). Experimental investigation of the influence of slenderness ratio and of the in-plane/out-of-plane interaction on the out-of-plane strength of URM infill walls. Construction and Building Materials, 191, 507–522.
131. Ricci, P., Di Domenico, M., & Verderame, G. M. (2018c). Empirical-based out-of-plane URM infill wall model accounting for the interaction with in-plane demand." Earthquake Engineering & Structural Dynamics, 47(3), 802–827.
132. Ricci, P., Di Domenico, M., and Verderame, G. M. (2020). Effects of the In-Plane/Out-of-Plane Interaction in URM Infills on the Seismic Performance of RC Buildings Designed to Eurocodes. Journal of Earthquake Engineering, 1–35.

133. Rodrigues, H., Varum, H., & Costa, A. (2010). Simplified macro-model for infill masonry panels. Journal of Earthquake Engineering, 14:390–416.

134. Sagar, S. L., Singhal, V., & Rai, D. C. (2019). In-Plane and Out-of-Plane Behavior of Masonry-Infilled RC Frames Strengthened with Fabric-Reinforced Cementitious Matrix. Journal of Composites for Construction, 23(1), 04018073. https://doi.org/10.1061/(ASCE)CC.1943-5614.0000905

135. Shing, P.B., & Mehrabi, A.B. (2002). Behaviour and Analysis of Masonry-Infilled Frames. Progress in Structural Engineering and Materials 4, 320–331.

136. Silva, L., Vasconcelos, G., Lourenço, P., & Akhoundi, F. (2016). Experimental evaluation of a constructive system for earthquake resisting masonry enclosure walls. In C. Modena, F. da Porto, & M. R. Valluzzi (Eds.), Brick and Block Masonry (0 ed., pp. 1333–1340). CRC Press. https://doi.org/10.1201/b21889-165

137. Singhal, V., & Rai, D. C. (2016). In-plane and out-of-plane behavior of confined masonry walls for various toothing and openings details and prediction of their strength and stiffness: Behavior of Confined Masonry Walls and Predictions of Their Response. Earthquake Engineering & Structural Dynamics, 45(15), 2551–2569. https://doi.org/10.1002/eqe.2783

138. Smith B.S., & Carter, C. (1969). A Method of Analysis for Infilled Frames, in: Proceedings of the Institution of Civil Engineers, 31–48.

139. Smith, B (1962). Lateral Stiffness of Infilled Frames. ASCE Journal of Structural Division 88, 183–199.

140. Spesdar, R. (2017). Experimental investigation on the out-of-plane behaviour of the concrete masonry infilled RC frames [Master's thesis]. Dalhousie University https://dalspace.library.dal.ca/handle/10222/72875
141. Talaat, M., & Mosalam, K.M. (2009). Modeling progressive collapse in reinforced concrete buildings using direct element removal, *Earthquake Engineering and Structural Dynamics*, **38**(5), 609-634.
142. Thiruvengadam, V. (1985). On the Natural Frequencies of Infilled Frames. Earthquake Engineering & Structural Dynamics 13, 401–419.
143. Timoshenko S., & Woinowsh-Krieger S. 1959. Theory of plates and shells. McGraw-Hill.
144. Tondelli, M., Beyer, K., & DeJong, M. (2016). Influence of boundary conditions on the out-of-plane response of brick masonry walls in buildings with RC slabs: Out-of-plane Response of Masonry Walls in Buildings with RC Slabs. Earthquake Engineering & Structural Dynamics, 45(8), 1337–1356. https://doi.org/10.1002/eqe.2710
145. Tu, Y.-H., Chuang, T.-H., Liu, P.-M., & Yang, Y.-S. (2010). Out-of-plane shaking table tests on unreinforced masonry panels in RC frames. Engineering Structures, 32(12), 3925–3935.
146. Tu, Y.-H., Liu, P.-M., & Lin, H.-P. (2007). Out-of-Plane Seismic Behavior of Unreinforced Masonry In-filled Walls. New Horizons and Better Practices, 1–10. https://doi.org/10.1061/40946(248)48.
147. Vailati, M., Monti, G., & Di Gangi, G. (2018). Earthquake-Safe and Energy-Efficient Infill Panels for Modern Buildings. In R. Rupakhety & S. Ólafsson (Eds.), Earthquake Engineering and Structural Dynamics in Memory of Ragnar Sigbjörnsson (Vol. 44, pp. 233–261). Springer International Publishing. https://doi.org/10.1007/978-3-319-62099-2_12

148. Varela-Rivera, J. L., Navarrete-Macias, D., Fernandez-Baqueiro, L. E., & Moreno, E. I. (2011). Out-of-plane behaviour of confined masonry walls. Engineering Structures, 33(5), 1734–1741. https://doi.org/10.1016/j.engstruct.2011.02.012

149. Varela-Rivera, J., Moreno-Herrera, J., Lopez-Gutierrez, I., & Fernandez-Baqueiro, L. (2012a). Out-of-Plane Strength of Confined Masonry Walls. Journal of Structural Engineering, 138(11), 1331–1341. https://doi.org/10.1061/(ASCE)ST.1943-541X.0000578

150. Varela-Rivera, J., Polanco-May, M., Fernandez-Baqueiro, L., & Moreno, E. I. (2012b). Confined masonry walls subjected to combined axial loads and out-of-plane uniform pressures. Canadian Journal of Civil Engineering, 39(4), 439–447. https://doi.org/10.1139/l2012-021

151. Varum, H., Furtado, A., Rodrigues, H., Dias-Oliveira, J., Vila-Pouca, N., & Arêde, A. (2017). Seismic performance of the infill masonry walls and ambient vibration tests after the Ghorka 2015, Nepal earthquake. Bulletin of Earthquake Engineering, 15(3), 1185–1212.

152. Verlato N., Guidi .G, & Da Porto F. (2014). Experimental testing and numerical modelling of infill masonry walls subjected to in-plane damage. In: Proc of the Second European Conference on Earthquake Engineering and seismology, 25-29, Istanbul, Turkey.

153. Verlato, N., Guidi, G., da Porto, F., & Modena, C. (2016). Innovative systems for masonry infill walls based on the use of deformable joints: Combined in-plane/out-of-plane tests. In C. Modena, F. da Porto, & M. R. Valluzzi (Eds.), Brick and Block Masonry (0 ed., pp. 1359–1366). CRC Press. https://doi.org/10.1201/b21889-168

154. Wang, C. (2017). Experimental investigation on the out-of-plane behaviour of concrete masonry infilled frames [Master's thesis]. Dalhousie University https://dalspace.library.dal.ca/handle/10222/73415

155. Wang, X., Zhao, W., Kong, J., & Zhao, T. (2020). Numerical Investigation on the Influence of In-Plane Damage on the Out-of-Plane Behavior of Masonry Infill Walls." Advances in Civil Engineering, 2020, 1–16.
156. Žarni´c ,R., & Gostič, S. (1997). Masonry infilled frames as an effective structural subassemblage. Seismic design methodologies for the next generation of codes, 1997; P. Fajfar and H. Krawinkler, eds., A.A. Balkema, Rotterdam, Netherlands, 335–346.
157. Žarnić, R., Gostič, S., Crewe, A. J., & Taylor, C. A. (2001). Shaking table tests of 1:4 reduced-scale models of masonry infilled reinforced concrete frame buildings. Earthquake Engineering & Structural Dynamics, 30(6), 819–834. https://doi.org/10.1002/eqe.39

Appendix A

OpenSees code for the macro-model generation and IP/OoP analysis

An example of the OpenSees code for the generation of macro-model for the IP and OoP analysis of infilled frames. The provided code refers to the case of specimen #1 from Ricci et al. (2018a).

This total file can be saved as file_analysis.tcl

```
# Create ModelBuilder (with three-dimensions and 6 DOF/node)
wipe;

model basic -ndm 3 -ndf 6;

# Set parameters for model geometry
set width    2620.0; #centre to centre of columns
set height   2100.0; # centre to centre of beams

# Create nodes
#    tag       X      Y      Z
node  1      0.0     0.0     0.0
node  2    $width     0.0     0.0
node  3     0.0   $height   0.0
node  4    $width   $height   0.0
node  61    [expr  $width/2] [expr $height/2] 0.0
node  62    [expr  $width/2] [expr $height/2] 0.0
node  63   [expr  $width/2] [expr $height/2] 0.0
node  64   [expr  $width/2] [expr $height/2] 0.0
node  5     [expr  $width/2]  0.0 0.0
node  9     [expr  $width/2] $height 0.0
node  12    0.0 [expr $height/2] 0.0
node  15   [expr  $width] [expr $height/2] 0.0
```

```
# Define boundary conditions
#    tag   DX   DY  DZ   RX RY RZ
fix   1     1      1     1     1     1    1
fix   2     1      1     1     1     1    1
fix   3     0      0     1     1     1    0
fix   4     0     0    1    1    1    0
fix   5     0     1    0    1    1    0
fix   9     0     0    0    1    1    0

# Assign any constraints

 equalDOF 61 62  3
          equalDOF 61 63  3
                              equalDOF 61 64  3

# Define materials for frames
# -------------------------------------------
# CONCRETE
# Core concrete (confined)
#                                  Tag     fpc        epsc0      fpcu      epscu     lambda   ft        Et
uniaxialMaterial Concrete02   1     -43.2      -0.0030    -12.96   -0.0060      0.1     0.36     0.00
# Cover concrete (unconfined)
#                                  Tag     fpc        epsc0      fpcu      epscu     lambda   ft        Et
uniaxialMaterial Concrete02   2     -36.0      -0.0024    -10.8    -0.0048      0.1     0.36     0.00

# -------------------------------------------
# this information can be saved in a separate a file material_concrete.tcl and can be sourced to main file as
# source material_concrete.tcl
# -------------------------------------------

# STEEL: Reinforcing steel
set fy 550.0;      # Yield stress
set E 210000.0;    # Young's modulus
#                                  tag     fy   E0     b         R0   cR1     CR2
uniaxialMaterial Steel02  3   $fy   $E   0.015     18   0.925    0.15

# -------------------------------------------
# this information can be saved in a separate a file material_steel.tcl and can be sourced to main file  as
# source material_steel.tcl
```

```
# ----------------------------------------
# Define materials for equivalent struts
# ----------------------------------------
# MASONRY
#                                  Tag   fpc     epsc0      fpcu      epscu   lambda    ft     E
uniaxialMaterial Concrete02        4    -0.85  -0.00049   -0.51    -0.0057   0.07      0.0    0.0 ;
uniaxialMaterial Concrete02        5    -0.85  -0.00049   -0.51    -0.0057   0.07      0.0    0.0 ;

#Assign MinMax material to control the drop of the stress in the masonry fibers
# uniaxialMaterial MinMax $matTag $otherTag <-min $minStrain> <-max $maxStrain>
uniaxialMaterial MinMax    404       4          -min -0.0057       -max 0.0057
uniaxialMaterial MinMax    505       5          -min -0.0057       -max 0.0057

# ----------------------------------------
# this information can be saved in a separate a file material_masonry.tcl and can be sourced to main file as
# source material_masonry.tcl
# ----------------------------------------

# Define cross-section for COLUMNS
# ----------------------------------------
# set some paramaters for COLUMNS sections
set colWidth 200.0;
set colDepth 270.0;

set cover  25.0
set As    113.09;    # area of 1 bar

set y1 [expr $colDepth/2.0]
set z1 [expr $colWidth/2.0]

section Fiber 1 {

        # Create the concrete core fibers
   patch rect 1 30 30 [expr $cover-$y1] [expr $cover-$z1] [expr $y1-$cover] [expr $z1-$cover]

        # Create the concrete cover fibers (top, bottom, left, right)
   patch rect 2 20 20  [expr -$y1] [expr $z1-$cover] $y1 $z1
   patch rect 2 20 20  [expr -$y1] [expr -$z1] $y1 [expr $cover-$z1]
   patch rect 2 20 20  [expr -$y1] [expr $cover-$z1] [expr $cover-$y1] [expr $z1-$cover]
```

```
   patch rect 2 20 20  [expr $y1-$cover] [expr $cover-$z1] $y1 [expr $z1-$cover]

            # Create the reinforcing fibers (left, middle, right)
   layer straight 3 3 $As [expr -$y1+$cover] [expr $z1-$cover] [expr $y1-$cover] [expr $z1-$cover]
   layer straight 3 2 $As [expr -$y1+$cover] 0.0 [expr $y1-$cover] 0.0
   layer straight 3 3 $As [expr -$y1+$cover] [expr -$z1+$cover] [expr $y1-$cover] [expr -$z1+$cover]
}

# Define Shear and torsion for 3D column section
set Gc 25000000
set C250 10
#_____________________
# column torsional stiffness
# Linear elastic torsion for the column

set GJcol [expr $Gc*$C250*$colDepth*pow($colWidth,3)]
set GAcol [expr $Gc*$colWidth*$colDepth*5/6]

uniaxialMaterial Elastic 500 $GJcol
uniaxialMaterial Elastic 501 $GAcol

# Attach torsion to the column section
#section Aggregator $secTag   $matTag1 $string1 $matTag2 $string2 ..... <-section $sectionTag>
section Aggregator     10              501        Vy       501            Vz       500   T      -section 1
#_____________________
# Define cross-section for BEAMS
# ------------------------------------------
# set some paramaters for BEAMS sections
set beamWidth 270.0; insert the actual depth of beam
set beamDepth 200.0; insert the actual width of beam

set cover  25.0
set Ast    78.54;     # area of 1 bar

set zb1 [expr $beamDepth/2.0]
set yb1 [expr $beamWidth/2.0]

section Fiber 4 {
```

```
            # Create the concrete core fibers
   patch rect 1 40 40 [expr $cover-$yb1] [expr $cover-$zb1] [expr $yb1-$cover] [expr $zb1-$cover]

            # Create the concrete cover fibers (top, bottom, left, right)
   patch rect 2 20 10  [expr -$yb1] [expr $zb1-$cover] $yb1 $zb1
   patch rect 2 20 10  [expr -$yb1] [expr -$zb1] $yb1 [expr $cover-$zb1]
   patch rect 2 20 10  [expr -$yb1] [expr $cover-$zb1] [expr $cover-$yb1] [expr $zb1-$cover]
   patch rect 2 20 10  [expr $yb1-$cover] [expr $cover-$zb1] $yb1 [expr $zb1-$cover]

            # Create the reinforcing fibers (left, middle, right)
   layer straight 3 3 $Ast [expr -$yb1+$cover] [expr $zb1-$cover] [expr -$yb1+$cover] [expr -$zb1+$cover]
   layer straight 3 3 $Ast [expr $yb1-$cover] [expr $zb1-$cover] [expr $yb1-$cover] [expr -$zb1+$cover]
}
# ----------------------------------------
# Define Shear and torsion for 3D beam section
# BEAM torsional stiffness
# Linear elastic torsion for the equivalent strut

set GJbea [expr $Gc*$C250*$beaDepth*pow($beaWidth,3)]
set GAbea [expr $Gc*$beaWidth*$beaDepth*5/6]

uniaxialMaterial Elastic 54 $GJbea
uniaxialMaterial Elastic 55 $GAbea

# Attach torsion to the beam section
#section Aggregator $secTag  $matTag1 $string1 $matTag2 $string2 ..... <-section $sectionTag>
section Aggregator      40          55          Vy      55          Vz    54    T         -section 4

#_____________________
# Define cross-section for foundation BEAMS
# ----------------------------------------
# set some paramaters for foundation beam
set beaWidth 400.0; insert the actual depth of beam
set beaDepth 400.0; insert the actual width of beam

set cover  40.0
set Ast    254.47;     # area of 1 bar
```

```
# some variables derived from the parameters
set zb1 [expr $beaDepth/2.0]
set yb1 [expr $beaWidth/2.0]

section Fiber 200 {

        # Create the concrete core fibers
   patch rect 1 40 40 [expr $cover-$yb1] [expr $cover-$zb1] [expr $yb1-$cover] [expr $zb1-$cover]

       # Create the concrete cover fibers (top, bottom, left, right)
   patch rect 2 20 10  [expr -$yb1] [expr $zb1-$cover] $yb1 $zb1
   patch rect 2 20 10  [expr -$yb1] [expr -$zb1] $yb1 [expr $cover-$zb1]
   patch rect 2 20 10  [expr -$yb1] [expr $cover-$zb1] [expr $cover-$yb1] [expr $zb1-$cover]
   patch rect 2 20 10  [expr $yb1-$cover] [expr $cover-$zb1] $yb1 [expr $zb1-$cover]

        # Create the reinforcing fibers (left, middle, right)
   layer straight 3 4 $Ast [expr -$yb1+$cover] [expr $zb1-$cover] [expr -$yb1+$cover] [expr -$zb1+$cover]
   layer straight 3 2 $As 0 [expr -$zb1+$cover] 0.0 [expr $zb1-$cover]
   layer straight 3 4 $Ast [expr $yb1-$cover] [expr $zb1-$cover] [expr $yb1-$cover] [expr -$zb1+$cover]
}
#_____________________________________

# Define Shear and torsion for 3D beam section
# BEAM torsional stiffness
# Linear elastic torsion for the equivalent strut

set GJbea [expr $Gc*$C250*$beaDepth*pow($beaWidth,3)]
set GAbea [expr $Gc*$beaWidth*$beaDepth*5/6]

uniaxialMaterial Elastic 64 $GJbea
uniaxialMaterial Elastic 65 $GAbea

# Attach torsion to the beam section
#section Aggregator $secTag $matTag1 $string1 $matTag2 $string2 ..... <-section $sectionTag>
section Aggregator     2000    65 Vy      65 Vz    64 T      -section 200
#_____________________
```

```
# Define cross-section for struts
#the geometry of the struts can be saved in a separate file geometry_strut.tcl and source to main file as
# source geometry_strut.tcl
# -----------------------------------------
# DIAGONAL STRUT

set dWidth 440.6; # wd'
set dDepth 198.2;  # t'

set coverstr 10.0;

set Asp   0.5;     # area of 1 bar

# some variables derived from the parameters
set zs1 [expr $dDepth/2.0]
set ys1 [expr $dWidth/2.0]

section Fiber 3 {

        # Create the concrete core fibers
  patch rect 404 30 30 -$ys1 -$zs1 $ys1 $zs1

        # Create the reinforcing fibers (left, middle, right)
  layer straight 3 3 $Asp [expr -$ys1+$coverstr] [expr $zs1-$coverstr] [expr -$ys1+$coverstr] [expr -$zs1+$coverstr]
  layer straight 3 2 $Asp [expr -$ys1/2] [expr $zs1-$coverstr] [expr -$ys1/2] [expr -$zs1+$coverstr]
  layer straight 3 2 $Asp 0.0  [expr $zs1-$coverstr] 0.0 [expr -$zs1+$coverstr]
  layer straight 3 2 $Asp [expr $ys1/2] [expr $zs1-$coverstr] [expr $ys1/2] [expr -$zs1+$coverstr] ;
 layer straight 3 3 $Asp [expr $ys1-$coverstr] [expr $zs1-$coverstr] [expr $ys1-$coverstr] [expr -$zs1+$coverstr]
}
# -----------------------------------------

# Define Shear and torsion for strut
# torsional stiffness for diagonal struts
# Linear elastic torsion for the strut

set GJstr [expr $Gc*$C250*$strDepth*pow($strWidth,3)]
set GAstr [expr $Gc*$strWidth*$strDepth*5/6]
```

```
uniaxialMaterial Elastic 60 $GJstr
uniaxialMaterial Elastic 61 $GAstr

# Attach torsion to the diagonal strut
#section Aggregator $secTag $matTag1 $string1 $matTag2 $string2 ..... <-section $sectionTag>
section Aggregator     30          61              Vy         61          Vz         60    T       -section 3
# ------------------------------------------

# VERTICAL STRUT
# ------------------------------------------
set vWidth 231.4; wv'
set vDepth 198.2; t'

set coverv 10.0

set Asv    1.0;     # area of 1 bar

 # some variables derived from the parameters
set zv [expr $vDepth/2.0]
set yv [expr $vWidth/2.0]

 section Fiber 5 {

              # Create the concrete core fibers
  patch rect 505 30 30 -$yv -$zv $yv $zv

              # Create the reinforcing fibers (left, middle, right)
  layer straight 3 3 $Asv [expr -$yv+$coverv] [expr $zv-$coverv] [expr $yv-$coverv] [expr $zv-$coverv]
  layer straight 3 2 $Asv [expr -$yv+$coverv] 0.0 [expr $yv-$coverv] 0.0
 layer straight 3 3 $Asv [expr -$yv+$coverv] [expr -$zv+$coverv] [expr $yv-$coverv] [expr -$zv+$coverv]
 }
# ------------------------------------------

# torsional stiffness for vertical strut
# Linear elastic torsion for the strut

set GJv [expr $Gc*$C250*$vDepth*pow($vWidth,3)]
set GAv [expr $Gc*$vWidth*$vDepth*5/6]
```

```
uniaxialMaterial Elastic 70 $GJv
uniaxialMaterial Elastic 71 $GAv

# Attach torsion to the vertical strut
# section Aggregator $secTag $matTag1 $string1 $matTag2 $string2 ..... <-section $sectionTag>
section Aggregator     50          71          Vy          71          Vz       70    T        -section 5

# HORIZONTAL STRUT
# -----------------------------------------
set hWidth 180.2; wh'
set hDepth 198.2; t'

set coverstrh 10.0

set Ash    1.0;     # area of 1 bar

# some variables derived from the parameters
set zh [expr $hDepth/2.0]
set yh [expr $hWidth/2.0]

 section Fiber 8 {

            # Create the concrete core fibers
  patch rect 505 30 30 -$yh -$zh $yh $zh

            # Create the reinforcing fibers (left, middle, right)
  layer straight 3 3 $Ash [expr -$yh+$coverstrh] [expr $zh-$coverstrh] [expr -$yh+$coverstrh] [expr -$zh+$coverstrh]
  layer straight 3 2 $Ash 0 [expr $zh-$coverstrh] 0 [expr -$zh+$coverstrh]
  layer straight 3 3 $Ash [expr $yh-$coverstrh] [expr $zh-$coverstrh] [expr $yh-$coverstrh] [expr -$zh+$coverstrh]
 }
# -----------------------------------------

# torsional stiffness for horizontal strut
# Linear elastic torsion for the strut

set GJh [expr $Gc*$C250*$hDepth*pow($hWidth,3)]
```

```
set GAh [expr $Gc*$hWidth*$hDepth*5/6]

uniaxialMaterial Elastic 80 $GJh
uniaxialMaterial Elastic 81 $GAh

# Attach torsion to the horizontal strut
# section Aggregator $secTag $matTag1 $string1 $matTag2  $string2 ..... <-section $sectionTag>
section Aggregator     80          81          Vy          81          Vz          80    T      -section 8
# ------------------------------------------


#Build Geometry
# ------------------------------------------

#COLUMNS
# Geometry of column elements
#                    tag
set tranfColTag  1;
geomTransf Linear 1  0 0 1; # Geometric Transformation

set np 5; # Number of integration points along length of element
set eleType  forceBeamColumn;


# Create the nonlinear COLUMNS using Beam-column elements
#  element   elementtype          tag   ndI    ndJ    nsecs  secID   transfTag
element     $eleType               1     1     12     $np    10     $tranfColTag
element     $eleType              101    12    3      $np    10     $tranfColTag
element     $eleType               2     2     15     $np    10     $tranfColTag
element     $eleType              202    15    4      $np    10     $tranfColTag

#BEAMS#
# Geometry of beam elements
#                       tag
set tranfBeamTag    2;
geomTransf Linear 2  0 0 1; # Geometric Transformation

set np 5; # Number of integration points along length of element
set eleType  forceBeamColumn;
```

```
# Create the nonlinear BEAMS  using Beam-column elements
#  element   elementtype              tag   ndI   ndJ  nsecs  secID   transfTag
set eleType forceBeamColumn;
element      $eleType                 3     3     9     $np    40     $tranfBeamTag
element      $eleType                 4     9     4     $np    40     $tranfBeamTag
element      $eleType                 11    1     5     $np    2000   $tranfBeamTag
element      $eleType                 12    5     2     $np    2000   $tranfBeamTag

#STRUTS#
# Geometry of diagonal strut elements
#                          tag
set tranfDiagonalTag  3;
geomTransf Corotational 3  0 0 1; # Geometric Transformation

# Create the nonlinear BEAMS using Beam-column elements
set eleType2 dispBeamColumn;
set nps 9;
#  element   elementtype              tag   ndI    ndJ    nsecs   secID    transfTag
element      $eleType2                5     3      61     $nps    30     $tranfDiagonalTag
element      $eleType2                6     61     2      $nps    30     $tranfDiagonalTag
element      $eleType2                7     1      62     $nps    30     $tranfDiagonalTag
element      $eleType2                8     62     4      $nps    30    $tranfDiagonalTag

# Geometry of vertical strut elements
#                          tag
set tranfVerticalTag    4
geomTransf Corotational 4  0 0 1; # Geometric Transformation
set eleType2 dispBeamColumn
set nps 9
#  element   elementtype              tag   ndI   ndJ   nsecs   secID    transfTag
Element      $eleType2                9     5     63     $nps    50     $tranfVerticalTag
element $eleType2                     10     63    9     $nps    50     $tranfVerticalTag


# Geometry of horizontal strut elements
#                           tag
set tranfHorizontalTag  5;
geomTransf Corotational 5  0 0 1; # Geometric Transformation
```

```
set eleType2 dispBeamColumn;
set nps 9
#  element   elementtype          tag   ndI   ndJ   nsecs  secID     transfTag
Element      $eleType2            13    12    64    $nps    80    $tranfHorizontalTag
element      $eleType2            14    64    15    $nps    80    $tranfHorizontalTag


# Define gravity loads
# --------------------

# Set a parameter for the axial load
set P   0.0;              # No axial load used in the experiment

# Create a Plain load pattern with a Linear TimeSeries
pattern Plain 1 "Linear" {
      # Create nodal loads at nodes 3 & 4
            #    nd    FX     FY       FZ     Mx   My  Mz
            load  3   0.0   [expr -$P] 0.0   0.0  0.0  0.0
            load  4   0.0   [expr -$P] 0.0   0.0  0.0  0.0

}
# ------------------------------
# End of model generation
# ------------------------------

# ------------------------------
# Start of analysis generation
# ------------------------------

system BandGeneral; # Create the system of equation, a sparse solver with partial pivoting

constraints Transformation; # Create the constraint handler, the transformation method

numberer RCM; Create the DOF numberer, the reverse Cuthill-McKee algorithm

test NormDispIncr 1.0e-12  1000  3; # Create the convergence test, the norm of the residual with a tolerance
                                    # of 1e-12 and a max number of iterations of 10

algorithm Newton; # Create the solution algorithm, a Newton-Raphson algorithm
```

```
integrator LoadControl 0.1; # Create the integration scheme, the LoadControl scheme using steps of 0.1

analysis Static; # Create the analysis object

# ------------------------------
# End of analysis generation
# ------------------------------

# ------------------------------



# Finally perform the analysis
# ------------------------------
analyze 10; # perform the gravity load analysis, requires 10 steps to reach the load level

# Gravity analysis completed

# Define in-plane loads (cyclic)
# --------------------
# set parameters for in-plane analysis
loadConst -time 0.0 ; # Set the gravity loads to be constant & reset the time in the domain
set LunitTXT 1
set node 3
set dof  1

set LCol 1965; # height of the infilled frame =height of infill+half the height of the top beam

# display displacement shape of the column
#.....................................................#
            recorder display "Displaced shape1" 10 10 500 500 -wipe
            prp 200. 100. 1;
            vup  0 1 0;
            vpn  0 0 1;
            display 1 5 4
#..................................#

# Create a recorder to monitor nodal displacements
recorder Node -file IPd.out -node 3  -dof 1    disp; # IPd.out  file is created
```

```
recorder Node -file IPf.out -node 1 2 -dof 1    reaction; # IPf.out file  is created


set IDctrlNode $node;# node where displacement is monitored
set IDctrlDOF $dof;                    # degree of freedom of the control node

set iDmax "0.001 0.0016" ; # 0.16% drift exact according to test
% set iDmax "$IPdrift" ; # drift history can be source directly from the file IPdrift.tcl

# vector of displacement-cycle peaks, in terms of storey drift ratio
set Dincr [expr 0.00005*$LCol]; # displacement increment for pushover analysis
set Fact $LCol;
set CycleType Full;    #Full for the in-plane cyclic analysis
set Ncycles 1; # specify the number of cycles at each peak

# create load pattern for lateral pushover load
 set Hload  1;
 set iPushNode "3 4";  # define nodes where lateral load is applied in static lateral analysis
 pattern Plain 200 Linear {;          # define load pattern -- generalized
              foreach PushNode $iPushNode {
                           load $PushNode $Hload 0.0 0.0 0.0 0.0 0.0
               }
 }

# ---------- set up analysis parameters
source LibAnalysisStaticParameters.tcl;       #constraints Handler, DOF numberer, system-of equations,
convergence Test, solution Algorithm, integrator,, obtain this file from Openees library
#  ---------------------------------
# perform Static Cyclic Displacements Analysis
source LibGeneratePeaks.tcl; # obtain this file from Openees library

set fmt1 "%s Cyclic analysis: CtrlNode %.1i, dof %.1i, Disp=%.4f %s"; # format for screen/file output
foreach Dmax $iDmax {
     set iDstep [GeneratePeaks $Dmax $Dincr $CycleType $Fact]; # this proc is defined above
     for {set i 1} {$i <= $Ncycles} {incr i 1} {
                          set zeroD 0
                          set D0 0.0
        foreach Dstep $iDstep {
                                  set D1 $Dstep
```

```
                                set Dincr [expr $D1 - $D0]
                                integrator DisplacementControl  $IDctrlNode $IDctrlDOF $Dincr
                                analysis Static
                                # -----------------------first analyze command----------------------
                                set ok [analyze 1]
                                # -----------------------if convergence failure-------------------------
            if {$ok != 0} {
                        if {$ok != 0} {
                                                        puts "Trying NewtonWithLineSearch .."
                                                        algorithm NewtonLineSearch 0.8
                                                        set ok [analyze 1]
                                                        algorithm $algorithmTypeStatic
                          }
                           if {$ok != 0} {
                             set putout [format $fmt1 "PROBLEM" $IDctrlNode $IDctrlDOF [nodeDisp $IDctrlNode $IDctrlDOF] $LunitTXT]
                             puts $putout
                             return -1
                             }; # end if
              }; # end if

              set D0 $D1;                               # move to next step
         }; # end Dstep
     };                     # end i
}; # end of iDmaxCycl
# ------------------------------------------------------------------------------------------------
if {$ok != 0 } {
puts [format $fmt1 "PROBLEM" $IDctrlNode $IDctrlDOF [nodeDisp $IDctrlNode $IDctrlDOF] $LunitTXT]
} else {
puts [format $fmt1 "DONE"  $IDctrlNode $IDctrlDOF [nodeDisp $IDctrlNode $IDctrlDOF] $LunitTXT]
}

# in-plane analysis completed
# ------------------------------------------------------------------------------------------------


# Define out-of-plane loads (cyclic)
# --------------------
```

```
# set parameters for out-of-plane analysis
loadConst -time 0.0

#display displacement shape of the column
#.....................................................#
recorder display "Displaced shape2" 20 20 500 500 -wipe
prp 300. 200. 1;
vup  0 0 1;
vpn  0 1 0;
display 1 5 40
#.....................................................#

set H 1;     # Reference lateral load
set nodo 61; #node where out-of-plane load is applied
set dof 3; dof of the control node 61

# Set lateral load pattern with a Linear TimeSeries
pattern Plain 3 "Linear" {

        #     node    FX  FY   FZ   MX   MY   MZ
      load   $nodo    0.0  0.0   $H   0.0    0.0      0.0
}
# ---------- set up analysis parameters
set dU 0.2; # Displacement increment
#                                          node  dof     init  Jd    min     max
integrator DisplacementControl  $nodo $dof   $dU   1    $dU     $dU

# Create a recorder to monitor node.....................................................
recorder Node -file OoPd.out  -node 61 -dof 3 disp;  # OoPd.out  file is created
recorder Node  -file OoPf.out  -node 1 2 3 4  -dof 3  reaction; # OoPf.out  file is created
# ---------------------------------
# End of recorder generation
# ---------------------------------

# Perform the out-of-plane analysis
# -------------------------------
set maxU 60;                    # Max displacement accordint to test result
set currentDisp 0.0;
```

```
set ok 0

while {$ok == 0 && $currentDisp < $maxU} {

        set ok [analyze 1]

        # if the analysis fails try initial tangent iteration
        if {$ok != 0} {
          puts "regular newton failed .. lets try an initial stiffness for this step"
          test NormDispIncr 1.0e-4  2000
          algorithm ModifiedNewton
                #-initial
          set ok [analyze 1]
          if {$ok == 0} {puts "that worked .. back to regular newton"}
          test NormDispIncr 1.0e-4  2000
          algorithm Newton
        }

  set currentDisp [nodeDisp $nodo $dof]
}

if {$ok == 0} {
  puts "Pushover analysis completed SUCCESSFULLY";
} else {
  puts "Pushover analysis FAILED";
}
wipe;
```

Appendix B

MATLAB code for linking the randomly generated parameters with OpenSees for IP/OoP analysis of infilled frames and storage of information for the fragility calculation

```
%Clear and close all
clc
clear
close all

% _____________________________________________________________________
% Define the dimension of the frame
width = 2900.0; % c/c distance between the columns for aspect ratio 1.0
height = 3000.0; % c/c height of the beam

% Define geometry of infill
l = 2600; % length of infill wall for aspect ratio 1.0
h = 2600; % height of infill wall for aspect ratio 1.0

%  calculate the geometry of struts
d = round(sqrt(width.^2+height.^2));
theta = round(atand(h/l),2);
wd = round(d./3);
wh = round(h-wd./cosd(theta));
wv = round(l-wd./sind(theta));

% _____________________________________________________________________
%Define number of samples for each variable of the random generation
nsamples = 400; % define accoridng to number of output assumed
n = 1:nsamples;
% _____________________________________________________________________

% Generation of random variables with uniform distribution
% _____________________________________________________________________
for i = 1:nsamples;
```

```
   t(i) = 100+rand(1)*200; % maximum value equals to 300 ; % case of orthotropic masonry
   f(i) = 20+rand(1)*10; % maximum value equals to 30
   % dri(i) = rand(1)*0.007; % maximum value equals to 0.7%; % case of low IP damage
   % dri(i) = 0.007+rand(1)*0.007; % maximum value equals to 1.4%; % case of medium IP damage

   dri(i) = 0.014+rand(1)*0.006; % maximum value equals to 2.0%; % case of low high damage

end

tm = round(t,3); % roundup to a integer valued
fc = round(f,3); % roundup to a integer valued
drift = round(dri,4); % roundup to a integer valued

% calculate the volume of the infill wall
V = l*h*tm/1000000000; % unit m3
% _____


% % Generation of random variables with gaussian distribution
% _____
masonry_case = 1; % type 1 for orthotropic case and 2 for isotropic case

if masonry_case ==1
% CASE OF ORTOTROPIC MASONRY (low strength hollow masonry)
fmv = 0;
mfmv = 2; %mean
std0 = 1; %dev. standard
j = 0;

while length(fmv)<nsamples

   x=mfmv+std0*randn(1);

   if x<=3 && x>=1
      j=j+1;
      fmv(j)=x;
   end
end
```

```
% Generation random values of fmv2 from the fmv vector
fmv2=randsample(fmv,nsamples); % to calulate fmh based on fmv2 so that fmh+fmv is not always 4
% Elastic modulus of masonry (ortotropic)
Emv = 1000*fmv;
fmh = -fmv2+4;
Emh = 1000*fmh;

fm = sqrt(fmv.*fmh);
Em = sqrt(Emv.*Emh);

elseif masonry_case ==2
% CASE OF ISOTROPIC MASONRY (solid masonry)
fmi=0;
mfm=5; %mean
std0=1.0; %dev. standard
jj=0;

while length(fmi)<nsamples

   y=mfm+std0*randn(1);
                if y<=7 && y>=3
                   jj=jj+1;
                   fmi(jj)=y;
                end
end
% _____________________________________________________________________

fm = round(fmi,1); % roundup the vlue to 1 decimal place

% _____________________________________________________________________
% Elastic modulus of masonry (isotropic)
Em=1000*fm;
end

% _____________________________________________________________________

% Calculate values of fmEm
% _____________________________________________________________________
```

```
fmEm = fm .*Em; % .* ensures scalar multiplication
% _____

% Calculate values of fmo
% _____

for i= 1:nsamples
        if (fmEm(i) > 40000)
        fmo(i) = 3;
        else
        fmo(i) = round(0.61+0.0001.*fmEm(i)-10^(-9).*fmEm(i)^2,3);
        end
end
% _____

% Calculate values of fmu
% _____
fmu = round(0.6.*fmo,3);
% _____

%Calculate values of emo
% _____
for i = 1:nsamples
        if (fmEm(i) > 90000)
        emo(i) = 0.04;
        else
        emo(i) = round(4*10^(-8).*fmEm(i)+0.00039,4);
        end
end
% _____

% Calculate values of emu
% _____
emu = 10.*emo;
% _____

% Calculate the surrgate (transformed) geometry of struts wd', wv' and wh' as well as thickness t'
% _____
```

```
for i = 1:nsamples
        wd_tr(i) = round(fmo(i)./fm(i)*wd);
        wv_tr(i) = round(fmo(i)./fm(i)*wv);
        wh_tr(i) = round(fmo(i)./fm(i)*wh);
        t_tr(i) = round(fm(i)./fmo(i)*tm(i));
end
% _____________________________________________________________________

% calculate the properties of concrete
% _____________________________________________________________________

a = sqrt(fc);
k = 1.2; % effect of confinement
Ec = round(5000.*a,0);
eco = round(2.*fc./Ec,4);
fc2 = round(0.4.*fc,2);
ecu = round(2.*eco,4);
kfc = round(k.*fc,2);
kfc2 = round(0.4.*kfc,2);
lambda_c = 0.1 ;  % ratio of unloading stiffness for concrete
ft = 0;
Et = 0;
% _____________________________________________________________________

lambda_m = 0.07 ; % ratio of unloading stiffness for masonry
% _____________________________________________________________________


% _____________________________________________________________________
% linking MATLAB with OpenSees to perform analysi and store data
% _____________________________________________________________________

for i=1:nsamples
   fprintf('the analysis number is:%d\n',i); % to track the ongoing analysis number
   % Input variable
   % create a file name material_concrete.tcl
   fid=fopen('material_concrete.tcl', 'wt'); % create a file name material_concrete.tcl
```

```
    fprintf(fid,'uniaxialMaterial Concrete02  1  %g %#g %#g %g %#g %#g %#g\n',-kfc(i),-eco(i), -
kfc2(i), -ecu(i),lambda_c,ft,Et);
    fprintf(fid,'uniaxialMaterial Concrete02  2  %g %#g %#g %g %#g %#g %#g\n',-fc(i), -eco(i), -fc2(i),
-ecu(i),lambda_c,ft,Et);
   fclose(fid);

 % create a file name IPdrift.tcl
% _____________________________________________________________________
  fid=fopen('IPdrift.tcl', 'wt'); % create a file name IPdrift.tcl
  fprintf(fid,'set IPdrift  %#g\n',drift(i));
  fclose(fid);
 % _____________________________________________________________________

 % create a file name material_masonry.tcl
% _____________________________________________________________________
 fid=fopen('material_masonry.tcl', 'wt'); % create a file name material_masonry.tcl
 fprintf(fid,'uniaxialMaterial Concrete02  4  %g %#g %#g %g %#g %#g %#g\n',-fmo(i), -emo(i), -fmu(i),
-emu(i),lambda_m,ft,Et);  % defined using Concrete02 law
fprintf(fid,'uniaxialMaterial Concrete02  5  %g %#g %#g %g %#g %#g %#g\n',-fmo(i), -emo(i), -fmu(i),
-emu(i),lambda_m,ft,Et);
fprintf(fid,'set  ustrain %#g\n',-emu(i)); # ustrain is to be used with MinMax material
fclose(fid);
% _____________________________________________________________________

 % create a file name geometry_strut.tcl
% _____________________________________________________________________
 fid=fopen('geometry_strut.tcl', 'wt');
 fprintf(fid,'set strWidth  %d\n',wd_tr(i));
 fprintf(fid,'set strDepth  %d\n',t_tr(i));
 fprintf(fid,'\n');
 fprintf(fid,'set vWidth  %d\n',wv_tr(i));
 fprintf(fid,'set vDepth  %d\n',t_tr(i));
 fprintf(fid,'\n');
 fprintf(fid,'set hWidth  %d\n',wh_tr(i));
 fprintf(fid,'set hDepth  %d\n',t_tr(i));
 fclose(fid);
% _____________________________________________________________________
```

```
   % Run OpenSees file from MATLAB
%-------------------------------------------------------------------------------
   if tm(i)< 200
   !opensees file_analysis_d+h+v.tcl; % for all struts in the model
            else
   !opensees file_analysis_d+h.tcl; % no horizontal strut in the model
   End
%% note: file_analysis is the mainfile prepared as shown in Appendix A %%
%-------------------------------------------------------------------------------------------


 % Import output variables in MATLAB
%-------------------------------------------------------------------------------------------
            load('IPf.out');  % data is loaded from the file name IPf.out
            load('IPd.out');  % data is loaded from the file name IPd.out
            IPload=-(IPf(:,1)+IPf(:,2))/1000;
            IPdisplacement=IPd(:,1);

            load('Output/OoPf.out'); % data is loaded from the file name OoPf.out
            load('Output/OoPd.out'); % data is loaded from the file name OoPd.out
            OOPload=-(OOPf(:,1)+OOPf(:,2)+OOPf(:,3)+OOPf(:,4))/1000;
            OOPdisplacement=OOPd(:,1);
%-------------------------------------------------------------------------------------------


  % Identify maximum OOP force and locate corresponding displacement
%-------------------------------------------------------------------------------------------
   [max_OOPforce,location_maxOOPforce]= max(OOPload);% select maximum force and its location
% select displacement at maximum OOP force
   OOP_Displacement(i)=OOPdisplacement(location_maxOOPforce,1);
   OOP_Force(i)=max(OOPload(:,1)); % this is equal to  max_OOPforce
%-------------------------------------------------------------------------------------------


 % Identify the one-third of OOP force and locate corresponding displacement
%-------------------------------------------------------------------------------------------
    OOPforce_third= max_OOPforce/3; % one third of the maximum OOP force
% to ensure displacement corresponding to one-third force is not taken from the softening branch
    OOPload_select= OOPload(1:location_maxOOPforce,1);
```

```
   [val,idx]= min(abs(OOPforce_third-OOPload_select));
% one-third of maximum OOPforce requested
   OOPforce_req= OOPload(idx);
% displaacement corresponding to one-third of maximum OOPforce requested
OOPdis_req= OOPdisplacement(idx);
 %-------------------------------------------------------------------------------------------------

   % Print the input and output in a file
%-------------------------------------------------------------------------------------------------
   if masonry_case ==1
   fid=fopen('result_numerical_ortho.txt', 'at'); % create a file result_njumerical_ortho.txt
   fprintf(fid,'%#g %#g %#g %#g %#g %#g %#g %#g %#g %#g %#g %#g %#g %#g %#g\n', fc(i),
   Ec(i),drift(i),tm(i),fmv(i),Emv(i),fmh(i),Emh(i),fm(i),Em(i),OOP_Force(i),OOP_Displacement(i),V(i),
OOPforce_req,OOPdis_req);
   fclose(fid);

   elseif masonry_case ==2
   fid=fopen('result_numerical_iso.txt', 'at'); % create a file result_njumerical_iso.txt
   fprintf(fid,'%#g %#g %#g %#g %#g %#g %#g %#g %#g %#g\n', fc(i), Ec(i), drift(i), tm(i),
fm(i),Em(i),OOP_Force(i),OOP_Displacement(i),V(i),OOPforce_req,OOPdis_req);
   fclose(fid);
   end
%-------------------------------------------------------------------------------------------------

end
```